UNIVERSIDADE
BEIRA INTERIOR

Contribution to the Physical Understanding of Supercritical Fluid Flows: A Computational Perspective

Leandro Barbosa Magalhães

Tese para obtenção do Grau de Doutor em
Engenharia Aeronáutica
(3º ciclo de estudos)

Orientador: Prof. Doutor André Resende Rodrigues da Silva

Júri:
Prof. Doutor Joaquim Mateus Paulo Serra
Prof. Doutor José Carlos Fernandes Pereira
Prof. Doutor Jorge Manuel Martins Barata
Prof. Doutor Carlos Frederico Neves Bettencourt da Silva
Prof. Doutor Daniel Cardoso Vaz
Prof. Doutor André Resende Rodrigues da Silva
Prof. Doutor Miguel Rosa Oliveira Panão
Prof. Doutorora Ana Sofia Oliveira Henriques Moita

22 de Dezembro de 2022

Declaração de Integridade

Eu, Leandro Barbosa Magalhães, que abaixo assino, estudante com o número de inscrição 2308 de Engenharia Aeronáutica da Faculdade de Engenharia, declaro ter desenvolvido o presente trabalho e elaborado o presente texto em total consonância com o **Código de Integridades da Universidade da Beira Interior**.

Mais concretamente afirmo não ter incorrido em qualquer das variedades de Fraude Académica, e que aqui declaro conhecer, que em particular atendi à exigida referenciação de frases, extratos, imagens e outras formas de trabalho intelectual, e assumindo assim na íntegra as responsabilidades da autoria.

Universidade da Beira Interior, Covilhã, 10 de janeiro de 2023

Assinado por: **Leandro Barbosa Magalhães**
Num. de Identificação: 13930509
Data: 2023.01.10 02:07:27+00'00'

CHAVE MÓVEL

”It is difficult to say what is impossible, for the dream of yesterday is the hope of today and the reality of tomorrow.”
Robert H. Goddard

Acknowledgments

First, I would like to take this opportunity to thank my supervisor, professor André Silva for his support and for giving me the opportunity of working on such an exciting subject.

I am also indebted to professor Jorge Barata for the long, fruitful discussions, his comments, and his experience not only thesis-related but which covered virtually all aspects of science.

I also want to express my gratitude to my parents for their support and guidance during my journey and Maria for her encouragement and support, and for building some of the schemes and figures I needed.

During these 4 years, I also had the chance to work with a few master's students: Francisco, Rúben, and João; thank you for your interest and the discussions.

Lastly, I would like to thank the jury members for the comments which helped improve this manuscript.

Covilhã, 10 January 2023
Leandro Magalhães

The present work was performed under the scope of activities at the Aeronautics and Astronautics Research Center (AEROG) of the Laboratório Associado em Energia, Transportes e Aeronáutica (LAETA), and was supported by the Fundação para a Ciência e Tecnologia (Grant No. SFRH / BD / 136381 / 2018, Project Nos. UID / EMS / 50022 / 2019 and UIDB / 50022 / 2020).

Resumo

A modelação de fluidos em regimes supercríticos e transcríticos é levada a cabo em condições características daquelas encontradas em motores foguete de propelente líquido, nos quais a demanda por rendimentos mais elevados, para que sejam atingidos impulsos específicos superiores, faz com que as condições nas câmaras de combustão excedam o ponto crítico de combustíveis e oxidantes. No presente documento, azoto é utilizado como um substituto da mistura oxigénio-hidrogénio para que o comportamento turbulento das misturas possa ser estudado sem as influências de efeitos de combustão e de reações químicas.

Por contraste com o uso generalizado na literatura de ferramentas computacionais com formulações compressíveis, aqui uma hipótese distinta é formulada e investigada, focada no comportamento incompressível mas de massa volúmica variável de fluidos em condições supercríticas e transcríticas. A hipótese incompressível mas de massa volúmica variável surge da semelhança de visualização, nomeadamente da medição da eficiência da mistura através do grau de abertura dos jatos. Este documento tem como objetivo avaliar as capacidades e limitações de um método computacional (*Reynolds-averaged Navier-Stokes*) desenvolvido com base na hipótese incompressível mas de massa volúmica variável, quando aplicado em condições transcríticas e supercríticas.

Baseado no conceito de *breakup* térmico proposto na literatura, a descrição mecânica de um jato supercrítico é complementada, demonstrando que a quantidade de calor recebida pelo jato dentro do injetor determina a possibilidade de uma transição de *liquid-like* para uma condição de *gas-like* ter lugar. O decaimento axial da massa volúmica e da temperatura de jatos supercríticos e transcríticos é previsto para um leque de condições e geometrias de complexidade crescente, desde a injeção de uma espécie química, primeiro em regime supercrítico e depois transcrítico, num ambiente em repouso, até à injeção coaxial de uma e de várias espécies.

Os resultados sugerem que a hipótese incompressível mas de massa volúmica variável é capaz de prever as condições experimentais com um bom grau de precisão, indo de encontro às previsões de métodos mais complexos baseados em *large eddy simulation*. Ademais, a necessidade de incluir o injetor nas simulações para uma descrição mais precisa do escoamento é demonstrada e os erros associados com a sua ausência avaliados através da comparação entre condições de fronteira adiabática e isotérmica. O método proposto demonstra também a sua capacidade em prever o campo de temperatura, sendo que se trata de um dos poucos métodos atualmente disponíveis validados em termos da massa volúmica e da temperatura.

Palavras-chave

injeção em condições supercríticas; motores foguete de propelente líquido; escoamento de massa volúmica variável; injeção coaxial

Resumo Alargado

A modelação de fluidos em regimes supercríticos e transcríticos é levada a cabo em condições características daquelas encontradas em motores foguete de propelente líquido, nos quais a demanda por rendimentos mais elevados para que sejam atingidos impulsos específicos superiores, faz com que as condições nas câmaras de combustão excedam o ponto crítico de combustíveis e oxidantes. Ferramentas numéricas precisas podem contribuir para uma redução do tempo de desenvolvimento e do custo da próxima geração de lançadores espaciais. No entanto, vários desafios subjacentes à modelação de fluidos nestes regimes são espectáveis, sejam eles devido às suas próprias peculiaridades em termos das variações não lineares dos diferentes parâmetros termofísicos ou ao processo de desenvolvimento dos veículos. No presente documento, azoto é utilizado como um substituto da mistura oxigénio-hidrogénio para que o comportamento turbulento das misturas possa ser estudado sem as influências de efeitos de combustão e de reações químicas. A mistura de fluidos não reativos é fixada pela estrutura do escoamento, ao passo que em escoamentos reativos, reações químicas e transmissão de calor contribuem para um grau de complexidade superior.

Por contraste com o uso generalizado na literatura de ferramentas computacionais com formulações compressíveis, aqui uma hipótese distinta é formulada e investigada, focada no comportamento incompressível mas de massa volúmica variável de fluidos em condições supercríticas e transcríticas. A hipótese incompressível mas de massa volúmica variável surge da semelhança de visualização, nomeadamente da medição da eficiência da mistura através do grau de abertura dos jatos. Este documento tem como objetivo avaliar as capacidades e limitações de um método computacional (*Reynolds-averaged Navier-Stokes*) desenvolvido com base na hipótese incompressível mas de massa volúmica variável, quando aplicado em condições transcríticas e supercríticas.

Baseado no conceito de *breakup* térmico proposto na literatura, a descrição mecânica de um jato supercrítico é complementada, demonstrando que a quantidade de calor recebida pelo jato dentro do injetor determina a possibilidade de uma transição, através da linha de Widom de *liquid-like* para uma condição de *gas-like* ter lugar. Para injeção em condições de *liquid-like* em que o jato não recebe energia suficiente para que a transição ocorra, uma região densa de massa volúmica constante é formada na entrada da câmara de combustão, designada como *dense core*. Por outro lado, quando a injeção ocorre em condições de *gas-like* uma região designada por *sloped core* é observada, o que mostra a influência do mecanismo de *breaukp* térmico nestas condições. Esta análise demonstra que a quantificação da transmissão de calor dentro do injetor é fundamental no sentido de dotar qualquer ferramenta computacional de capacidades preditivas. Deste modo, o decaimento axial da massa volúmica e da temperatura de jatos supercríticos e transcríticos é previsto para um leque de condições e geometrias de complexidade crescente, desde a injeção de uma espécie química primeiro em regime supercrítico e depois transcrítico num ambiente em repouso, até à injeção coaxial de uma e de várias espécies. A análise de injeção simples em condições supercríticas é complementada com a descrição de injeção transcrítica, onde a temperatura se encontra abaixo do ponto crítico, pelo que escoamento multifásico é espectável com consequente separação de fases. Aqui demonstra-se a capacidade do método em modelar o regime transcrítico em termos do decaimento da massa volúmica e da abertura do jato em termos da quantidade de movimento e da temperatura, sendo que este é mais elevado tendo em conta a temperatura, o que demonstra que a propagação de calor é dominante em relação ao transporte da quantidade de movimento. De seguida o método é posto à prova em configuração de injeção coaxial, para validação do campo de temperatura sendo que o injetor apresenta um recesso e as condições experimentais contemplam razões de velocidade (jato exterior para interior) elevadas, condizentes com o limite de estabilidade da combustão em motor foguete de propelente líquido. A zona de recirculação entre os jatos exterior e interior é capturada numericamente, permitindo a validação do campo de temperatura. Por fim, a análise é estendida a uma configuração coaxial em que azoto é injetado pelo orifício principal e hidrogénio através do orifício secundário. Ao passo que existem algumas incertezas em relação aos dados experimentais, o que não permite fazer uma comparação quantitativa, são demonstradas previsões semelhantes de ferramentas computacionais compressíveis baseadas em *large eddy simulation*.

Os resultados sugerem que a hipótese incompressível mas de massa volúmica variável é capaz de prever as condições experimentais com um bom grau de precisão, indo de encontro às previsões de métodos mais complexos baseados em *large eddy simulation* e *direct numerical simulation*. Ademais, a necessidade de incluir o injetor nas simulações para uma descrição mais precisa do escoamento é demonstrada e os erros associados com a sua ausência avaliados através da comparação entre condições de fronteira adiabática e isotérmica. O método proposto demonstra também a sua capacidade em prever o campo de temperatura, sendo que se trata de um dos poucos métodos atualmente disponíveis validados em termos da massa volúmica e da temperatura.

Abstract

The modeling of fluids at supercritical and transcritical regimes is addressed at conditions characteristic of liquid propelled rocket engines, whose increasing performance demands have led to conditions in the combustion chambers to exceed the critical point of both fuels and oxidizers in the pursuit of higher specific impulses. In the present document, nitrogen is used as a surrogate for the commonly encountered oxygen-hydrogen mixture so that turbulence mixing can be looked into without influences from combustion and chemically reacting effects.

In contrast to the widespread use of compressible formulations in the literature, a distinct hypothesis is formulated and investigated, focusing on fluids' incompressible but variable-density behavior at supercritical and transcritical conditions. The incompressible but variable-density hypothesis arose from the similarity of visualization data, namely measuring mixing efficiency through jet spreading rates. This document evaluates the capabilities and limitations of a computational method (Reynolds-averaged Navier-Stokes) developed based on the incompressible variable-density hypothesis when applied to supercritical and transcritical conditions.

Based on the so-called ”thermal breakup mechanism concept” proposed in the literature, the mechanical description of supercritical jets is complemented, demonstrating that the amount of heat a jet receives inside the injector determines if a change from supercritical liquid-to-gas-like condition takes place, highlighting the importance of including the injector flow in the computations. Axial density and temperature decay rates of supercritical and transcritical jets are predicted for a wide range of conditions and geometries of increasing complexity, ranging from single species injection at supercritical and later transcritical conditions into quiescent environments to coaxial single and multi-species configurations.

The results suggest that the incompressible but variable density hypothesis can sufficiently replicate the experimental data, rivaling the predictions of more sophisticated methods relying on large eddy simulation formulations. Moreover, the need to include the injector into the computations for an accurate flow description is demonstrated. Furthermore, the errors resulting from its absence are assessed and evaluated by comparing adiabatic and isothermal boundary conditions. Finally, the proposed solver has also demonstrated its capabilities in the temperature field predictions, making it one of the few solvers currently available to have been validated in terms of density and temperature.

Keywords

supercritical injection; liquid rocket propulsion; variable density flows; coaxial injection

Contents

List of Figures

List of Tables

List of Symbols

Non-dimensional Numbers

Kn	$\frac{\lambda}{L}$	Knudsen number
Pe	$\frac{VL}{\alpha}$	Péclet number
Pr	$\frac{\mu c_p}{\lambda}$	Prandtl number
Re	$\frac{\rho VL}{\mu}$	Reynolds number
y^+	$\frac{u_\tau y}{\nu}$	Local Reynolds number at the solid boundary

Roman Symbols

a, A'	-	Species-dependent parameter
A, B	-	Cubic EoS auxiliary parameters
a	$\mathrm{m^5 s^{-2}\,kg^{-1}}$	Attractive potential
b	$\mathrm{m^3\,kg^{-1}}$	Repulsive potential
c	$\mathrm{J\,kg^{-1}\,K^{-1}}$	Specific heat
c, C	-	Center
c, σ	-	Turbulence models' constants
D	-	Destruction term
d	m	Distance from the cell center to the nearest wall
	mm	Injector diameter
E	J	Total energy
e	J	Internal energy
F	-	Flux
F_s	-	Safety factor
$f_{\nu 1}$	-	SA model damping function
g	$\mathrm{m\,s^{-2}}$	Gravitational acceleration
H	J	Total enthalpy
h	J	Enthalpy
I	s	Impulse
	%	Turbulence intensity
l, L	-	Left
L	m	Representative physical length scale
M	-	Momentum ratio
$\mathcal{M}$	$\mathrm{g\,mol^{-1}}$	Molar mass
$\dot{m}$	$\mathrm{kg\,s^{-1}}$	Mass flow rate
N	-	Number of realizations
n	mol	Amount of substance
	-	Shape parameter
O	-	Truncation error
P	-	Production term
p	Pa	Pressure

q	$\mathrm{J\,s^{-1}}$	Heat transfer by conduction
$\mathcal{R}$	$\mathrm{J\,kg^{-1}\,mol^{-1}}$	Universal gas constant
r	m	Radial distance
r, R	-	Right
$\tilde{S}$	$\mathrm{rad\,s^{-1}}$	Modified vorticity
T	K	Temperature
$\mathcal{T}$	N	Thrust
t	s	Time
u, v	$\mathrm{m\,s^{-1}}$	Velocity
u_{τ}	$\mathrm{m\,s^{-1}}$	Friction velocity
v	$\mathrm{m^3\,mol^{-1}}$	Molar volume
V	$\mathrm{m\,s^{-1}}$	Representative physical velocity scale
x	m	Axial distance
Z	-	Compressibility factor

Greek Symbols

α	$\mathrm{m^2\,s^{-1}}$	Thermal diffusivity
θ	-	Under relaxation factor
γ	-	Adiabatic index
δ_{ij}	-	Kronecker's delta function
δ	-	Cubic EoS dependent parameter
Δ	-	Variation
ε	$\mathrm{m^2\,s^{-3}}$	Turbulence kinetic energy dissipation
ε/κ	K	Lennard-Jones energy parameter
θ	-	Under-relaxation factor
κ	$\mathrm{m^2\,s^{-2}}$	Turbulence kinetic energy
κ_B	$\mathrm{J\,kg^{-1}}$	Boltzmann constant
$\mathrm{\kappa}$	-	von Karman constant
λ	$\mathrm{W\,m^{-1}\,K^{-1}}$	Thermal conductivity
	m	Mean free path
μ	$\mathrm{Pa\,s}$	Dynamic viscosity
ν	$\mathrm{m^2\,s}$	Kinematic viscosity
$\tilde{\nu}$	$\mathrm{m^2\,s}$	Modified eddy viscosity
η	-	Dipole moment
ρ	$\mathrm{kg\,m^{-3}}$	Density
σ	nm	Lennard-Jones size parameter
ξ_{ij}, ζ_{ij}	-	Binary interation parameters
τ_{ij}	Pa	Shear stress tensor
ϕ	-	General property
Ω	$\mathrm{rad\,s^{-1}}$	Magnitude of the vorticity
	-	Collision integral
ω	-	Acentric factor

s^{-1}	Turbulence kinetic energy specific dissipation

Additional Turbulence Model Parameters

$f_{\nu 1}, f_{\nu 2}, \chi, g, r,$
$\psi, \psi_0, \psi_\kappa, \psi_\omega, \theta_1,$
$\theta_2, F_1, F_2, \arg_1, \arg_2,$
$\lambda, U^*, \eta, CD^+, \Pi_{ij},$
$\varepsilon_{ij}, C_{ijk}, \hat{\alpha}, \hat{\beta}, \hat{\gamma}$

Subscripts

a	Advection
c	Critical point condition
d	Diffusion
e	Nozzle exit condition
eff	Effective
i	Inner jet condition
i, j, k	Counters/Directional vectors
inj	Injection conditions
max	Maximum value
mix	Mixture
o	Outer jet condition
p	Isobaric
pb	Pseudoboiling
r	Reduced condition
ref	Reference
sp	Specific
t	Turbulence
v	Isochoric
w	Wall
0	Initial value
∞	Combustion chamber condition

Superscripts

$<>$	Ensemble average
$-$	Reynolds average
$'$	Reynolds fluctuation
$\tilde{}$	Favre average
$''$	Favre fluctuation
$*$	Normalized variable
0	Ideal gas
c	Critical enhancement

i	Inner
n	Iteration number
o	Outer
r	Departure function

Acronyms

AFRL	Air Force Research Laboratory
ATAG	Air Transport Action Group
BC	Boundary Conditions
BSL	Baseline
BWR	Benedict Webb Rubin
CFD	Computational Fluid Dynamics
DES	Detached Eddy Simulation
DLR	Deutches Zentrum für Luft und Raumfahrt
DNS	Direct Numerical Simulation
EoS	Equation of State
ESA	European Space Agency
FDM	Finite Difference Method
FK	Fluoroketone
FVM	Finite Volume Method
FWHM	Full Width at Half Maximum
GCI	Grid Convergence Index
HOT	Higher Order Terms
LIF	Laser-Induced Fluorescence
LITA	Laser-Induced Thermal Acoustics
LES	Large Eddy Simulation
LRE	Liquid Rocket Engine
NASA	National Aeronautics and Space Administration
NIST	National Institute of Standards
PDE	Partial Differential Equations
PR	Peng Robinson
QUICK	Quadratic Upstream Interpolation for Convective Kinematics
RANS	Reynolds-averaged Navier-Stokes
RK	Redlich Kwong
RLV	Reusable Launching Vehicles
RNG	Re-Normalization Group
SA	Spalart Allmaras
SGS	Sub-Grid Scale
SRK	Soave Redlich Kwong
SSME	Space Shuttle Main Engine
SST	Shear Stress Transport
VoF	Volume of Fluid

VR	Velocity Ratio

Chapter 1

Introduction

For billions of years, crystal formation in aqueous solutions at supercritical conditions has been a naturally occurring process in the depths of the planet [1]. However, only in the nineteenth century has this process been reproduced in the laboratory to create mineral crystals. In 1822 Cagniard de la Tour proved experimentally the existence of a critical temperature above which a pure substance could exist as neither a liquid nor a gas but as a fluid [2]. From this technological development to the conquest of the final frontier in the second half of the twentieth century, the replication of the natural process where fluids enter a supercritical state saw no end, and its applications rose in number and diversity [3, 4].

A fluid is considered in a supercritical state if both its pressure and temperature are above their critical point values, which identify pure fluids' characteristics. Additionally, the ratio between a variable value and its value at the critical point is labeled a reduced property. In this sense, reduced pressure and temperature are defined as $T_r = \frac{T}{T_c}$ and $p_r = \frac{p}{p_c}$, respectively, with p the pressure, T the temperature, r reduced condition and c the critical point condition. Consequently, reduced values of both pressure and temperature above 1 mean the fluid is in a supercritical state, as depicted in Figure 1.1.

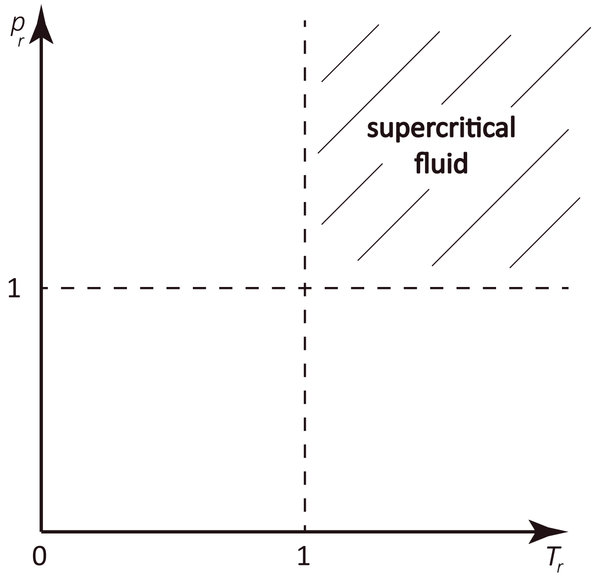

Figure 1.1: Definition of the supercritical regime.

1.1 Framework

In an age where space exploration is increasingly privatized, efforts are devoted toward the improvement of already-available concepts and designs under constrained budgets and reduced schedules to reduce costly trial-and-error phases of development [5]. Accurate and validated numerical tools may reduce new engines' development time and costs for the next generation of launchers. With the great demands and competition for cheaper and safer launchers' access to space, the design of advanced reusable launching vehicles (RLV) is required to have a higher payload-to-cost ratio and reliability [6].

The increasing performance demands of liquid rocket engines (LREs) have led to conditions in the combustion chamber exceeding the critical point of both the fuels and oxidizers to pursue higher specific impulses. In contrast to solid propelled rocket engines, LREs offer higher specific impulses and launch abort capabilities. Generally, a rocket engine operates as an energy conversion system [7] through the release of propellants' molecules' internal energy, its acceleration, and release through the bell-shaped nozzle.

A simple thermodynamic analysis of a rocket thrust chamber shows that the rocket size may decrease as chamber pressure increases. However, this results in higher thrust chamber stresses and heat transfer rates. For combustion, effects of increased chamber pressure decrease dissociation of the product molecules and increase effective heat release, which leads to higher specific impulse [8]. To produce a flame, fuel and an oxidizer are needed. The fuel and oxidizer are called rocket propellants. If a lower flame temperature is desired, it is usually better to have more fuel than an oxidizer, known as burning ”off-ratio” or ”fuel-rich”. This condition is less severe on the rocket engine than burning at stoichiometric oxygen-rich conditions.

The specific impulse, I_{sp}, is defined as the thrust per unit weight flow at sea level, according to equation 1.1, with $\mathcal{T}$ the thrust, g the gravitational acceleration, $\dot{m}$ the mass flow rate, and v_e the nozzle exit velocity.

$$I_{sp} = \frac{\mathcal{T}}{g\dot{m}} = \frac{v_e}{g} \quad (1.1)$$

Introducing steady and isentropic flow assumptions, an energy balance can be built (equation 1.2), considering $h + \frac{v^2}{2}$, where h is the enthalpy and its definition for an ideal gas c_pT, with ∞ indicating conditions in the combustion chamber, and c_p the isobaric specific heat.

$$c_pT_e + \frac{v_e^2}{2} = c_pT_\infty + \frac{v_\infty^2}{2} \quad (1.2)$$

Finally, defining the isobaric specific heat as a function of the adiabatic index, γ, and the ideal gas constant $\mathcal{R}$, the equation describing the specific impulse of a liquid propelled rocket engine is given according to equation 1.3.

$$I_{sp} = \frac{1}{g}\left[\frac{2\gamma \mathcal{R} T_\infty}{\gamma - 1}\left(1 - \left(\frac{p_e}{p_\infty}\right)^{\frac{\gamma-1}{\gamma}}\right)\right]^{0.5} \tag{1.3}$$

From equation 1.3 we can evaluate the conditions that make it possible to achieve a high specific impulse. It can be concluded that the combustion temperature (T_∞) needs to be high. This temperature results from the chemical interaction between fuel and oxidizers, whose molecular weight needs to be low. For example, considering the combination of oxygen/hydrogen, the mixture will burn at a specific temperature, the so-called adiabatic flame temperature, whose value arises from the heat of reaction. In this sense, the specific impulse depends on the propellants used to adjust the fuel-to-oxidizer ratio. In particular, LRE performance is greatly influenced by propellant mixing near the injector. Equation 1.3 indicates that besides adjusting the fuel-to-oxidizer ratio, the only option remaining to increase the specific impulse is the increase in engine operating pressure leading mixtures to supercritical regimes, where due to the vanishing surface tension, propellant atomization does not take place, resulting in propellant and oxidizer mixing to be sensitive to variations in pressure and temperature [9].

The improved performance of LREs associated with operation at high-pressure conditions [10] is not restricted to the pursuit of an improved specific impulse or even to rocket propulsion. The trend of increasingly higher engine operating pressure, seeking combustion efficiency and higher energy conversion rates extends to internal combustion engines [11, 12] and gas turbines [13, 14] alike. In addition, more efficient power combustion systems are also desired to reduce emissions. In fact, according to Figure 1.2 detailing the Air Transport Action Group (ATAG) goals, 50% of the reduction in the world's emissions of carbon dioxide (CO_2) until 2050 is expected to be achieved through the reduction of aircraft fuel burn. Since the level of emissions is determined by the combustion of fuels or propellants, high-efficiency, and clean combustion technologies are currently being explored [15, 16].

Fuel burn optimization is the common ground between rocket engines, gas turbines, and internal combustion engines, built upon the efficiency gains determined by high pressure and temperature conditions.

In fuel injection phenomena, both fuels and oxidizers' operating conditions can exceed their critical point as a means to increase the engine's efficiency [18–20]. A gas can be converted to a liquid at an arbitrary constant temperature by increasing the pressure. As temperature increases, so does the kinetic energy of the molecules, requiring a higher pressure to bring

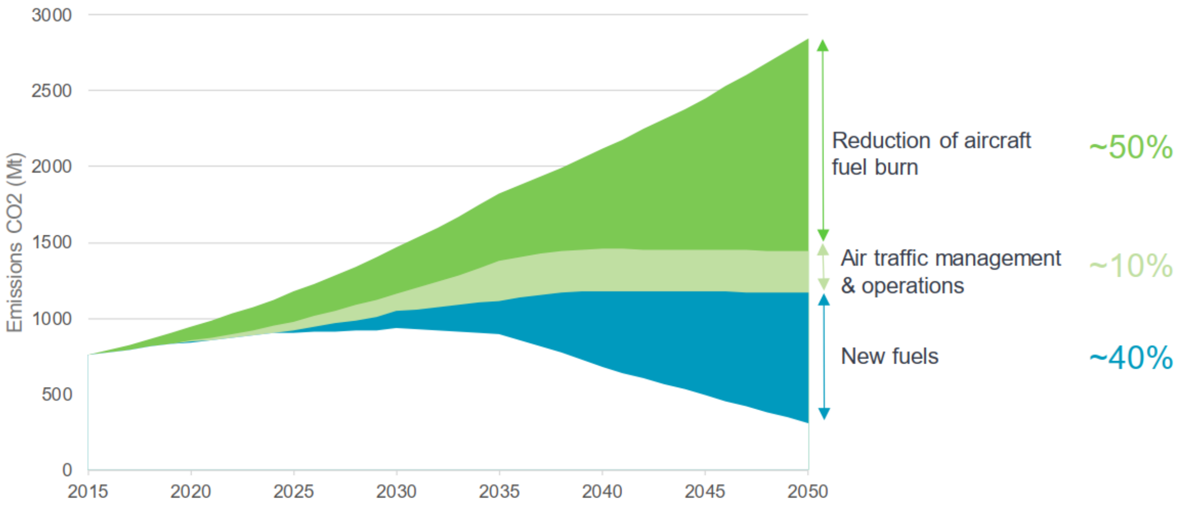

Figure 1.2: Schematics of the Air Transport Action Group (ATAG) goals and change drivers [17].

the gas to a liquid. The critical temperature marks when a transition to the liquid phase is no longer possible, no matter the applied pressure. The vapor pressure at the critical temperature is defined as the critical pressure. The critical point then marks the end of the vapor pressure line, where both temperature and pressure reach their critical values.

Supercritical mixing layers occur, for example, in various combustion engines and the planetary atmospheres of Jupiter and Venus. The deepest parts of Venus' atmosphere behave like a supercritical fluid [21], where the mixtures' molecular diffusion coefficient includes terms due to composition, temperature, and pressure gradients. On the other hand, gas giants such as Saturn and Jupiter have their atmospheres comprised mostly of supercritical hydrogen (H_2) [22, 23]. Other examples of naturally occurring supercritical phenomena include hydrothermal vents [24], volcanic lava and oil in underwater reservoirs [25] and supercritical water (H_2O) in underwater volcanoes [3]. Supercritical H_2O is also used as a coolant in nuclear reactors [26–28]. Supercritical fluids are broadly used in chemical-related applications [4], for instance, in the pharmaceutical industry as solvents [29, 30].

The versatility of supercritical fluids results from their particular thermophysical properties [4], which can be tuned to best suit any particular application.

1.2 Liquid Rocket Engines Operation

A widely used propellant combination in liquid rocket engines is liquid oxygen-hydrogen (LOX-H_2), where LOX works as an oxidizer injected through a central orifice with a co-flowing H_2 stream working as a fuel. Propellants are injected into the thrust chamber by a coaxial injector (Figure 1.3), a configuration to be analyzed in detail in the present thesis and which can be encountered in several systems (old and new), such as the space shuttle main engine (SSME), depicted in Figure 1.4. LOX has been the choice of oxidizer since the V-2 rockets in the 1940's [31].

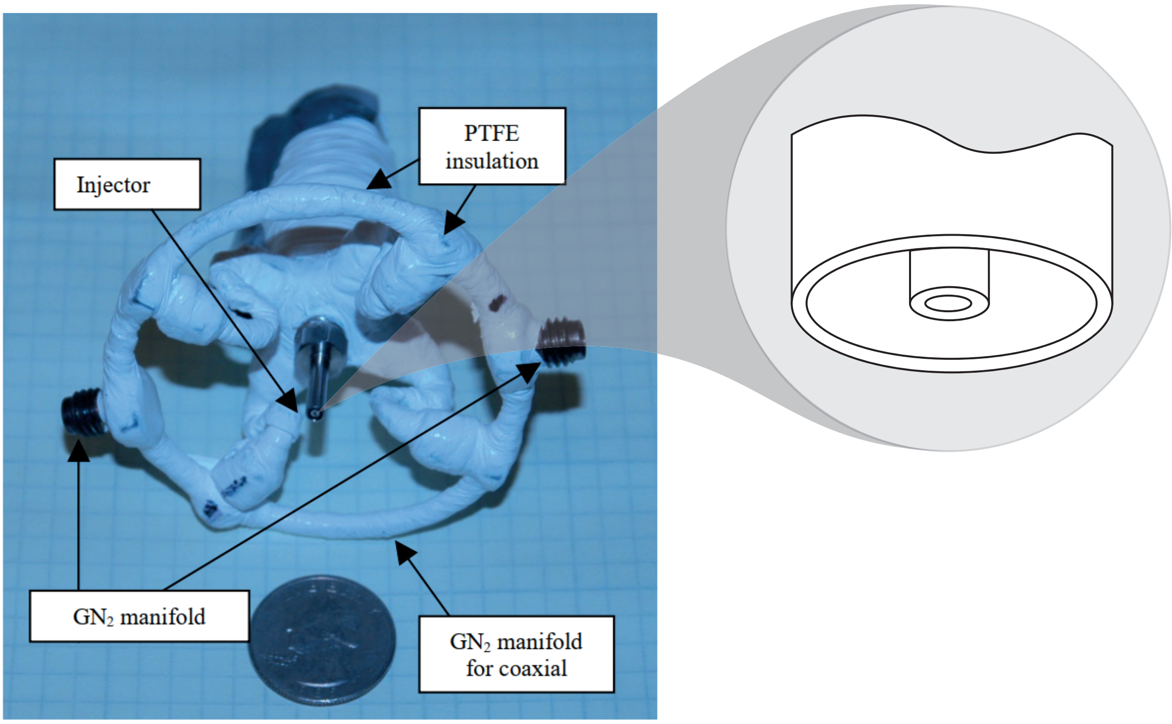

Figure 1.3: Example of a shear coaxial injector, adapted from Davis and Chehroudi [32].

The main component of the rocket engine which determines mixing characteristics and efficiency is the injector [33, 34]. Injection, incredibly close to the injector exit plane, determines mixing efficiency and disintegration [35] due to varying surface tension in multi-component mixing [36]. The study of injection is a challenging task due to the coupling of different phenomena such as diffusion, mixing, and combustion [37]. From Reynolds-averaged Navier-Stokes (RANS) to large eddy simulation (LES), Tucker et al. [38] compared the fidelity required to accurately model the injector flow field while maintaining the computational load within reasonable parameters. In this regard, the study of injection phenomena has evolved substantially from the dilute spray region analysis, located downstream from the injector exit plane [39]. For example, recent experimental results [10] show how the change of fluid properties at supercritical injection affects mixing, where it was concluded that for single-component mixing of fluoroketone injected into fluoroketone at different temperatures, mixing behavior is enhanced as the injected jet temperature increases.

In the coaxial injector, the two jets mix at the injector exit leading to interactions in the shear layer resulting in the jet breakup and the release of heat to produce thrust [32]. The distinction between jet and spray is based on the objective [25]. When dealing with the disintegration of fluid columns, the terminology jet is used, while when the objective is to track droplets that are separated from the jet, the term spray is more appropriate. However, oxygen is injected in a transcritical state (with its temperature below the critical point), while hydrogen is injected at supercritical conditions after being used for regenerative cooling. An experimental study was conducted by Kobayashi et al. [37] on the application of H_2 for regenerative cooling, while Ma et al. [40] considered the relevance of regenerative cooling in rocket engines, where one of the propellants is used to cool the combustion chamber prior to

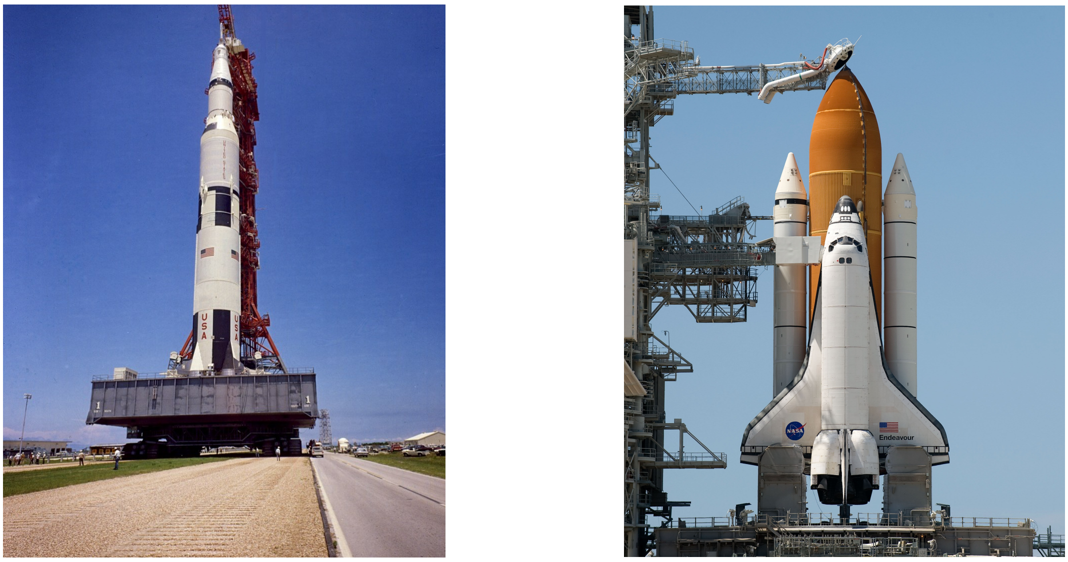

Saturn V

Space Shuttle

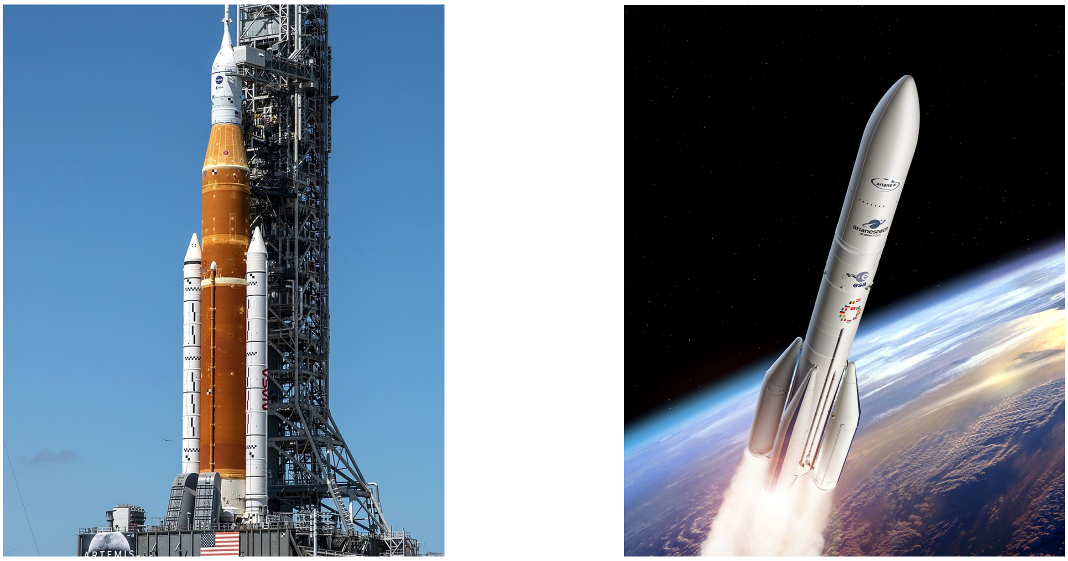

Space Launch System

Ariane 6

Figure 1.4: Historical Liquid Rocket Engines operating on LOx-H_2 propellant mixture (National Aeronautics and Space Administration (NASA) and European Space Agency (ESA)).

injection. Here, thermal stratification and wall heat fluxes [41, 42] play a significant role and lead to similar challenges as the modeling of injector flow and heat transfer. Additionally, conventional hydrocarbon fuels are being considered as coolants in new aircraft engine concepts [43]. Thermal stratification taking place in the cooling channels [44] and injectors [45] of liquid rocket engines is a challenge to the design of such systems, where the variations of thermophysical properties limit the fidelity of Nussel number-based correlations [46].

The LOX-H_2 mixture does not have a single critical point, as defined for pure fluids, but critical mixing lines [47], owing to the different critical point conditions of the individual species, depending on the amount of each chemical species at a given time. In order to study the behavior of such a mixture without the inclusion of combustion and reacting effects, nitrogen is employed [48] as a surrogate for its chemical similarity with oxygen.

1.3 Challenges

Challenges associated with the modeling of flows at transcritical and supercritical conditions can either derive from the complexities and non-linear behaviors of the various thermophysical parameters or from the development process of vehicles that operate at such conditions.

The increasing role of the private sector as a primary stakeholder in the space industry contributes to an improvement of already available concepts with restricted budgets and shortened development cycles, mitigating the trial-and-error phase of development to achieve a higher payload-to-cost ratio. At the same time, competition between companies increases the number of proprietary studies, which are needed by the scientific community to validate numerical solvers and solutions [49] and to develop generalizations at the expense of sophisticated equipment and complicated measurement techniques. For example, direct measurements of velocities and temperature distributions are difficult [50] due to the high pressures and the small diameters of injectors, making it a challenge to obtain relevant and needed quantitative measurements without perturbing the flow. Usually, sophisticated experimental techniques [12, 51] such as spectroscopy have been used through the years [52].

On the other hand, thermodynamic singularities, which refer to the non-linear behavior of thermodynamic properties at the critical point, need to be accurately replicated in any numerical effort dedicated to the successful description of supercritical fluid behavior. For example, when the isobaric specific heat becomes infinite at the critical point, the surface tension and latent heat become zero. Besides, the discontinuity between the liquid and gas phases observed at subcritical conditions disappears, resulting in single-phase behavior under supercritical conditions [53]. The resulting fluid will have liquid-like density and gas-like properties, with mass diffusion replacing vaporization as the governing parameter, dominating the jet atomization process.

Consequently, contradictions in theories between subcritical, transcritical, and supercritical conditions hinder the development of models which can accurately replicate the transition from one regime to the other, characterizing typical engine operation, such as in the case of jet engines, where operational regimes change between take-off/landing and cruise [54] or in LRE, where the mixing between propellants and oxidizers could lead to conditions in the combustion chamber below the critical point of an individual chemical species. High-pressure conditions in multicomponent mixtures led Harstad and Bellan [55] to propose a modified Lewis number formulation. For example, theories of liquid jet breakup in multiphase flows assume that the pressure and temperature are much lower than their critical values with clearly defined boundaries between liquid and gas, which is not the case at supercritical conditions [56] or at transcritical conditions where diffuse interfaces are expected [57].

The effectiveness of a computational method to replicate the behavior of flows under supercritical conditions depends on several factors, ranging from physical models that accurately capture the non-linear behavior of the various thermophysical parameters to relevant experimental data for its validation and mathematical models with the ability to simulate the flow behavior. In this way, numerical solvers are validated using the relatively small number of available quantitative experimental data sets [35, 58–64]. While the density is retrieved using a real gas equation of state (EoS), the description of derived caloric properties makes use of the departure function formalism. In addition, relevant conditions at injection which are not available from current experimental data [65] and a broader range of experimental conditions describing mixing between various chemical species would allow for the generalization of conclusions and extend current theories.

1.4 Objectives and Structure

1.4.1 Objectives

This thesis aims at evaluating and demonstrating the suitability of an incompressible but variable density approach [66] as an effective way of describing transcritical and supercritical fluid behavior. First, Barata et al. [66] employed the incompressible but variable density approach by solving the conservation equations for mass and momentum, complemented with the mixture fraction definition, which is uniquely related to scalars such as temperature and density under the assumption of chemical equilibrium. Later, Antunes [67] introduced energy conservation in the formulation and replaced the mixture fraction with different real gas EoS and the description of transport properties through the departure function formalism.

A more in-depth and broader evaluation of the incompressible but variable density approach is carried out in the present work. Different injection configurations are evaluated, ranging from single and coaxial to multi-component mixing focusing on near-injector behavior and mixing layer formation, which is naturally formed from the interaction between two fluids moving with relative parallel velocity.

The analysis is restricted to non-reacting configurations. The mixing of non-reactive fluids is fixed by the flow structure [68], while in the case of reactive fluids, chemical reactions and heat transfer add another degree of complexity to the problem. By focusing mainly on nitrogen, single and multispecies mixing layers can be modeled as representative of the mixing between hydrogen and oxygen in most LRE configurations. Since combustion is controlled in part by the mixing between fuel and oxidizer, surrogate non-reacting species can be used to study the influence of density and velocity ratios [32]. In particular, N_2–H_2 was used to model LOX–H_2 mixture. However, in order to gain insight into the mixture behavior inside the thrust chamber of a given liquid rocket engine operating with a bi-propellant mixture (i. e. oxygen–hydrogen), the temperature and pressure range of the surrogate nitrogen need to be defined as representative of the actual phenomena occurring in the chamber [35]. In other words, if oxygen and hydrogen are injected into the combustion chamber separately and at supercritical conditions, the resulting mixing behavior can be characterized by variations of temperature that are locally lower than the critical mixing temperature, putting the mixture in the transcritical regime, from where the conditions in the chamber would lead to an increase in the mixing temperature, which would eventually cross the critical point, approaching supercritical liquid-like conditions, be subjected to pseudo-boiling effects, and ultimately cross the Widom line [53] into supercritical gas-like conditions, if enough heat is received by the jet. Each of these effects and regimes has very particular natures which need to be understood and replicated in any numerical effort attempting to predict and model the behavior of fluids under these conditions, which is the focus of the work carried out.

1.4.2 Structure

The present document is organized as follows:

- Firstly, in Chapter 2, details about supercritical and transcritical fluid behavior are explored by looking into the non-linear behavior of thermophysical properties, the physical meaning of transition at supercritical conditions, and the distinct mechanisms characterizing injection at subcritical and supercritical conditions.

- Secondly, Chapters 3 and 4 frame the fundamental and physical laws and the discretization of the physical domain. Here the incompressible but variable density hypothesis to be tested is formulated, and its implications addressed.

- Thirdly, several injection configurations are tested, considering the flow stratification inside the injector. These range from single species injection at supercritical conditions in Chapter 5 to transcritical injection in Chapter 6. Single species coaxial injection is addressed in Chapter 7 alongside the temperature field validation. A coaxial multi-species injection is analyzed in Chapter 8.

- Finally, the main findings are summarized in the conclusions, highlighting the main contributions and making suggestions for future work.

Chapter 2

Characterization of the Supercritical Regime

Supercritical and transcritical conditions are going to be thoroughly investigated in this work. As a result, the supercritical and transcritical regimes are defined in the present chapter, while the distinct nature of the critical point for pure fluids and mixtures is described. Furthermore, in light of recent research, the meaning of phase change at supercritical conditions and phase separation under transcritical ones is looked into, and the implications for the flow modeling are assessed. Lastly, available experimental data is reviewed to distinguish between qualitative and quantitative experiments and establish which thermophysical parameters replicated numerically can be compared and validated against experiments.

2.1 Introduction

The increasing performance demands of rocket engines have led to conditions in the combustion chamber that exceed the critical point of both the fuels and oxidizers, entering the domain of supercritical fluids. The critical point delimits the supercritical regime and is characterized by pressure and temperature values that become identifiers in the case of pure fluids. Thermodynamic singularities, which refer to the singular behavior of thermodynamic properties at the critical point, need to be accurately replicated in any numerical effort dedicated to the successful description of supercritical fluid behavior. When the isobaric specific heat becomes infinite, the surface tension and latent heat become zero. Since the kinematic viscosity of supercritical fluids is lower than that of correspondent liquid and gas phases [69], the Reynolds number is conversely higher for the same velocity, potentiating the formation of a turbulent flow. Besides, the discontinuity between the liquid and gas phases observed at subcritical conditions disappears, resulting in single-phase behavior under supercritical conditions [70]. In such situations, the injection cannot be thought of as leading to spray formation but as describing a fluid-fluid mixing process [71]. However, single-phase behavior does not imply a uniform behavior across the supercritical regime. In fact, Banuti and Hannemann [45] introduce the concept of thermal disintegration as complementary to the pure mechanical description of supercritical jet disintegration. The research carried out in this manuscript is built upon the mechanical and thermal disintegration concepts [45].

As a result of the surface tension being zero, finger-like structures would dissolve into the flow [72, 73], instead of breaking into several droplets and ligaments. In the case of coaxial injection at constant injection velocity, as the pressure in the chamber increases progressively, smaller structures detach from the central jet [74]. The exact mechanism responsible for the formation of these finger-like structures is not yet understood [75]. Energy dissipation becomes dominant at this point due to the decrease in density, with LES studies [76] demonstrating that the large density gradients between the jet and the chamber environment hinder the development of Kelvin–Helmholtz vortical structures, thus delaying the breakup.

After the critical point is reached, further increases in pressure and temperature may result in the fluid entering the so-called Widom region [77], separating supercritical liquid- and gas-like behavior. Here, several Widom lines have been studied [58, 77, 78] as consequences of singularities in different thermodynamic response functions. These can be characterized by a local maximum or an inflection point. In particular, the response functions associated with the maxima in isobaric specific heat and compressibility are of particular interest [58].

2.2 Classification According to the Critical Point Positioning

According to the positioning concerning the critical point values for temperature and pressure, four different regimes are typically identified. A fluid is considered in a supercritical state if both its pressure and temperature are above their critical point values. On the other hand, if pressure and temperature are below their critical point values, a subcritical fluid is present. The commonly represented fluid state diagram lies in this region, with gas, liquid, and solid phases and the corresponding coexistence lines. Combining values of pressure and temperature below or over the critical point, two more regimes can be defined: a superheated regime, in the case of pressure below the critical point and temperature over it, and a transcritical regime, in the case of pressure above the critical point value and temperature below it. A compressed liquid is observed in the transcritical regime until the temperature is elevated above the critical point value. Currently, this regime is the one less understood by the current state of the science. In the superheated regime, a behavior close to an ideal gas is expected. The representation of these four regimes is made in Figure 2.1.

When a fluid reaches its critical point, mass diffusivity, surface tension, and latent heat are zero, while isentropic compressibility, specific heat, and thermal conductivity tend to infinity. Critical divergence is defined by Zong et al. [79] as the evolution of specific heat to infinity and thermal diffusivity to zero. The distinction between liquid and gas phases disappears, and the terminology fluid is used. At the same time, diffusion coefficients become functions of pressure, in addition to temperature, while the solubility of the gas phase in the liquid phase increases significantly at high pressures [80]. The disappearance of latent heat leads to mass diffusion being the governing parameter instead of vaporization. The absence of surface tension causes the diffusion process to dominate over the jet atomization. Since vaporization does not occur at supercritical conditions, DeSouza and Segal [81] propose the use of ’emission rate’ and ’emission constant’ to describe mixing at supercritical conditions.

It is well known that in a subcritical injection, surface instabilities are responsible for the liq-

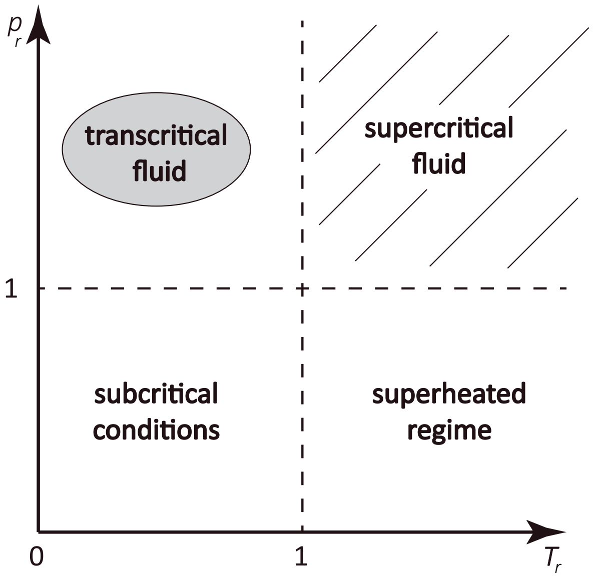

Figure 2.1: Regime definition according the critical point.

uid jet atomization, small discrete ligaments begin to break up, and droplets are ejected from the jet core [72]. In a supercritical injection, however, the breakup mechanics are entirely different. Mayer [82] describes one of the main characteristics of supercritical fluids as the impossibility of a two-phase flow. Similar effects are reported by Oschwald et al. [72], where the surface tension is measured for oxygen from subcritical temperatures, with higher values, up to the critical temperature, for which it completely vanishes. Several other authors describe this breakup mechanism where the drops and ligaments are no longer detected, and no distinct surface interface can be determined. Mayer [82] notes that this disintegration mechanism more closely resembles turbulent and diffusive mixing than the traditional jet disintegration and Banuti and Hannemann [45] describe a thermal-breakup mechanism where the limit of the jet core is defined by the transition of the fluid across the pseudo-critical line.

2.3 From Subcritical to Supercritical Conditions

In the subcritical regime, a distinct interface between liquid and gas phases is clearly visible [83]. For example, Figure 2.2 depicts the injection of liquid nitrogen at three different reduced pressures: 0.91, 1.22 and 2.71 (from left to right) into a chamber filled with nitrogen at $300\,\mathrm{K}$.

The first case corresponds to the classical jet disintegration process under subcritical conditions, where ligaments and droplets are visible separating from the jet. According to Oschwald et al. [72], it corresponds to the second-wind induced jet breakup mode, being the theory of Rayleigh [84] on jet disintegration suitable for its description. As the critical point is crossed, in the middle case, no droplets are visible. Instead, thread- or finger-like structures are formed, dissolving rather than breaking in the classical mechanical theory. At present, Lagarza-Cortés et al. [75] indicate that no model exists capable of predicting the

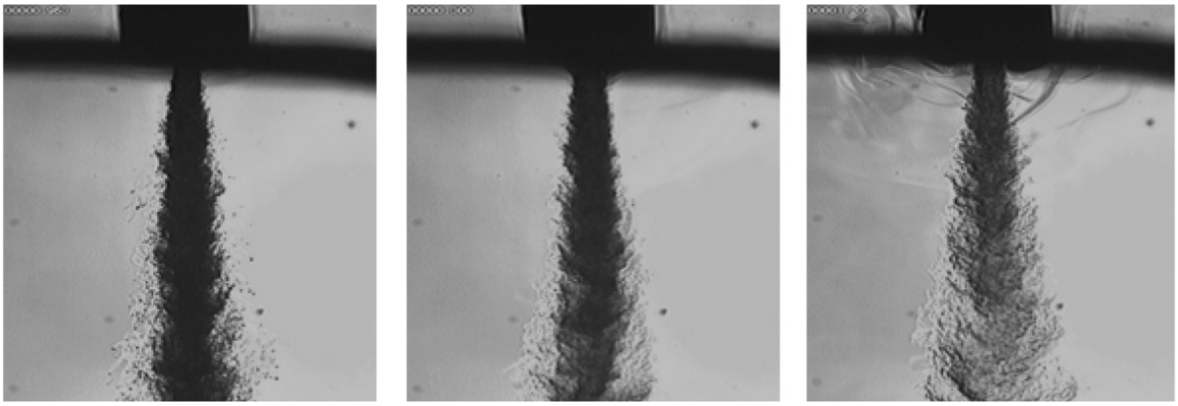

Figure 2.2: Single species nitrogen injection into nitrogen analysis from sub- to supercritical conditions, from Oschwald et al. [72]. From left to right: $p_r = 0.91$, 1.22 and 2.71.

formation of the thread-like structures, while Cho et al. [85] studied nitrogen injection from subcritical to supercritical conditions from a swirl injector, concluding that the flow structure is highly affected by the phase-change process. Lastly, as the reduced pressure increases further to 2.71, the jet resembles subcritical gaseous jets.

As the jet is heated up past the critical point, a condition is reached where heat does not contribute to a discernible temperature increase [86] but to the jet expansion.

Shadowgraph results such as the one depicted in Figure 2.2 indicated a need to evolve from Lagrangian droplet tracking methods [87] to continuous Eulerian approaches [88]. In this way, research evolved from the study of droplets [25, 31, 89–96], also considering microgravity conditions in order for their behavior not be influenced by natural convection (induced by buoyancy) [97–101], modeled through Eulerian-Lagrangian formulations [102], towards jets and shear layer dynamics [25, 96].

The jet's structure can then be divided into three distinct regions: a potential core, a transition, and a fully developed region [59], as depicted in Figure 2.3. The potential core length is the distance at which the center-line density remains relatively constant (typically, 99% is taken as the delimiting factor). Further downstream, there is a self-similar region in which the absolute values of the flow variables can still change. Still, their radial profiles are no longer a function of axial direction. In between lies the transition region, characterized by turbulent and diffusive mixing. As the potential core breaks and the density decreases, dense pockets of liquid-like nitrogen are separated from the jet core, leading to an increase in density fluctuations. Energy dissipation becomes dominant at this point due to the decrease in density, with LES studies [76] demonstrating that the large density gradients between the jet and the chamber environment hinder the development of Kelvin-Helmholtz vortical structures, thus delaying the breakup.

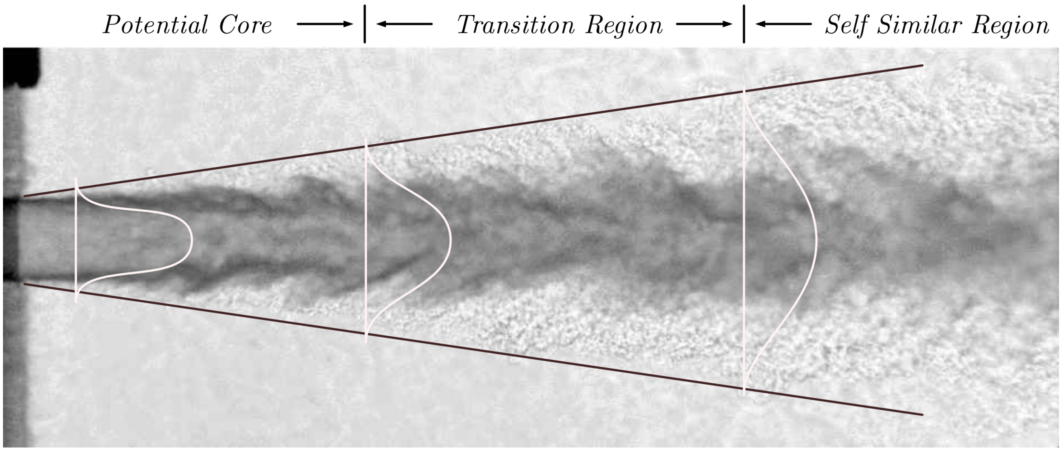

Figure 2.3: Schematic representation of the jet mixing flow field [59].

2.4 The Physical Meaning of Transition at Supercritical Conditions

As it is well known, the critical point marks the end of the co-existence line between liquid and gas phases, characteristic of subcritical conditions. After this point, the discontinuities cease to be since both liquid and gas merge into one another, reaching the same values at the critical point. Since no macroscopic interface is seen at the region near the critical point, a debate was sparked if a phase change due to the large density gradients in this region occurred. Eventually, the existence of a microscopic interface was demonstrated [103, 104]. Nishikawa and Tanaka [105] performed x-ray measurements on supercritical CO_2 showing how the gas-liquid co-existence line extends towards the supercritical regime, while Tsuchiya et al. [106], through spectroscopy in supercritical H_2O and CO_2 demonstrated that the supercritical regime is not homogeneous, identifying two states: liquid-like and gas-like.

While it has been shown by Santoro and Gorelli [107], Simeoni et al. [108] and Maxim et al. [109], for example, that a fluid in a supercritical state is not homogeneous, instead of being characterized by pseudo liquid and gaseous states, the processes involved are not yet fully understood, and the definition of transition is surrounded in some ambiguities. In an attempt to solve some of the underlying contradictions, Banuti et al. [110] perform molecular dynamics simulations to argon, dividing transitions at the supercritical fluid state into two categories: a thermodynamic one, with a macroscopic nature, and a dynamic one, microscopic. The thermodynamic transition corresponds to the crossover across the Widom line, representing a continuation of the co-existence line at supercritical conditions. For its resemblance to the phenomenon of subcritical boiling, it is also labeled a pseudo-boiling line. On the other hand, the dynamic transition is related to the Frenkel line, marking the division from a ”rigid” liquid state to the ”nonrigid” gas-like fluid state, of particular importance in the modeling of planetary gas giants as Jupiter and Saturn [23]. This phenomenon is universal in systems where a liquid-gas transition is not present [111]. Additionally, Yang et al. [112] also perform molecular dynamic analysis to determine the location of the Frenkel line for water, methane, and carbon dioxide and discuss the relationship between the Frenkel line location and the solubility maxima. Additionally, Bolmatov et al. [113] debates the fact that relatively simple microscopic theories could be capable of predicting supercritical transition. For binary mixtures of Ar and N_2, Fu et al. [114] assessed the shear layer growth. The conclusions drawn by Banuti et al. [110], in the form of a revised phase state diagram (Figure 2.4), are adopted into the present work.

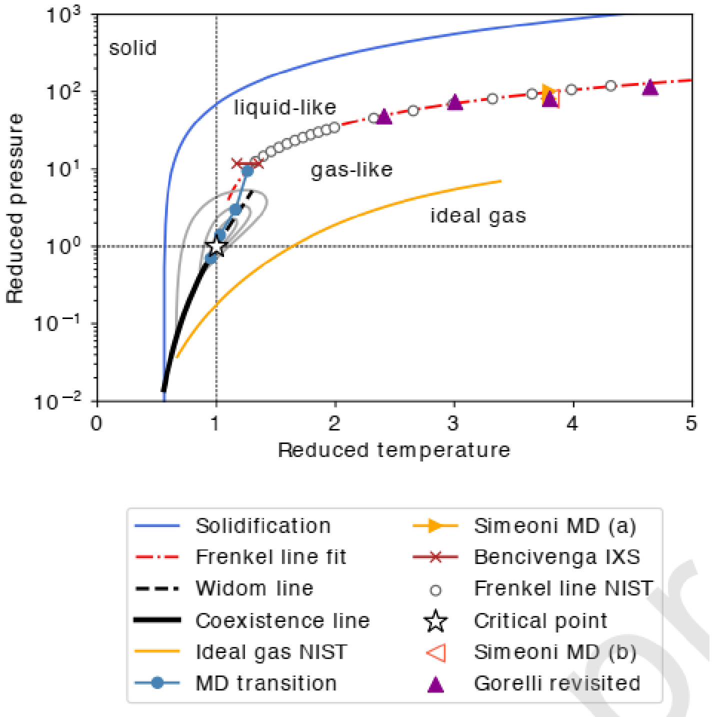

Figure 2.4: Transition across the Widom line from liquid-like to gas-like conditions [110].

The transition across the Widom line is only physically relevant for $p_c < p < 3p_c$, where the phenomenon of pseudo-boiling can be tracked by the locus of the maxima in isobaric specific heat [53]. The reason for the approximation of the Widom line to the locus of the maxima in isobaric specific heat is also addressed and justified by the lack of correlation lengths to estimate the microscopic interface. In fact, several Widom lines are possible depending on the thermodynamic property considered [115] such as heat capacity, compressibility coefficient, and density, which merge asymptotic into one [115] as the critical point is approached. If this state is then heated to $T > 2.5T_c$, the supercritical fluid behaves as an ideal gas. Kobayashi et al. [37] experimentally confirmed the disappearance of the peak in isobaric specific heat for hydrogen with a reduced temperature higher than 2 and reduced pressure higher than 10. The existence of both the Widom line and the pseudo-boiling phenomena has been experimentally verified for water by Maxim et al. [109] and later analyzed quantitatively [115]. On the other hand, a quantitative theory of pseudo-boiling has been proposed by Banuti [53], where it is explained that at supercritical conditions and in contrast to the subcritical case, the energy supplied to the fluid is used to overcome molecular attraction and to raise its temperature, corresponding to structural and thermal contributions. This differentiation will ultimately impact the jet evolution, owing to the crossing of the Widom line and associated pseudo-boiling temperature. This temperature then replaces the critical temperature as the transition criterion. Interestingly enough, Banuti et al. [70] can identify there is no contradiction between the fluid being supercritical and behaving as an ideal gas (Figure 2.4). It is also shown that for pressures smaller than three times the critical pressure, any isobaric heating process from a liquid to an ideal gas state requires approximately the same energy, regardless of pressure. The transition from liquid- to gas-like conditions is a continuous non-equilibrium process within a narrow temperature range, where all fluid properties vary significantly [116]. At pressures close to the Widom line, the stratification in the various thermophysical properties can influence the stability of boundary layers [117] and mass flux terms exceed values for ideal gases [118].

As opposed to the thermodynamic transition, dynamic transition across the Frenkel line is not supported by thermodynamic arguments because there is no abrupt change in the thermodynamic fluid properties. Dynamic transition, very simply put, is framed on the changes in molecular motion [110]. At higher pressures than those where a thermodynamic transition is relevant, a dynamic transition is observed [23, 108]. The distinction between thermodynamic and dynamic transition is highlighted by Artemenko et al. [119], stating that for $p_c > 20$, dynamic transition characteristics should be considered instead of thermodynamic ones.

The Widom region, also labeled as pseudo-boiling in the literature [53, 77, 120] can be defined as the region where a slight pressure or temperature variation yields a significant response (Figure 2.5). Crossing the Widom region from liquid- to gas-like conditions is a similar process to a phase change at subcritical conditions, albeit without the phase change and taking place at a narrow temperature range [53]. The nature of the response was studied by Gorelli et al. [78], who confirmed the relationship between the dynamic and thermodynamic behavior of supercritical fluids at a point well past the influence of the c_p-Widom line. Given that the c_p-Widom line is only visible up to $T_r \approx 3$, the authors consider the minima of thermal diffusivity and kinematic shear viscosity, whose effects are observed for the considered temperature range ($T_r = 4.64$). In this way, Gorelli et al. [78] extend their molecular dynamics computations past the region where the c_p-Widom line effects stop being visible, indicating that a supercritical jet is affected by thermodynamic and dynamic factors. On the other hand, Banuti [53] proposes the transition across the Widom line to be a purely thermodynamic concept, where a pseudo-phase change takes place similar to boiling at subcritical conditions. Between these two interpretations of the nature of the Widom line crossover, Gorelli et al. [78] thermodynamic-dynamic, based on the dynamic response to perturbations, and Banuti [53] purely thermodynamic, based on the concept of pseudo-boiling, the present text follows the theory of pseudo-boiling [53] and is in light of this theory that the results now presented should be interpreted.

Figure 2.5 shows the variation of density, ρ, and isobaric specific heat, c_p, with temperature, T, for nitrogen, taken from experimental data available from the National Institue of Standards and Technology (NIST) database. The density and isobaric specific heat are represented over a temperature range of $100\,\mathrm{K}$ and $200\,\mathrm{K}$ and pressure levels of 4, 5, and $6\,\mathrm{MPa}$. Pseudo-boiling behavior is represented by the maximum of c_p for the considered pressure values, with a more pronounced effect as one moves in the direction of the critical temperature (critical pressure of N_2 is $3.34\,\mathrm{MPa}$, with a critical temperature of $126.2\,\mathrm{K}$). The inclusion of density variations allows one of the essential aspects of pseudo-boiling to be identified, namely the variation of a couple of Kelvin in temperature associated with a density variation significant enough to substantially alter the results if the accurate temperature is not used. A higher structural energy contribution is needed to overcome the so-called 'heat shield' represented by the c_p peak in the Widom line region [121].

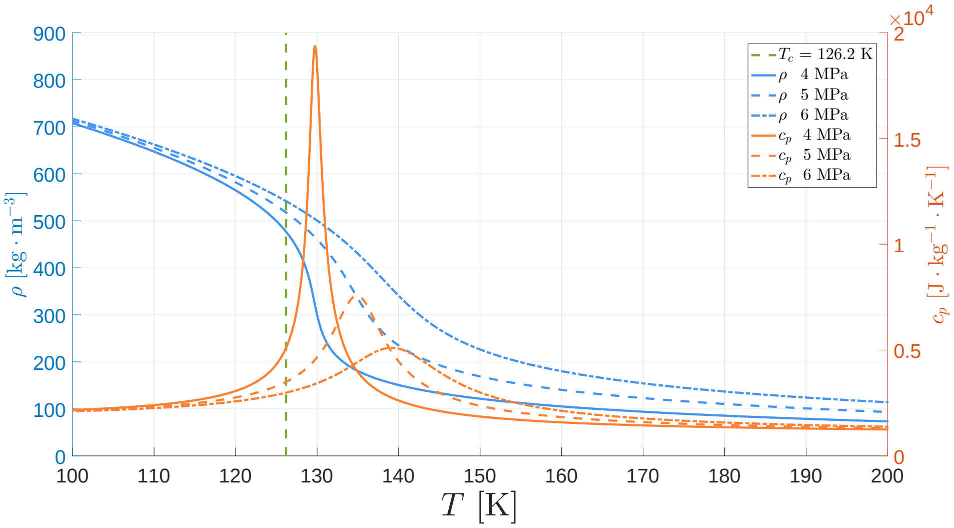

Figure 2.5: Density and isobaric specific heat values for nitrogen for pressure levels of 4, 5 and $6\,\mathrm{MPa}$ (data from the NIST database).

After the critical point is reached, a further increase in pressure pushes the isobaric specific heat to reach a maximum value different from the infinite value at the critical point. Up to the maximum isobaric specific heat corresponds to a temperature labeled the pseudo-boiling temperature. As the pressure is increased further, the maximum isobaric specific heat will become less and less pronounced. As the temperature increases further, the liquid-like supercritical oxidizer crosses the pseudo-critical line and transitions to a gas-like fluid. This transition from a liquid-like to a gas-like state could be compared to a subcritical boiling. The main difference is that the isothermal vaporization typical of subcritical fluids is replaced by a continuous non-equilibrium process that takes place over a finite temperature range (Figure 2.6). As this happens, the specific heat capacity goes through a maximum and tends to infinity when approaching the critical point, as shown in Figure 2.5.

Similarly to Oschwald et al. [72], this transition phenomenon is labeled pseudo-boiling, and the maxima of the specific heat capacity as pseudo-boiling temperature. It represents a continuation of the saturation line well into the supercritical regime. Using the data retrieved from such analysis, a curve of the pseudo-boiling points, known as the Widom line, can be obtained (Figure 2.6). The physical significance [53] of this line is the pseudo-transition between liquid- and gas-like supercritical behavior, effectively making it an extension of the co-existence line into the supercritical regime. If the discussion concerns mixtures rather than single-species behavior, the linear gradient theory of Dahms and Oefelein [122] can be used to show that the residual surface tension in the chemical species is above the critical point before the Widom line is crossed.

Pseudo-boiling is similar to subcritical boiling [27], without discontinuities encountered in thermophysical properties. Since the discontinuities between liquid and gas do not exist, a fluid at supercritical conditions behaves as a single-phase substance [80].

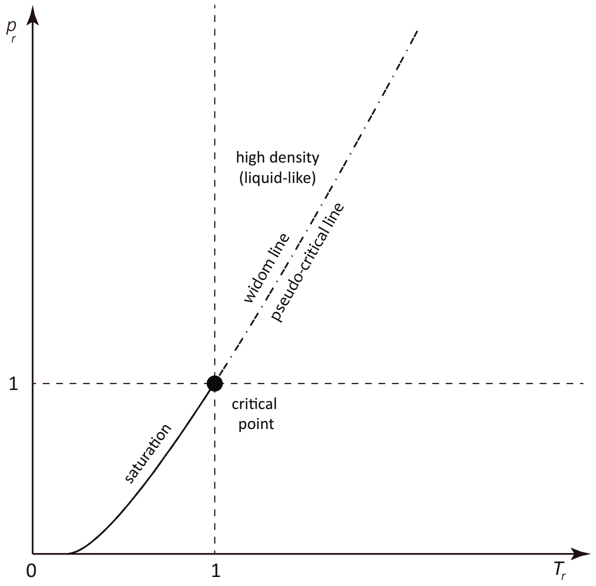

Figure 2.6: Overall pressure temperature diagram.

The two parameters $\left(\frac{\partial \rho}{\partial T}\right)$ and $c_{p_{max}}$ can therefore be used to identify pseudo-boiling temperatures for different pressures values as shown in Figure 2.5. For nitrogen, it is visible that as the pressure approximates the critical value of $3.39\,\mathrm{MPa}$, and the peak in specific heat becomes more noticeable along with the slope of $\left(\frac{\partial \rho}{\partial T}\right)$.

A generalized expression for the determination of the Widom line is proposed by Banuti et al. [123], with A' and a species-dependent parameters given by the authors for several species.

$$p_r = \exp\left[A'\left(T_r - 1\right)^a\right] \quad (2.1)$$

As shown by Banuti and Hannemann [45], the pseudo-boiling line acts as a separation between jet disintegration mechanisms (Figure 2.7). As presented in classical jet breakup theory, mechanical interactions in the shear layer are the reason behind jet disintegration, ultimately contributing to the length of the potential core of the jet. This parameter indicates breakup efficiency, one of the few parameters possible to measure in high-pressure flows. On the other hand, crossing the Widom line allows a thermal breakup to dominate over a mechanical breakup, no longer occurring due to fluid entrainment but by the significant density variation resulting from temperature effects.

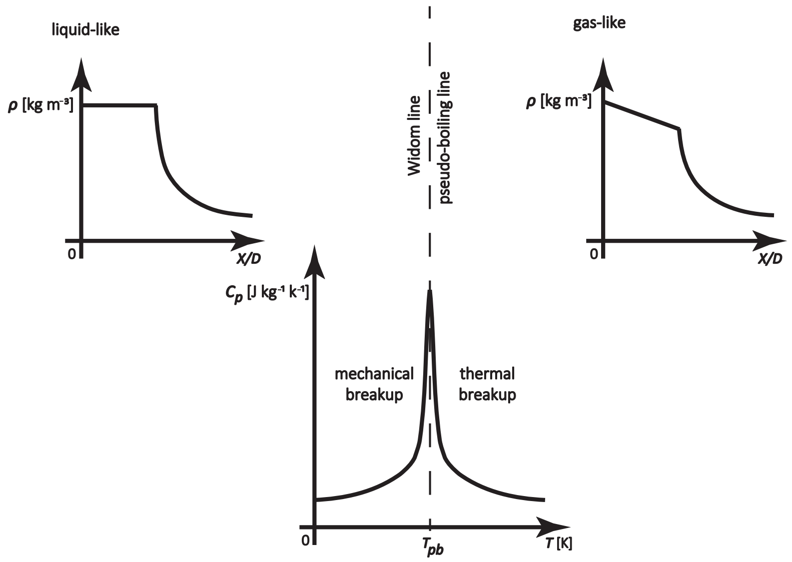

Figure 2.7: Transition across the Widom line from liquid-like to gas-like conditions.

However, Banuti and Hannemann [45] work is not the only one attempting to characterize the non-homogeneous supercritical state and the pseudo-phase-transitions. For instance, Gopal et al. [124] suggests a division based on the temperature ranges in which property changes take place. In this way, they define transitional, dense gas-like, and ideal gas-like regions. The transitional area encompasses the temperature range between the critical temperature and the temperature where heat capacity returns to its value at the critical point. Following Gopal et al. [124] the transitional region corresponds to the region where the most drastic property variations occur, including the pseudo-boiling effects. Moreover, the dense gas-like region extends from the end of the transitional region until the compressibility factor reaches 0.95, from where the ideal gas-like region takes shape. The characterization proposed by Gopal et al. [124] reflects the fact that transitions or phase-changes are not instantaneous processes.

2.5 Multi-component Mixing

At supercritical conditions, diffusion coefficients become functions of pressure and temperature, while in mixtures, the solubility of the gas phase in the liquid one increases with increasing pressure. This means that the critical pressure of a mixture can be several times higher than that of one of its constituents. In this regard, the critical point conditions of a mixture cannot be inferred by those of the species it is composed of. Experimentally, this is observed in the injection of nitrogen into a helium environment, depicted in Figure 2.8. The mixture's critical pressure becomes a dynamic value because it depends on the amount of each constituent species at any given time during the injection.

The critical point begins to shift dynamically with the fuel and oxidizer mixing and dissolving at elevated pressures. The critical mixing temperature and/ or pressure must be exceeded for a supercritical stage to be realized under these conditions. The use of multiple experimental techniques in the same facility has been an increasingly valuable way of characterizing the jet disintegration process for comparison and validation [81].

Figure 2.8 depicts the coaxial injection of a N_2–He mixture, where N_2 is injected through the central stream and He through the coaxial one, at subcritical (left and middle) to transcritical (right) conditions (in relation to the nitrogen pure fluid). Comparing this coaxial injection with the single N_2 injection in Figure 2.9 at the same pressure levels, the influence of the co-flowing He can be analyzed.

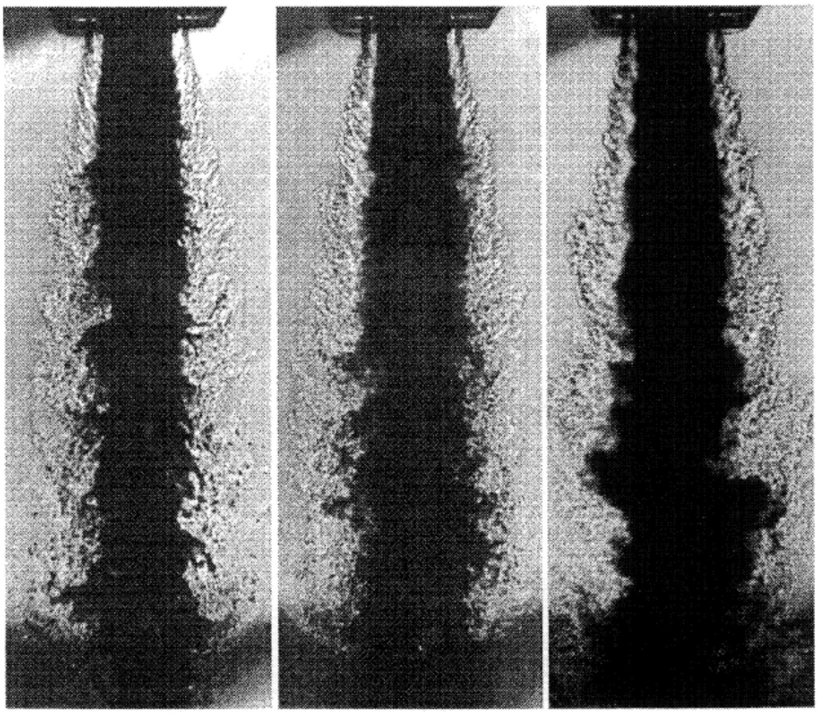

Figure 2.8: Coaxial injection of N_2–He. From left to right: chamber pressure of $2\,\mathrm{MPa}$, $3\,\mathrm{MPa}$ and $4\,\mathrm{MPa}$, with an inner injector (N_2) diameter of $1.9\,\mathrm{mm}$ and a coaxial (He) slit of $0.2\,\mathrm{mm}$. The injection velocities are $5\,\mathrm{m\,s^{-1}}$ for N_2 and $50\,\mathrm{m\,s^{-1}}$ for He, while the injection temperatures are $100\,\mathrm{K}$ for N_2 and $275\,\mathrm{K}$ for He [71].

A diffusion dominated process takes place for pressure above the critical point if a pure substance is considered (Figure 2.9 right) or in the case of a mixture this is a bit more complex since transition cannot be directly determined from the critical point conditions of the mixture components (Figure 2.8 right) [83, 122].

The Knudsen number $\left(\mathrm{Kn} = \frac{\lambda}{L}\right)$ describes the degree of departure from the continuum to be defined as the ratio of the molecular free path (λ) to the characteristic length of the problem (L). Dahms et al. [125] use the Knudsen number definition to explain the conditions in which surface tension is diminished for multi-component mixing. Surprisingly, it is found that the interface thickness increases while the surface tension decreases. However, diffusion layers at the interface develop due to the reduction between the molecular mean free path

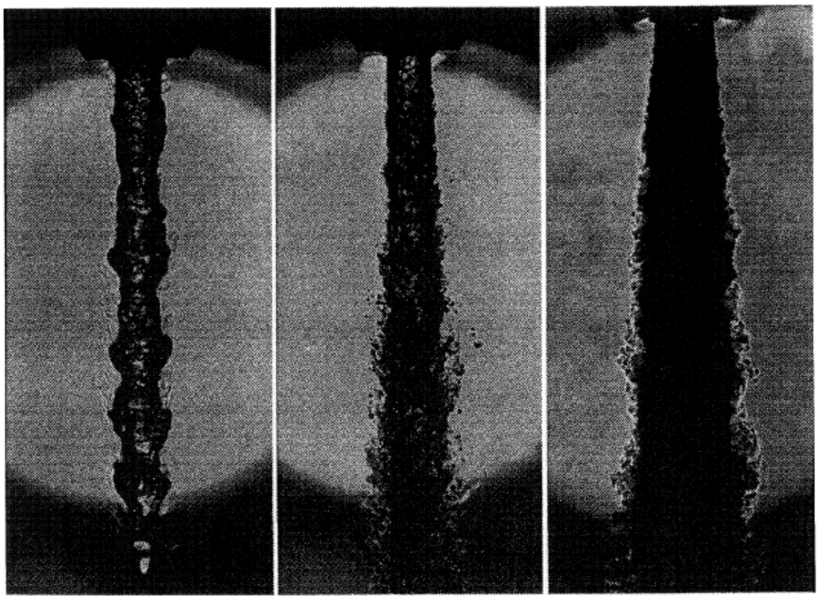

Figure 2.9: N_2 cold flow injection. From left to right: chamber pressure of $2\,\mathrm{MPa}$, chamber pressure of $3\,\mathrm{MPa}$, chamber pressure of $4\,\mathrm{MPa}$, with an injector diameter of $1.9\,\mathrm{mm}$, injection velocity of $1\,\mathrm{m\,s^{-1}}$ and an injection temperature of $105\,\mathrm{K}$ [71].

and the diffuse interface enlargement, not necessarily because of the surface tension. As a result, the governing equations can be used across the interface according to the notion of single-phase flow. Furthermore, in an attempt to quantify the transition from two- to single-phase, Dahms and Oefelein [122] use liner gradient theory to describe the interface region and the conditions in which the transition occurs.

Moreover Raju et al. [126] perform molecular dynamics simulations for binary mixtures, providing evidence of the existence of multiple Widom lines. According to the authors, distinct behaviors are encountered between miscible and immiscible binary mixtures. While for miscible mixtures, similar behaviors to those of pure fluids are discovered, in immiscible mixtures, several Widom lines are recovered due to transitions at different temperatures. These results, which gave the first indication of Widom line transition for multi-component mixtures, highlight the need for more accurate models to describe supercritical mixtures.

2.6 Experimental Data Assessment

The need for quantitative experimental data sets cannot be understated since these allow for the validation of computational codes, reducing the trial-and-error phase in developing a propulsion system. Unfortunately, quantitative experimental data are hard to obtain given the difficulties encountered due to the harsh conditions of combustion chambers [127]. Whether through cold flow or combustion experiments, the behavior of supercritical mixing and combustions can be significantly enhanced.

The behavior of fluids in supercritical conditions has been successfully examined in various experiments. Table 2.1 details several experimental datasets that offer qualitative and quantitative descriptions of supercritical fluid behavior with and without combustion, allowing the numerical solvers developed through the years to be validated. Additionally, Table 2.2 summarizes the critical temperatures and pressures of the fluids in Table 2.1, taken from the NIST database.

Initially, the focus has been the study of single cryogenic nitrogen jets into nitrogen chamber conditions both above and below nitrogen's critical pressure [35, 128]. The logical next step dwelt with coaxial nitrogen–helium or hydrogen [74, 120, 129, 130]. Overviews are presented in Habiballah et al. [60], Oschwald et al. [72] and Chehroudi [73].

Recently, quantitative speed of sound measurements for multi-component mixing [131] work as a surrogate mean for an indirect validation of the temperature field. Through laser-induced thermal acoustics (LITA), the local speed of sound is inferred from periodic oscillations without the need for an EoS or a theoretical mixing model. Since the correct speed of sound prediction depends on pressure, temperature, and composition determination, an indirect validation of the temperature field is possible. Unfortunately, as shown in Table 2.1, quantitative experimental data are scarce and restricted to a few binary systems. The associated studies focused on measuring mean quantities such as the axial density distribution and corresponding radial profiles and the full width at half maximum (FWHM) of the density. Determining the exact initial conditions used in the experimental studies is an added difficulty [65], as they are not often published.

Quantitative cold flow data provides insight into jet mixing at supercritical conditions without introducing the complexities of turbulence. Mayer et al. [59] conducted Raman scattering measurements on a cryogenic nitrogen jet temperatures above and below its critical point into quiescent nitrogen environments with pressure above nitrogen's critical point. Over the years, this has become a canonical test case for the validation of numerical solvers. It remains the most comprehensive source of information for single species injection at supercritical conditions. Coaxial injection for the LN_2–GH_2 binary system was conducted by Oschwald and Schik [35]. The quantitative results from these two studies, as well as visual and qualitative observations of jets at supercritical conditions, are summarized by Oschwald et al. [72] as a result of research conducted at the Deutsches Zentrum für Luft- und Raumfahrt (DLR) and Air Force Research Laboratory (AFRL) laboratories. Another experimental study concerning nitrogen in a single component injection has been undertaken by Tani et al. [132]. Laser-induced fluorescence (LIF) has been used by Roy and Segal [62], Roy et al. [133] and Roy et al. [63] for the study of fluoroketone injection into nitrogen in supercritical-to-supercritical and subcritical-to-supercritical injection configurations. While the first configuration is characteristic of the combustion chambers of LREs, the second one is encountered in hypersonic applications. Of particular importance is the authors' observation of the dependence of the core length on momentum ratio in the case of supercritical-to-supercritical injection and the more efficient mixing in this configuration. Additional LIF measurement into binary systems from sub- to supercritical conditions highlighted the differences between regimes, and linear stability analysis showcases the domination of diffusion over jet atomization.

Table 2.1: Overview of experimental studies. Abbreviations: exp tech - experimental technique, v_{inj} - injection velocity, T_{inj} - injection temperature, p_{inj} - injection pressure, T_∞ - chamber temperature, p_∞ - chamber pressure, FK - fluoroketone, h. s. photography - high-speed photography, LIF - laser induced fluorescence, LITA - laser induced thermal acoustics, n/a - not available.

Reference	Mixture	exp tech	v_{inj} [m s^{-1}]	T_{inj} [K]	p_{inj} [MPa]	T_{ch} [K]	p_{ch} [MPa]
[134]	$CO_2 \rightarrow CO_2/N_2$	shadowgraphy	2–4	0.97	n/a	0.97–1.09	0.86–1.23
[83]	$N_2 \rightarrow N_2/He$	shadowgraphy	1.8–2.2	0.7–0.91	n/a	2.21–2.46	0.83–2.03
[130]	$N_2 \rightarrow N_2$	shadowgraphy	1.0	0.83	n/a	2.38	0.59–1.18
[130]	$N_2 \rightarrow He$	shadowgraphy	1.7	0.66	n/a	2.31	1.62–2.44
[35]	$N_2 \rightarrow N_2$	Raman	5.0–20	0.79–1.11	n/a	2.36	1.17–1.76
[120]	$N_2+H_2 \rightarrow N_2$	Raman	5.0–20	0.79–1.11	n/a	2.36	1.17–1.76
[128]	$N_2 \rightarrow N_2$	h. s. photography	10–15	0.71–0.87	n/a	2.38	0.23–2.74
[59]	$N_2 \rightarrow N_2$	Raman	1.8–5.4	1.0–1.11	n/a	2.36	3.95–5.98
[56]	$FK \rightarrow N_2$	LIF	7.0–25	0.68–1.28	0.2–2.22	0.66–1.07	0.05–1.86
[62, 63]	$FK \rightarrow N_2$	LIF	7.07–30	1.0–1.31	1.34–1.98	0.69–1.09	1.26–1.88
[135]	$FK \rightarrow He$	LIF	<2.0	0.71	n/a	0.97–1.07	0.85–1.2
[135]	$FK \rightarrow He/N_2$	LIF	<2.0	0.92–1.06	n/a	0.72–1.04	0.85–1.2
[81]	$FK \rightarrow N_2$	LIF/shadowgraphy	3.56–31.30	0.8–1.21	n/a	0.77–1.21	0.53–1.92
[131]	n-hexane $\rightarrow N_2$	LITA	91	1.24	1.81	0.58	1.65
[131]	n-pentane $\rightarrow N_2$	LITA	76–96	1.13–1.28	1.61–1.62	0.63	1.48
[131]	$FK \rightarrow N_2$	LITA	41–72	1.13	2.11	0.67	1.34–2.11
[10]	$FK \rightarrow FK$	shadowgraphy	n/a	0.68–0.93	n/a	1.07	0.5–1.09
[136]	$N_2 \rightarrow N_2$	Raman	n/a	0.97–1.19	1.59	2.22	1.09

Table 2.2: Critical point conditions of relevant chemical species [137].

Species	T_c [K]	p_c [MPa]
CH_4	190.45	4.60
CO_2	304.25	7.38
fluoroketone	441.8	1.87
He	5.19	0.23
H_2	32.97	1.29
H_2O	647	22.06
kerosene	685.95	2.34
C_6H_{14}	507.8	3.03
C_5H_{12}	469.7	3.37
N_2	126.21	3.39
O_2	154.59	5.04

2.7 Summary

This chapter evaluated the definitions of supercritical and transcritical conditions, the nonlinearities in thermodynamic and transport properties, and the complexities they introduce in modeling these high-pressure flows. In addition, the concept of phase transition under supercritical conditions was re-evaluated regarding the non-uniform fluid behavior. In contrast, phase separation and the dynamic nature of the critical point for mixtures reveal different understanding levels and state-of-the-art concerning pure fluid behavior. Finally, experimental data suitable for the validation of numerical solvers is shown to be scarce, which hinders advancements in the field.

Chapter 3

Governing Equations and Physical Models

The system of Partial Differential Equations (PDE) to be solved is presented in this chapter, following an incompressible but variable density hypothesis. The implications of departure from ideal gas behavior through considering a real gas equation of state and an appropriate description of thermodynamic and transport variables are also addressed. Finally, the different methods and models are described, focusing on their impact and implications in modeling supercritical fluid behavior.

3.1 Governing Equations

Many references could be used as the basis for the derivation of the governing equations. For the most part, in this document, the work of Hirsh [138] is followed, where the tensor notation is adopted since it allows for the description of phenomena independently of the system of coordinates utilized.

The general principles of conservation of mass, momentum, and energy are considered, focusing on the contribution and impact of advective and diffusive fluxes. Here conservation means that the variation of the total amount of a given quantity in a given domain, designated as a control volume, is provided by the balance between the amount of the quantity entering and leaving the control volume added to the contribution of sources generating it. Moreover, the amount of the conserved quantity entering or leaving the domain is a flux. While advection respects the conserved property transport by the flow, whose non-linearity leads to the appearance of turbulence, diffusion is a phenomenon related to molecular thermal agitation.

An incompressible formulation is sought after. In conjunction with an appropriate EoS and the constant pressure in which experiments are conducted form the backbone of the described computational modeling effort.

3.1.1 Conservation of Mass

Conservation of mass expresses the empirical fact that mass cannot disappear nor be created in a fluid system, shown by taking density as the conserved property, mass per unit volume. Conservation of mass is expressed according to equation (3.1), where ρ is the density and u_i and x_i the velocity and distance in the ith direction, respectively.

$$\frac{\partial \rho u_i}{\partial x_i} = 0 \quad (3.1)$$

3.1.2 Conservation of Momentum

Conservation of momentum is achieved by multiplying density by the velocity vector. As a result, there will be a conservation equation for momentum for each velocity component, per the geometric dimensions. The momentum conservation principle is expressed by equation (3.2), and it represents Newton's second law of motion, where p corresponds to the pressure and τ_{ij} to the viscous shear stress tensor, meaning the internal friction force of fluid layers against each other.

$$\frac{\partial \rho u_i u_j}{\partial x_j} = -\frac{\partial p}{\partial x_i} + \frac{\partial \tau_{ij}}{\partial x_j} \quad (3.2)$$

The momentum conservation equation results from the balance between fluxes and source terms, whose non-linearities lead to the appearance of fluxes that act as apparent stresses throughout the flow - advective fluxes. Effectively the relation between fluid stresses and fluid strain rate is of paramount importance for the description of turbulence and can be written according to equation (3.3), where μ is the dynamic viscosity and δ_{ij}, the Kronecker's delta function.

$$\tau_{ij} = \mu \left[\frac{\partial u_i}{\partial x_j} + \frac{\partial u_j}{\partial x_i} - \frac{2}{3}\delta_{ij}\frac{\partial u_k}{\partial x_k} \right] \quad (3.3)$$

3.1.3 Conservation of Energy

The conserved property is the total energy per unit volume, ρE. The total energy is defined according to equation (3.4), where the first term on the right-hand side is the internal energy and the second one is the kinetic energy.

$$E = e + \frac{u_i u_i}{2} \quad (3.4)$$

Based on the first law of thermodynamics, energy conservation is given by the work of the forces acting on the fluid added to the contribution of heat sources other than conduction. The advective flux is determined according to equation (3.5), while the diffusive flux is retrieved through Fourier's law of conduction (equation (3.6)), where q corresponds to the heat transfer by conduction, T to the temperature, and λ, to the thermal conductivity.

$$F_{a_i} = \rho u_i E \quad (3.5)$$

$$F_{d_i} = \frac{\partial q_j}{\partial x_j} = -\lambda \frac{\partial T}{\partial x_i} \quad (3.6)$$

The diffusivity coefficient is determined according to equation (3.7), where Pr is the Prandtl number of equation (3.8). The Prandtl number represents the ratio between momentum and thermal diffusivity, being c_p the isobaric specific heat coefficient.

$$\lambda = \rho c_p \alpha = \frac{\mu \, c_p}{\mathrm{Pr}} \quad (3.7)$$

$$\mathrm{Pr} = \frac{\mu c_p}{\lambda} \quad (3.8)$$

The energy conservation principle can still be rewritten, accounting for the definition of total enthalpy. First the concept of enthalpy is defined in equation (3.9) and total enthalpy in equation (3.10).

$$h = e + \frac{p}{\rho} \quad (3.9)$$

$$H = e + \frac{p}{\rho} + \frac{u_i u_i}{2} = h + \frac{u_i u_i}{2} = E + \frac{p}{\rho} \quad (3.10)$$

Finally, the conservation equation for energy can be written according to equation (3.11).

$$\frac{\partial \rho u_j H}{\partial x_j} = \frac{\partial \tau_{ij} u_i}{\partial x_j} - \frac{\partial q_j}{\partial x_j} \quad (3.11)$$

The conservation equations for mass, momentum, and energy here described are not yet closed. The thermodynamic properties, such as density and temperature, are related through an equation of state. On the other hand, transport properties such as thermal conductivity and dynamic viscosity need to be expressed through accurate formulations able to replicate the peculiar behavior of supercritical fluids. First, however, the hypothesis of incompressible flow needs to be evaluated and its use justified in the modeling of supercritical and transcritical fluids.

3.2 Incompressible but Variable Density

The simplification of the incompressible but variable density jet is a hypothesis which arose from the similarity of visualization data. The assumption was tested and evaluated by Barata et al. [66], deserving testing in other, broader situations given the previous encouraging results. As reviewed by Banuti [88], the seemingly overwhelming variety of computational fluid dynamics (CFD) codes is misleading, being successful approaches and methods used as almost canonical procedures.

One of the first arguments in favor of a variable-density jet behavior arose in the early experiments of Newman and Brzustowksi [134], where the injection of carbon dioxide into a chamber filled with a mixture of carbon dioxide and nitrogen is considered at near-critical conditions. Through shadowgraph, it was possible to visualize the inhibition of spray formation as the critical temperature of carbon dioxide was reached and surpassed, which led to the conclusion that the jet could be treated as a variable-density single-phase turbulent submerged jet at pressures ranging from subcritical to supercritical conditions, as long as the temperature remained above the critical point. Quantitative evidence would be later provided by Chehroudi et al. [128] in the form of jet spreading rates, which are a measure of mixing efficiency [139] indicating that the similarity between supercritical and variable-density jet behavior went beyond a simple qualitative physical appearance [73] meeting the values predicted by established models and theories [140, 141] put forward precisely for incompressible variable-density mixing layers. Moreover, Roy et al. [133] performed LIF measurements of fluoroketone injected into nitrogen at conditions ranging from sub- to supercritical. These results are slightly beyond the theory of Abramovich [142], where the potential core length stays constant at ten jet diameters. Here supercritical jet behavior similarity to variable-density behavior is independent of the initial state of the jet, either at subcritical or supercritical conditions. Further experimental measurements [35, 59, 72, 120, 143, 144] provide further quantitative arguments in favor of the variable-density nature of supercritical jets, being similar descriptions encountered for diesel injection [125]. Typically these experiments are conducted at relatively constant pressure, resulting in the dependency of the density gradient solely on temperature, effectively considering density incompressible or weakly compressible. Here, compressibility effects are understood as changes in volume induced by pressure changes. Studies on the effects of compressibility on high-pressure injection systems [145] indicate how fuel density affects jet evolution. Furthermore, the low injection velocity at which the experiments are conducted allied to considering real gas properties allows employing incompressible solution schemes while considering the variable-density behavior of supercritical fluids.

Chehroudi et al. [8] compiled information detailing the growth rate of several jets and theories as depicted in Figure 3.1.

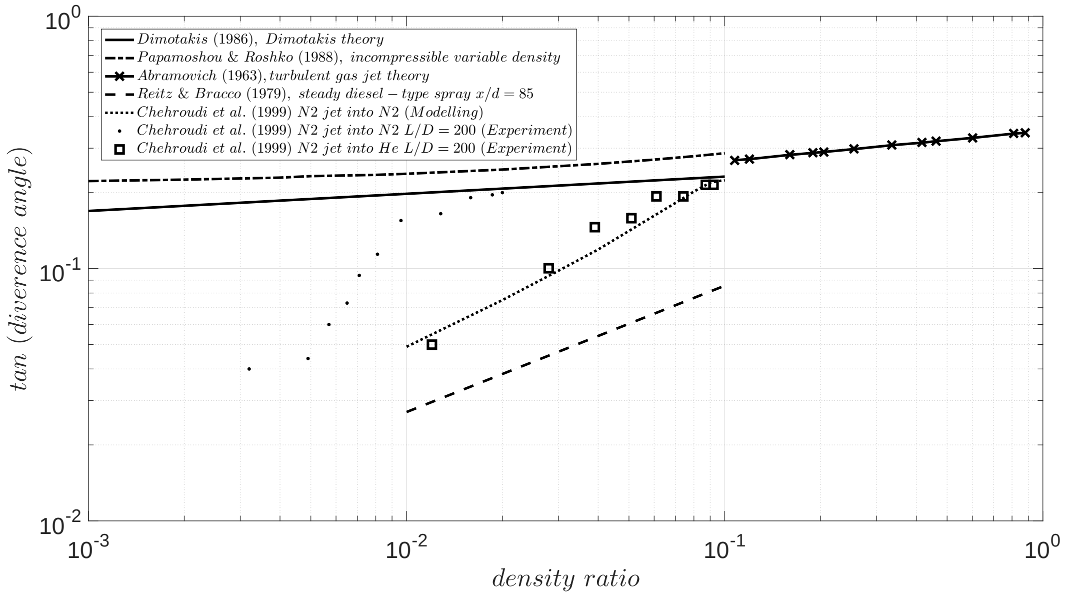

Figure 3.1: Tangent of the visual spreading angle versus chamber-to-injectant density ratio comparison between established theories [140–142] and different injection conditions [8, 146], adapted from Chehroudi et al. [8].

A jet's growth rate is a direct measure of mixing efficiency and provides essential information regarding jet development, as long as data is extracted in the jet's initial mixing region, ensuring the existence of a classical mixing layer. Figure 3.1 covers a density ratio of four orders of magnitude, considering several established theories against which subcritical-to-supercritical injection configurations are compared. Papamoschou and Roshko [141] studied compressible shear layers, focusing on the influence of compressibility in correlating them with incompressible shear layers through density and velocity ratios. Dimotakis [140] provides further evidence that seems to suggest the shear layer behavior is dependent on more than the velocity and density ratios in the free stream, which can help explain why the information in Figure 3.1 does not collapse into a single curve. Variable transformations that correlate compressible mixing layers with their incompressible counterparts show that at low-Mach numbers, turbulent mixing is an incompressible process [147]. However, since various authors use different equations and definitions, when analyzing Figure 3.1, we do not look at the magnitudes but at the jet's general evolution and the meaning of such evolution [148]. Moreover, Abramovich [142], who extensively studied the behavior of turbulent jets, proposes a semi-empirical equation that attempts to incorporate the effects of variable density through a characteristic velocity.

The theories detailing incompressible but variable density behavior are compared with results from single and multi-component mixing [8]. The injection of N_2 into N_2 and N_2 into He in Figure 3.1 shows that as the conditions approach the supercritical regime, the jet spreading rate resembles values obtained by Abramovich [142] for incompressible variable-density jets.

Given the amount of experimental evidence, the variable-density behavior of supercritical jets can then be modeled through the usage of real gas relationships for density (in the form of an EoS) and transport properties like dynamic viscosity and thermal conductivity, detailing ideal gas behavior and departure functions to account for high-pressure effects. In opposition, the numerical modeling of supercritical fluid flows has been traditionally done by resorting to compressible solvers; however, as pointed out by Lapenna and Creta [149], flows at such conditions fall below the significant Mach number threshold of 0.3 and, in conjunction with the low injection velocities, will impose severe restriction into the numerical solver. Nevertheless, variable-density behavior is widely recognized in the literature. For example Schmitt et al. [150] perform LES in nitrogen into nitrogen injection configuration. At the same time, the similarity to variable-density mixing is recognized in the mixing layer configuration oxygen-methane [151], and direct numerical simulations (DNS) of temporal mixing layers of heptane-hydrogen provide evidence of similarities between vortex dynamics, the most unstable compressible and incompressible wavelengths [152].

It is established [153], and it will also be here demonstrated that jet characteristics such as the spreading rate [128], the axial density rate of decay, and consequently the turbulence kinetic energy [154] are sensitive to variations in density. Density effects on coaxial injection configurations are of particular interest in the context of LREs, which typically comprise a central fluid injected with low-velocity and a coaxial stream with high-velocity. Besides considering the initial mixing density ratio [155, 156] between injected and chamber fluid(s) as a measure of mixing efficiency, also thermal effects, in particular, play a paramount role in the accurate description of the injection phenomena [157], further establishing the relation between density and temperature.

3.3 Averaging the Equations

Any flow system will remain laminar up to a particular value of the Reynolds number, Re. This is reflected in the appearance of statistical fluctuations of the variables around mean values. The fluctuations are a result of the non-linear behavior of the advective fluxes. As a result, the conservation equations for mass, momentum, and energy need to reflect the contribution of mean property and fluctuating property components. The question then is how we can define mean and fluctuation?

The first option is to define an ensemble average - equation (3.12), where ϕ_k represents the values of ϕ for statistically independent realizations of the turbulent flow at a given position in space and time, while N is the number of independent realizations.

$$< \phi >= \frac{1}{N} \lim_{N \to \infty} \sum_{k=1}^{N} \phi_k \quad (3.12)$$

On the other hand, eliminating the need for various observations of the turbulent flow, a time average can be defined according to equation (3.13), where T needs to be large enough when compared to the turbulence's time scale.

$$\overline{\phi}_T(x_i, t) = \frac{1}{T} \int_{t-\Delta t}^{t+\Delta t} \phi(x_i, t) dt \quad (3.13)$$

If the steady flow consideration can be extended into the statistics of average and fluctuation, then the ensemble average of equation (3.12) does not depend on time, and ensemble and time averages can be considered to be equal in the approximation to infinity. This is stated in mathematical terms in equation (3.14).

$$< \phi > (x_i) = \overline{\phi}(x_i) \quad (3.14)$$

According to the so-called ergodicity hypothesis, this analysis allows for the definition of average. The averaging process assumes an averaging time much larger than the largest time scale of the turbulent fluctuations. As such, for turbulence that is both stationary and homogeneous, the ensemble, spatial and temporal averages are equal.

Generally, the decomposition of properties in turbulent flows into average and fluctuation components is called Reynolds decomposition and is expressed according to equation (3.15). However, if this were to be applied to the conservation equations, considering that in this specific work, the object of study is flows with extreme density variations, the final formulation would be far too complex. Furthermore, the difficulty of searching for closure approximations would increase by a great deal [156] since the correlations involving density fluctuations would require additional models. Statistical averaging variable-density flows is reported by Chassaing et al. [158], focusing precisely on the argument that other correlations would appear, following this averaging procedure in variable-density flows. These correlations would be additional fluctuation correlation terms due to non-linearities associated with the variable density.

$$\phi = \overline{\phi}_i + \phi_i' \quad (3.15)$$

The question then revolves around choosing a decomposition process in accord with the physics of the problem under consideration. An incompressible but variable density approach is followed, in accordance to Barata et al. [66]. The Favre decomposition is then used, represented mathematically by equations (3.16), (3.17) and (3.18). Otherwise, the averaging process would produce fluctuations between density and variables such as velocity or internal energy. Since the density-weighted average is introduced, their explicit occurrence is prevented.

$$\phi = \tilde{\phi} + \phi'' \quad (3.16)$$

$$\tilde{\phi}_i = \frac{1}{\overline{\rho}} \lim_{t \to \infty} \int_t^{t+\Delta t} (\rho \phi_i)\, dt \quad (3.17)$$

$$\tilde{\phi}_i = \frac{\overline{\rho \phi_i}}{\overline{\rho}} \quad (3.18)$$

The Favre averaged conservation equations for mass, momentum and energy are then represented in equations (3.19), (3.20) and (3.22), respectively.

$$\frac{\partial \overline{\rho} \tilde{u}_i}{\partial x_i} = 0 \quad (3.19)$$

$$\frac{\partial}{\partial x_j} (\overline{\rho} \tilde{u}_i \tilde{u}_j) = -\frac{\partial \overline{p}}{\partial x_i} + \frac{\partial \overline{\tau_{ij}}}{\partial x_j} - \frac{\partial \overline{\rho} \widetilde{u_i'' u_j''}}{\partial x_j} \quad (3.20)$$

The Reynolds stress tensor, resulting from the averaging process, is given according to equation (3.21).

$$\overline{\tau_{ij}} = -\bar{\rho}\widetilde{u_i''u_j''} \quad (3.21)$$

$$\frac{\partial \bar{\rho}\tilde{u}_j\tilde{H}}{\partial x_j} = \frac{\partial \overline{\tau_{ij}u_i}}{\partial x_j} - \frac{\partial \tilde{u}_i\bar{\rho}\widetilde{u_i''u_j''}}{\partial x_j} - \frac{\partial\left(\overline{q}_j + \bar{\rho}\widetilde{u_j''h''}\right)}{\partial x_j} \quad (3.22)$$

Like for the Favre-averaged momentum equation, also in the energy equation, additional terms appear as a consequence of the averaging process, namely the Reynolds stresses (equation (3.21)) and the turbulent heat flux: $\bar{\rho}\widetilde{u_j''h''}$.

Molecular terms in the conservation equations, such as the relation between fluid stresses and fluid strain rate, $\overline{\tau_{ij}}$, the heat flux, $\overline{q_j}$ and $\overline{\tau_{ij}u_i}$ are rewritten accounting for the decomposition into average and fluctuation. Mathematically, this is expressed in equations (3.23), (3.24) and (3.25), respectively.

$$\overline{\tau_{ij}} =\approx \tilde{\mu}\left(\frac{\partial \tilde{u}_i}{\partial x_j} + \frac{\partial \tilde{u}_j}{\partial x_i} - \frac{2}{3}\delta_{ij}\frac{\partial \tilde{u}_k}{\partial x_k}\right) \quad (3.23)$$

$$\overline{q_j} \approx -\frac{\tilde{\mu}}{\mathrm{Pr}}\frac{\partial \tilde{h}}{\partial x_j} \quad (3.24)$$

$$\overline{\tau_{ij}u_i} \approx \overline{\tau_{ij}}\tilde{u}_i \quad (3.25)$$

At this point, the focus shifts to the pursuit of an adequate representation of averages and fluctuations. Here, the term adequate should not be interpreted as having a universal meaning. Instead, the "adequate" choice relates to the objectives of a given study and the inherent computational cost of any given representation. At present, a RANS representation of turbulence [159] is followed, where average quantities are evaluated over the entire wavelength of turbulence fluctuations. In contrast, fluctuations are modeled following a semi-empirical model in what is commonly referred to as the closure problem.

On the other hand, in LES, the fluctuations are computed directly above a given threshold, defined by a filter. In contrast, the smaller scales are modeled below the threshold with a semi-empirical, labeled sub-grid scale (SGS) model. The underlying conception in LES is that the large eddies carry most of the Reynolds stresses. At the same time, the SGSs are more in accord with isotropic behavior, carrying less of the Reynolds stresses, and are therefore modeled [160]. The choice of the SGS is significant in regards to the advective fluxes, which can lead to the propagation of non-physical spurious pressure oscillations polluting the solution, and artificial dissipation may need to be introduced to stabilize the numerical solution. Lastly, in DNS, all the wavelengths of turbulence fluctuations are computed, increasing computational cost. Since the size of the smaller eddies is inversely proportional to $\mathrm{Re}^{3/4}$, following Kolmogorov's scale with the same moniker, DNS computations are performed at reduced Reynolds numbers. For instance, an increase in the Reynolds number by 10 increases the needed computational power by 1000. The proportionality between the small scales eddies and the inverse of $\mathrm{Re}^{3/4}$ is important for LES and DNS since the inertial subscales it respects allow to evaluate the solution quality.

Synergism between experiments and numerical modeling efforts is frequently invoked. Following that, experiments provide qualitative and quantitative data to deepen our understanding of the physical processes associated with supercritical fluid flow and provide measurements against which numerical solvers can be compared and validated. On the other hand, numerical models can help direct experimental campaigns to regions and quantities of interest. Could we follow similar descriptions, talk about synergism between RANS, LES, and DNS, and, if so, determine that the ”adequate” modeling approach depends on the objectives we aim to achieve and their constraints?

The computational cost in capturing the dynamics of the smaller eddies increases the computational cost to prohibitive levels [161], leaving LES and RANS as valid modeling approaches. Furthermore, multiple model evaluation requirements can leave RANS as the only reasonable option. DNS is usually a research tool used to understand the fundamental mechanisms of turbulence, which can assert the results obtained in LES and RANS.

3.4 The Search for Closure Approximations

The search for a closure approximation for the system of equations expresses the need for unknown terms to be modeled as a function of the current dependent variables. Closure models can be classified into first or second order. In first-order closure models, the Reynolds stress tensor is expressed as a function of the mean flow velocities. In contrast, in second-order (or Reynolds stress transport models), the correlation is a function of the mean flow velocities and the Reynolds stresses. An underlying hypothesis in most turbulence closure models is the Boussinesq hypothesis, which states that the relationship between Reynolds stresses and the average rate of strain is similar to the Newtonian relationship between viscous stresses and the rate of strain. This is achieved by introducing an eddy (or turbulent) viscosity, μ_t, while the turbulence models that rely on this concept are labeled eddy viscosity models. Mathematically, the Boussinesq approximation is expressed in equation (3.26).

$$-\widetilde{\bar{\rho} u_i'' u_j''} = -\frac{2}{3}\rho k \delta_{ij} + \mu_t \left(\frac{\partial \tilde{u}_i}{\partial x_j} + \frac{\partial \tilde{u}_j}{\partial x_i} - \frac{2}{3}\frac{\partial \tilde{u}_k}{\partial x_k}\delta_{ij} \right) \quad (3.26)$$

Two points are of paramount importance here: the relations between Reynolds stresses and the mean flow quantities are unknown, and the available turbulence models offer an approximation, while turbulence is an anisotropic phenomenon, which means the normal stress components are unequal. Based on the Boussinesq hypothesis, the eddy viscosity models are isotropic, meaning the normal Reynolds stresses are considered equal.

The eddy viscosity is modeled according to equation (3.27), based on density, velocity, and length scales. The way the velocity and length scales are determined contributes to the classification of turbulence models. For example, if both are determined algebraically from mean flow data, the turbulence model is a zero-equation model. On the other hand, if the length scale is determined algebraically and the velocity from a field equation, then the model is classified as a one-equation model. Finally, a two-equation model is used if both scales are determined from field equations. While accurately capturing the flow physics, an ideal closure model needs to introduce the minimum amount of complexity.

$$\mu_t = \rho L V \quad (3.27)$$

In algebraic models, the eddy viscosity is assumed to depend only on the local average flow quantities, not taking history into account. On the other hand, one- and two-equation models consider that the eddy viscosity will be different at any given distance from a wall, depending on the pressure gradient (adverse, favorable, or null). Thus, the turbulence kinetic energy constitutes a natural velocity scale.

The turbulence heat flux, $\widetilde{\bar{\rho} u_j'' h''}$, is modeled according to equation (3.28), where Pr_t is the turbulent Prandtl number, which expresses the eddy diffusivity of momentum to the eddy diffusivity of heat (equation(3.29)). Sarh and Gökalp [157] provide theoretical and experimental arguments indicating that mixing efficiency is higher for heat than for momentum. The inclusion of variable turbulent Prandtl number models is mostly used in the determination of heat transfer coefficients [50, 162]. However, the generalization of such models [163] to different fluids and configurations is difficult.

$$\widetilde{\bar{\rho} u_j'' h''} = -\frac{c_p \mu_t}{\mathrm{Pr}_t}\frac{\partial \tilde{T}}{\partial x_j} = -\frac{\mu_t}{\mathrm{Pr}_t}\frac{\partial \tilde{h}}{\partial x_j} \quad (3.28)$$

$$\mathrm{Pr}_t = \frac{\nu_t}{\alpha_t} \quad (3.29)$$

RANS and LES solvers are validated using the relatively small number of available quantitative experimental data sets [35, 58, 59, 72, 120]. While the density is retrieved using a real gas EoS, the description of derived caloric properties uses the departure function formalism. The highly non-linear behavior [164] in both thermodynamic and transport properties can lead to distinct coupling mechanisms than those observed at subcritical conditions: the inclusion of the Soret and Dufour effects [25, 152] in the computations or of the filtered density in the scope of the EoS [151], may play an additional role. In particular, Taşkinoğlu and Bellan [165] found through an a-priori analysis, in the context of LES, the need to include a correction term for the SGS contribution of the heat flux in the filtered energy equation. Temporal mixing layers as studied by this research group [166] by either LES or DNS, where DNS is used to generate the database used to model enclosed terms in the filtered LES equations, while Kawai and Oikawa [118] propose an extension of the κ-ω SST model with a correction for the turbulence kinetic energy equation, to increase the model accuracy to variable-density flows.

Moreover, to address the high-resolution LES requirements for the boundary layer, Wu et al. [167] propose to use detached eddy simulation (DES), where LES is to be used in the regions where large eddies dominate, with RANS used to model the boundary layer. Similarly, Cheng and Schulenberg [26] proposes the introduction of additional production terms in the turbulence kinetic energy equation to account for the variable property behavior of the fluid flow. Finally, Müller et al. [168] conclude that the SGS modeling leads to no differences in the mean density, indicating that SGS modeling is not as important if the objective is only to evaluate the mean flow. Therefore, the focus has also been on developing variable turbulent Prandtl number models [169, 170] instead of developing the turbulence models themselves.

The effect of variable density in the production of turbulence due to variations in the isobaric specific heat and thermal conductivity affects the effectiveness of heat transfer [116]. However, proposed modifications to the conventional turbulence model usually result in complicated and computationally costly solutions. For these reasons, low-pressure turbulence models [160, 171] continue to be used [154, 172, 173].

3.4.1 Spalart-Allmaras

A one equation model is simple enough to be generated from scratch, allowing for better performance and fuller control over its mechanisms. This is the case of the Spalart and Allmaras [174] turbulence model.

In this model, eddy viscosity is evaluated according to equation (3.30), where $\tilde{\nu}$ is a modified eddy viscosity and f_{v1} a damping function - equation (3.31), being c_{v1} a model constant.

$$\mu_t = \overline{\rho}\tilde{\nu} f_{v1} \quad (3.30)$$

$$f_{\nu 1} = \frac{\chi^3}{\chi^3 + c_{\nu 1}^3}, \quad \chi \equiv \frac{\tilde{\nu}}{\nu} \quad (3.31)$$

The full Spalart-Allmaras (SA) turbulence model is presented on equation (3.32). It comprises production, P, destruction, D, and transport terms.

$$u_j \frac{\partial \tilde{\nu}}{\partial x_j} = P - D + \frac{1}{\sigma}\left[\frac{\partial}{\partial x_j}\left((\nu + \tilde{\nu})\frac{\partial \tilde{\nu}}{\partial x_j}\right) + c_{b2}\frac{\partial \tilde{\nu}}{\partial x_i}\frac{\partial \tilde{\nu}}{\partial x_i}\right] \quad (3.32)$$

The production (by vorticity) and destruction terms (by pressure) are defined by equations (3.33) and (3.34), respectively.

$$P = c_{b1}\tilde{S}\tilde{\nu} \quad (3.33)$$

$$D = c_{w1} f_w \left(\frac{\tilde{\nu}}{d}\right)^2 \quad (3.34)$$

The modified vorticity, $\tilde{S}$ is given in equation (3.35), where κ is the von Karman's constant and Ω the magnitude of the vorticity, defined in equation (3.36). d represents the distance to the nearest wall.

$$\tilde{S} = \Omega + \frac{\tilde{\nu}}{\kappa^2 d^2} f_{\nu 2} \quad (3.35)$$

$$\Omega = \sqrt{2W_{ij}W_{ij}}, \quad W_{ij} = \frac{1}{2}\left(\frac{\partial u_i}{\partial x_j} - \frac{\partial u_j}{\partial x_i}\right) \quad (3.36)$$

The parameter f_w is defined on equation (3.37).

$$f_w = g\left[\frac{1+c_{w3}^6}{g^6+c_{w3}^6}\right]^{1/6} \quad (3.37)$$

With:

$$g = r + c_{w2}(r^6 - r), \quad r = \min\left[\frac{\tilde{\nu}}{\tilde{S}\kappa^2 d^2}, 10\right] \quad (3.38)$$

The SA turbulence model has source terms - production and destruction - non-zero in the free stream, even when the vorticity is zero.

The last constant is defined in equation (3.39). It has the function of balancing the production, destruction, and diffusion of the modified eddy viscosity. All the parameters included in this equation are constants specific to the Spalart-Allmaras model, which are defined in Table 3.1.

$$c_{w1} = \frac{c_{b1}}{\kappa^2} + \frac{1+c_{b2}}{\sigma} \quad (3.39)$$

Table 3.1: Spalart-Allmaras model constants [174].

Parameter	Value
c_{b1}	0.1355
σ	2/3
c_{b2}	0.622
κ	0.41
c_{w2}	0.3
c_{w3}	2
$c_{\nu 1}$	7.1
c_2	0.7
c_3	0.9

3.4.2 kappa-epsilon family

In the standard $\kappa - \varepsilon$ model [175], both scales are determined from the field equations. In this model eddy viscosity is stated according to equation (3.40), where κ (equation (3.41)) represents the turbulence kinetic energy and ε (equation (3.42)) its dissipation. This model is only valid for fully turbulent flows.

$$\mu_t = C_\mu f_\mu \frac{\rho \kappa^2}{\varepsilon} \quad (3.40)$$

$$\frac{\partial(\rho u_j \kappa)}{\partial x_j} = P - p\varepsilon + \frac{\partial}{\partial x_j}\left[\left(\mu + \frac{\mu_t}{\sigma_\kappa}\right)\frac{\partial \kappa}{\partial x_j}\right] \quad (3.41)$$

$$\frac{\partial(\rho u_j \varepsilon)}{\partial x_j} = C_{\varepsilon 1} f_1 \frac{\varepsilon}{\kappa} P - C_{\varepsilon 2} f_2 \frac{\rho \varepsilon^2}{\kappa} + \frac{\partial}{\partial x_j}\left[\left(\mu + \frac{\mu_t}{\sigma_\varepsilon}\right)\frac{\partial \varepsilon}{\partial x_j}\right] \quad (3.42)$$

In the previous representation and a general common representation of two-equation turbulence models, the dissipation rate assumes a similar formulation as the turbulence kinetic energy, containing production, destruction, and dissipation terms. This is related to the difficulty in modeling unknowns related to the smaller scales of turbulence.

The production term is evaluated using equation (3.43)

$$P = \tau_{ij} \frac{\partial \tilde{u}_i}{\partial x_j} \quad (3.43)$$

The standard κ-ε model constants are presented on Table 3.2.

Table 3.2: Standard $\kappa - \varepsilon$ model constants [175].

Parameter	Value
σ_κ	1.0
σ_ε	1.3
C_μ	0.09
$C_{\varepsilon 1}$	1.35
$C_{\varepsilon 2}$	1.8
f_1	1.0

The initial values for the turbulence quantities - the turbulence kinetic energy (κ_0) and its dissipation (ε_0) are set, according to equations (3.44) and (3.45), respectively. A turbulence intensity of 5% is selected. A preliminary study showed that the influence of its variation is meager. The length scale used equals 0.014 the jet diameter, and the velocity scale equals the mean jet exit velocity.

$$\kappa_0 = \frac{3}{2}(Iu)^2 \quad (3.44)$$

$$\varepsilon_0 = \frac{c_\mu^{3/4}\kappa^{3/2}}{0.014l} \quad (3.45)$$

Re-Normalization Group (RNG) methods can provide a more accurate representation of the different motion scales and present a more accurate representation of the turbulent Prandtl number. As such, the resulting turbulence model is called the RNG $\kappa - \varepsilon$ turbulence model, according to Yakhot et al. [176]. While the eddy viscosity is evaluated similarly to the standard version, the transport equations for turbulence kinetic energy and its dissipation are slightly altered. They are given in equations (3.46) and (3.47), respectively. Model constants are given in Table 3.3.

$$\frac{\partial \overline{\rho}\tilde{u}_i\kappa}{\partial x_i} = \tau_{ij}\frac{\partial \tilde{u}_j}{\partial x_i} - \overline{\rho}\varepsilon + \frac{\partial}{\partial x_j}\left[\left(\psi_\kappa \mu_{eff}\right)\frac{\partial \kappa}{\partial x_j}\right] \quad (3.46)$$

$$\frac{\partial \overline{\rho}\tilde{u}_i\varepsilon}{\partial x_i} = c_{\varepsilon 1}\frac{\varepsilon}{\kappa}\tau_{ij}\frac{\partial \tilde{u}_j}{\partial x_i} - \tilde{c}_{\varepsilon 2}\overline{\rho}\frac{\varepsilon^2}{\kappa} + \frac{\partial}{\partial x_j}\left[\left(\psi_\varepsilon \mu_{eff}\right)\frac{\partial \varepsilon}{\partial x_j}\right] \quad (3.47)$$

In RNG methods the smallest scales of turbulence are systematically removed up to a point where the remaining scales can be resolvable with the available computational power. $c_{\varepsilon 2}$ is no longer a constant as was the case in the standard version and as such it must be defined accordingly:

$$\tilde{c}_{\varepsilon 2} = c_{\varepsilon 2} + \frac{c_\mu \lambda^3\left(1 - \lambda/\lambda_0\right)}{1 + \beta\lambda^3} \quad (3.48)$$

$$\lambda = \frac{\kappa}{\varepsilon}\tilde{S} \quad (3.49)$$

$$\left|\frac{\psi - 1.3929}{\psi_0 - 1.3929}\right|^{0.6321}\left|\frac{\psi - 2.3929}{\psi_0 - 2.3929}\right|^{0.3679} = \frac{\mu}{\mu_{eff}} \quad (3.50)$$

Table 3.3: RNG $\kappa - \varepsilon$ model constants [176].

Parameter	Value
$c_{\varepsilon 1}$	1.42
$c_{\varepsilon 2}$	1.68
c_μ	0.0845
β	0.012
λ_0	4.38
ψ_0	1.0

In an attempt to solve a problem which is the possibility of the normal Reynolds stresses having negative values, another $\kappa - \varepsilon$ variation exists, that is, the realizable version proposed by Shih et al. [177]. As such, the constant c_μ becomes flow-dependent, while ε is obtained through the fluctuation of the mean vorticity. In terms of the field equation, the novelty lies in the fact that the production of turbulence kinetic energy dissipation no longer relies on the production of turbulence kinetic energy. This can be easily seen in equations (3.51) and (3.52).

The term realizable used to label this model means the model mathematically satisfies the Reynolds stresses following the physics of the flow under consideration. Specifically, the Reynolds stresses obtained are always positive. However, the same is not valid for both the standard and RNG variations, which are "conditionally" realizable. Model constants are given in Table 3.4.

$$\frac{\partial \overline{\rho}\tilde{u}_j\kappa}{\partial x_j} = \tau_{ij}\frac{\partial \tilde{u}_i}{\partial x_j} - \overline{\rho}\varepsilon + \frac{\partial}{\partial x_j}\left[\left(\mu + \frac{\mu_t}{\sigma_\kappa}\right) + \frac{\partial \kappa}{\partial x_j}\right] \quad (3.51)$$

$$\frac{\partial \overline{\rho}\tilde{u}_j\varepsilon}{\partial x_j} = c_1\overline{\rho}S\varepsilon - c_2\frac{\overline{\rho}\varepsilon^2}{\kappa + \sqrt{\nu\varepsilon}} + \left[\left(\mu + \frac{\mu_t}{\sigma_\varepsilon}\right)\frac{\partial \varepsilon}{\partial x_j}\right] \quad (3.52)$$

$$c_\mu = \frac{1}{A_0 + A_s U^* \kappa/\varepsilon} \quad (3.53)$$

$$U^* = \sqrt{\tilde{S}_{ij}\tilde{S}_{ij} + \tilde{\Omega}_{ij}\tilde{\Omega}_{ij}} \quad (3.54)$$

$$A_s = \sqrt{6}\cos\xi \quad (3.55)$$

$$\xi = \frac{1}{3}\arccos(\sqrt{6}\chi) \quad (3.56)$$

$$\xi = \frac{\tilde{S}_{ij}\tilde{S}_{jk}\tilde{S}_{ki}}{\hat{S}^3} \quad (3.57)$$

$$\hat{S} = \sqrt{\tilde{S}_{ij}\tilde{S}_{ij}} \quad (3.58)$$

$$c_1 = \max\left[0.43, \frac{\eta}{5+\eta}\right] \quad (3.59)$$

$$\eta = \frac{\tilde{S}\kappa}{\varepsilon} \quad (3.60)$$

Table 3.4: Realizable $\kappa - \varepsilon$ model constants [177].

Parameter	Value
σ_κ	1.0
σ_ε	1.2
c_2	1.9
A_0	4.04

3.4.3 kappa-omega family

In the $\kappa - \omega$ family of turbulence models [178], the dissipation of turbulence kinetic energy is replaced by the specific dissipation. This is expressed in equation (3.61).

$$\omega = \frac{\varepsilon}{\kappa} \quad (3.61)$$

In the standard $\kappa - \omega$ turbulence model, the turbulence kinetic energy and its specific dissipation rate are given according to equations (3.62) and (3.63), respectively.

$$\frac{\partial \overline{\rho} \tilde{u}_j \kappa}{\partial x_j} = \tau_{ij} \frac{\partial \tilde{u}_i}{\partial x_j} - \overline{\rho} \beta^* f_{\beta^*} \kappa \omega + \frac{\partial}{\partial x_j} \left[\left(\mu + \sigma_\kappa \frac{\overline{\rho} \kappa}{\omega} \right) \frac{\partial \kappa}{\partial x_j} \right] \quad (3.62)$$

$$\frac{\partial \overline{\rho} \tilde{u}_j \omega}{\partial x_j} = \frac{\omega}{\kappa} \tau_{ij} \frac{\partial \tilde{u}_i}{\partial x_j} - \overline{\rho} \beta f_\beta \omega^2 + \frac{\partial}{\partial x_j} \left[\left(\mu + \sigma_\omega \frac{\overline{\rho} \kappa}{\omega} \right) \frac{\partial \omega}{\partial x_j} \right] \quad (3.63)$$

$$f_{\beta^*} = \begin{cases} 1 & , \chi_\kappa \leq 0 \\ \frac{1+680\chi_\kappa^2}{1+400\chi_\kappa^2} & , \chi_\kappa > 0 \end{cases} \quad (3.64)$$

$$\chi_\kappa \kappa = \frac{1}{\omega^3} \frac{\partial \kappa}{\partial x_j} \frac{\partial \omega}{\partial x_j} \quad (3.65)$$

$$f_\beta = \frac{1 + 70\chi_\kappa \omega}{1 + 80\chi_\omega} \quad (3.66)$$

$$\chi_\omega = \left| \frac{\tilde{\Omega}_{ij} \tilde{\Omega}_{jk} \tilde{S}_{ki}}{(\beta^* \omega)^3} \right| \quad (3.67)$$

As in the realizable version of the $\kappa - \varepsilon$ model, an attempt is made to reduce the round-jet anomaly by relating the turbulence kinetic energy dissipation with the mean deformation of the flow-through variables f_β and χ_ω. However, the standard $\kappa - \omega$ turbulence model's behavior outside the shear layer is a significant setback. The standard $\kappa - \omega$ model constants are given in Table 3.5.

The shear stress transport (SST) $\kappa - \omega$ [179] model is a hybrid version between the standard

Table 3.5: Standard $\kappa - \omega$ model constants [178].

Parameter	Value
σ_κ	2.0
σ_ω	2.0
β^*	0.09
β	0.072

variation of the $\kappa - \omega$, thus retaining its advantage in the shear layer while also retaining the resilient formulation of the $\kappa - \varepsilon$ in the free-stream. First, the transport equation for ε is reconstructed into a similar formulation as ω. Then, they are multiplied by a blending function F_1, designed to be one in the viscous sub-layer and zero in the log-layer, thus switching coefficients between the ε and ω formulations when appropriate. After the multiplication by the blending function, both formulations are added up together. Equation (3.68) and (3.69) detail the transport equations for the turbulence kinetic energy and specific dissipation rate, respectively, while the model constants are reproduced in Table 3.6.

$$\frac{\partial \overline{\rho} \tilde{u}_j \kappa}{\partial x_j} = \tau_{ij} \frac{\partial \tilde{u}_i}{\partial x_j} - \beta^* \overline{\rho} \kappa \omega + \frac{\partial}{\partial x_j} \left[\left(\mu + \sigma_\kappa \mu_t \right) \frac{\partial \kappa}{\partial x_j} \right] \quad (3.68)$$

$$\frac{\partial \overline{\rho} \tilde{u}_j \omega}{\partial x_j} = \frac{\gamma}{\nu_t} \tau_{ij} \frac{\partial \tilde{u}_i}{\partial x_j} - \beta \overline{\rho} \omega^2 + \left[\left(\mu + \sigma_\omega \mu_t \right) \frac{\partial \omega}{\partial x_j} \right] + \left(1 - F_1 \right) 2 \overline{\rho} \frac{1}{\omega \sigma_{\omega 2}} \frac{\partial \kappa}{\partial x_j} \frac{\partial \omega}{\partial x_j} \quad (3.69)$$

Where:

$$\phi = F_1 \phi_1 + \left(1 - F_1 \right) \phi_2 \quad (3.70)$$

$$\gamma_1 = \frac{\beta_1}{\beta^*} - \frac{\kappa^2}{\sigma_{\omega_1} \sqrt{\beta^*}} \quad (3.71)$$

$$\gamma_2 = \frac{\beta_2}{\beta^*} - \frac{\kappa^2}{\sigma_{\omega_2} \sqrt{\beta^*}} \quad (3.72)$$

$$F_1 = \tanh(\arg_1^4) \quad (3.73)$$

$$\arg_1 = \min\left[\max\left(\frac{\sqrt{\kappa}}{0.09\omega d}, \frac{500\nu}{d^2\omega}\right), \frac{4\rho\kappa}{\sigma_{\omega 2} CD_\omega^+ d^2}\right] \quad (3.74)$$

In equation (3.74), d is the distance to the closest surface, and CD_ω^+ the positive part of the cross-diffusion term.

$$CD_\omega^+ = \max\left(2\rho\frac{1}{\omega\sigma_{\omega 2}}\frac{\partial\kappa}{\partial x_j}\frac{\partial\omega}{\partial x_j}, 10^{-10}\right) \quad (3.75)$$

$$\mu_t = \frac{\overline{\rho}\kappa}{\omega}\frac{1}{\max\left[1, \left(\tilde{S}F_2\right)/(a_1\omega)\right]} \quad (3.76)$$

$$F_2 = \tanh(\arg_2^2) \quad (3.77)$$

$$\arg_2 = \max\left(2\frac{\sqrt{\kappa}}{0.09\omega d}, \frac{500\mu}{d^2\omega\overline{\rho}}\right) \quad (3.78)$$

Two eddy viscosity approximations approximate Reynolds stresses through the blending function F_2, equal to zero in the free-stream and 1 in the boundary layer. In the boundary layer, τ is assumed to be proportional to κ, through which better results are possible to obtain only in the boundary layer since outside the definition of eddy viscosity revolves back to the initial description, $\overline{\rho}\kappa/\omega$.

$$\tau = \overline{\rho}a_1\kappa \quad (3.79)$$

Table 3.6: $\kappa - \omega$ SST model constants [179].

Parameter	Value
$\sigma_{\kappa 1}$	1.176
$\sigma_{\kappa 2}$	1.0
$\sigma_{\omega 1}$	2.0
$\sigma_{\omega 2}$	1.168
β_1	0.075
β_2	0.0828
β^*	0.09
κ	0.4187
a_1	0.31

3.4.4 Shear Stress Transport - Reynolds stress BSL

A transport equation for the Reynolds stress tensor is derived (equation (3.80)), coupled with another transport equation for ε or ω. Dissipation, turbulent diffusion and pressure strain are then defined following equations (3.81),(3.82) and (3.83), respectively.

$$\frac{\partial \tilde{u}_k \tau_{ij}}{\partial x_k} = -\tau_{ik}\frac{\partial \tilde{u}_j}{\partial x_k} - \tau_{jk}\frac{\partial \tilde{u}_i}{\partial x_k} + \overline{\rho}\varepsilon_{ij} - \Pi_{ij} + \frac{\partial}{\partial x_k}\left[\overline{-t_{kj}u_i'' + t_{ki}u_j''} + \overline{\rho}C_{ijk}\right] \quad (3.80)$$

$$\overline{\rho}\varepsilon_{ij} = \overline{t_{kj}\frac{\partial u_i''}{\partial x_k} + t_{ki}\frac{\partial u_j''}{\partial x_k}} \quad (3.81)$$

$$\overline{\rho}C_{ijk} = \overline{\rho u_i'' u_j'' u_k''} + \overline{p' u_i''}\delta_{jk} + \overline{p' u_j''}\delta_{ik} \quad (3.82)$$

$$\Pi_{ij} = \overline{\frac{p'}{\rho}\left(\frac{\partial u_i''}{\partial x_j} + \frac{\partial u_j''}{\partial x_i}\right)} \quad (3.83)$$

With:

$$\varepsilon_{ij} = \frac{2}{3}\overline{\rho}\beta^* \kappa \omega \delta_{ij} \quad (3.84)$$

$$C_{ijk} = \frac{\partial}{\partial x_k}\left(\frac{\mu_t}{\sigma_\kappa \kappa}\frac{\partial \overline{u_i'' u_j''}}{\partial x_k}\right) \quad (3.85)$$

$$\Pi_{ij} = \beta^* C_1 \omega \left(\tau_{ij} + \frac{2}{3}\kappa\delta_{ij}\right) - \hat{\alpha}\left(P_{ij} - \frac{1}{3}P_{kk}\delta_{ij}\right) - \hat{\beta}\left(D_{ij} - \frac{1}{3}P_{kk}\delta_{ij}\right) - \hat{\gamma}\kappa\left(S_{ij} - \frac{1}{3}S_{kk}\delta_{ij}\right) \quad (3.86)$$

$$P_{ij} = \tau_{ik}\frac{\partial \tilde{u}_j}{\partial x_k} + \tau_{jk}\frac{\partial \tilde{u}_i}{\partial x_k} \quad (3.87)$$

$$D_{ij} = \tau_{ik}\frac{\partial \tilde{u}_k}{\partial x_j} + \tau_{jk}\frac{\partial \tilde{u}_k}{\partial x_i} \quad (3.88)$$

$$\hat{\alpha} = \frac{8 + c_2}{11} \quad (3.89)$$

$$\hat{\beta} = \frac{8c_2 - 2}{11} \quad (3.90)$$

$$\hat{\gamma} = \frac{60c_2 - 4}{55} \quad (3.91)$$

Table 3.7: Reynolds stress BSL model constants [178].

Parameter	Value
$\sigma_{\kappa 1}$	2.0
$\sigma_{\omega 1}$	2.0
β_1	0.075
$\sigma_{\kappa 2}$	1.0
$\sigma_{\omega}2$	1.168
β_2	0.0828
β^*	0.09
κ	0.4187
c_1	1.8
c_2	0.52

3.5 Wall treatment

Since some turbulence models are not valid up to the solid walls, they need to be calibrated according to wall functions to ensure that the boundary layer is properly resolved. Consequently, wall function modeling bridges the gap between the region affected by viscosity and the fully turbulent region, in which turbulence models such as the κ-ε can be used. Wall functions are formed based on the concept of y^+, defined in equation (3.92), where u_τ is the friction velocity defined in equation (3.93), y the distance from the wall and ν the kinematic viscosity. Physically, y^+ comes from the universal law of the wall, which states that the velocity distribution in proximity to the wall is similar for the vast majority of turbulent flows. The y^+ is a local Reynolds number that balances the viscous and turbulent processes in the boundary layer (Figure 3.2).

$$y^+ = \frac{u_\tau y}{\nu} \quad (3.92)$$

$$u_\tau = \sqrt{\frac{\tau_w}{\rho}} \quad (3.93)$$

The boundary layer is divided into an inner and outer region on the threshold of y^+ of 500. Below this value, shear stresses are directly affected by viscosity, while above it, the effect of viscosity is negligible. In the inner region, increasing y^+ from the wall makes it possible to define the viscous sub-layer, the buffer layer, and the logarithmic layer. The fluid is dominated by viscous effects (as indicated by the y^+ ratio) in the viscous sub-layer, and shear stress can be assumed to be negligible ($u^+ = y^+$). On the other side, $50 > y^+ > 30$ the logarithmic area represents the dominance of turbulence stresses over the flow, and the velocity profiles vary with a logarithmic function ($u^+ = \frac{1}{\kappa} \ln{(y^+)} + B$). Finally, the buffer layer lies between ($5 < y^+ < 30$), where viscous and turbulence stresses have similar magnitudes, and

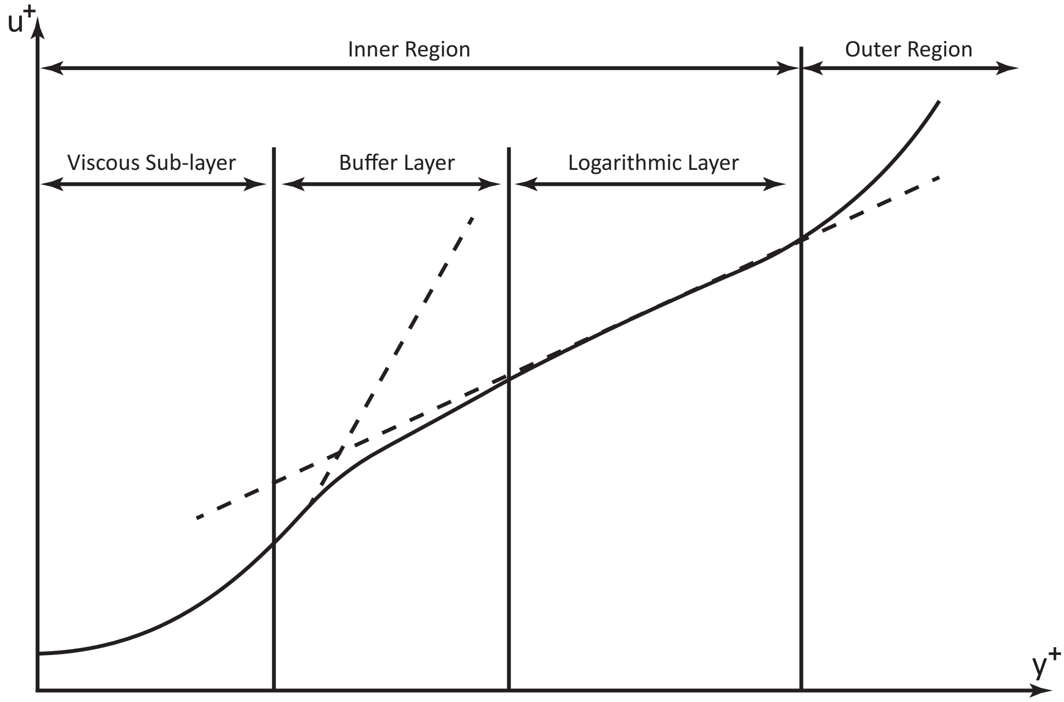

Figure 3.2: Representation of the turbulent boundary layer.

the velocity profile is not well defined.

For example, in the κ-ε, a value of y^+ of 11.63 is considered for the first cells adjacent to the walls. Below this value, the flow is assumed to be purely viscous; above this value, it is considered purely turbulent. As well as the y^+ value, there is a need to define a minimum number of points in the grid located inside the boundary layer. Typically, around 20 points are taken to be inside the boundary layer. The y^+ restrictions and the minimum number of grid points in the boundary layer are fixed parameters that must be maintained during the mesh refinement process and the testing of different grid configurations.

3.6 Turbulence uncertainty

Attempts to quantify the structural uncertainty of turbulence models, either by performing sensitivity studies on the calibration constants [171], attempting to develop additional formulations with improved performance [180] or explicitly quantifying the uncertainty levels [181, 182], is a research topic of increasing interest. Considering the injection configurations of interest in the description of supercritical injection, eddy viscosity models are known to produce an initial low mixing rate [181], which leads to the formation of a longer jet potential core. Further downstream, the mixing rate is higher, underpredicting the experimental data. Here, by comparing several eddy viscosity models, as well as a second-order closure not based on Boussinesq's eddy viscosity concept, it will be demonstrated that the second-order closure leads to the appearance of a longer potential core than, for instance, the Launder and Spalding [175] model. However, by using the second-order closure, some underprediction of the experimental data is corrected. This could be interpreted as the level of pseudo-boiling being [45, 53] responsible for the longer potential core and not the uncertainties associated with eddy viscosity models. Moreover, since the low-pressure law of the wall models the interaction wall-fluid, the study of free jets could be used to circumvent the uncertainty surrounding the nature of the interaction [65]. Nonetheless, the uncertainties associated with eddy viscosity models and their quantification should be acknowledged and taken into account in the description of the results [183]. As described in Georgiadis et al. [180], the capture of the initial jet growth region is a challenge for these models, especially for the standard models, being improvements in the description of the mean and turbulent field still required. RANS provide higher fidelity for axisymmetric cold jets than for heated and non-axisymmetric confgurations [181]. However, predicting uncertainties associated with eddy viscosity models is complex, and it is not clear at present how the uncertainty could be included in the model [181, 182], considering that uncertainties are not uniform in the computational domain. Parametric studies on the calibration constants [161] could be effective in discriminating which regions of the computational domain turbulence uncertainty are most problematic. These increase the computational cost of the solution, given that uncertainty quantification techniques are computationally expensive since a single model evaluation is not sufficient

3.7 Equations of State

The departure from ideal gas behavior paves the way for implementing a real gas EoS [79]. These can be cubic or more complex formulations explicit in the Helmholtz energy. Cubic EoS such as the Peng Robinson (PR) [184] or Soave Redlich Kwong (SRK) [185] expressions are often used due to the compromise they represent between accuracy and simplicity. However, more complex multi-parameter EoS have also been employed, using a modified Benedict Webb Rubin (BWR) equation [186] or formulations based on the Helmholtz energy. In these last two EoSs groups, the EoS is solved before the computations, effectively removing the associated computational load on the numerical solver. Tables are then compiled, from which the values of interest can be retrieved during the iterative procedure. Unfortunately, these tabulation methods are generally not extended to mixtures of more than two species due to prohibitive memory allocation.

Implications resulting from choosing an appropriate EoS go beyond simply accuracy and predictive capabilities. Numerical stability and turbulence modeling are two other areas where the choice of an EoS and consequently the modeling of transport properties can affect the accuracy of the entire solver, regardless of it following RANS, LES, or DNS formulations. The recognition that inaccuracies in the prediction of critical point properties afflict commonly used cubic EoS is not new [187], but the prohibitive cost of most complex formulations gave rise to several correction factors that intend to improve any given aspect of the baseline EoS. These non-linearities in the EoS, and consequently in the transport properties, can contribute to altering the structure of turbulence [164], derived from the non-linearity associated with advective fluxes, eventually raising the question of needing to add correction factors to the turbulence models.

An EoS can be written in a general formulation, in reduced properties according to equation 3.94. The principle of corresponding states indicates that equation 3.94 is approximately true for all substances following the non-dimensional representation in reduced properties, according to the similar shape of $p - V - T$ data. For non-spherical molecules where predictions are not very accurate, the concept of acentric factor has been introduced [188], leading to what is commonly referred to as the extended corresponding state principle (equation 3.95).

$$p_r = p_r\left(V_r, T_r\right) \quad (3.94)$$

$$p_r = p_r\left(V_r, T_r, \omega\right) \quad (3.95)$$

The compressibility factor, Z, is a measure of deviation from ideal gas behavior:

$$Z = \frac{p}{\rho \mathcal{R} T} \quad (3.96)$$

Figure 3.3 depicts the density for nitrogen at pressure levels ranging from $1\,\mathrm{MPa}$ to $10\,\mathrm{MPa}$, with data extracted from the NIST database. The blue dashed line observed for pressures up to $3\,\mathrm{MPa}$ denotes the discontinuity between liquid and gas phases under subcritical conditions. Then, entering the supercritical regime, this discontinuity ceases, starting at the pressure level of $4\,\mathrm{MPa}$ and large density gradients are observed, whose effect becomes less pronounced as the pressure is continuously increased. The choice of the EoS needs to take into account fluid behavior at these different regimes and still lead to accurate density predictions.

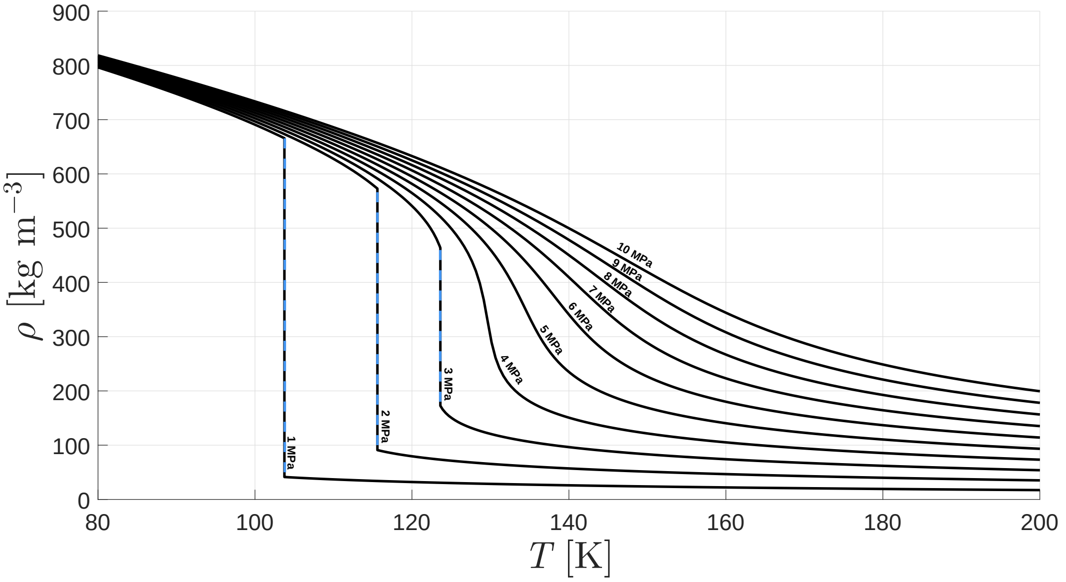

Figure 3.3: Plots of density for nitrogen from 1 MPa to 10 MPa, with data from the NIST database [137] (dashed lines represent liquid–vapor discontinuity).

3.7.1 Multi-parameter

The multi-parameter equation of state belongs to the group of the modified BWR equations, according to Span and Wagner [189] since the original BWR equation of state is not accurate enough for today's technical applications.

Multi-parameter equations of state can be created through polynomial and exponential expansions where the coefficients multiplied by each term are specific to each fluid. These coefficients must be fitted through the available experimental data for the conditions in which the EoS is valid. The 32-term modified BWR [186] EoS achieves a relative density error smaller than 0.5% above and below the critical point, while Span and Wagner [189] propose a 12-term EoS with available coefficients for a series of substances, nitrogen included, while Span et al. [190] provide a highly accurate 18-term EoS optimized directly for nitrogen. This type of EoS has the advantage of fitting a particular substance, provided enough coefficients are available. However, this comes at the expense of computational time [191]. A modified BWR Equation of State is used by Yang [96] due to its superior accuracy when compared with its cubic counterparts. These equations require many fitted coefficients, which are not readily available for every substance.

For this reason, an extended principle of corresponding states is used. It is assumed that the properties of a single-phase fluid can be evaluated via conformal mappings of temperature and density to those of a given reference fluid. The principle of corresponding states that all fluids, when compared at the same reduced conditions, that is, pressure and temperature, have approximately the same compressibility, therefore deviating from ideal gas behavior in the same degree

Work has been undertaken to improve the performance of the BWR equation of state, with greater accuracy achieved in the superheated regime for non-polar substances [192].

Another motive for developing functional forms for multi-parameter EoSs relates to the under-correlation of its coefficients: another reason for their under-performance. Span and Wagner [189] postulated a simplistic formulation, to the detriment of high accuracy in the critical region, pursuing numerical stability above all else. As a result, the EoS can be fitted for as many fluids as possible and be extrapolated to conditions beyond experiments.

Another option, where an EoS is applied in different fluid states, is a formulation based on the Helmholtz reduced energy. To reach the equilibrium state of closed thermodynamic systems, the minimization of the Gibbs free energy is pursued [193]. However, it was found that the minimization of another thermodynamic potential, the Helmholtz free energy, is an alternative, inclusively being computationally cheaper [194]. This thermodynamic potential is made by contributing two components: one describing the hypothetical ideal gas behavior and another accounting for real fluid departure from ideal gas behavior.

The lack of relevant experimental data for a range of fluids is the main reason for unoptimized equations of the state still being used today. However, a change in the paradigm has occurred in recent years, and researchers are now concerned with developing optimized equations of state for a representative group of fluids with the same characteristics. The objective is no longer to obtain an equation providing the best results for a single fluid but for an entire representative group [189]. In this sense, reference tables are increasingly being replaced by interactive programs.

Multiparameter EoSs have predictive capabilities and minor deviations to the experimental data when compared, for example, to their cubic counterparts. However, the computational burden they introduce makes them prohibitive to use in the present work. Nonetheless, there have been works that introduced the notion of a pre-compiled library to counteract this issue [195]. In this way, the computational cost of solving the EoS would be removed from the solver, which would limit itself to load each of the necessary properties from the pre-compiled table at run-time. However, while this provided a breakthrough allowing the use of a more accurate EoS for less computational cost, the approach is generally limited to mixtures of two different species due to constraints in memory allocation [196].

3.7.2 Cubic

The compressibility factor can be interpreted as a relation between the acting pressure and the pressure an ideal gas exerts.

The prediction of real gas behavior in the EoS can be traced back to van der Waals [197], now represented in equation (3.97). Concerning the real gas behavior, parameters a and b are introduced, representing the attractive potential and the molecular volume, respectively. If these two parameters are taken to be zero, equation (3.97) reduces to the ideal gas relation.

Over time, many equations were developed which accounted for the basic principles already expressed by van der Waals [197], namely liquid-vapor coexistence and critical point [198]. The remaining parameters of equation (3.97) represent the amount of substance, n, the molar volume, v and the universal gas constant $\mathcal{R}$.

$$\left(p+\frac{an^2}{v^2}\right)(v-nb)=n\mathcal{R}T \quad (3.97)$$

The term cubic, labeling these EoSs, arises from the fact that if expanded in terms of the molar volume v or the compressibility factor, a cubic expression is retrieved [191]. Advantageous as they may be, allowing for the representation of pressure curves without the need to calculate additional parameters in thermodynamic representations, uncertainties in the critical parameters could lead to poor calculations of derived thermodynamic properties of significant importance, such as heat capacity and enthalpy. Nevertheless, cubic EoS are broadly used in modeling supercritical fluid flows since they represent a compromise between accuracy, simplicity, and computational cost. No two greater examples can be found by looking no further than the SRK [185] and the PR [184] EoS, to be discussed further ahead.

In general form cubic equations of state can be written according to equation (3.98) [199].

$$p=\frac{RT}{v-b}-\frac{a\left(T\right)}{\left(v+\delta_1 b\right)\left(v+\delta_2 b\right)} \quad (3.98)$$

In equation (3.98), δ_1 and δ_2 are characteristic of each cubic Equation of State. The parameter b is assumed to be independent of temperature, while a is depends upon it, based on the critical temperature and a calibration function, according to equation (3.99).

$$a\left(T\right)=a\left(T_c\right)f\left(T\right) \quad (3.99)$$

Several studies deal with the evolution of modifications into cubic EoS such as Ghanbari et al. [200], where a comparison in terms of performance both in original formulations as well as modified ones is made for a variety of polar and non-polar fluids.

3.7.2.1 Soave-Redlich-Kwong

The SRK EoS [185] introduces, concerning its predecessor, the RK [201], the acentric factor, which is a measure of the non-spherical shape of the molecules. The SRK Equation of State is given by equation (3.100). It is obtained from the general formulation of cubic EoS represented in equation (3.98) by taking δ_1 to be zero and δ_2 to be 1. In addition to parameters being expressed in terms of the critical point (critical pressure and temperature), they are also expressed in terms of the acentric factor.

$$p = \frac{RT}{v-b} - \frac{a\left(T\right)}{v\left(v+b\right)} \quad (3.100)$$

The SRK differs from the RK EoS by replacing the term $a/T^{0.5}$ with more general dependence upon temperature. For reference, the RK equation of state is here reproduced in equation (3.101).

$$p = \frac{RT}{v-b} - \frac{a(T)/T^{0.5}}{v\left(v+b\right)} \quad (3.101)$$

The more general dependence of the SRK EoS on temperature can be stated in the form of equation (3.102).

$$a\left(T\right) = a(T_c).a\left(T_r, \omega\right) \quad (3.102)$$

In equation (3.102), a_c is the parameter at the critical point and $a\left(T_r, \omega\right)$ a non-dimensional parameter which corrects the value of $a\left(T\right)$ for temperatures other than the critical. The attractive potential at the critical point, the molecular volume parameter and the correction of temperature are given in equations (3.103) to (3.105).

$$a(T_c) = 0.42747 \frac{\mathcal{R}^2 T_c^2}{p_c} \quad (3.103)$$

$$b = 0.08664 \frac{\mathcal{R} T_c}{p_c} \quad (3.104)$$

$$a(T_r,\omega) = \left[1 + \left(0.48 + 1.57\omega + 0.17\omega^2\right)\left(1 - \sqrt{T_r}\right)\right]^2 \quad (3.105)$$

By writing in terms of the compressibility factor, Z (equation (3.106)), the cubic form of the equation is retrieved. However, first, the roots of the polynomial must be found for Z, from which density is then calculated.

$$\mathrm{Z}^3 - \mathrm{Z}^2 + \mathrm{Z}\left(A - B - B^2\right) - AB = 0 \quad (3.106)$$

Auxiliary parameter A and B are evaluated from equations (3.107) and (3.108), respectively.

$$A = \frac{a\left(T_r,\omega\right)p}{\mathcal{R}^2T^2} \quad (3.107)$$

$$B = \frac{bp}{RT} \quad (3.108)$$

Several modifications were proposed to the SRK EoS, improving its various aspects. Its wide range of validity and easy implementation leads to a modified version to be used by Zong et al. [79], developed from pure hydrocarbon vapor pressure data. The original work of Soave on the modification of the RK was based on an accurate correlation of hydrocarbon vapor pressures in terms of reduced temperature, pressure, and acentric factor, therefore resulting in an accurate prediction of phase equilibrium behavior. The modified SRK proposed by Graboski and Daubert [202] used for hydrocarbons and non-hydrocarbons [203] requires only knowledge of the three parameters of each component. Thus, it helps treat mixtures containing sub- and supercritical elements. An attempt is made by Fuller [204] to incorporate a more general temperature dependence for factors a and b. However, only compressed liquid water was tested.

3.7.2.2 Peng-Robinson

The PR EoS [184] is another example whose basis can be traced back to the work of van der Waals, this time by the modification of the pressure attraction term, providing good accuracy at supercritical conditions [205]. Its general formulation is given in equation (3.109). It is obtained from the general formulation of equation (3.98) by taking δ_1 to be $1 + \sqrt{2}$ and $\delta_2 = 1 - \sqrt{2}$.

$$p = \frac{RT}{v-b} - \frac{a\left(T\right)}{v\left(v+b\right)+b\left(v-b\right)} \quad (3.109)$$

The various coefficients arising from this formulation, namely the attractive potential, correlation function, and molecular volume, are presented in equations (3.110) to (3.113), while additional parameters A and B take the same form as in the SRK Equation of State.

$$a(T) = a(T_c).a\left(T_r, \omega\right) \quad (3.110)$$

$$a(T_c) = 0.45724\frac{R^2T_c^2}{p_c} \quad (3.111)$$

$$a\left(T_r, \omega\right) = \left[1 + \left(0.37464 + 1.54226\omega - 0.26992\omega^2\right)\left(1 - \sqrt{T_r}\right)\right]^2 \quad (3.112)$$

$$b = b_c = 0.07780\frac{RT_c}{p_c} \quad (3.113)$$

By rewriting as a function of the compressibility factor, the cubic formulation (equation (3.114)) is obtained.

$$Z^3 - \left(1-B\right)Z^2 + \left(A - 2B - 3B^2\right)Z - \left(AB - B^2 - B^3\right) = 0 \quad (3.114)$$

In the same way, as was described for the SRK, the PR EoS was also the subject of proposals for improvement over the years, with the introduction of empirical coefficients that would enhance one particular aspect of the EoS, often substance-dependent. For instance, an improved prediction method for saturated liquid densities, with an empirical correction term, is proposed by Mathias et al. [206], while Harvazinski et al. [207] describe efforts to increase the EoS predictive capabilities at transcritical conditions. Finally, an extensive review of proposed modifications on the PR EoS is given by Lopez-Echeverry et al. [208].

The choice of a particular EoS for the description of supercritical fluid behavior can impact further than the degree of prediction of a specific model. For example, numerical stability issues, resulting from the appearance of non-physical spurious oscillations, leading to oscillations in the thermodynamic property gradients, needs to be considered by either DNS, RANS, and LES-based solvers [9].

In general, cubic EoSs use is widespread and sustained mainly because they represent a compromise between accuracy, simplicity, and computational cost. The PR and SRK cubic EoS provide good predictions at high-pressure conditions, as is the case of supercritical fluid flows. However, fundamentally relevant to high-pressure studies, they differ because while the PR EoS contributes to a better representation of density up to two times the critical pressure, the SRK one provides a better representation of phase equilibrium.

Figure 3.4 depicts a comparison in the prediction of the density evolution of nitrogen at a pressure of $4\,\mathrm{MPa}$ for a temperature range of 100 to $300\,\mathrm{K}$. Ideal gas, PR [184] and SRK [185] Equations of State are compared with data obtained from the NIST database [137]. The ideal gas EoS is insufficient in modeling the high-pressure nitrogen represented. Between the two cubic EoSs represented in the figure, the PR [184] is used in the work here presented. The PR EoS leads to a closer representation of the thermodynamic properties in the critical point's vicinity, while the SRK corresponds to a closer representation of temperature at low temperatures.

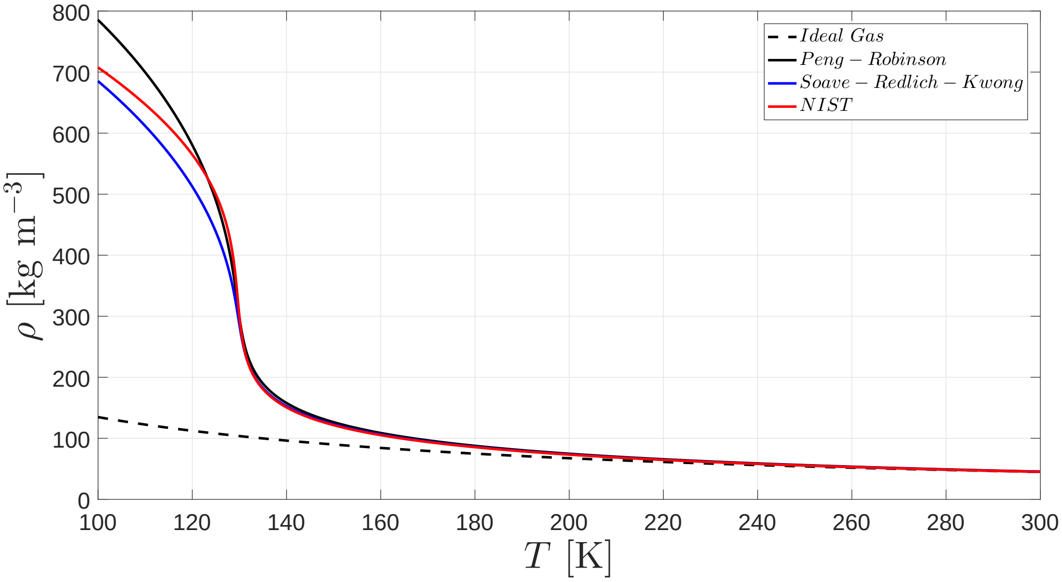

Figure 3.4: Comparison between ideal, SRK and PR EoS for nitrogen at $4\,\mathrm{MPa}$ and temperature ranging from 100 to $300\,\mathrm{K}$.

3.7.2.3 Volume Translation Methods

To increase the performance of the PR EoS, the volume translation method of Abudour et al. [209] is considered in the modeling of coaxial multi-species injection. The method is applicable to saturated and single-phase regions. It can include only fluid-specific parameters, generalized from properties such as the critical compressibility factor, the acentric factor, and the dipole moment. It involves a translation to improve prediction in density without affecting vapor-liquid equilibrium.

Generically the method is represented in equations (3.115) and (3.116), where v_{VTPR} and v_{PR} are the translated and untranslated molar volumes, with c the translation term, δ_c is the volume correction at the critical temperature and 0.35 a universal constant for all fluids.

$$v_{VTPR} = v_{PR} + c \quad (3.115)$$

$$v_{VTPR} = v_{PR} + c - \delta_c \frac{0.35}{0.35 + d} \quad (3.116)$$

The parameter c is evaluated according to equation (3.117), with c_1 a constant fluid-dependent parameter. For nitrogen it assumes the value of 0.01386.

$$c = \frac{\mathcal{R} T_c}{p_c} \left[c_1 - (0.004 + c_1) \exp(-2d) \right] \quad (3.117)$$

Parameter δ_c is obtained from equation (3.118), where Z_c^{EOS} has the universal value of 0.3074 for the PR EOS.

$$\delta_c = \frac{\mathcal{R} T_c}{p_c} \left(Z_c^{EOS} - Z_c^{exp} \right) \quad (3.118)$$

Lastly, the distance function d, obtained from the untranslated EoS to avoid iterative solutions, is defined in equation (3.119), dependent on the isothermal partial derivative of pressure concerning density, also from the untranslated EoS.

$$d = \frac{1}{\mathcal{R} T_c} \left(\frac{\partial p^{PR}}{\partial \rho} \right)_T \quad (3.119)$$

3.8 Thermodynamic Properties

Considering the PR EoS used, the definition of a thermal EoS in terms of any given thermodynamic potential, such as, for instance, internal energy or enthalpy, is a straightforward process. Departure functions are an exact description of the thermodynamic variable because they are state variables, depending only on initial and final states and not on the path between them [210], being the only constraint in terms of hypothesis or approximations, the choice of the EoS.

Internal energy in equation (3.120) and enthalpy in equation (3.121) are derived in accordance to Maxwell's relations and the fundamental laws of thermodynamics [211]. Internal energy and enthalpy are evaluated by adding to the ideal gas contribution (subscript zero) departure functions that account for real gas effects (the second term on the right hand side of equations (3.120) and (3.121)). Figure 3.5 depicts the variation of nitrogen's enthalpy in the temperature range of interest [137].

$$e\left(p,T\right) = e_0\left(T\right) + \int_{\rho_0}^{\rho} \left[\frac{p}{\rho^2} + \frac{T}{\rho^2}\left(\frac{\partial p}{\partial T}\right)_{\rho}\right]_T d\rho \quad (3.120)$$

$$h(p,T) = h_0(T) + \int_{p_0}^{p} \left[\frac{1}{\rho} + \frac{T}{\rho^2}\left(\frac{\partial \rho}{\partial T}\right)_{p}\right]_T dp \quad (3.121)$$

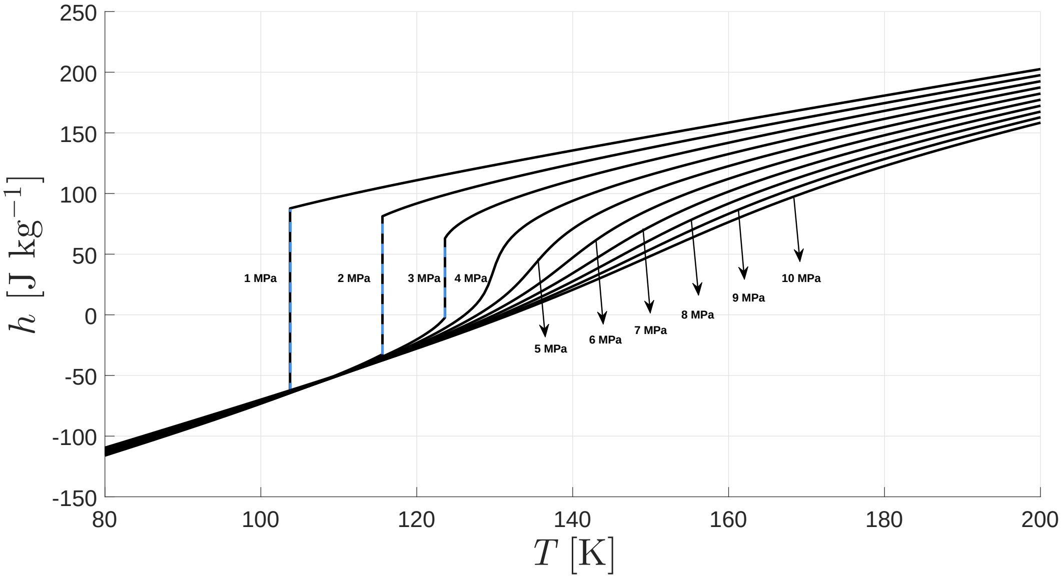

Figure 3.5: Plots of enthalpy for nitrogen from 1 MPa to 10 MPa, with data from the NIST database [137] (dashed lines represent liquid–vapor discontinuity).

Ideal gas enthalpy ($h_0(T)$) is evaluated from the 7 coefficient NASA polynomials [212], replicated in equation (3.122). The coefficients a_1 to a_6 are given in Table 3.8, for nitrogen and hydrogen.

$$\frac{h_0\left(T\right)}{\mathcal{R}T} = a_1 + a_2\frac{T}{2} + a_3\frac{T^2}{3} + a_4\frac{T^3}{4} + a_5\frac{T^4}{5} + a_6\frac{1}{T} \quad (3.122)$$

Table 3.8: Coefficients of the polynomial for the determination of ideal gas properties [212].

Coefficient	Nitrogen	Hydrogen
a_1	$0.241\,594\,29 \times 10^{1}$	$3.337\,279\,20$
a_2	$0.174\,890\,65 \times 10^{-3}$	$-4.940\,247\,31 \times 10^{-5}$
a_3	$-0.119\,023\,69 \times 10^{-6}$	$4.994\,567\,78 \times 10^{-7}$
a_4	$0.302\,262\,45 \times 10^{-10}$	$-1.795\,663\,94 \times 10^{-10}$
a_5	$-0.203\,609\,82 \times 10^{-14}$	$2.002\,553\,76 \times 10^{-14}$
a_6	$0.561\,337\,73 \times 10^{5}$	$-9.501\,589\,22 \times 10^{2}$

Explicitly formulations for the internal energy and the enthalpy are retrieved for the PR EoS [211], according to equations (3.123) and (3.124), respectively. Finally, the partial derivative $\frac{\partial a}{\partial T}$ is give following equation (3.125).

$$\frac{e\left(p,T\right) - e_0\left(T\right)}{\mathcal{R}T} = \frac{a(T)a\left(T_r,\omega\right) - T\frac{\partial a}{\partial T}}{\mathcal{R}T\sqrt{8b^2}} \ln\left(\frac{2v + 2b - \sqrt{8b^2}}{2v + 2b + \sqrt{8b^2}}\right) \quad (3.123)$$

$$\frac{h\left(p,T\right) - h_0\left(T\right)}{\mathcal{R}} = \frac{a(T)a\left(T_r,\omega\right) + T\frac{\partial a}{\partial T}}{\mathcal{R}T\sqrt{8b^2}} \ln\left(\frac{2v + 2b - \sqrt{8b^2}}{2v + 2b + \sqrt{8b^2}}\right) - 1 + Z \quad (3.124)$$

$$\frac{\partial a}{\partial T} = -\frac{\left(0.37464 + 1.54226\omega - 0.26992\omega^2\right)a(T_c)}{T_c T_r^{1/2}} \quad (3.125)$$

Several partial derivatives of interest such as $\left(\frac{\partial p}{\partial V}\right)_T$, $\left(\frac{\partial p}{\partial T}\right)_T$ and $\left(\frac{\partial V}{\partial T}\right)_p$ can also be defined:

$$\left(\frac{\partial p}{\partial v}\right)_T = -\frac{\mathcal{R}T}{\left(v - b\right)^2} + \frac{2a\left(v + b\right)}{\left[v\left(v + b\right) + b\left(v - b\right)\right]^2} \quad (3.126)$$

$$\left(\frac{\partial p}{\partial T}\right)_v = \frac{\mathcal{R}}{v-b} - \frac{\frac{\partial a}{\partial T}}{v\left(v+b\right)+b\left(v-b\right)} \quad (3.127)$$

$$\left(\frac{\partial v}{\partial T}\right)_p = \frac{\mathcal{R}}{p}\left(T\left(\frac{\partial Z}{\partial T}\right)_p + Z\right) \quad (3.128)$$

Where:

$$\left(\frac{\partial Z}{\partial T}\right)_p = \frac{\left(\frac{\partial A}{\partial T}\right)_p\left(B-Z\right)+\left(\frac{\partial B}{\partial T}\right)_p\left(6BZ+2Z-3B^2-2B+A-Z^2\right)}{3Z^2+2\left(B-1\right)Z+\left(A-2B-3B^2\right)} \quad (3.129)$$

$$\left(\frac{\partial A}{\partial T}\right)_p = \frac{p}{\left(\mathcal{R}T\right)^2}\left(\frac{\partial a}{\partial T}-\frac{2a}{T}\right) \quad (3.130)$$

$$\left(\frac{\partial B}{\partial T}\right)_p = -\frac{bp}{\mathcal{R}T^2} \quad (3.131)$$

Lastly it remains to define the isobaric and isochoric specific heat which are going to be needed in the determination of thermal conductivity. The isochoric specific heat is defined in equation (3.132).

$$c_v\left(\rho,T\right) = c_{v0} - \int_{\rho_0}^{\rho}\left[\frac{T}{\rho^2}\left(\frac{\partial p}{\partial T}\right)_\rho\right]_T d\rho \quad (3.132)$$

The ideal gas component (c_{v0}) is related to the ideal gas isobaric specific heat through Meyer's relation: $c_v = c_{p0} - \mathcal{R}$. c_{p0} is evaluated from equation (3.133) from the NASA 7 coefficient polynomials [212].

$$\frac{c_{p,0}\left(T\right)}{\mathcal{R}} = a_1 + a_2T + a_3T^2 + a_4T^3 + a_5T^4 \quad (3.133)$$

Real gas isochoric specific heat is retrieved by differentiating the internal energy with respect to temperature at constant volume:

$$c_v^R = \left(\frac{\partial e}{\partial T}\right)_v = \frac{T\frac{\partial^2 a}{\partial T^2}}{b\sqrt{8}} \ln\left[\frac{Z + B\left(1+\sqrt{2}\right)}{Z + B\left(1-\sqrt{2}\right)}\right] \quad (3.134)$$

Where:

$$\frac{\partial^2 a}{\partial T^2} = \frac{a(T_c)k\left(1+k\right)\sqrt{T_r}}{2TT_c} \quad (3.135)$$

$$k = 0.37464 + 1.54226\omega - 0.26992\omega^2 \quad (3.136)$$

Lastly the isobaric specific heat departure function (c_p^R) is evaluated from equation (3.137) based on the calculated p–v–T partial derivatives.

$$c_p^R = c_v^R + T\left(\frac{\partial p}{\partial T}\right)_v \left(\frac{\partial v}{\partial T}\right)_p - \mathcal{R} \quad (3.137)$$

3.9 Transport Properties

Transport properties such as dynamic viscosity, thermal conductivity, and diffusion need to be evaluated, considering the deviation from the ideal gas behavior described before. Viscosity represents the transport of momentum across a velocity gradient [213], thermal conductivity the transport of energy across a temperature gradient, and diffusion the transport of the species in a mixture across the gradient of concentration. They are to be expressed as a sum of their ideal gas behavior plus a departure function accounting for real gas behavior. Two different methods for each property are considered. Initially, the method proposed by Lemmon and Jacobsen [214] was employed in the modeling of single nitrogen injection. However, when moving to the modeling of coaxial combinations of nitrogen and hydrogen, the model of Chung et al. [215] is adopted due to its validity for hydrogen. Finally, several methods for the calculation of transport properties and equations of state are reviewed and compared by Congiunti et al. [191].

Transport properties determine the mass and energy transport that dictate the interface conditions and consequently the vaporization rate and supercritical regime [92]. The classical gas kinetic theory fails to predict correctly transport properties for high pressures. However, it is always possible to estimate a low-pressure value and correct it by considering high-pressure effects. Each of these methods is comprised of two or three contributions [31, 96], depending on the near-critical behavior of the property. A dilute gas contribution represents ideal gas behavior, therefore independent of density. A departure function considers the deviation from ideal gas for properties that do not exhibit sudden variations near the critical point. Finally, a critical enhancement component intends to represent the singular behavior in proximity to the critical point.

The use of real gas relationships for transport and thermodynamic properties allows the physical model to capture the weak compressibility effects when using an incompressible variable-density approach. Thermodynamic properties such as enthalpy are evaluated by their ideal gas value and departure function to account for real gas effects.

3.9.1 Lemmon and Jacobsen's Model for Dynamic Viscosity

The dynamic viscosity of equation (3.138) results from a dilute gas contribution and a residual component, representing a departure from an ideal gas. The dilute gas contribution, μ^0 is given by equation 3.139, while the residual component of viscosity, μ^r is represented in equation (3.141). Ω represents the collision integral (equation (3.140)), $\mathcal{M}$ is the molar mass, and σ the Lennard-Jones size parameter, while ρ_r and T_r represent reduced density and temperature, respectively. The remaining parameters are tabulated constants reproduced in Table 3.9, for the collision integral constants and Table 3.10 for the remaining constants.

$$\mu = \mu^0(T) + \mu^r(\rho_r, T_r) \quad (3.138)$$

$$\mu^0(T) = \frac{0.0266958\sqrt{\mathcal{M}T}}{\sigma^2\Omega(T^*)} \quad (3.139)$$

$$\Omega(T^*) = \exp\left(\sum_{i=0}^{4} b_i \left[\ln(T^*)\right]^i\right) \quad (3.140)$$

$$\mu^r(\rho_r, T_r) = \sum_{i=1}^{n} N_i \rho_r^{t_i} T_r^{d_i} \exp\left(-\gamma_i T_r^{l_i}\right) \quad (3.141)$$

Table 3.9: Coefficients for the collision integral equation [214].

i	b_i
0	0.431
1	-0.4623
2	0.08406
3	0.005341
4	-0.00331

Table 3.10: Coefficients and exponents of the residual fluid viscosity equations [214].

i	N_i	t_i	d_i	l_i
1	10.72	0.1	2	0
2	0.03989	0.25	10	1
3	0.001208	3.2	12	1
4	-7.402	0.9	2	2
5	4.620	0.3	1	3

3.9.2 Chung's Model for Dynamic Viscosity

Chung et al. [215] model for the determination of dynamic viscosity is here described. Close attention should be paid to the units in which the different variables are given.

Dynamic viscosity, μ, given in μP is evaluated according to equation (3.142), as a contribution of low-pressure viscosity, μ_κ, and a correction term for high-pressure, μ_p. The low-pressure component, μ_k, on equation (3.143) is dependent upon the dilute gas viscosity, μ_0, parameters y and G_2, and A_6, a linear function of the acentric factor, ω, reduced dipole moment, η_r and association factor, κ, a correction factor for hydrogen-bonding effects, that is assumed to be zero.

$$\mu = \mu_k + \mu_p \quad (3.142)$$

$$\mu_k = \mu_0 \left(\frac{1}{G_2} + A_6 y \right) \quad (3.143)$$

The dilute gas viscosity is computed from equation (3.144).

$$\mu^0 = 26.69 \times 10^{-6} F_c \frac{\sqrt{\mathcal{M} T}}{\sigma^2 \Omega^*} \quad (3.144)$$

Additional parameters F_c, to account for molecular and polar effects and y are computed from:

$$F_c = 1 - 0.2756\omega + 0.059035\eta_r^4 + k \quad (3.145)$$

$$y = \frac{\rho v_c}{6} \quad (3.146)$$

With the dimensionless dipole moment, η^r:

$$\eta_r = \frac{131.3\mu}{(v_c T_c)^{1/2}} \quad (3.147)$$

The collision integral is given according to equation 3.148, whose constants are given in Table 3.11

$$\Omega^* = \frac{A}{T^{*B}} + \frac{C}{\exp(DT^*)} + \frac{E}{\exp(FT^*)} + GT^{*B}\sin(ST^{*W} - H) \quad (3.148)$$

Table 3.11: Constants used for generalized viscosity correlation [215].

Constant	Value
A	1.16145
B	0.14874
C	0.52487
D	0.77320
E	2.16178
F	2.43787
G	-6.435×10^{-4}
H	7.27371
S	18.0323
W	-0.76830

A_i coefficients are evaluated from equation (3.149), while constants a_0 to a_3 are given in Table 3.12, reproduced from Chung et al. [215]. For non-polar substances only the first two terms of equation (3.149) are considered.

$$A_i = a_0(i) + a_1(i)\omega + a_2(i)\mu_r^4 + a_3(i)k \quad i = 1, 10 \quad (3.149)$$

Table 3.12: Constants used for the generalized viscosity correlation [215].

$a_0(i)$	$a_1(i)$	$a_2(i)$	$a_3(i)$
6.32402	50.41190	-51.6801	1189.02
0.0012102	-0.0011536	-0.0062571	0.037283
5.28346	254.209	-168.481	3898.27
6.62263	38.0957	-8.46414	31.41780
19.7454	7.63034	-14.3544	31.5267
-1.89992	-12.5367	4.98529	-18.1507
24.27450	3.44945	-11.29130	69.3466
0.79716	1.11764	0.012348	-4.11661
-0.23816	0.067695	-0.8163	4.02528
0.068629	0.34793	0.59256	-0.72663

The high-pressure contribution to the evaluation of dynamic viscosity is given in equation (3.150). $\mathcal{M}$ is the molar volume, T_c the critical temperature, v_c the critical volume, coefficients A_7 to A_{10} linear functions of the acentric factor, reduced dipole moment and association factor and T^* the dimensionless temperature. Additional parameters G_1, G_2, and the reference temperature, T^*, are defined in equations (3.151), (3.152) and (3.153), respectively, where κ_B is the Boltzmann's constant and ε the potential energy parameter.

$$\mu_p = \left[36.3446\text{E-}6 \frac{(\mathcal{M}T_c)^{0.5}}{v_c^{2/3}} \right] A_7 y^2 G_2 \exp(A_8 + A_9/T^* + A_{10}/T^{2*}) \quad (3.150)$$

$$G_1 = \frac{1 - 0.5y}{(1-y)^3} \quad (3.151)$$

$$G_2 = \left[A_1 \left(1 - \exp\left[-A_4 y\right]\right)/y + A_2 G_1 \exp\left(A_5 y\right) + A_3 G_1\right] / \left(A_1 A_4 + A_2 + A_3\right) \quad (3.152)$$

$$T^* = \frac{k_B T}{\varepsilon} \quad (3.153)$$

Figure 3.6 compares the models of Chung et al. [215] and Lemmon and Jacobsen [214] in conjunction with the PR EoS [184], with experimental data from the NIST database [137] for nitrogen taken at a pressure of $4\,\mathrm{MPa}$. It is observed a good agreement with the experimental data at temperatures above nitrogen's critical temperature ($126.2\,\mathrm{K}$) and a deviation in the transcritical regime, as was expected due to the PR EoS.

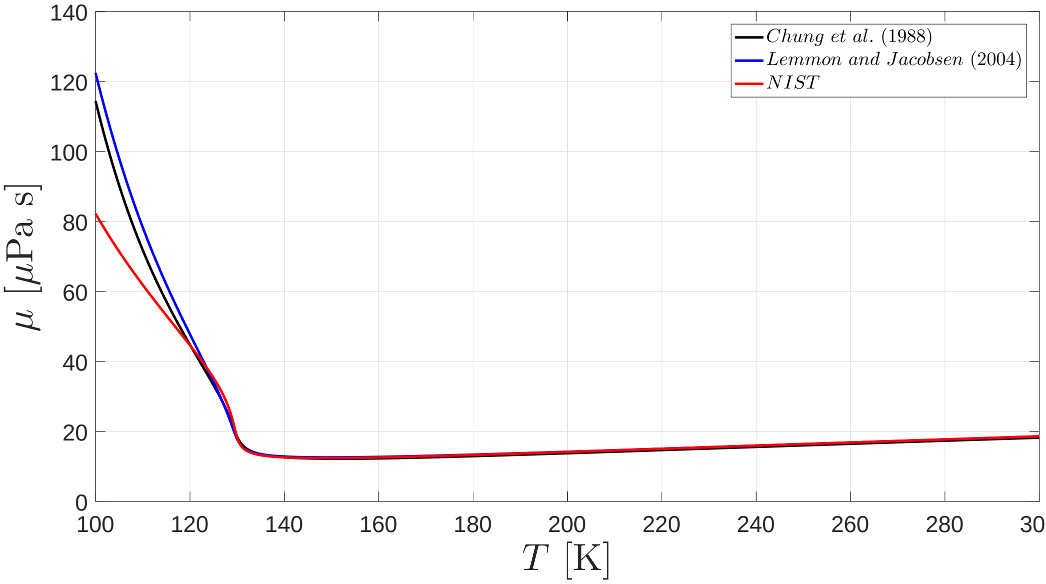

Figure 3.6: Comparison of dynamic viscosity for nitrogen at $4\,\mathrm{MPa}$, with the PR EoS.

The variation of viscosity at pressure levels from 1 to $10\,\mathrm{MPa}$ is shown in Figure 3.7. It can be seen that the pressure level of $4\,\mathrm{MPa}$ (the first supercritical value) still holds some influence of the critical divergence taking place at the critical point, decreasing with increasing temperature as pseudo-boiling effects become less preponderant.

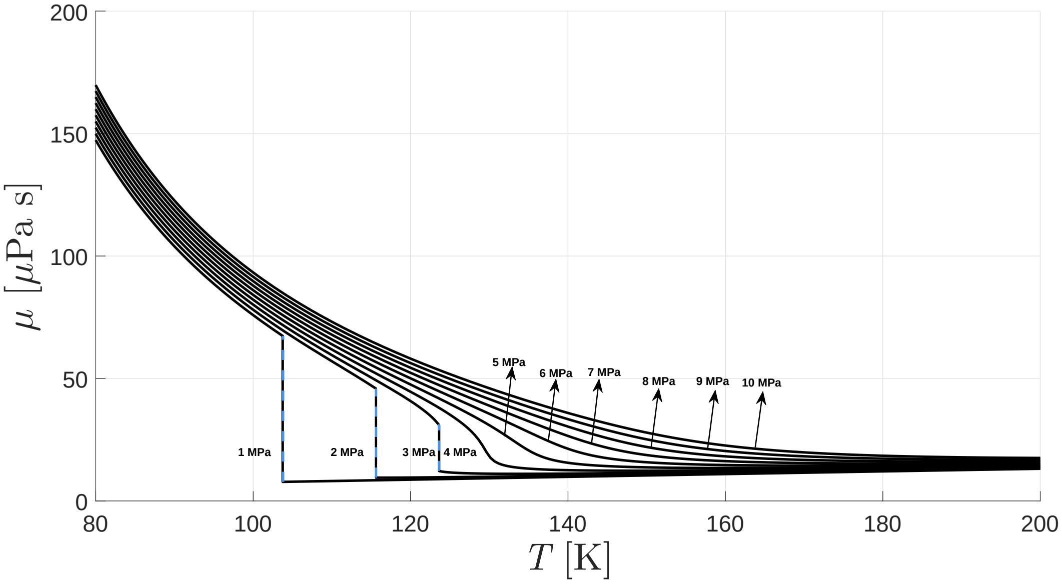

Figure 3.7: Plots of viscosity for nitrogen from $1\,\mathrm{MPa}$ to $10\,\mathrm{MPa}$, with data from the NIST database [137] (dashed lines represent liquid–vapor discontinuity).

3.9.3 Lemmon and Jacobsen's Model for Thermal Conductivity

The thermal conductivity of equation (3.154) results from a dilute gas contribution representing ideal gas (λ^0), a residual contribution (λ^r), and a third component representing the singular behavior of thermal conductivity in the vicinity of the critical point, designated "critical enhancement", λ^c. While the first two components are defined similarly to the dynamic viscosity [214], the critical enhancement is introduced to deal with the critical point singularity [216].

$$\lambda = \lambda^0(T) + \lambda^r(\rho_r, T_r) + \lambda^c(\rho_r, T_r) \quad (3.154)$$

In equations (3.155) and (3.156), the additional parameters represent constants [214], reproduced in Table 3.13, while in equation (3.157), $\tilde{\Omega}$ is a consequence of the specific heat at constant pressure and volume, where c_v, c_p, $\left(\frac{\partial\rho}{\partial p}\right)_T$ are obtained from the EoS at specified density and temperature. For the PR EoS, these thermodynamic relations are specified in Section 3.8, while the critical enhancement constants are defined in Table 3.14.

$$\lambda^0(T) = N_1 \left[\frac{\mu^0(T)}{1\mu\text{Pa}\cdot\text{s}}\right] + N_2\rho_r^{t_2} + N_3\rho_r^{t_3} \quad (3.155)$$

$$\lambda^r(\rho_r, T_r) = \sum_{i=1}^{n} N_i \rho_r^{t_i} T_r^{d_i} \exp\left(-\gamma_i T_r^{l_i}\right) \quad (3.156)$$

$$\lambda^c = \rho c_p \frac{\kappa_B R_0 T}{6\pi\xi\mu(T,\rho)}\left(\tilde{\Omega} - \tilde{\Omega}_0\right) \quad (3.157)$$

Table 3.13: Coefficients and exponents of the residual fluid thermal conductivity equations [214].

i	N_i	t_i	d_i	l_i
1	1.511	-	-	-
2	2.117	-1.0	-	-
3	-3.332	-0.7	-	-
4	8.862	0.0	1	0
5	31.11	0.03	2	0
6	-73.13	0.2	3	1
7	20.03	0.8	4	2
8	-0.7096	0.6	8	2
9	0.2672	1.9	10	2

$$\tilde{\Omega} = \frac{2}{\pi}\left[\left(\frac{c_p - c_v}{c_p}\right)\tan^{-1}(\xi/q_D) + \frac{c_v}{c_p}(\xi/q_D)\right] \quad (3.158)$$

$$\tilde{\Omega}_0 = \frac{2}{\pi}\left[1 - \exp\left(-\frac{1}{(\xi/q_D)^{-1} + \frac{1}{3}(\xi/q_D)^2(\rho_c/\rho)^2}\right)\right] \quad (3.159)$$

$$\xi = \xi_0\left[\frac{\tilde{x}(T,\rho) - \tilde{x}(T_{ref},\rho)\frac{T_{ref}}{T}}{\Gamma}\right]^{\nu/\gamma} \quad (3.160)$$

$$\tilde{x}(T,\rho) = \frac{p_c\rho}{\rho_c^2}\left(\frac{\partial\rho}{\partial p}\right)_T \quad (3.161)$$

$$T_{ref} = 2T_c \quad (3.162)$$

$$if\ \xi \leq\ 0\ then\ \lambda_c = 0 \quad (3.163)$$

Table 3.14: Critical enhancement constants [214].

Variable	Value
ξ_0	0.17
q_D	0.40
Γ	0.055
ν	0.63
γ	1.2415
R_0	1.01
κ_B	$1.380\,658 \times 10^{-23}$

3.9.4 Chung's for Thermal Conductivity

The method of Chung et al. [215] for the evaluation of the thermal conductivity is described as follows. Similar to the description of dynamic viscosity, thermal conductivity (λ) is based on the contributions from a low-pressure component, λ_k added a correction accounting for high-pressure effects, λ_p. The dilute gas thermal conductivity is evaluated from equation (3.165)

$$\lambda = \lambda_k + \lambda_p \quad (3.164)$$

The auxiliary parameters are evaluated according to equations (3.165) through (3.173), while the coefficients of polynomials B_i are given in Table 3.15.

$$\lambda_0 = \frac{7.452\mu_0\psi}{\mathcal{M}} \quad (3.165)$$

$$\psi = 1 + \alpha\left[\frac{0.215 + 0.28288\alpha - 1.061\beta + 0.26665Z}{0.6366 + \beta Z + 1.061\alpha\beta}\right] \quad (3.166)$$

$$\alpha = \frac{c_v}{\mathcal{R}} - \frac{3}{2} \quad (3.167)$$

$$\beta = 0.7862 - 0.7109w + 1.3168w^2 \quad (3.168)$$

$$Z = 2 + 10.5T_r^2 \quad (3.169)$$

$$\lambda_k = \lambda_0\left(\frac{1}{H_2} + B_6 y\right) \quad (3.170)$$

$$\lambda_p = \left[3.0396\text{E-4}\left(\frac{T_c}{\mathcal{M}}\right)^{0.5}\frac{1}{v_c^{2/3}}\right]B_7 y^2 H_2 T_r^{1/2} \quad (3.171)$$

$$H_2 = \left[B_1\left(1 - \exp(-B_4 y)\right)/y + B_2 G_1 \exp(B_5 y) + B_3 G_1\right]/(B_1 B_4 + B_2 + B_3) \quad (3.172)$$

$$B_i = b_0(i) + b_1(i) + b_2(i)\mu_r^4 + b_3(i)k \quad (3.173)$$

Table 3.15: Constants used for generalized thermal conductivity correlation [215].

$b_0(i)$	$b_1(i)$	$b_2(i)$	$b_3(i)$
2.41657	0.74824	-0.91858	121.721
-0.50924	-1.50936	-49.9912	69.9834
6.61069	5.62073	64.7599	27.0389
14.5425	-8.91387	-5.63794	74.3435
0.79274	0.82019	-0.69369	6.31734
-5.8634	12.8005	9.58926	-65.5292
81.171	114.158	-60.841	466.775

Figure 3.8 depicts a comparison between the models of Chung et al. [215] and Lemmon and Jacobsen [214] for thermal conductivity, taking into account the PR EoS [184], and experimental data from the NIST [137] for nitrogen taken at a pressure of $4\,\mathrm{MPa}$. Contrary to what was observed for dynamic viscosity in Figure 3.6, there are visible differences in the predictions of both methods due to the inclusion of critical enhancement in the model from Lemmon and Jacobsen [214].

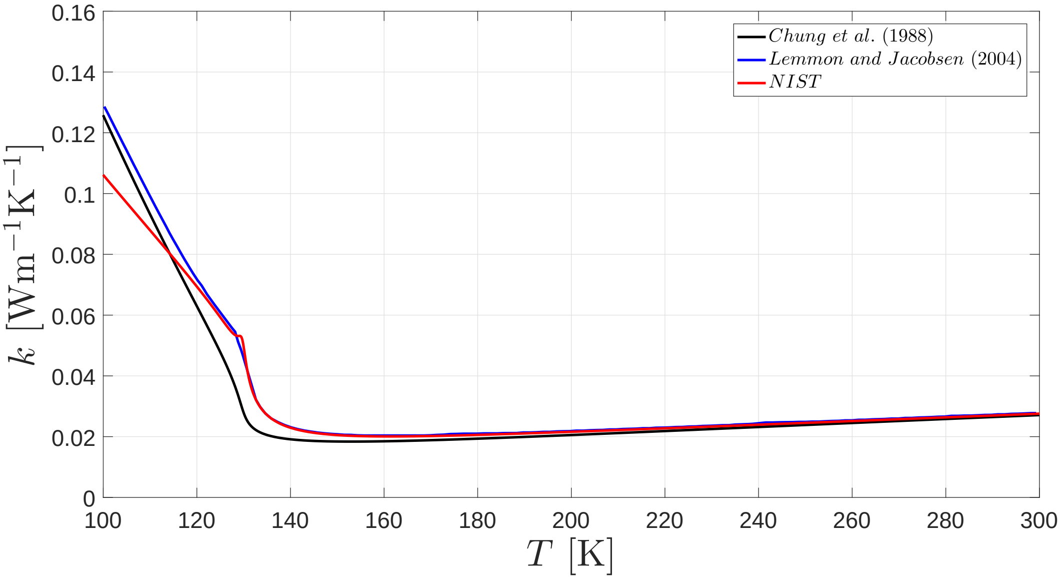

Figure 3.8: Comparison of thermal conductivity for nitrogen at $4\,\mathrm{MPa}$, with the PR EoS.

Figure 3.9 depicts the evolution of thermal conductivity for the pressure levels considered. It can be seen that the effect of the critical point is much more pronounced than for the viscosity, as indicated by the $4\,\mathrm{MPa}$ line. The computational model could benefit from including a critical enhancement component to predict the thermal conductivity.

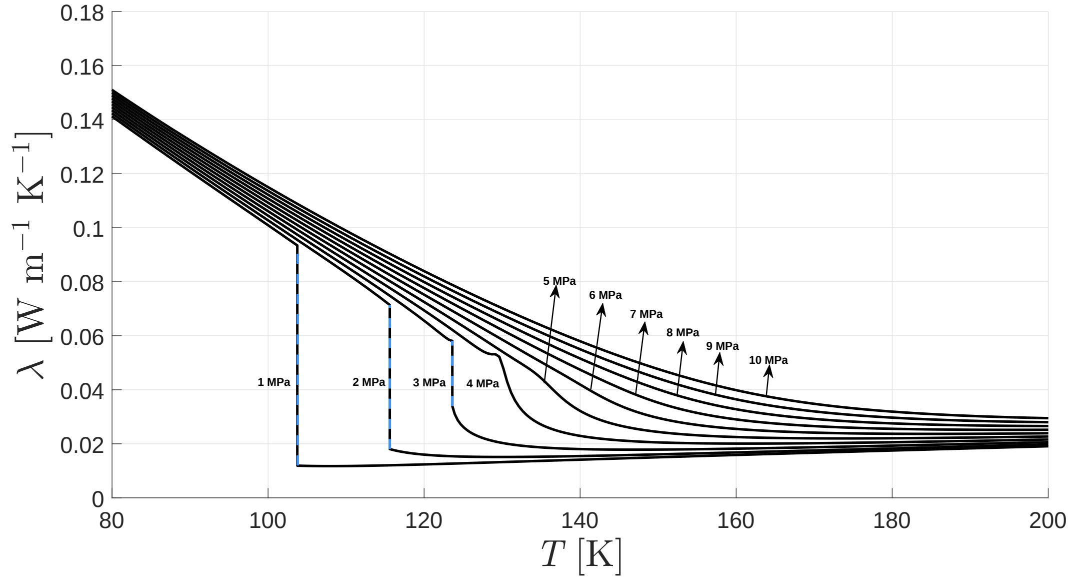

Figure 3.9: Plots of thermal conductivity for nitrogen from $1\,\mathrm{MPa}$ to $10\,\mathrm{MPa}$, with data from the NIST database [137] (dashed lines represent liquid–vapor discontinuity).

3.9.5 Mixture rules

The mixture properties are evaluated following Chung et al. [215], according to equations (3.174) to (3.182), where subscript mix means mixture.

$$\sigma_{mix}^3 = \sum_i^n \sum_j^n \sigma_{ij}^3 \quad (3.174)$$

$$\frac{\varepsilon_{mix}}{k} = \left[\sum_i^n \sum_j^n X_i X_j \left(\frac{\varepsilon_{ij}}{k}\right) \sigma_{ij}^3\right] / \sigma_{mix}^3 \quad (3.175)$$

$$v_{c,mix} = \left(\frac{\sigma_{mix}}{0.809}\right)^3 \quad (3.176)$$

$$T_{c,mix} = 1.2593 \varepsilon_m / k \quad (3.177)$$

$$w_{mix} = \left[\sum_{i}^{n} \sum_{j}^{n} X_i X_j w_{ij} \sigma_{ij}^3 \right] / \sigma_{mix}^3 \quad (3.178)$$

$$M_{mix} = \left[\left(\sum_{i}^{n} \sum_{j}^{n} X_i X_j \frac{\varepsilon_{ij}}{k} \sigma_{ij}^2 \mathcal{M}_{ij}^{1/2} \right) / \left(\frac{\varepsilon_{mix}}{k} \sigma_{mix}^2 \right) \right]^2 \quad (3.179)$$

$$\mu_{mix}^4 = \left[\sum_{i}^{n} \sum_{j}^{n} X_i X_j \mu_i^2 \mu_j^2 / \left(\frac{\varepsilon_{ij}}{k} \sigma_{ij}^3 \right) \right] \sigma_{mix}^3 \frac{\varepsilon_{mix}}{k} \quad (3.180)$$

$$k_{mix} = \sum_{i}^{n} \sum_{j}^{n} X_i X_j k_{ij} \quad (3.181)$$

$$\mu_{r,mix} = \frac{131.3 \mu_{mix}}{\left(v_{c,mix} T_{c,mix} \right)^{1/2}} \quad (3.182)$$

The binary interaction parameters (ξ_{ij} and ζ_{ij}) are evaluated as described below [215]. ξ_{ij} and ζ_{ij} are set to unity for most systems, except in mixtures where polar substances and hydrogen-bonding effects are included, or even in mixtures where its components present large differences in their molecular structure.

$$\sigma_{ij} = \xi_{ij} \left(\sigma_i \sigma_j \right)^{1/2} \quad (3.183)$$

$$\varepsilon_{ij} = \zeta_{ij} \left[\left(\varepsilon_i / k \right) \left(\varepsilon_j / k \right) \right]^{1/2} \quad (3.184)$$

$$w_{ij} = \frac{1}{2} \left(w_i + w_j \right) \quad (3.185)$$

$$\mathcal{M}_{ij} = \frac{2M_iM_j}{M_i + M_j} \quad (3.186)$$

$$k_{ij} = (k_ik_j)^{1/2} \quad (3.187)$$

3.10 Summary

This chapter introduced the governing equations that constitute the system of partial differential equations to be solved. The incompressible but variable density hypothesis is reviewed. An appropriate description of thermodynamic and transport properties evaluation procedures based on departure function formalism was evaluated, given the nature of the flows under consideration. The consequences of the physical models will be evaluated in Chapter 4.

Chapter 4

Numerical Considerations

In order for a numerical solution to be retrieved, the governing equations presented in Chapter 3 are discretized algebraically. This is achieved through a finite volume/ finite difference method. With these methods, the solution of the system of partial differential equations (PDE) is only found for a set of discrete points in the domain. Conservation at the discrete level is automatically ensured in the finite volume method (FVM) due to using the conservation equations directly in the integral formulation. Finite differences are used at the faces of the control volumes. Discretization, consisting of the transformation of the system of PDE into a set of linear equations, is the subject of the following few sections.

4.1 Discretization of the Physical Domain

The governing equations described in Chapter 3 are going to be discretized into a finite domain to obtain a system of linear equations to be solved numerically. The FVM describes the integration of the PDEs system into each control volume as defined by the grid. Each control volume is associated with a point in the mesh. FVM has the advantage of automatically ensuring conservative discretization, which means that for two opposite cell faces, the difference between both quantities is not dependent on the cell in which the face is considered [138].

A staggered grid configuration ensures that the well-known odd-even decoupling of pressure and velocity does not happen, i.e., that pressure and velocity do not affect each other. Velocity and pressure values are stored in different positions for which the control volumes are no longer equal. Ultimately, the pressure values are calculated directly for the cell face, and no interpolation is needed. This eliminates the decoupling of the pressure and velocity fields and any possible oscillations.

The systematic discretization of the domain and the dependent variables makes it possible to replace the governing equations with simple algebraic equations. In this way, numerical schemes define the way dependent variables are represented at the face of each control volume as the function of its neighbors, playing a preponderant role in the stability of the numerical solution. Except for velocity components, all variables are located in the cell centers. The location of velocity components midway through each point allows for the direct determination of velocity values from pressure gradients and mass fluxes through each control volume face, preventing the decoupling between pressure and velocity. As a result, the

FVM is based on the equilibrium between inflows and outflows at the four faces of the control volume.

On the discrete level, a partial derivative of the general conserved property ϕ can be evaluated according to equation (4.1).

$$\frac{\partial \phi}{\partial x} = \lim_{\Delta x \to \infty} \frac{\phi\left(x + \Delta x\right) - \phi\left(x\right)}{\Delta x} \quad (4.1)$$

Expanding the derivative in a Taylor expansion, we obtain equation (4.2), where HOT represents the truncated higher-order terms.

$$\frac{\phi\left(x + \Delta x\right) - \phi\left(x\right)}{\Delta x} = \frac{\partial \phi}{\partial x} + \Delta x \frac{\partial \phi}{\partial x} + \frac{\Delta x^2}{2!}\frac{\partial^2 \phi}{\partial x^2} + \frac{\Delta x^3}{3!}\frac{\partial^3 \phi}{\partial x^3} + \text{HOT} = \frac{\partial \phi}{\partial x} + O\left(\Delta x\right) \quad (4.2)$$

Endless approximations can be made to the partial derivative of equation (4.2). In Figure 4.1 the numerical molecule is depicted, which can help us to develop several of these approximations.

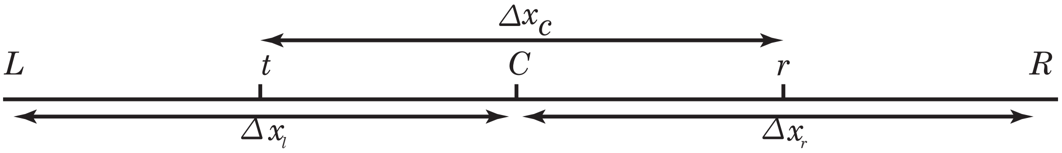

Figure 4.1: Representation of the numerical molecule.

For example, equations (4.3), (4.4) and (4.5), represent first-order forward, backward and second-order central approximations, respectively, considering $\Delta x \neq 0$. In these equations, $O\left(\Delta x^n\right)$ represents the truncation error, which goes to zero with the power of Δx, while R stands for right, L for left and C for center. For the first-order forward (equation (4.3)) and backwards (equation (4.4)) approximations, the truncation error goes to zero with Δx, making them first-order approximations, while in equation (4.5) the truncation error goes to zero with Δx^2, leading to a second-order approximation as the name implies.

$$\frac{\partial \phi_c}{\partial x} = \frac{\phi_R - \phi_C}{\Delta x_r} - \frac{\Delta x}{2!}\frac{\partial^2 \phi_C}{\partial x^2} - \frac{\Delta x^2}{3!}\frac{\partial^3 \phi_C}{\partial x^3} = \frac{\phi_R - \phi_C}{\Delta x_r} + O(\Delta x) \quad (4.3)$$

$$\frac{\partial \phi_C}{\partial x} = \frac{\phi_C - \phi_L}{\Delta x_l} + \frac{\Delta x}{2!}\frac{\partial^2 \phi_C}{\partial x^2} - \frac{\Delta x^2}{3!}\frac{\partial^3 \phi}{\partial x^3} = \frac{\phi_C - \phi_L}{\Delta x_l} + O\left(\Delta x\right) \quad (4.4)$$

$$\frac{\partial \phi_C}{\partial x} = \frac{\phi_R - \phi_L}{\Delta x_l + \Delta x_r} - \frac{\Delta x^2}{3!}\frac{\partial^3 \phi}{\partial x^3} = \frac{\phi_R - \phi_L}{\Delta x_l + \Delta x_r} + O\left(\Delta x^2\right) \quad (4.5)$$

The choice of an appropriate discretization scheme depends on the physics we want to represent. As such, the directional behavior of the advective fluxes and the non-directional behavior of diffusive fluxes described in the governing equations in Chapter 3 needs to be maintained at the discrete level. Given the characteristics of each type of flux and the discretization schemes described, advective fluxes are associated with forwarding differences and diffusive fluxes with central differences. Using central differences for the discretization of advective fluxes can lead to the appearance of negative coefficients at the control volume faces [217], which would limit the approach to low Reynolds numbers. However, these are not without limitations, making them inappropriate for describing supercritical fluid behavior, as is the case of the appearance of non-physical pressure oscillations. Considering a generic location, diffusive fluxes are affected by changes in the conditions on either side of that location.

In contrast, advective fluxes are only affected by condition changes on one side of the location. Taking into account the behavior of both types of fluxes, the incompressible but variable density approach used resembles time marching parabolic codes [66]. These, however, can lead to convergence difficulties [218] at low speeds such as the ones encountered in the flows of interest [59].

In order better understand these limitations, we can start by defining a cell-based Péclet number, according to equation (4.6), as a ratio between advective and diffusive fluxes, where V is a reference velocity, L a reference length, and α the thermal diffusivity. As now defined, large Pe means advection effects values will have a greater preponderance than thermal transfer. Considering the second-order central scheme, it is diagonal dominant for values of the Péclet number of less than two; however, for values higher than two, meaning that advective processes dominate over diffusion, the matrix system loses its diagonal dominance, and the system may not present a linear solution, leading to the appearance of non-physical pressure oscillations. It may be recalled that the importance of the diagonal dominance has been highlighted in Chapter 3 since the non-linear behavior of the advective terms in the conservation equations is the source of turbulence.

$$\mathrm{Pe} = \frac{VL}{\alpha} \quad (4.6)$$

To circumvent the numerical stability problems of central schemes for Péclet numbers higher than two, we can then resort to first-order schemes such as the first-order forward scheme represented in equation (4.3). Although these schemes are accurate for one-dimensional flows, they are over-diffusive for multidimensional problems, introducing numerical diffusion, which requires appropriate treatment. In summary, the stability achieved with the introduction of numerical diffusion comes at the expense of accuracy. The idea is then to look for a higher-order scheme that allows to overcome the stability issues of central schemes and retain at the same time the directional behavior of upwind schemes. Such is the case of the third-order accurate quadratic upstream interpolation for convective kinematics (QUICK) scheme [219]. As defined in Figures 4.2 and 4.3 the values at right and left faces are defined according to equations (4.7) and (4.9). As depicted in the figures, four nodal points are needed, assuming that the normal component of velocity has the same sign for each two opposite walls [219]. It may also be interpreted as a linear interpolation, however, corrected with a term proportional to the upstream curvature as depicted in Figure 4.2, given that for a parabola, the slope halfway between two points is equal to the chord joining these points. While grid refinement could, in principle, alleviate the problem, its required level would be impracticable for most engineering applications. While dissipation is recognized as the key to controlling oscillatory numerics, high-order schemes are not the only way of introducing it to the computations since sensors of localized artificial viscosity can alternatively be used [9]. In summary, using the QUICK scheme to estimate the values at the control volume walls with accuracy is intended to avoid instabilities occurring for high advection found in linear interpolation.

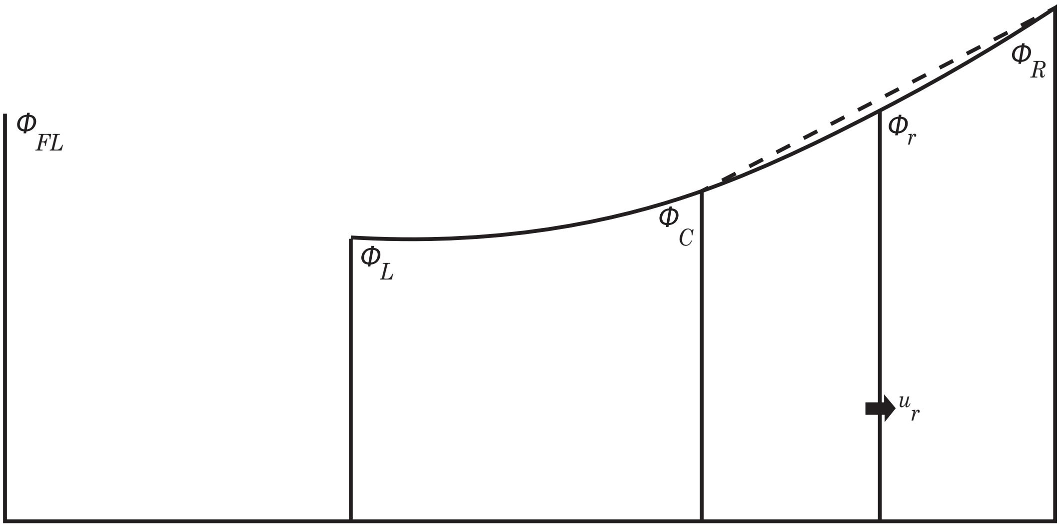

Figure 4.2: Interpolation of ϕ_r.

$$\phi_r = \frac{1}{2}(\phi_C + \phi_R) - \frac{1}{8}(\phi_L + \phi_R - 2\phi_C) \quad (4.7)$$

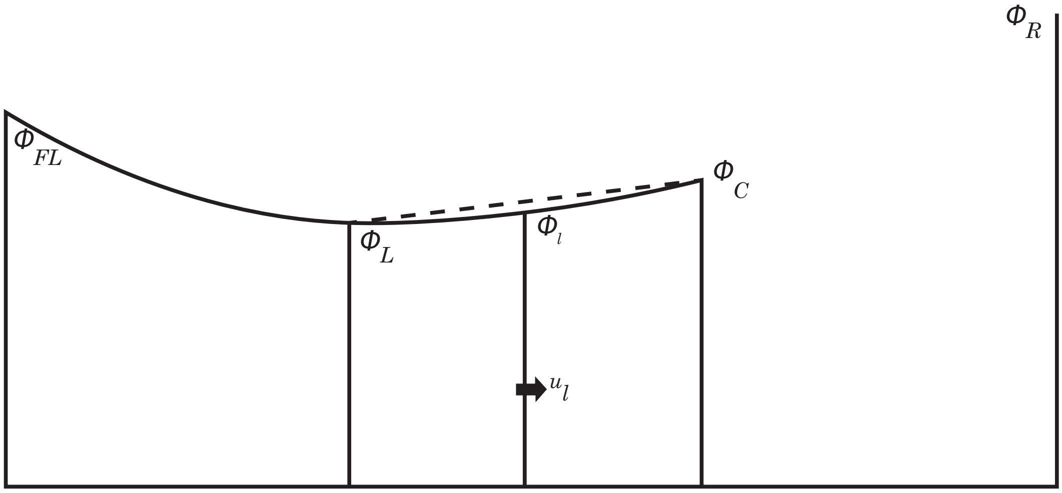

Figure 4.3: Interpolation of ϕ_l.

$$\left(\frac{\partial \phi}{\partial x}\right)_r = \frac{\phi_R - \phi_C}{\Delta x_r} \quad (4.8)$$

$$\phi_l = \frac{1}{2}\left(\phi_L + \phi_C\right) - \frac{1}{8}\left(\phi_{FL} + \phi_C - 2\phi_L\right) \quad (4.9)$$

$$\left(\frac{\partial \phi}{\partial x}\right)_l = \frac{\phi_C - \phi_L}{\Delta x_l} \quad (4.10)$$

While the stability achieved with the QUICK scheme solves the oscillatory behavior of the discretization process and contributes to mitigating the appearance of non-physical pressure oscillation, it is not its only source. For example, in the modeling of supercritical fluid behavior, non-linearities associated with the EoS and the Widom line could have a role to play in the appearance of pressure oscillations, polluting the numerical solution, and different approaches may need to be pursued to deal with them, depending on whether RANS, LES or DNS is being used. In general, the variation in density, viscosity, and specific heat increases the non-linearity of the equations, which have to be evaluated at each iteration [220].

4.2 Spurious Pressure Oscillations

Despite the complexities associated with the description of supercritical fluid flows, several advancements have been made in their numerical simulations. Either by considering the flow as compressible [196, 221] or taking a variable density but incompressible approach [66], the predictive capabilities of computational methodologies have increased. On the other hand, aspects of the modeling such as the EoS and the Widom region introduce non-physical pressure oscillations into the flow, which need to be dealt with [222–224]. Consequently, entropy stable schemes have been used to improve numerical stability [196], while the production of entropy is used for the flow description [225–227].

The thermodynamic non-linearities in the vicinity of the Widom line may induce the generation of pressure oscillations originating in minor density variations generated from the non-linearities associated with the real fluid EoS [224]. As reported by Lacaze et al. [224], LES-based solvers are the ones where this problem needs to be accounted for and where more effort needs to be employed to deal with it. In the case of RANS, as described in section4.1, with the introduction of the QUICK scheme, numerical diffusion is introduced while ensuring that the gradients are well resolved. On the other hand, in DNS, all scales are solved [65], while in LES of supercritical fluids, the Reynolds at which the simulations are run is higher than in the case of DNS. Furthermore, coarser grids are employed against which the ability to replicate the inertial grid-scale behavior in the form of Kolmogorov's $-5/3$ law is compared.

Numerical dissipation can appear due to the use of localized artificial viscosity to ensure solutions convergence under a grid refinement process [228] or high-order numerical methods with dissipative characteristics [9], which in appropriate conditions is changed to non-oscillatory numerical schemes, as described above. Localized artificial viscosity needs to be applied consistently to all variables [150], in order to maintain the characteristics of the physical phenomena. In this sense, Terashima and Koshi [229] employ an artificial viscosity term to limit the appearance of pressure oscillations in high-density gradient regions; sensors are commonly used [76] to identify high-gradient regions and to establish the transition between high-order dissipative and low-order non-dissipative numerics. On the other hand, entropy stable schemes have been recently introduced [230], since spurious oscillations violate neither the stability of entropy nor the principle of minimum entropy. As a consequence, however, in these schemes, the conservation of total energy is forsaken [223, 231], effectively moving from a fully conservative formulation to a quasi-conservative one. Entropy stable schemes have been introduced into the modeling of supercritical flows by Ma et al. [196], through the extension of the double flux model [230] to real fluids. Due to the non-achievable energy conservation, quasi-conservative methods lead to non-physical fluid heating [232].

Quasi conservative formulations can help alleviate the effect of spurious pressure oscillations considering a transport equation for pressure (a non-conserved variable). Terashima and Koshi [229, 233], [234] extended the pressure transport equation to supercritical conditions, where pure advection numerical tests [233, 235] were used to compare conservative and pressure-based formulations. A more in-depth comparison between conservative and quasi-conservative formulations would be later performed by Lacaze et al. [224]. They compare the fully conservative energy-based formulation impacted by spurious oscillations with quasi-conservative pressure- and enthalpy-based formulations, concluding that the enthalpy-based formulation avoids spurious oscillation and is more accurate in the representation of mixing thermodynamics.

For multi-component mixtures, Ma et al. [236] show that mixing follows the limiting cases of adiabatic and isochoric mixing models when fully- and quasi-conservative formulations are employed, occurring as a consequence of numerical diffusion appearing due to insufficient grid resolution, in the case of LES. Therefore, it is concluded that the adiabatic mixing model may be inadequate. Also Boyd and Jarrahbashi [232] propose a hybrid method where quasi-conservative, double flux, and fully conservative formulations are switched based on a criterion resorting to heat ratio and reference internal energy.

Maeda and Ihme [237] report on the fact that supercritical fluids having variable properties can be a source of numerical instabilities required purposely built techniques such as double flux and quasi-conservative formulation and *a priori* grid refinement. They develop a discontinuous Galerkin method for transcritical and supercritical fluid flows.

Lastly, it is worth mentioning that these studies on the appearance of spurious pressure oscillations were conducted under compressible flow conditions. It is not clear what their impact would be in an incompressible but variable density approach using LES.

4.3 Under-relaxation

Under-relaxation of variables alters the value of the variable ϕ between consecutive iterations through a parameter called the under-relaxation factor (θ). For example, considering two consecutive iterations of the variable ϕ and taking $\Delta\phi$ its variation between the considered iteration, under-relaxation can be expressed according to equation (4.11).

$$\phi^n = \phi^{n-1} + \theta\Delta\phi \quad (4.11)$$

For steady-state simulations, it is recommended to use the highest possible levels of under-relaxation since it accelerates the solution's convergence. Furthermore, it is practical since it can help avoid the divergence of the iterative solution in the presence of strongly non-linear equations. First, however, it is necessary to verify if the converged solution is affected by the values of the under-relaxation factors used. As such, under-relaxation is applied as follows: first, a high level of under-relaxation is applied to the variables that have reached convergence. A lower level of under-relaxation is then applied, and the iterative solver is re-started for about 100–200 iterations. If the lower under-relaxation has no significant influence on the residuals, the solution is independent of the under-relaxation factors used.

The under-relaxation values typically employed in the simulations are reported in Table 4.1, with initial and verification factors.

Table 4.1: Under-relaxation factors.

Variable	Initial value	Verification
p	0.5	0.75
ρ	0.3	0.4
μ_t	0.5	0.75
κ	0.4	0.75
ε	0.3	0.75
ω	0.4	0.75
$\tilde{\nu}$	0.4	0.75

4.4 Grid Independence

Mesh quality can have many definitions. The number of points can be a good one as far as DNS is concerned. Nevertheless, it is not sufficient. One must ensure that all the scales (including Kolmogorov scales) are being solved. So, this means that 10^{256} might correspond to a grid with good quality if it solves all the scales in the domain, or it can be a much poorer quality grid than 10^5 if it does not solve all scales. Additionally, with DNS, it depends on the domain size because in a 5x5x5mm domain, the small scales have the same size as in a 20x20x20cm, but in the latter, one will need 6.4×10^4 times more points.

In the RANS case, we need to ensure that the algebraic equations obtained by discretization of the PDEs (that govern the phenomena) are equivalent. This means that the solution of the algebraic equations should be close to the solution of the PDEs that they represent. We know that the difference between them is due to the approximation of the derivatives, which are continuum quantities in the PDEs. However, in the algebraic analogs, discrete quantities are obtained through a discretization method with an error proportional to the power of the distance between two node points (what we call mesh size). Also, theoretically, a first derivative would tend to the discrete when the mesh size tends to zero. However, this is impossible because the mesh size appears in the denominator, and a computer cannot deal with such an operation. So, what is done is to successfully divide the area or volume of the control volumes defined by the mesh points and represent the monitor results in an adequate position of the domain. At a particular stage, what is gained by refinement (increasing the number of points) does not correspond to a significant change in the results. In this situation, the results are independent of the grid size, and the last but one grid is then used for the rest of the calculation. This process may seem equivalent to increasing the number of points, but it is not because it is not needed to increase the grid resolution where the gradients are small. In this case, the gradients are calculated accurately with fewer points. So, the number of points can be increased selectively by putting more points where the gradients are steeper and fewer points where the gradients are smaller.

Nevertheless, to solve a Kolmogorov scale, the same number of points is always needed for a given Re since it only depends on it (velocity scale and viscosity scale). The LES approach is something in between: it is like a RANS method as far as the large eddies are concerned, and then we need to solve the energy cascade to go into the Kolmogorov scales. So, a vast amount of points is also needed in this case.

One can address this question in a non-numerical way. For example, an a priori analysis of typical supercritical injection experiments indicates the central regions of interest consist of the injector(s) and the region around the jet center-line in the chamber. In this sense, these regions require a substantially higher nodal distribution than, for example, the region close to the chamber wall and further downstream of the jet. The knowledge obtained from previous studies in the literature dealing with the same experiments contributed to this analysis, which was complemented with additional refinement as different computations were being carried out. To the meshes used for the grid independence study contributed three different aspects: the rule of thumb of dividing each cell volume into two, an *a priori* analysis of the physics of the computational configuration under consideration to determine regions of higher gradients and the residuals. This analysis is valid for both RANS and LES, dealing with these experimental conditions.

Just outlining the number of grid points is not enough for the RANS study, since more points do not directly correlate with better physical representation [228]. Since the high Reynolds closures are used, it is necessary to patch the effect of the boundary layer to the outer layers through a wall function, which requires that the value of the y^+ of the closest point to the wall is always larger than 11.63. For this particular case, since the key lies in capturing the heat transfer in the injector, we also need to ensure a proper resolution of the boundary layer. Typically 20 points are considered.

As mentioned before, LES differs from RANS. These simulations directly involve the grid's step size for the cutoff length between the modeled sub-grid scales and the resolved large scales. The "quality" (whatever it means) of LES (and DNS) results is evaluated through the ability to accurately reproduce small scales and the energy cascade expressed through the plot of Kolmogorov's -5/3 power law. A general comparison between LES and RANS is performed in Fröhlich and von Terzi [238]. In the context of high-pressure conditions, differences between RANS, LES, and DNS and in the interpretation of numerical results were critically reviewed by Bellan [65]. Grid requirements for LES are always larger than for RANS due to the issues mentioned above.

4.5 Uncertainty Quantification

In order to complement the grid independence studies, an attempt is made to quantify numerical uncertainty employing Richardson's extrapolation and the grid convergence index (GCI) [239]. It will allow comparing the nominal order of convergence of the discretization schemes with their actual order of convergence in the computations, typically lower. The discretization of the continuous domain in sets of grid cells and boundary and initial conditions and the approximations used are the causes for the decrease in the method's nominal order of convergence.

The order of convergence can be defined according to equation (4.12) as the difference between the discretized and exact solutions, with C being a constant, h measuring grid spacing and the order of convergence. Suppose we neglect the HOT and use logarithmic notation as represented in equation (4.13). In that case, the discretization error (round-off and iterative errors are neglected) can be obtained as the slope of the curve between the order of convergence and the grid spacing. The analysis of truncation error only provides a conservative estimation of discretization error convergence [240]. Furthermore, only relative error trends are typically sought after by comparing deviations between experimental data and numerical results. In the case of FVM, the discretization error constitute the main measure of accuracy [240].

$$E = f(h) - f_{exact} = Ch^p + \text{HOT} \quad (4.12)$$

$$\log(E) = \log(C) + p\log(h) \quad (4.13)$$

Considering that typically three different grids are used in the refinement process, equation (4.14) can be used to evaluate the order of accuracy with a constant grid refinement ratio (r).

$$p = \ln\left(\frac{f_3 - f_2}{f_2 - f_1}\right) / \ln(r) \quad (4.14)$$

One pre-requisite to determining the order of accuracy is to ensure that the grid refinement is such that the numerical solution lies in the asymptotic range of convergence, meaning that the ratio between the error and grid spacing must scale as a constant (equation (4.15)).

$$C = \frac{E}{h^p} \quad (4.15)$$

Depending on the value of the constant C in equation (4.15) four different classifications are possible, such as monotone convergence for $0 \leq C \leq 1$, oscillatory convergence for $-1 < C < 0$, oscillatory divergence for $C < -1$ and monotonic divergence for $C > 1$. If oscillatory convergence is observed, considering the absolute value of C can still be used as an estimator of the discretization error rate of decay [241].

The importance of achieving monotone convergence lies in the fact that since the exact solution is not known, techniques such as Richardson's extrapolation [239] can be used, assuming the numerical solution is in the asymptotic range. Ensuring that this condition holds allows to neglect the HOT and to estimate the solution and the errors based on the grid refinement process, whose number must be explicitly stated *a priori*. Based on the order of convergence obtained from equation (4.14), Richardson's extrapolation allows us to evaluate the value of the solution in the case of zero grid spacing through equation (4.16), using the two most refined grids. Richardson's extrapolation is based on a Taylor series expansion.

$$f_{h=0} \approxeq f_1 + \frac{f_1 - f_2}{r^p - 1} \quad (4.16)$$

The uncertainty in the computations can be further quantified by taking into account the so-called grid convergence index (GCI) [239]. In general terms, the GCI measures the uncertainty for each grid, quantifying how much the solution is from the asymptotic value. The GCI is defined in equation (4.17), being F_s a safety factor of 1.25, considering that three different grids are used in the computations and ε the relative error defined in equation (4.18).

$$\mathrm{GCI} = \frac{F_s|\varepsilon|}{r^p - 1} \quad (4.17)$$

$$\varepsilon = \frac{f_2 - f_1}{f_1} \quad (4.18)$$

Lastly, the asymptotic range of each grid can be confirmed by considering two GCI values, following equation (4.19).

$$r = \left(\frac{\mathrm{GCI}_{12}}{\mathrm{GCI}_{23}}\right)^{1/p} \quad (4.19)$$

4.6 Summary

The numerical discretization of the system of PDEs has been discussed in this chapter. Then the principal numerical issues affecting result accuracy, stability and convergence are reviewed and discussed in light of the variable thermophysical properties characteristic of supercritical fluid flows.

Chapter 5

Supercritical Cryogenic Nitrogen Injection

While increased pressure and temperature contribute to an overall efficiency gain in the mixing of propellants and oxidizers, characteristic of conditions in the combustion chambers of LREs, they also propel mixtures to trans- and supercritical conditions. In these conditions, the engine flow exhibits a gas jet-like behavior that may be described using an approach developed for variable density incompressible flows. The present chapter focuses on an approach using the Reynolds-averaged Navier-Stokes equations to evaluate the jet topology for different injectors' conditions. Based on the so-called 'thermal breakup mechanism concept' proposed in the literature, the axial density decay in supercritical nitrogen jets is predicted for a wide range of conditions. The results show the influence of thermal breakup, providing a better insight into the available experimental data.

5.1 Modeling Supercritical Injection

In the field of liquid rocket propulsion, nitrogen is used as neither a propellant nor an oxidizer. Nevertheless, nitrogen is commonly used to replicate the turbulent mixing behavior of such engines without including chemical equilibrium and combustion influences. This is sustained on the similar behavior at injection between oxygen and nitrogen [73]. As a cold flow surrogate for the oxygen-hydrogen mixture combination, a few experimental data sets have been put forward in the last two decades, allowing to broaden and to extend the state of knowledge regarding supercritical mixing behavior while at the same time working as the validation needed for the development of numerical solvers. In particular, the axial density decay at the jet centerline works as an indication of the jet dissipation concerning the injector exit plane [143], detailing mixing efficiency. Jet dissipation will be affected by the velocity ratio between conditions at injection and in the chamber and the variable density leading to thermal stratification as a consequence of the high-density ratios. The evaluation of velocity and density ratios is used to measure momentum and thermal dissipation from the jet to the chamber fluid.

Incidentally, numerical efforts in modeling supercritical fluid behavior began by establishing the differences between subcritical and supercritical conditions and the influence of thermophysical properties on jet development. For example, Zong et al. [79] studied through LES the injection of a cryogenic jet, with a temperature below and above the critical point into a quiescent nitrogen environment, showing a qualitative agreement between both conditions, where the formation of Kelvin-Helmholtz instabilities and the entrainment of low-density nitrogen from the chamber into the jet potentiate the formation of vortical structures leading to jet breakup and enhancing mixing between both fluids. However, large density gradients hinder jet breakup, having a stabilizing effect on jet development [87, 242]. Eventually, the effect of pseudo-boiling [53] would gain prominence [45] and its impact on mixing efficiency became a target of more detailed research either by LES [243] (details of LES modeling of supercritical injection is reviewed by Ries and Sadiki [14]) or trough DNS [121, 149, 244], constrained on the appearance of spurious pressure oscillation in the former and limitations to low Reynolds numbers and simple geometries in the later since turbulence statistics are challenging to measure in high-pressure experiments at conditions characteristic of engine operation, as are initial and boundary conditions. DNS [245] is also used to infer their effect in the temperature field. Sharan and Bellan [245] performed DNS of nitrogen injected into a nitrogen-filled chamber at conditions ranging from subcritical to supercritical where the sensitivity of velocity fluctuations with pressure is shown, meaning that this information could be essential to acquire experimentally. This is just one example of how numerical studies can help guide experimental campaigns toward quantities of interest, creating synergism between experiments and numerical simulations and using experimental data to validate numerical models. For example, even in low-velocity turbulent jets [246] exiting from round nozzles, decay coefficients are dependent upon nozzle outlet velocity and area. On the other hand, Maeda [247] employs artificial boundary conditions, considering only the chamber geometry, while modeling the nozzle effect by considering the flux at the boundary domain.

RANS [45, 66, 68, 118, 248, 249], LES [76, 250–253], DNS [121, 226, 254] or DES [167] studies have demonstrated their ability in predicting several features of supercritical jets such as the spreading rate (the importance of which was demonstrated by Chehroudi et al. [128]), mean flow, and thermodynamic properties. The different intrinsic nature of the various numerical and modeling approaches, the definition of grid requirements, as well as difficulties in defining common initial and boundary conditions associated to the interpretation of experimental data [59] remain challenging [65].

5.2 The Experiment

The experimental conditions of Mayer et al. [59] have become the canonical case for validating computational methods that aim at predicting supercritical fluid behavior. To date, it remains the most comprehensive database for single-species injection at supercritical conditions, as depicted in Figure 5.1. According to the conditions of Table 5.1, the injection of a single supercritical liquid nitrogen jet into a chamber filled with gaseous nitrogen is considered, where the pseudo-vaporiation power [45] quantifies the amount of energy required to reach the maxima in isobaric specific heat. Here, nitrogen is a surrogate for the mixture of hydrogen/oxygen, which is characteristic of LREs. By choosing nitrogen, supercritical behavior can be studied without including finite-rate chemistry and combustion effects in the computations. In this way, real gas mixing can be evaluated at each considered injection configuration for a single substance.

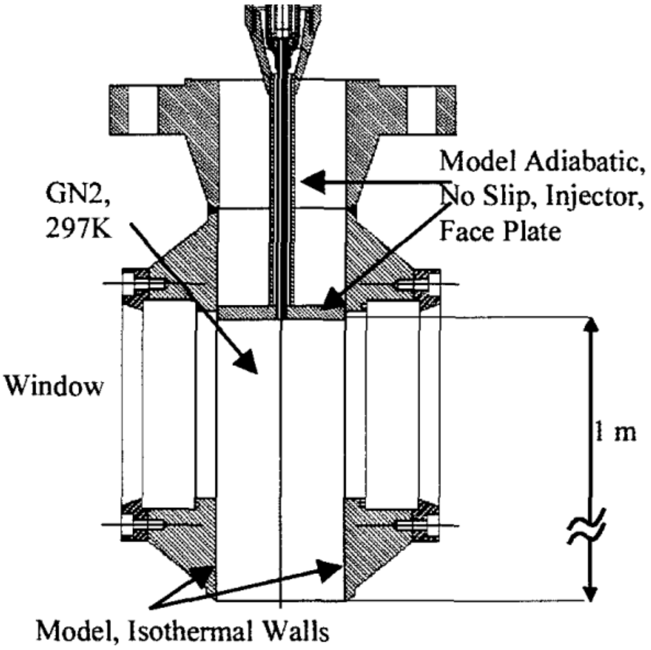

Figure 5.1: Experimental setup [143].

The experimental study used Raman scattering to measure the axial evolution of density and to evaluate the spread of variable-density jets.

The experimental test conditions are graphically represented in Figure 5.2. Variations of density, ρ, and isobaric specific heat capacity, c_p, with temperature, T, are represented for nitrogen, with the experimental data available from the NIST database [137]. The test cases correspond to pressures of 4, 5, and $6\,\mathrm{MPa}$ and the measured temperatures of Table 5.1.

Table 5.1: Experimental conditions (Mayer et al. [59]).

Case	Calculated Velocity $[\mathrm{m\,s^{-1}}]$	Measured Chamber Pressure $[\mathrm{MPa}]$	Measured Temperature [K]	Pseudo-vaporization Power [W] [45]
3	4.9	3.97	126.9	310.88
4	5.4	3.98	137.0	-265.30
5	2.0	4.90	131.0	103.59
6	1.9	4.90	140.0	-113.30
7	4.5	5.01	126.2	448.72
8	4.9	5.00	135.7	-51.88
9	2.0	5.85	135.0	81.22
10	1.9	5.88	140.5	-34.27

Uncertainties in the measured values of the injection temperature [59] need to be discussed [8, 32, 129] since they have a profound impact on the jet evolution under the considered conditions. The experimental temperature in Mayer et al. [59] experiment was not controlled accurately due to the complexity of the piping system. For example, the temperature at the injector's exit was measured during a separate measurement campaign. In addition, the heat transfer from the injection system (particularly in the injector) is usually neglected in the

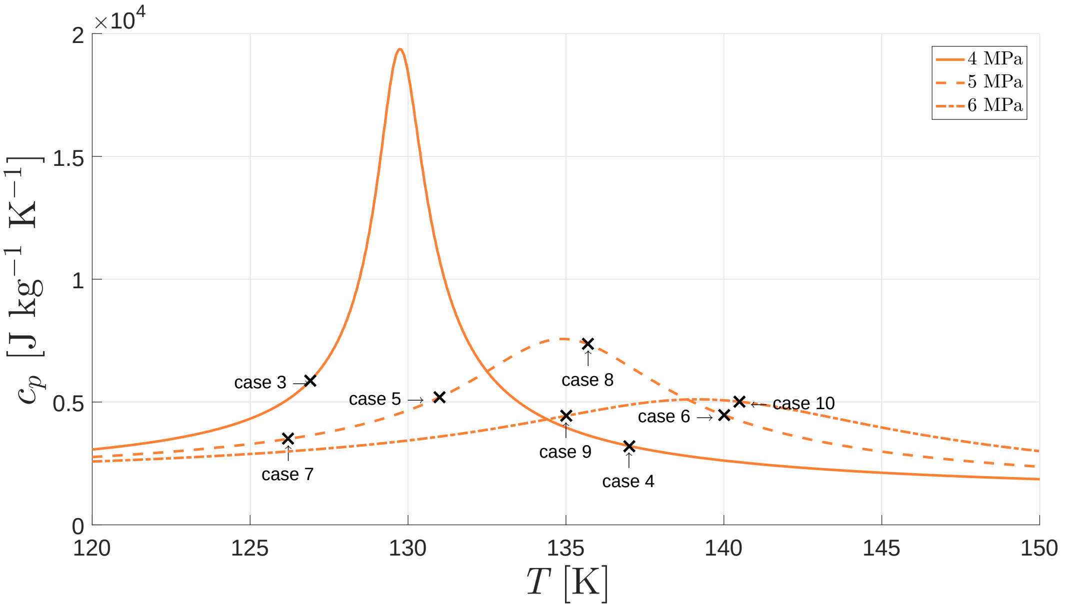

Figure 5.2: Experimental data distribution in relation to the maxima in isobaric specific heat.

computations, despite indications of its importance. Banuti and Hannemann [45] critically reviewed the influence of temperature uncertainty measurement in several cryogenic experiments, focusing on the neglected injector heat transfer. However, it is still necessary to define an injection temperature and its influence on the results. In Figure 5.2, considering the density decay for nitrogen for the 4 and $5\,\mathrm{MPa}$ it is possible to observe that a slight variation in the injection temperature will result in a significant variation in density, especially for case 3, where the steepest slope of density is registered. Given the uncertainties surrounding the injection temperature, any numerical results comparison, an absolute match with experiments, cannot be sought. Instead, a qualitative description and comparison with the experiments is desired.

In what the injection temperature concerns, this is not the only interpretation. For example, Müller et al. [253], use the density values close to the injector for the determination of the injection temperature of case 3. Going even further, Lee et al. [136] propose an additional concept than thermal disintegration to explain temperature inversion at certain conditions, considering the relaxation effect from high to low pressures by studying positive sound dispersion, which requires the use of molecular dynamics simulations not readily suited for practical applications.

In the present work, the inclusion of injector heat transfer, as introduced by Banuti and Hannemann [45] is considered. However, the inclusion of the injector in the computations is not restricted to the acknowledgment of heat transfer between nitrogen and the injector wall. Evidence of heat transfer rates in the injector is also obtained by considering zero fuel rate flow [32]. For instance, in cases where the injector length is long enough for a fully turbulent flow to develop, such as the one under consideration [59] the specification of the velocity profile and turbulence (in the case of turbulence kinetic energy and its dissipation) can affect the length of the potential core [227]. Chassaing et al. [158] report different values of spreading rate, velocity decay, and turbulence kinetic energy in the self-similar region than those available in the literature, while Rodi [255] reports a 20 % change in the velocity decay when modifying the velocity profile at the inlet from a plug flow to a 1/7th power law.

The computational domain corresponding to the experimental setup of Mayer et al. [59] is represented in Figure 5.3, detailing the boundary conditions (BCs). The chamber and the injector have diameters of 122 mm and 2.2 mm and lengths of 250 mm and 90 mm, respectively. A constant axial velocity profile is set at the inlet, while the radial component is set to zero. At the chamber and injector walls, both the normal and tangential velocity components are set to zero. A pressure outlet is defined with a gauge pressure of 0 MPa. For comparison purposes, adiabatic and isothermal injector wall configurations are tested. For the adiabatic configuration, along with the faceplate, the heat flux is zero, while for the isothermal walls of the injector and chamber, a constant temperature of 298 K is applied [45].

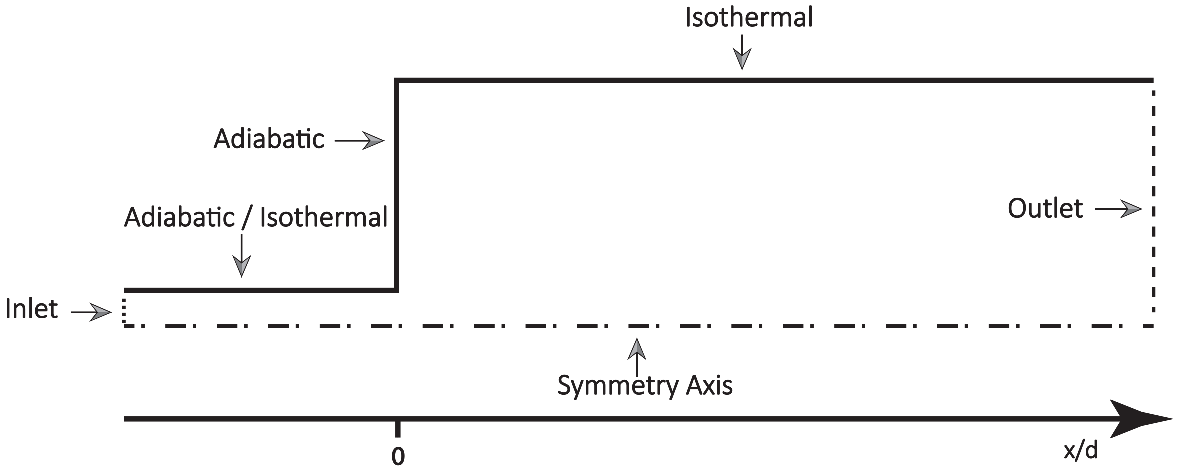

Figure 5.3: Boundary conditions and computational domain, corresponding to Mayer et al. [59] experiment.

Mayer et al. [59] experiments are used extensively for the validation of numerical solvers [45, 75, 76, 172, 173, 196, 221, 226, 248–254]. While the focus has been on demonstrating models suitability for the description of liquid- and gas-like supercritical behavior, generally, only cases 3 and 4 (Figure 5.2) are computed. Moreover, the experimentally measured temperature values [59] seemed to indicate that considerable heat transfer from the injection system would affect the jet development. However, heat transfer inside the injector is usually neglected in the computations. Table 5.2 summarizes the studies dealing with Mayer et al. [59] experimental data, in terms of the physical models and effects.

When the jet exits the injector, shear layers are formed at opposite jet surfaces between the jet and the chamber fluid [256], which grow until they meet at the jet centerline, defining the potential core length.

Figures 5.4 and 5.5 depict comparisons between the experimental [59] axial density decays of cases 3 and 4, respectively, with numerical computations available from the literature, encompassing RANS, LES, and DNS results, which represent prevailing trends and model choices, as indicated by the broader summary in Table 5.2. Since the temperature profile influence in the injector is not considered, discrepancies are observed between experiments and numerical simulations, especially in case 4 (Figure 5.5).

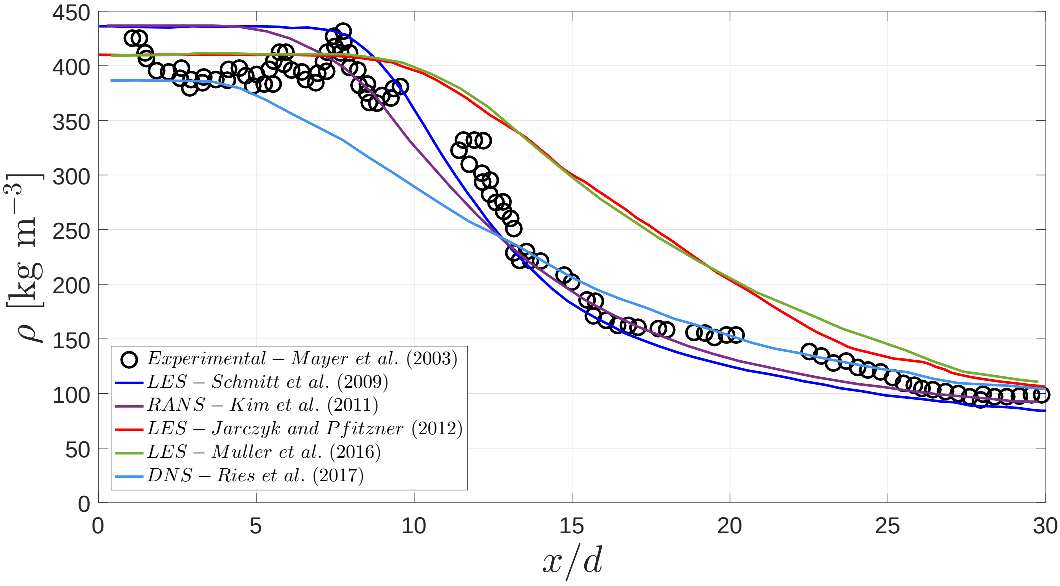

Figure 5.4: Overview of selected (Schmitt et al. [76], Ries et al. [226], Kim et al. [248], Jarczyk and Pfitzner [252], Müller et al. [253]) numerical results on experimental case 3 [59].

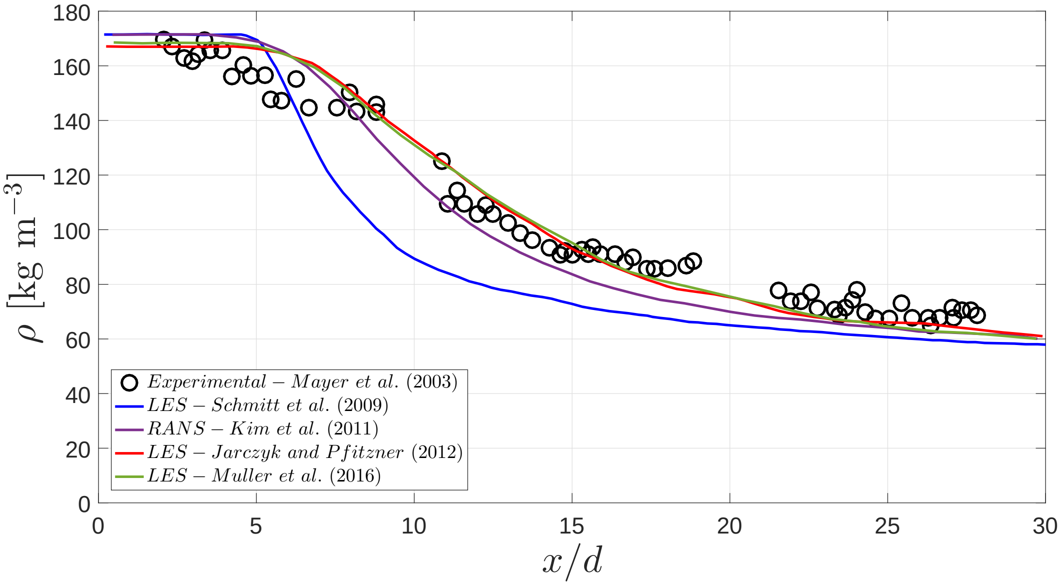

Figure 5.5: Overview of selected (Schmitt et al. [76], Kim et al. [248], Jarczyk and Pfitzner [252], Müller et al. [253]) numerical results on experimental case 4 [59].

The analysis of Table 5.2 on studies using Mayer's experimental data for the validation of various numerical solvers is also a journey through the evolution of supercritical fluid flow modeling throughout the years and a recollection of everything the scientific community has learned about these types of flows in the two decades since the experimental data came about. Schmitt et al. [76] references the fact that SGS terms usually neglected at low-pressure conditions may have a role to play at supercritical ones [257], an idea also reported in RANS studies [154, 249].

The highly non-linear behavior [164] in both thermodynamic and transport properties can lead to distinct coupling mechanisms than those observed at subcritical conditions: the inclusion of the Soret and Dufour effects [25, 152, 257] in the computations or of the filtered density in the scope of the EoS [151], may play an additional role. On the other hand, low-pressure turbulence models [160, 171] continue to be used [154, 172, 173]. Conversely, the EoS choice could be more relevant than the turbulence model [249].

Noteworthy is the relation between the potential core length and the pronouncement of real gas effects. Alternatively, Jarczyk and Pfitzner [252] propose to forfeit solving the mass conservation equation in favor of a conservation equation for pressure, developed from an incompressible approach. However, developing such an equation is troublesome since pressure is a non-conservative variable. At the same time, density-based formulations [76] become very stiff in the incompressible limit leading to the need for preconditioning methods. Later, Müller et al. [253] would compare pressure- and density-based formulations showing marginal differences in terms of axial density evolution predicting for supercritical nitrogen jets.

Moreover, DNS provides information about the physics of supercritical mixing [254], indicating, for instance, a higher jet spreading in terms of temperature than velocity [226], implying heat propagation dominates over the transport of momentum. Also Tani et al. [258] studied a nitrogen temporal mixing layer through DNS to infer the effect of pseudo vaporization at the pseudo-critical temperature. At this temperature, the peak in isobaric specific heat causes the Prandtl number to exceed the value of one, leading to a smaller characteristic turbulence scale than Kolmogorov's, the Batchelor temperature scale. On the other hand, it was found [258] that the turbulent Prandtl number was not influenced by the pseudo-boiling temperature, leading to the conclusion that only density and not turbulent transport of momentum and heat are affected by the pseudo vaporization. Moreover, Lapenna and Creta [149] studied similar injection configurations to those of cases 3 and 4 to investigate the effect of pseudo-boiling in mixing.

Banuti and Hannemann [45], introduce the concept of thermal disintegration to complement the mechanical description of supercritical jets. In this way, the authors can demonstrate the amount of energy a supercritical jet receives [53] in the injector will determine if a change from liquid- to gas-like conditions takes place, influencing the jet development. With the introduction of thermal disintegration [45], it was possible to evolve from a purely mechanical description of supercritical jets, where a potential core would always be recovered as the jet discharged into the chamber, to the retrieval of a disintegrated core, given the pseudo-boiling power, as computed by Banuti and Hannemann [45]. These results were later confirmed by Lapenna and Creta [121] with DNS.

Table 5.2: Overview of numerical simulations corresponding to the experimental data [59, 144, 259]. Abbreviations: EoS - Equation of State, n/a - not applicable, HBMS - Hirshfelder-Buehler-McGee-Sutton, PR - Peng-Robinson, SRK - Soave-Redlich-Kwong, mBWR - modified Benedict-Webb-Rubin ,vcorr - volume correction, ref - reference, Helm - Helmholtz reduced energy, LES - Large Eddy Simulation, RANS - Reynolds-averaged Navier-Stokes, DNS - Direct Numerical Simulation, VoF - Volume of Fluid, id+dep - ideal gas state plus departure function, poli fit - polynomial fitting, axi - axisymmetric, 3D - three dimensional, incomp - incompressible, comp - compressible, adiab - adiabatic, infl temp - inflow temperature, iso- isothermal, inf turb - inflow turbulence

Reference	EoS	Turbulence	Transport	Dimension	Type	Injector	Condition
[59]	n/a	$\kappa-\varepsilon$	id+dep	axi	incomp	adiab	3, 8
[260, 261]	HBMS	$\kappa-\varepsilon$	id+dep	axi	incomp	adiab	3, 4
[262]	PR	$\kappa-\omega$	id+dep	axi	incomp	adiab	3–derived
[76, 250, 251]	PR	LES	id+dep	3D	comp	adiab	3, 4
[248]	PR/SRK	$\kappa-\varepsilon$	id+dep	axi	incomp	adiab	3, 4
[249]	PR/SRK	LES/RANS	Z form	3D	comp	adiab	3
[252]	PR+vcorr	LES	id+dep	3D	comp	adiab	3, 4
[172]	PR–SRK	LES	id+dep	3D	comp	adiab	3, 4
[253, 263]	PR+vcorr	LES	id+dep	3D	comp	infl temp	3, 4, 7
[234]	SRK	LES	id+dep	3D	comp	adiab	3, 4
[45]	mBWR	SA	look up table	axi	comp	iso	4
[168]	PR+vcorr	LES	id+dep	3D	comp	infl temp	3, 4
[173]	PR+vcorr	LES	n/a	3D	comp	adiab	4
[196]	PR	LES	id+dep	3D	comp	adiab	3, 4
[226, 254]	PR+vcorr	DNS	id+dep	3D	incomp	inf turb	3
[149]	ref	DNS	id+dep	3D	incomp	n/a [1]	3, 4
[264]	SRK	$\kappa-\varepsilon$	id+dep	axi	comp	adiab	3, 4
[265]	PR	LES	id+dep	3D	comp	inf turb	3, 4
[75]	SRK	LES	id+dep	3D	comp	adiab	3, 4
[266]	PR+vcorr	LES	id+dep	3D	comp	adiab	3, 4
[221, 267]	PR	LES	id+dep	3D	comp	adiab	3,4
[227]	n/a	LES	look up	3D	incomp	inf turb	3
[268]	SRK	LES	id+dep	3D	comp	iso	3, 4
[124, 269]	n/a	VoF – n/a	poli fit	3D	comp	adiab	9
[154]	Helm	κ-ε	id+dep	axi	incomp	adiab	3, 4

The present chapter aims at extending Banuti and Hannemann [45] conceptualization to a broader range of conditions. Several experimental test cases are considered to validate the computational approach, where it is possible to observe the effect of heat transfer in the injector as the trigger for the pseudo-phase change. A summary of the thermophysical models used in the calculations presented in this chapter is given in Table 5.3.

Table 5.3: Summary of thermophysical models.

Turbulence closure	EoS	Transport properties
κ–ε standard [175]	PR [184]	Lemmon and Jacobsen [214]

5.3 Validation

The grid independence was studied with three different refinement levels to ensure that the grid resolution did not influence the results. As depicted in Figures 5.6 and 5.7, the axial density decay, corresponding to the experimental case 4 from Mayer et al. [59], was selected for the independence study, for adiabatic and isothermal injector wall configurations, respectively. The turbulence closure used in the formulation corresponds to the standard version of the κ–ε model from Launder and Spalding [175]. As this is not valid up to the solid wall, the turbulence model needs to be calibrated according to the wall functions to ensure that the boundary layer is properly resolved. Consequently, wall function modeling bridges the gap between the viscosity affected region and the fully turbulent region, in which the κ–ε model can be applied. Therefore, a y^+ value of 11.63 was considered for the first cells adjacent to the walls. Below this value, the flow was assumed to be purely viscous; above this value, it was considered purely turbulent. As well as the y^+ value, there is a need to define a minimum number of points in the mesh located inside the boundary layer. Typically, around 20 points are taken to be inside the boundary layer, so this value was employed.

Figures 5.6 and 5.7 depict the grid independence results for a coarse mesh with $180\,000$ points, an intermediate mesh with $280\,000$ nodes, and a refined mesh with $495\,000$ nodes. As no variation in the slope of the results can be distinguished, grid independence has been achieved with the intermediate grid.

In Figure 5.8 we can observe how the error decreases as a function of the grid convergence index (GCI) [239] from the coarse to the refined mesh. From the slope, it is possible to retrieve the achieved order of convergence, 2.512, versus a nominal convergence rate of 3, being first- and second-order slopes represented for comparative purposes. The difference between nominal and achieved order of convergence is explained due to initial and boundary conditions and the discrete representation of the physical domain.

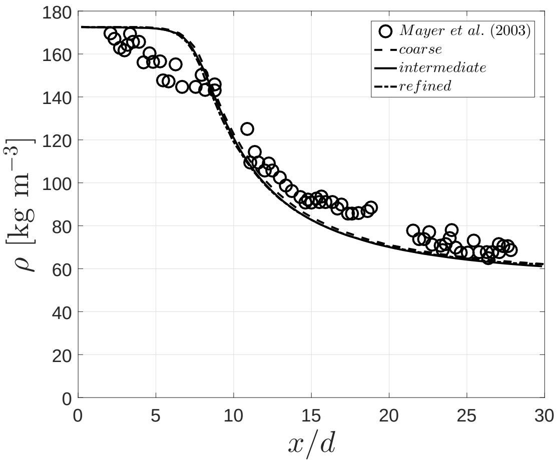

Figure 5.6: Grid independence study for adiabatic boundary conditions at the injector wall, corresponding to case 4.

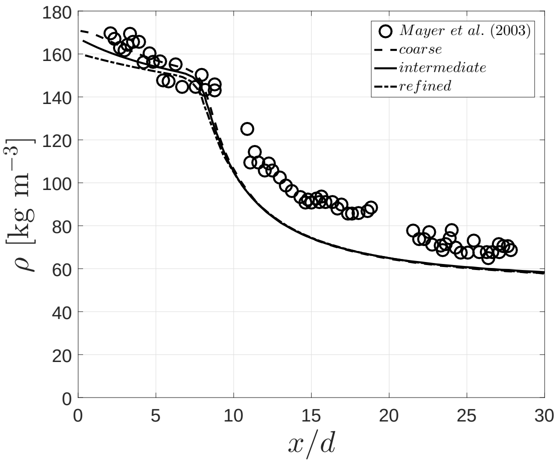

Figure 5.7: Grid independence study for isothermal boundary conditions at the injector wall, corresponding to case 4.

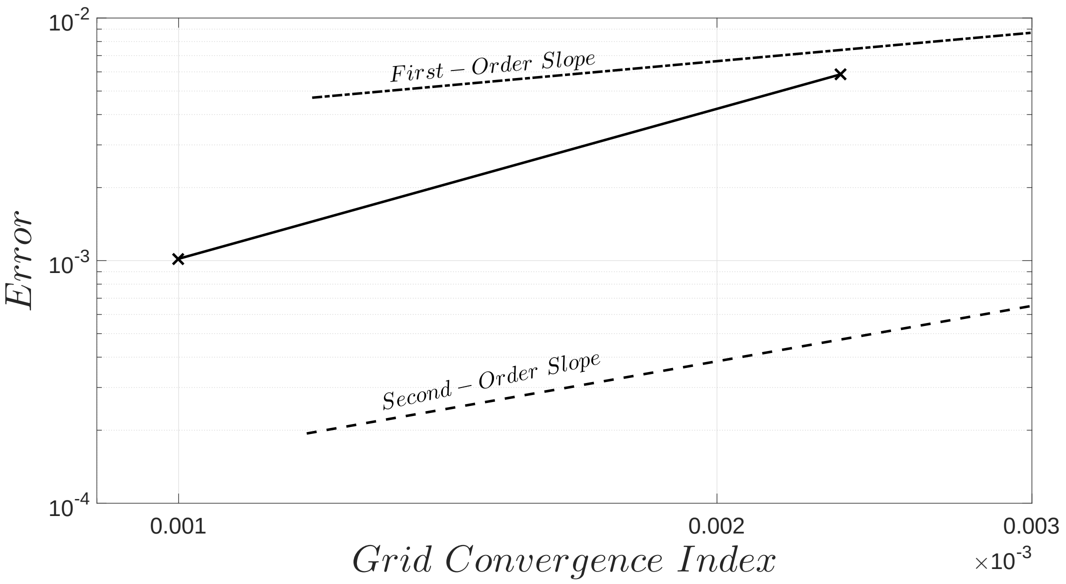

Figure 5.8: Comparison of grid independence study with Richardson's interpolation.

5.4 Results

5.4.1 Dense Core

Eventually, both the thermodynamic behavior and the breakup mechanism will play a role in determining the jet structure [45].

For the liquid-like injection configurations replicated here, the measured injection temperature of the experiments is below the peak in c_p. So the heating process of the potential core experiences a large density gradient, which acts as a solid wall damping radial oscillations [139, 242].

This is visible in Figure 5.2, where small temperature variations produce large density variations. A further indication of the large gradients that occur when crossing the Widom line can be seen through the transport properties of nitrogen, as depicted in Figures 3.7 and 3.9.

Figure 5.9 depicts the results for case 3. Adiabatic and isothermal injector configurations are compared based on their effect on the axial density decay in the combustion chamber. The experimental data of Mayer et al. [59] is presented for validation purposes, and the injector's diameter normalizes the axial distance from the injector.

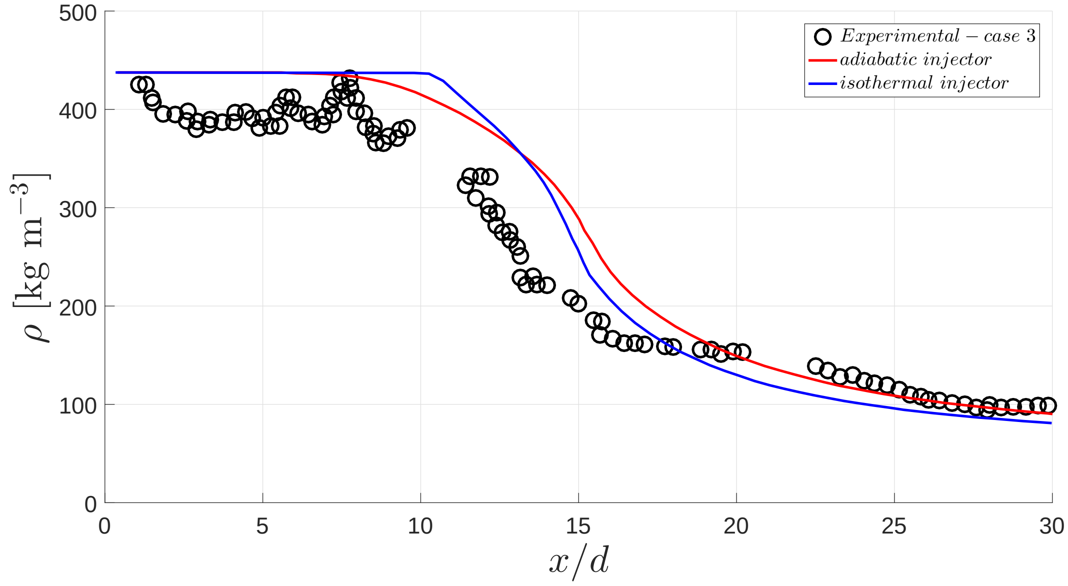

Figure 5.9: Axial density distribution for case 3 with adiabatic and isothermal injector wall configurations.

The stabilizing effect of the large density gradient for the liquid-like injection configurations is in accord with more sophisticated LES and DNS solvers [22, 205].

In agreement with the mechanical breakup theory, the prediction of a dense potential core is evident in the results. Although the adiabatic injector breakup occurs earlier ($x/d \approx 8$), for the isothermal [45] BCs, a denser core is observed ($x/d \approx 11$). According to Abramovich [142] different potential core lengths are expected for isothermal and adiabatic uniform-density jets, reporting lengths of 6 to 10 injector diameters in the former and up to 25 injector diameters in the latter. In terms of the core's breakup, we can observe a sharper decrease for the isothermal condition than for the adiabatic case. However, the obtained mean density of $437\,\mathrm{kg\,m^{-3}}$ represents an overprediction concerning the average of the experimental data. This can be justified by the Raman scattering technique used [59], which leads to underpredicted values for large density values.

The results of Figure 5.9 indicate a difference in the mean axial decay between the adiabatic and isothermal injector wall configurations. The difference between both configurations confirms that the thermal breakup introduced by Banuti and Hannemann [45] plays a role in the jet evolution, even though the jet does not receive enough energy to transition across the c_p-Widom line, as it happens in other cases studied.

Another possible interpretation for the more extended potential core obtained in the isothermal configuration could be related to the structural nature of eddy viscosity models. Attempts to quantify the structural uncertainty of turbulence models, either by performing sensitivity studies on the calibration constants [171], attempting to develop additional formulations with improved performance [180] or explicitly quantifying the uncertainty levels [181, 182], is a research topic that is of increasing interest.

Eddy viscosity models produce an initial low mixing rate [180], which leads to the formation of a more extended potential core, something that is visible in Figure 5.9. Further downstream, the mixing rate is higher, underpredicting the experimental data. Magalhães et al. [154] compared the performance of several eddy viscosity models but employed a second-order closure that is not based on Boussinesq's eddy viscosity concept. Under these experimental conditions, we observed that the second-order closure led to an even longer potential core than with the turbulence model of Launder and Spalding [175]. However, in the downstream region, the second-order closure corrected some underprediction of the experimental data. This means that the more extended potential core does not result from the uncertainties associated with eddy viscosity models but as a consequence of the level of pseudo-boiling, which requires the system to receive more energy in order to increase the temperature [45, 53].

The influence of the thermal effects can be further visualized in Figure 5.10 in terms of the dimensionless axial and radial distribution of density, where r is the radial distance taken from the jet's centerline. The small influence of thermal effects leads to different breakup times for jet's the potential core.

Figure 5.11 compares cases 3 and 7 in the isothermal injector configuration. According to Table 5.1, the difference between these cases is that case 7 occurs at a higher pressure, with less influence from pseudo-boiling (Figure 5.2). The results indicate better agreement between the experimental data and the numerical predictions than in case 3. The better performance of the model is visible when comparing cases 3 and 7 in terms of the length of the potential core and the downstream mixing rates. While turbulence model uncertainty plays a role in interpreting the results, the key is the ability to capture the effects of pseudo-boiling accurately. A comparison is also made with the LES computations of Müller et al. [253], who compared pressure- and density-based approaches. As depicted in Figure 5.11, the agreement found between the present results, experimental data, and the comparison with the compressible formulation [253] is an indicator of the suitability of the incompressible but variable density approach in the modeling of supercritical injection phenomena, where high pseudo-vaporization powers are present [45].

Generally, a closer agreement between experimental data is found for case 7 than case 3. For example, looking at Figure 5.2, it is possible to observe that case 3 would be the one most affected by uncertainties in the injection temperature, given the steepest slope of the density curve in this region ($4\,\mathrm{MPa}$). In comparison, uncertainties in the injection temperature for case 7 would play a less preponderant role, given that the slope in density is not as steep.

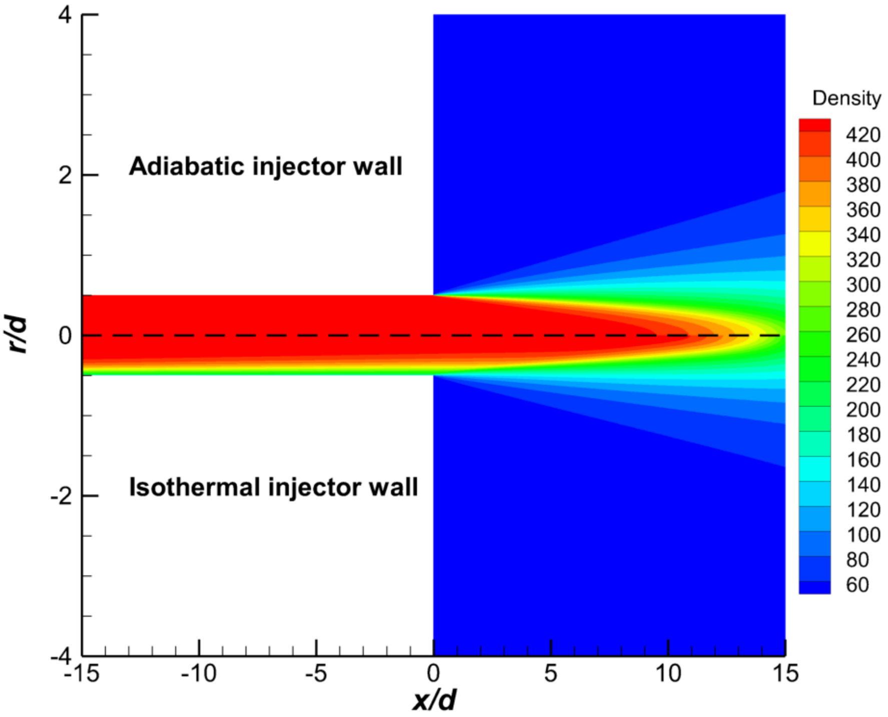

Figure 5.10: Density field for case 3 with adiabatic (top) and isothermal (bottom) injector wall configurations.

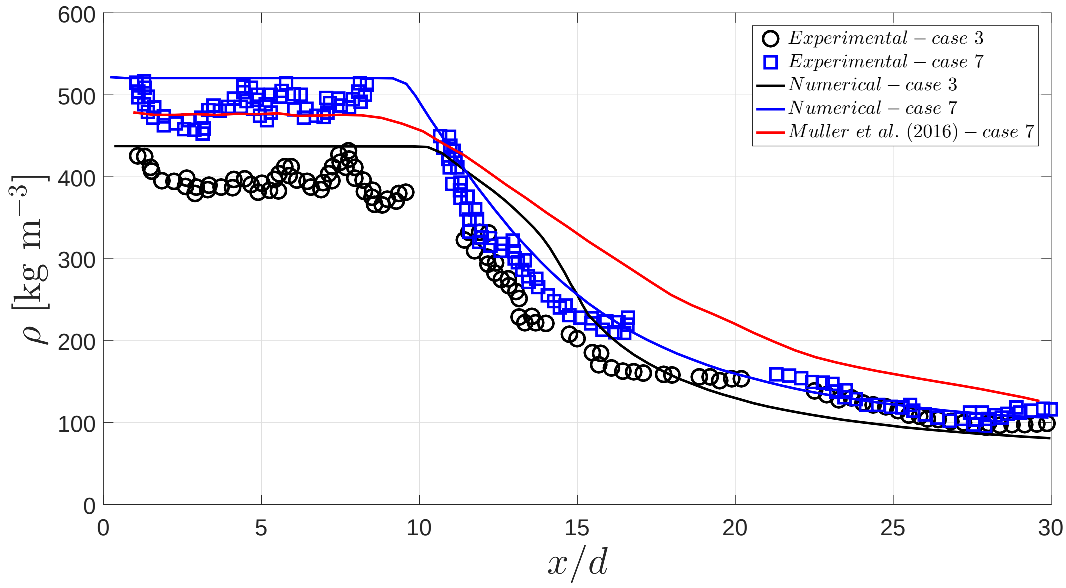

Figure 5.11: Axial density distributions for cases 3 and 7 with isothermal injector wall configurations.

5.4.2 Sloped Core

There are structural differences between jets in liquid- and gas-like conditions as previously described.

Figure 5.12 presents a comparison between adiabatic and isothermal injector wall configurations for experimental case 4 under gas-like injection conditions, therefore taking place after the Widom line has been crossed.

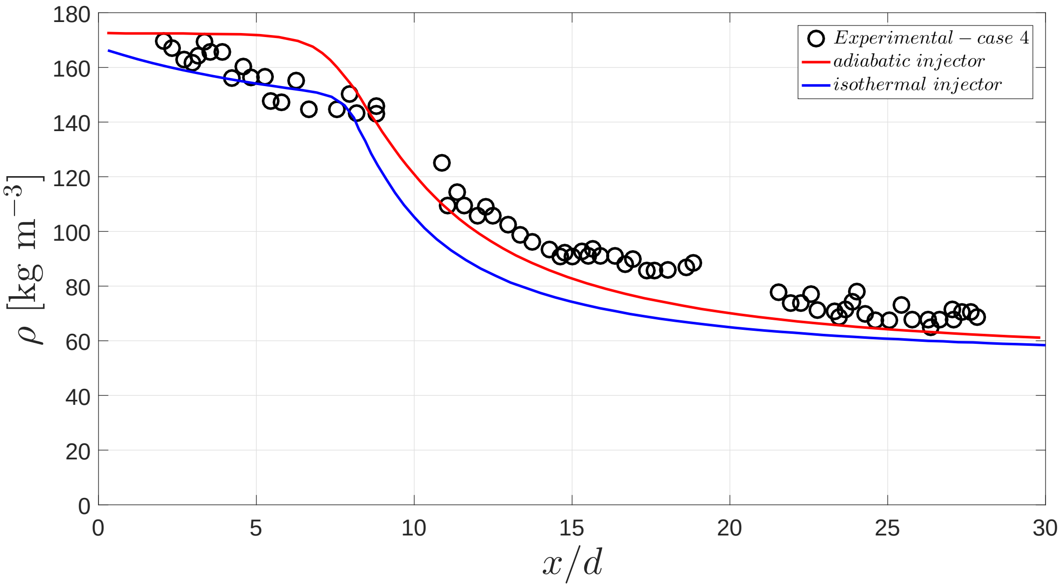

Figure 5.12: Axial density distribution for case 4 with adiabatic and isothermal injector wall configurations.

For the case of the adiabatic injector walls, a potential core can be observed until $x/d \approx 8$, in contrast to the experimental data. Then, experimentally, no potential core exists; instead, a sloped core [45] is present. Nevertheless, there is good agreement between the numerical predictions and the experiment after $x/d \approx 10$.

The sloped core [45] is only present when isothermal conditions are considered at the injector walls [45]. Then, a transitional region can be observed at $x/d \approx 8$, after which the jet evolution is dominated by the conditions present inside the combustion chamber due to the entrainment of chamber nitrogen. Comparing these results with the liquid-like injection considered in the previous section, we can see that the jet evolution is dominated by the conditions in the chamber to a greater and faster degree under gas-like conditions since enough energy has already been supplied to the system for a transition across the c_p-Widom line.

By analyzing the density contours for case, 4 in Figure 5.13, differences in the cases of adiabatic and isothermal BCs are visible. The density stratification is only seen in the isothermal configuration, resulting in lower density values along the jet's centerline. This is why the density values are different, even at $x/d = 0$ (Figure 5.12), as such plug-flow profiles of density cannot be used at the entrance to the combustion chamber. Instead, these profiles contribute to an altered jet state at both liquid- and gas-like, with a more profound impact on gas-like injection phenomena. Through these results, it is possible to support and extend the conclusions reached by Banuti and Hannemann [45] for a broad range of experimental conditions.

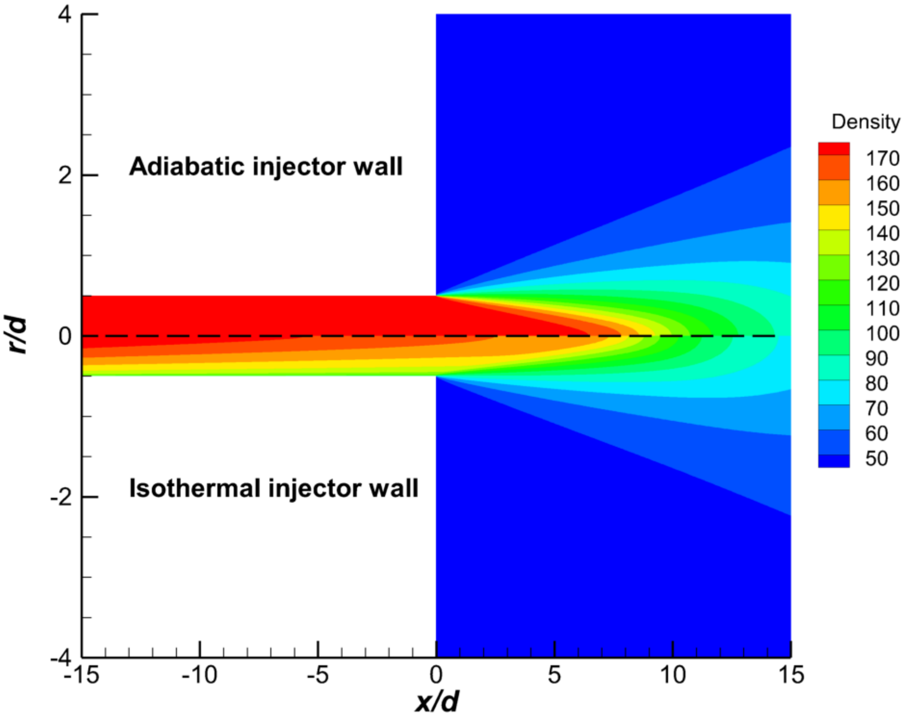

Figure 5.13: Axial density distribution for case 4 with adiabatic (top) and isothermal (bottom) injector wall configurations.

Even though a closer agreement is achieved for the initial gas-like configuration than for the liquid-like case, a comparison is also performed for higher-pressure conditions at a supercritical state. Figure 5.14 compares experimental cases 4 and 8. Once again, there is a striking difference between the higher pressure of case 8 in comparison to case 4. The increased pressure results in higher density values for case 8. The same problem of underpredictions of the experimental results arising from the Raman scattering technique is observed in the comparison of the disintegrated core. The numerical predictions match the experimental data for the remaining jet evolution, starting at $x/d \approx 10$ until the end of the available experimental data at $x/d \approx 30$.

In case 8 a sloped core [45] is expected ($\Delta\dot{H}_{pb} = -51.88\,\mathrm{W}$), meaning that the jet needs to receive less energy in the injector to trigger the pseudo-phase transition in comparison to case 7 ($\Delta\dot{H}_{pb} = 448.72\,\mathrm{W}$). First, a small region of constant density is observed over a distance of two injector diameters, followed by a slight decrease in density until an x/d of 8. Second, a faster rate of density decay is observed for its experimental counterpart, owing to the thermal stratification resulting from heat exchange between the injector and gas-like nitrogen. Finally, the entrainment of chamber nitrogen into the jet is responsible for the sharper decrease in density after a distance of 10 injector diameters until the end of the domain, corresponding

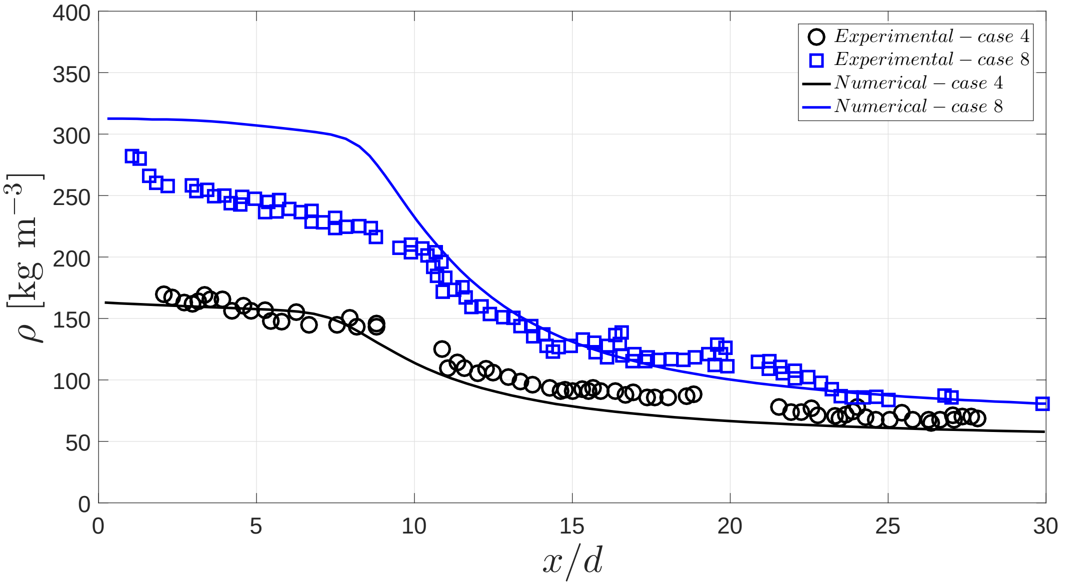

Figure 5.14: Axial density distributions for cases 4 and 8 with isothermal injector wall configurations.

to 30 diameters. Thus, while an over-prediction of the axial density values is observed, the proposed numerical solver can replicate the qualitative behavior of the jet, namely in terms of predicting different density rates of decay. Of all the considered experimental cases, case 8 is more susceptible to variations in the injection temperature due to its proximity to the peak in isobaric specific heat. Moreover, no other formulation was found in the literature against which the present computations could be compared.

The numerical results over-prediction in relation to the experiments observed in Figure 5.14 for case 8 until $x/d = 10$ could be related to the compressibility Widom line [77]. Similar to Soret and Dufour effects, compressibility effects [270] not encountered in low-pressure jets could lead to different coupling mechanisms in the Widom region. However, the inclusion of additional terms in the turbulence model is not a straightforward process [171], made more difficult due to the limited amount of experimental data.

5.4.3 Plateau Type Core

So far, two different configurations have been considered: the high pseudo-vaporization condition of cases 3 and 7, characterized by the appearance of a dense core, and the low pseudo-vaporization configuration of cases 4 and 8, corresponding to sloped cores [45], due to the thermal stratification occurring in the injector and leading to a decay in density at the beginning the chamber portion and the consequent formation o a subsided core. However, it may be the case such that the pseudo-vaporization power [45] may be intermediate between these two cases leading to the formation of a plateau type core as in cases 5, 6, 9, and 10.

Figure 5.15 depicts the obtained axial density evolution of cases 5 and 9, which have pseudo-vaporization powers of $103.59\,\text{W}$ for case 5 and $81.22\,\text{W}$ for case 9. Accordingly, the experimental data [59] indicates a similar jet development, with the formation of intermediate

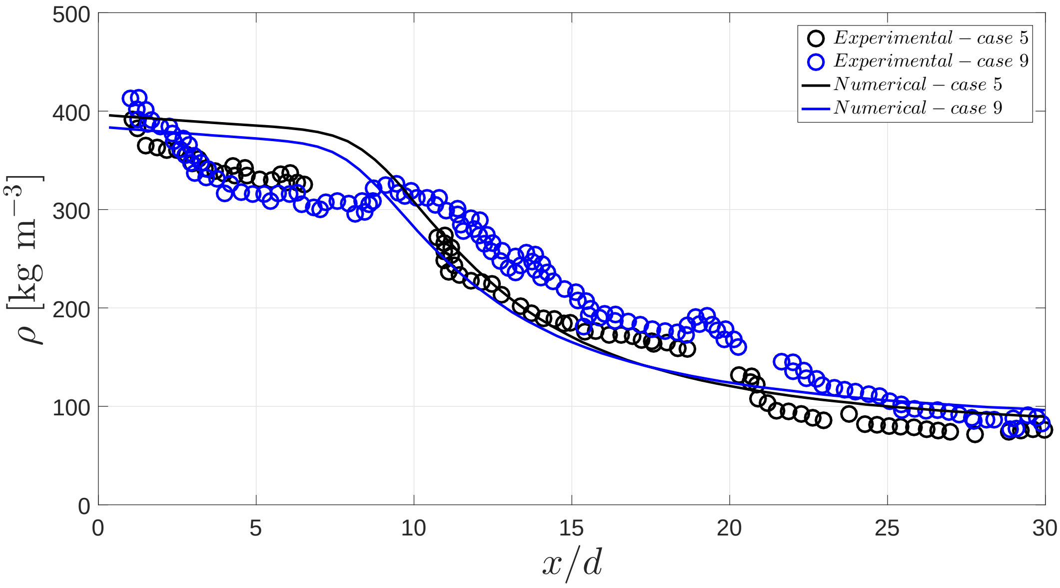

Figure 5.15: Axial density distribution comparison for cases 5 and 9.

plateaus. However, the numerical predictions cannot replicate the experimental plateau formation [59], instead of describing a behavior similar to the one encountered for low pseudo-vaporization power (cases 4 and 8 in Figure 5.14). Comparing these results with the compressible formulation of Gopal et al. [269] in Figure 5.16, where in addition to the experimental injection temperature of $135\,\mathrm{K}$, the authors considered another injection temperature of $142.5\,\mathrm{K}$, some more insights can be gathered. However, these do not consider the injector heat transfer, which leads to the appearance of dense potential cores, as indicated in the figure, extending up to a distance of 10 injector diameters downstream of the injector exit plane. Using an incompressible but variable density approach with an adiabatic injector configuration (not shown) was found to yield similar results to those of Gopal et al. [269] All in all, no definitive conclusion can be drawn about the numerical capture of the plateau. Moreover, employing an incompressible but variable density approach or a compressible formulation leads to a similar prediction.

Lastly, it remains to consider the intermediate pseudo-vaporization powers of cases 6 and 10, to the right of the peak in isobaric specific heat. These are depicted in Figure 5.17, where similar trends are encountered as those of Figure 5.15. Comparing the qualitative behavior of the numerical predictions and the experimental data, a low decay rate is present over 8 injector diameters. At this point, a portion of supercritical nitrogen starts to break from the jet, and chamber fluid entrains into it, increasing the axial decay of density for the remaining of the domain.

In a general way, it is possible to observe the formation of the experimental intermediate plateau at a distance between 5 and 10 injector diameters, a feature that the numerical solver cannot reproduce. The comparison of cases 6 and 10 in Figure 5.17 highlights a precise plateau formation in case 10. Of all the considered experimental cases, this is the one further away from the critical point. Consequently, the effects of pseudo-boiling are the weakest and

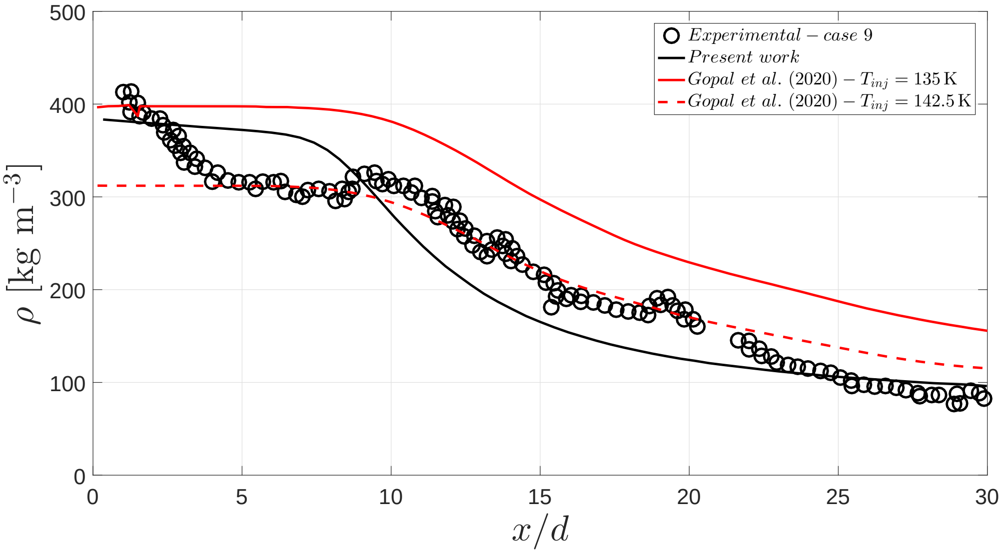

Figure 5.16: Comparison of the axial density distribution of case 9 with studies in the literature [269].

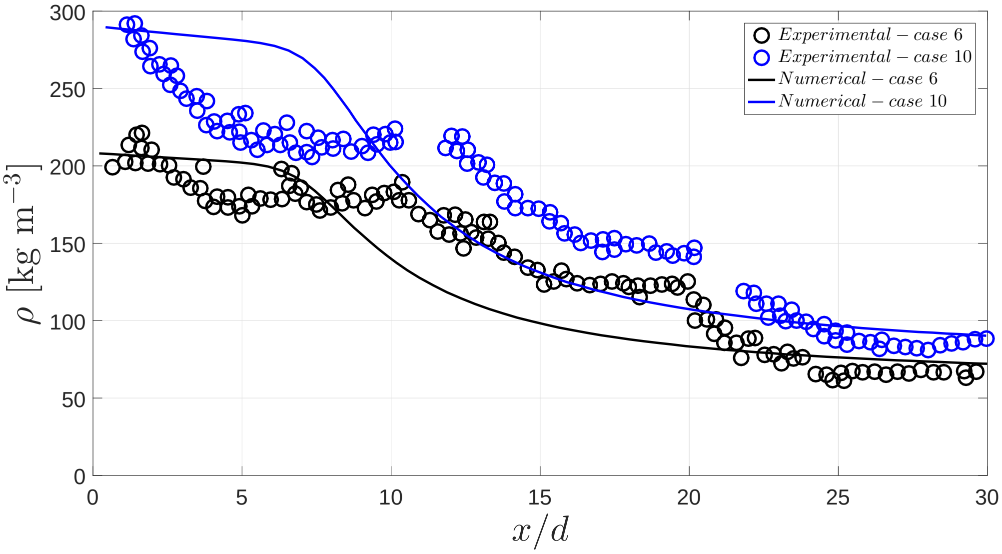

Figure 5.17: Axial density distribution comparison for cases 6 and 10.

where the most well-defined plateau is observed.

5.4.4 Turbulence Modeling

Figures 5.18 and 5.19 depict a comparison between several turbulence models described in Chapter 3 in the axial density decay of cases 3 and 4, respectively.

In Figure 5.18 is evident that except for the κ-ω model, all models predict similar lengths of the potential jet core, spanning from 6.4 to 7.6 injector diameters. Therefore, the κ-ω poor performance, which continues to be evident in Figure 5.19 for case 4, could be related to this model's poor performance at free stream conditions.

In the potential core, turbulence seems to have no impact on the jet development since the instabilities have not yet appeared and density remains constant. On the other hand, in the

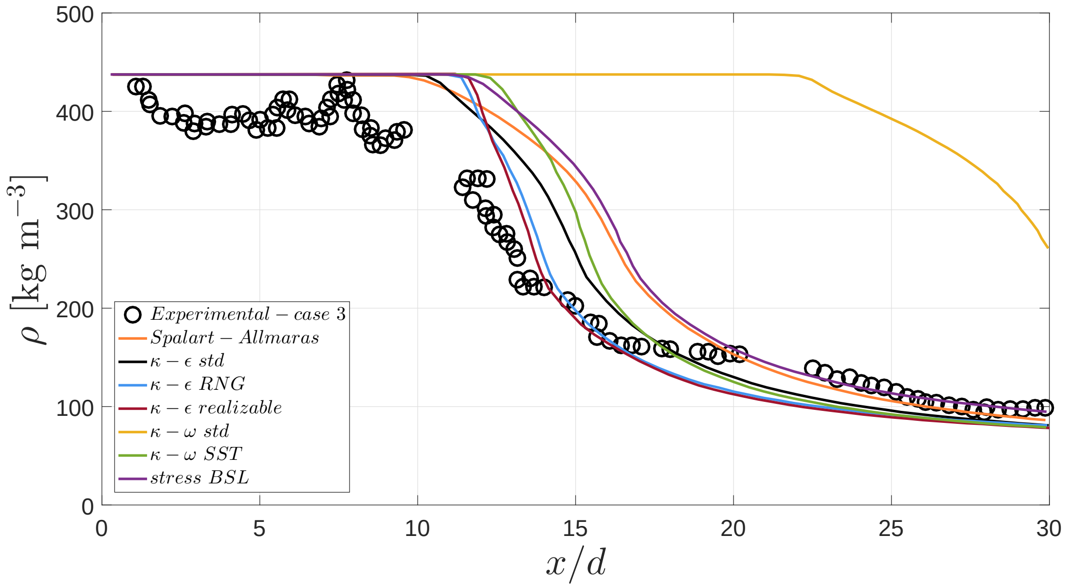

Figure 5.18: Axial density decay comparison between several turbulence models and comparison with experimental case 3.

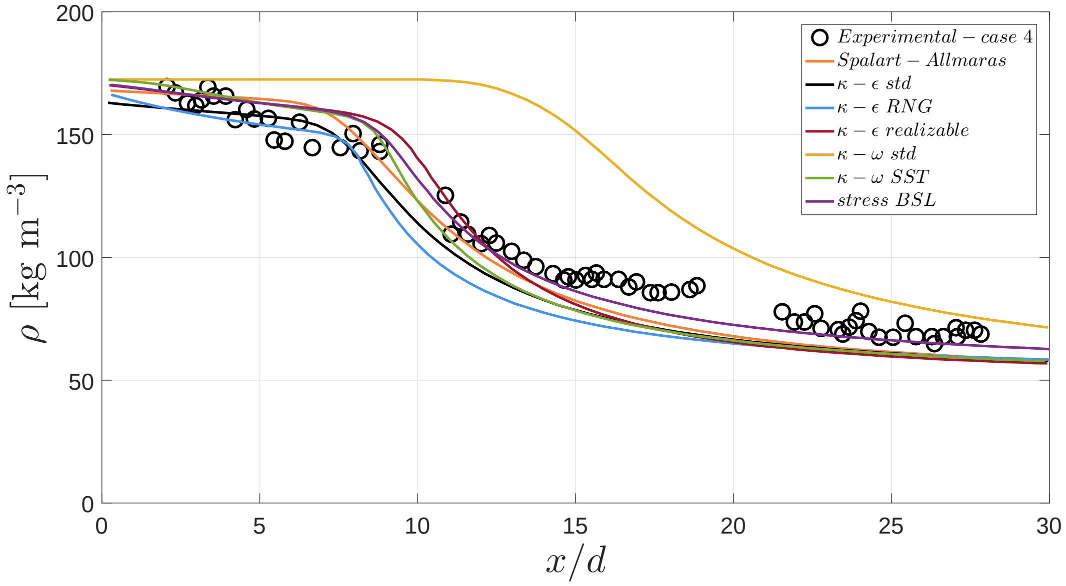

Figure 5.19: Axial density decay comparison between several turbulence models and comparison with experimental case 4.

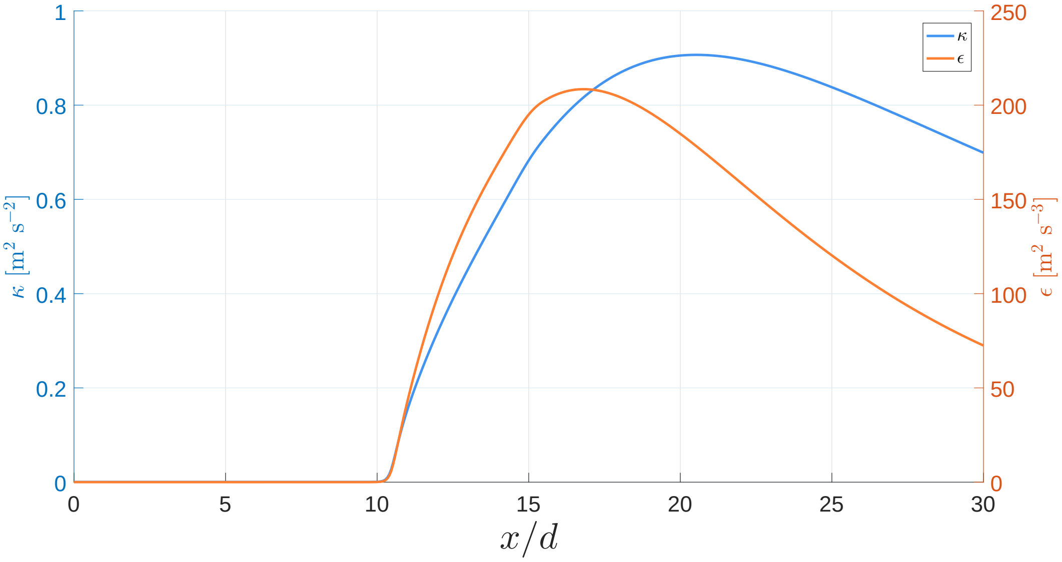

Figure 5.20: Turbulence kinetic energy and dissipation for case 3.

transition region, a maximum in density fluctuations is reported by Ries et al. [226], as a result of the availability of sufficient energy for nitrogen to cross the pseudo-boiling line. While the results do not directly show the increase in entropy production and a peak closer to the self-similar jet region as reported in Ries et al. [226] this can be indirectly assessed by looking into the turbulence kinetic energy and its dissipation rate. Figure 5.20 indicates how the dissipation rate (ε) reaches a peak in the transition region but begins to decrease as the fluid crosses the pseudo-boiling line, leading to a thermal expansion, responsible for the velocity variations observed through the increase in the turbulence kinetic energy (κ), an indication of intense turbulent mixing. As turbulence mixing grows, the models' prediction starts to diverge in the jet's transition region, owing to the energy dissipation and the decrease in the axial density. For example, the more complex κ-ω SST does not seem to lead to an improved description of the flow, which was to be expected since, as we move away from the wall, the model uses the κ-ε coefficients, evidenced by the proximity of the predictions to those of the standard κ-ε instead of the κ-ω. Furthermore, the five-equation stress BSL also overestimates the density decay between 7.5 and 20 injector diameters, probably due to its dependence on specific turbulence dissipation rate and its transport equation, being closer to the less complex, more computationally affordable Spalart-Allmaras.

In Figure 5.19 things change due to the thermal stratification taking place in the injector. No potential core is retrieved, and intense turbulent mixing plays a role. As the figure depicts, except for the standard κ-ω model, similar predictions are observed between the remaining turbulence models.

The turbulence choice model is based on this analysis, indicating no correlation between the turbulence model complexity and the quality of the results. Even though only cases 3 and 4 are here shown, a similar comparison was carried out for the remaining experimental conditions evidencing similar trends.

5.5 Summary

This chapter described the use of a RANS method to predict supercritical fluid behavior. Liquid- and gas-like injection conditions were analyzed, accounting for adiabatic and isothermal injector wall BCs. Both the injector and combustion chamber were considered in the computational domain.

The accurate description of supercritical fluid behavior relies on mechanical and thermal breakup mechanisms. Dense potential cores are retrieved for high pseudo-vaporization powers, whereas sloped cores provide more substantial evidence of the thermal breakup under gas-like conditions. Therefore, the concept of thermal breakup proposed in the literature is of central importance, and through it insights into the behavior of supercritical jets were achieved. As a result, the plug-flow profiles that are sometimes considered provide a false representation of the flow physics, as shown in the density contours at the chamber entrance.

In the case of high pseudo-vaporization powers, leading to the formation of dense potential cores, a higher level of agreement with the experiments is reached, highlighting the proposed solver's ability to replicate the jet's mean axial density distribution. On the other hand, in the case of the lowest pseudo-vaporization power, a qualitative agreement is found between experiments and numerical predictions. Lastly, for intermediate pseudo-vaporization powers characterized by an intermediate plateau formation, it was impossible to retrieve its formation, obtaining a similar axial density evolution instead as the one observed in the sloped core cases. Further work will be conducted towards replicating the plateau formation since it is currently absent from the literature.

The results suggest that the liquid-like configurations are similar in jet stabilization. However, the isothermal injector contributes to a more prolonged stabilization of the potential core.

Chapter 6

Extension to the Transcritical Regime

The injection of nitrogen under transcritical conditions, where the injection temperature is below nitrogen's critical point, but the pressure is above it, is considered in this chapter. The axial density decay is evaluated along with the jet spreading rate. Finally, a hypothesis for the appearance of the transitional regime identified in the previous chapter is formulated.

6.1 The Nature of Transcritical Flows

While the distinction between liquid and transcritical states is not based on any physical arguments [70], the term transcritical is here used when referring to a fluid with a temperature below the critical point condition and pressure above it, leaving the moniker subcritical reserved for the description of fluid with pressure and temperature bellow critical point values. As such, this is simply a matter of convenience.

The interest in studying transcritical injection into a supercritical quiescent environment is twofold. First, transition across the critical temperature from transcritical to supercritical conditions can take place in the LRE ignition sequence or the ignition of upper stages in space [57]. Additionally, in multi-species coaxial injection where the critical point assumes a dynamic nature, distinct transitions across the critical point or the pseudo-critical point can take place [126], local transcritical behavior can take place in the highly-couple phenomena combination in rocket combustors. One of the earliest attempts to study transcritical injection was conducted by Newman and Brzustowksi [134], who, through shadowgraph technique, studied the injection of CO_2 into mixtures of CO_2 and N_2.

Figure 6.1 depicts shadowgraph images of N_2 injected into N_2 (the first three columns) and a mixture of N_2–He (last column). From left to right nitrogen is injected into subcritical nitrogen ($p_r = 0.83$) and supercritical nitrogen ($p_r = 1.03$ and $p_r = 2.03$). The last column of Figure 6.1 represents the injection of nitrogen into a mixture of nitrogen and helium. From subcritical conditions ($p_r = 0.83$), it is possible to observe the liquid column with a clearly defined interface downstream from the injector exit plane, which is no longer the case in supercritical injection ($p_r = 1.03$ and $p_r = 2.03$), where no clear interface is discernible, and a diffusive mixing is observed. In the last column of Figure 6.1 for the multi-species mixing, a distinct interface is observed for a few millimeters, from where the nitrogen-helium in the chamber starts to entrain the jet and pockets of fluid break from the jet due to a combination of lack of capillary instabilities owing to the surface tension [221] and due to Kelvin-Helmholtz instabilities owing to diffusive mixing.

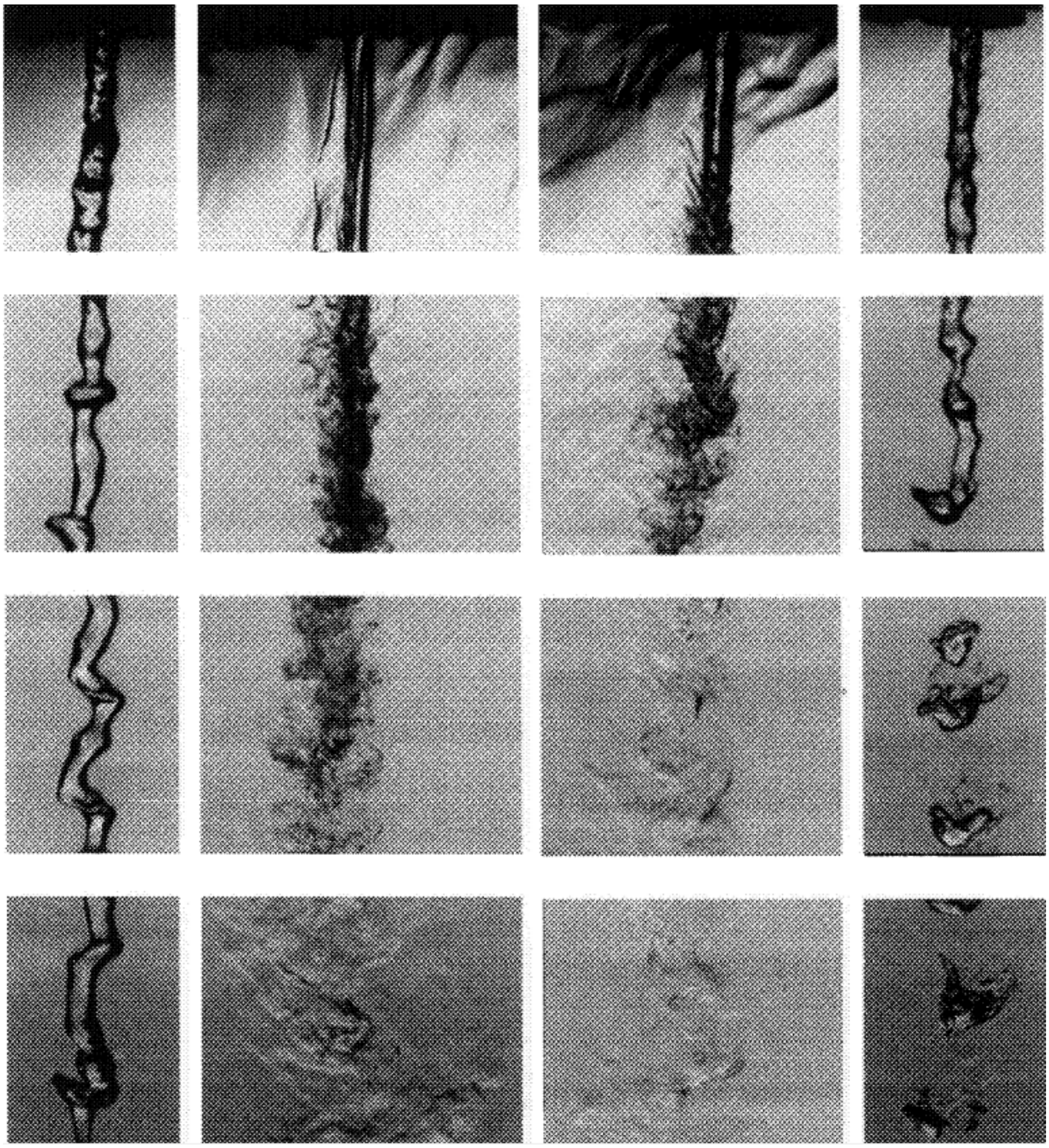

Figure 6.1: Shadowgraph images of liquid nitrogen jets issuing into a pressurized chamber [83]. From left to right: $p_r = 0.83$, $p_r = 1.03$, $p_r = 2.03$, nitrogen/helium. From top to bottom (positions downstream of the injector): 0 to $1.9\,\mathrm{mm}$, 7.4 to $9.5\,\mathrm{mm}$, 15 to $17.1\,\mathrm{mm}$, 22.6 to $24.7\,\mathrm{mm}$.

Interestingly, no droplets and ligaments are observed, and transition cannot be easily predicted since the critical points of the species in the mixture cannot be used directly [224]. Additional experiments conducted by Segal and Polikhov [56] corroborate the decreased importance of surface tension at transcritical conditions and jet breakup in the form of detached finger-like structures. As described by Oschwald and Schik [35], the importance of surface tension lies in the fact that in rocket combustors, there is no thermal equilibrium, and surface tension varies locally, as does the mixture critical point. Given the highly coupled phenomena, traditional experimental techniques experience difficulties in reporting the characteristic of dense sprays due to the variable density conditions, which make it difficult to distinguish between liquid and gas [271]. Poblador-Ibanez et al. [271] study laminar mixing between liquid and gas phases before instabilities growth, attempting to describe high-pressure atomization.

The question then becomes how to model the behavior of fluids under the influence of such highly coupled phenomena. Recent extensive review on transcritical flows were put together by Jofre and Urzay [57] and Ries and Sadiki [14]. Concepts such as partial-mass and partial-density were proposed [218] to be used as a means to treat a fluid flow over the relevant thermodynamic states. Oefelein et al. [272] attempted quantify, through LES the effects of real-fluid thermodynamics for conditions characteristic of diesel engines, while Yi et al. [273] studied the transcritical n-dodecane-nitrogen of relevance in internal combustion engines, focusing on the two-phase flow interaction in subcritical and transcritical injection conditions. Moreover, Sierra-Pallares et al. [274] analyzed nitrogen mixing layers at transcritical and supercritical conditions through RANS, following a mixture fraction formulation. On the other hand, DNS studies [149] aim to provide insights into the fundamentals of transcritical mixing, showing, for instance, that transcritical jets exhibit distinct behaviors at small and large scales due to the high-density stratification present in transcritical flows [79].

6.2 The Experiment

The experimental conditions of Oschwald and Schik [35], detailing the injection of nitrogen at transcritical and supercritical conditions into a chamber filled with nitrogen, are considered according to the conditions at injection and in the chamber given in Table 6.1. The experimental data was obtained through the use of Raman scattering, divided between supercritical and transcritical conditions for pressure levels of 4 and $6\,\mathrm{MPa}$ in the chamber, as depicted in Figure 6.2.

Table 6.1: Experimental test matrix, from Oschwald and Schik [35]

case	p_∞ [MPa]	v_{inj} [$\mathrm{m\,s^{-1}}$]	T_{inj} [K]	T_∞ [K]	ρ_{inj} [$\mathrm{kg\,m^{-3}}$]	ρ_∞ [$\mathrm{kg\,m^{-3}}$]
A4	4.0	5.0	140	298	150.06	45.39
B4	4.0	5.0	118	298	583.02	45.39
C4	4.0	20.0	100	298	706.82	45.39
A6	6.0	5.0	140	298	338.13	68.03
B6	6.0	5.0	118	298	608.94	68.03
C6	6.0	20.0	100	298	716.43	68.03

The velocity at injection, v_{inj}, varies from $5\,\mathrm{m\,s^{-1}}$, for cases A and B to $20\,\mathrm{m\,s^{-1}}$ in cases C. This variable is calculated from the measured mass flux. On the other hand, the injection temperatures (T_{inj}) are taken as $140\,\mathrm{K}$ for cases A4 and A6, well above the critical temperature of nitrogen ($126.2\,\mathrm{K}$), while for cases B4 and B6 an injection temperature of $118\,\mathrm{K}$ characterize the transcritical jet behavior. In contrast, an even lower temperature of $100\,\mathrm{K}$ is taken for transcritical jet cases C4 and C6. The temperature inside the chamber is kept constant at $298\,\mathrm{K}$ through the use of electrical heating [35]. Increasing the pressure in the flow channel from 4 to $6\,\mathrm{MPa}$ increases the density of the reservoir gas and, at the same time, significantly alters the thermodynamic behavior of the cryogenic nitrogen.

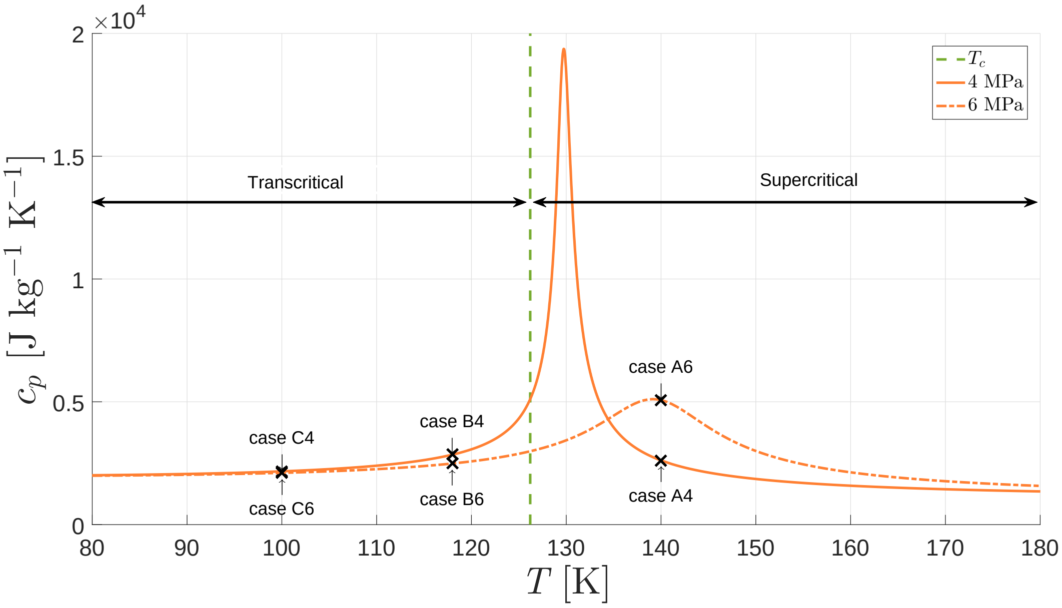

Figure 6.2: Location of the experimental test cases in relation to the critical point of nitrogen.

In Table 6.2 reduced values of pressure, evaluated concerning the pressure in the chamber, and temperature at injection, as well as the ratio between density at injection and in the chamber, are presented. While this allows to single out the position of each case with the conditions at the critical point of nitrogen, it also shows that injection conditions are dominant and will determine jet behavior.

Table 6.2: Non-dimensional evaluations [35].

case	p_∞/p_c	T_{inj}/T_c	ρ_{inj}/ρ_∞
A4	1.17	1.11	3.34
B4	1.17	0.94	12.5
C4	1.17	0.79	15.7
A6	1.76	1.11	5.01
B6	1.76	0.84	8.99
C6	1.76	0.79	10.6

The experimental setup is represented in Figure 6.3. The injector and chamber have diameters of $1.9\,\mathrm{mm}$ and $100\,\mathrm{mm}$, respectively. While the chamber has a total length of $1\,\mathrm{m}$, only $250\,\mathrm{mm}$ are considered in order to decrease the computational cost while ensuring the domain is large enough so that the outlet conditions do not affect the region of interest. Lastly, the length of the injector is considered to be $90\,\mathrm{mm}$.

Velocities and temperatures are imposed at the inlet, according to Table 6.1, with a gauge pressure of $0\,\mathrm{MPa}$ imposed at the outlet. In addition, isothermal wall boundary conditions are applied to the injector and chamber walls, with an adiabatic condition used for the chamber faceplate.

A summary of the thermophysical models used in the calculations presented in this chapter

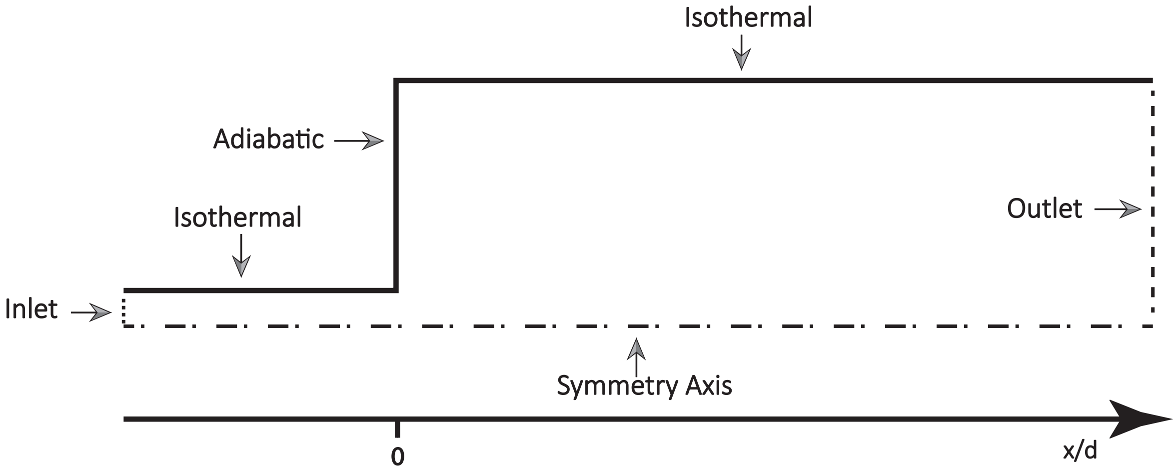

Figure 6.3: Boundary Conditions corresponding to the experimental conditions Oschwald and Schik [35].

is given in Table 6.3.

Table 6.3: Summary of thermophysical models.

Turbulence closure	EoS	Transport properties
κ–ε standard [175]	PR [184]	Lemmon and Jacobsen [214]

6.3 Validation

As depicted in Figures 6.4 and 6.5 three different mesh refinement levels were studied to ensure the grid resolution did not influence the results. A coarse mesh with $182\,988$ points, an intermediate one with $252\,459$ and a refined mesh with $480\,537$ are considered. Since no variation is observed between the slopes of the three configurations, grid independence is achieved for the intermediate mesh. Given that the standard $\kappa - \varepsilon$ turbulence model was used in the computations, wall functions were used to make the link between the viscosity affected region and the fully turbulent one. In this way a y^+ value of 11.63 is considered in the cells adjacent to the walls.

The non-dimensional density distribution is presented as the ratio between the difference of the density distribution to the density in the chamber, in relation to the conditions between injection and chamber. This ratio is defined in the present work as ρ^*, represented in equation 6.1. The axial density, measured from the injector's exit plane, x, is divided by its diameter, d.

Figure 6.6 details the decrease in the relative error as the grid is progressively refined as a function of the GCI, for the grid independence studies of cases A4 and B4 depicted in Figures 6.4 and 6.5, respectively.

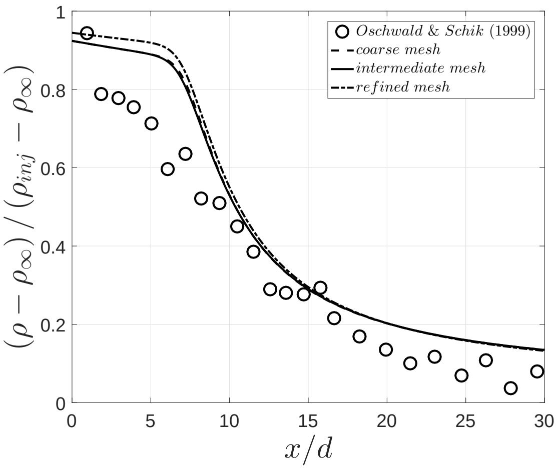

Figure 6.4: Grid independence study for supercritical case A4.

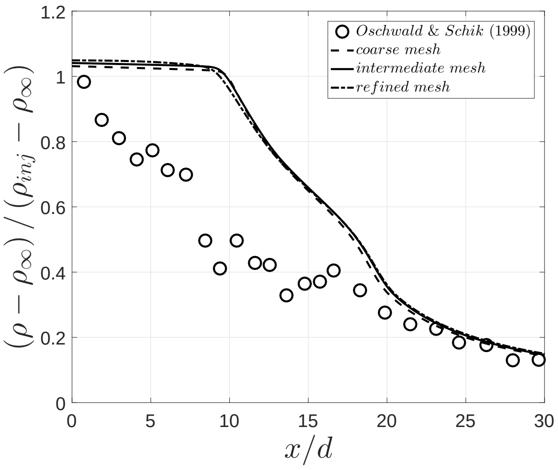

Figure 6.5: Grid independence study for transcritical case B4.

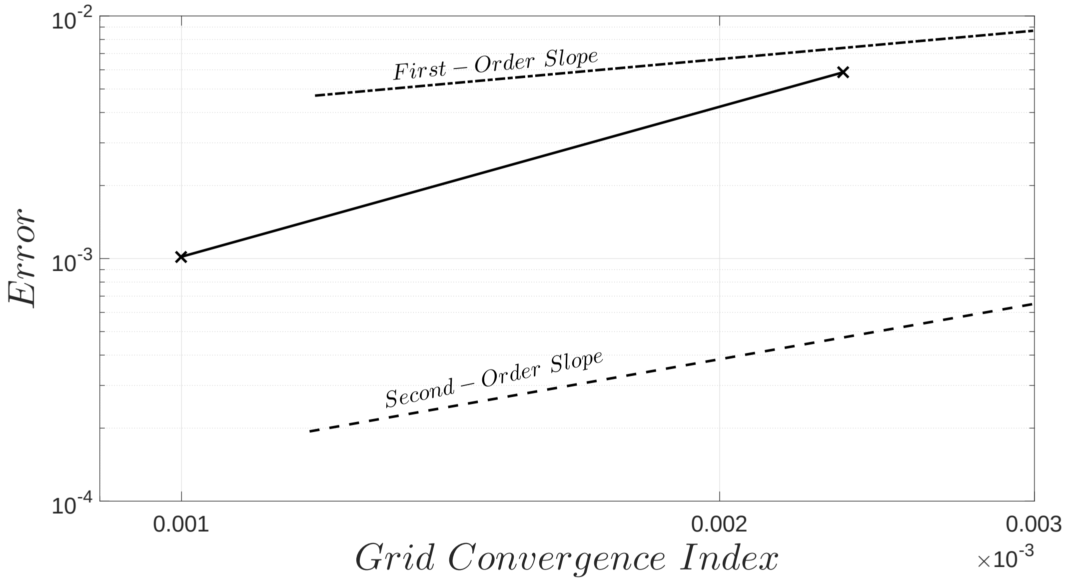

Figure 6.6: Comparison of grid independence study with Richardson's interpolation.

6.4 Results

Figure 6.7 depicts the comparison between the computations and the experimental data [35]. In the top figure, the non-dimensional axial density decay (ρ^*) of nitrogen is represented, defined according to equation (6.1). The middle figure represents the FWHM of density, which measures the jet spreading rate. Since the shear layer's edge is difficult to obtain from Raman scattering [143], the FWHM is calculated instead. Lastly, the bottom figure represents the shape parameter, n_ρ for density, evaluated from equation (6.2) [275], giving a measure of the axial density shape profile. Axial density, FWHM of density, and shape parameter are evaluated as a function of the non-dimensional distance from the injector exit plane, x/d. In (6.2), the n describes the dependence with the radial velocity component, while r_m is the radial position at which the profile reaches its half-value.

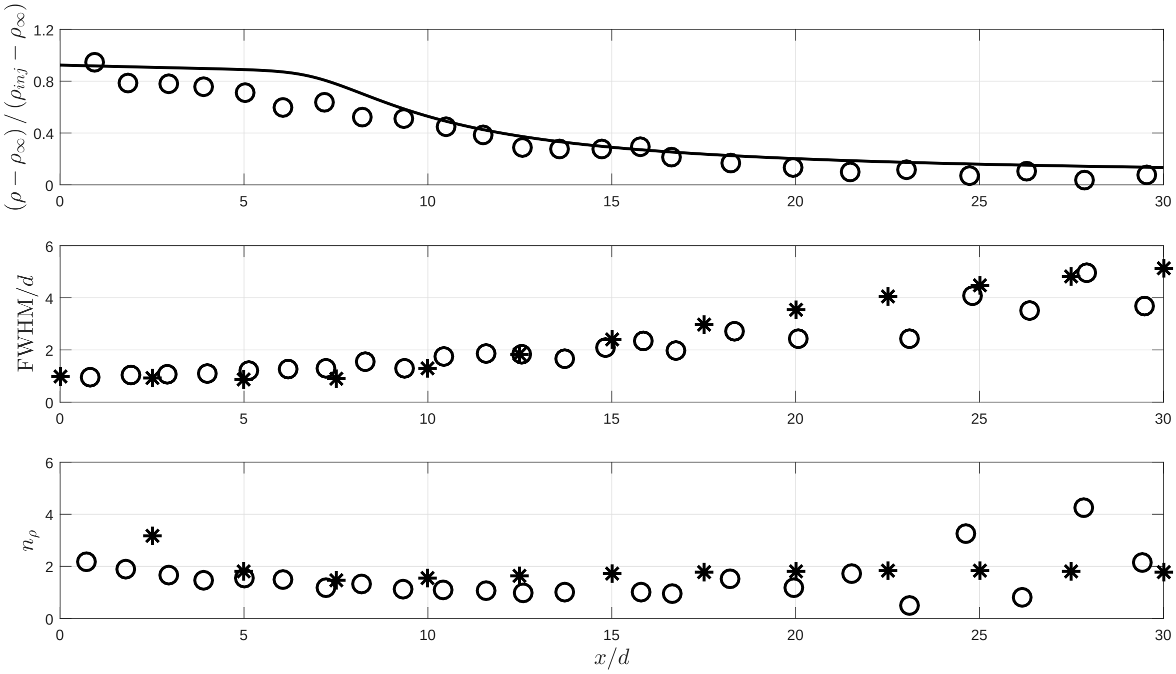

Figure 6.7: Comparison between numerical results and experimental results for case A4 (top: axial density distribution; middle: FWHM of density; bottom: shape parameter). Lines and star symbols correspond to numerical results, while open circles represent experimental data [35].

$$\rho^* = \frac{\rho - \rho_\infty}{\rho_{inj} - \rho_\infty} \quad (6.1)$$

$$f\left(\frac{r}{r_m}\right) = \tanh^2\left[0.881\left(\frac{r}{r_m}\right)^n\right] \quad (6.2)$$

Furthermore, Oschwald and Schik [35] use the NIST [137] database to convert the density profiles into temperature ones, which can be achieved, for instance, through Figure 2.5. Accordingly, Figure 6.8, depicts the axial temperature decay, FWHM of temperature and the temperature shape parameter, being the non-dimensional temperature (T^*) defined following equation (6.3).

$$T^* = \frac{T - T_\infty}{T_{inj} - T_\infty} \quad (6.3)$$

The case depicted in Figures 6.7 and 6.8 is located in the gas-like supercritical regime (Figure 6.2), after the crossing of the Widom line, for which a subsided core [45] can be observed until an $x/d \approx 7$. The decay rate until this point is slower than that of the experimental data.

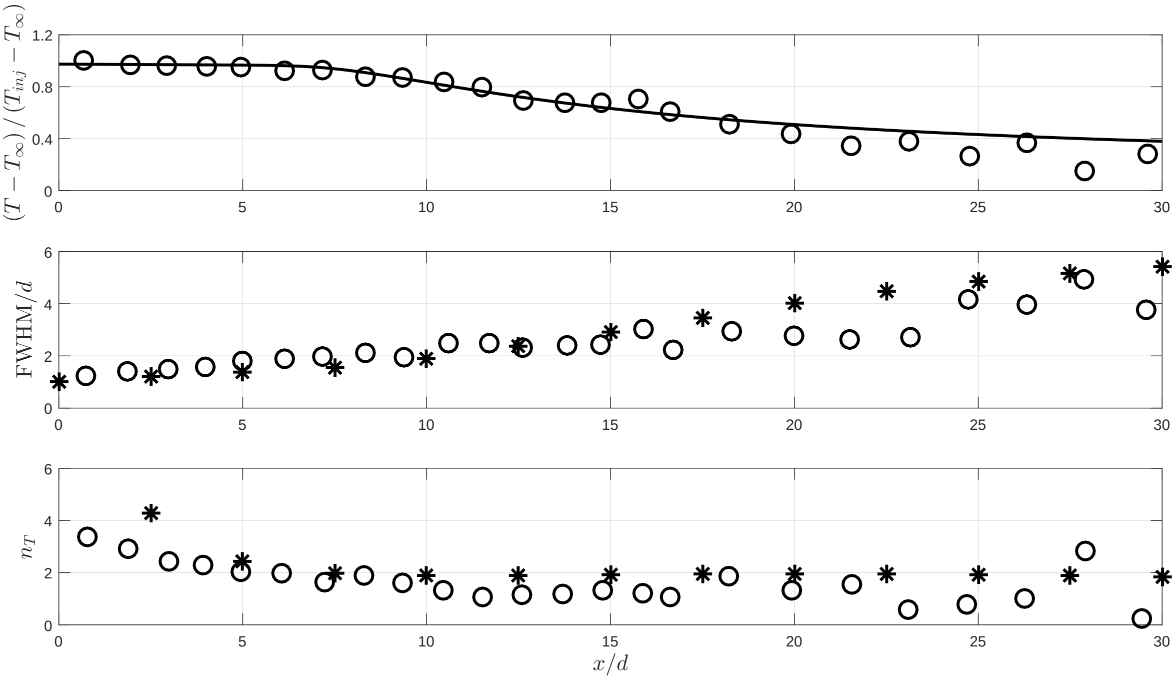

Figure 6.8: Comparison between numerical results and experimental results for case A4 (top: axial temperature distribution; middle: FWHM of temperature; bottom: shape parameter). Lines and star symbols correspond to numerical results, while open circles represent experimental data [35].

After $x/d \approx 7$, a closer agreement with the experimental data can be observed, where the jet evolution starts to be dominated by the conditions inside the chamber. This behavior is to be expected since no dense potential core is formed. On the other hand, gas-like conditions are connected to lower energy required to increase the temperature of the system (Figure 6.8) when compared to liquid-like supercritical conditions, where the effect of pseudo-boiling would need to be overcome.

Looking at the axial temperature distribution, it is possible to observe a similar trend as the one found for the axial density distribution. A low rate of temperature decay is seen until $x/d \approx 7$, after which it starts to increase up to $x/d \approx 18$. After this point, a higher temperature value is retrieved concerning the one obtained by Oschwald and Schik [35].

Increasing the pressure from the $4\,\mathrm{MPa}$ of case A4 to $6\,\mathrm{MPa}$, we obtain the axial density and temperature distributions for case A6 in Figures 6.9 and 6.10. The pressure increase from 4 to $6\,\mathrm{MPa}$ leads to a higher density of the nitrogen jet in the combustion chamber as expected since the ratio ρ_{inj}/ρ_∞ has increased from 3.34 in case A4 to 5.01 in case A6. This is reflected in the length of the subsided core, seen until $x/d \approx 8$. After this point, low-density nitrogen from the chamber entrains the jet, and a similar agreement between numerical and experimental results is observed as the one registered for case A4.

Worthy of note is also the fact that case A6 is located very close to the peak in isobaric specific heat (Figure 6.2), which according to the analysis carried out in Chapter 5 would correspond to the appearance of a plateau type core. However, since a slopped core is depicted, it is not

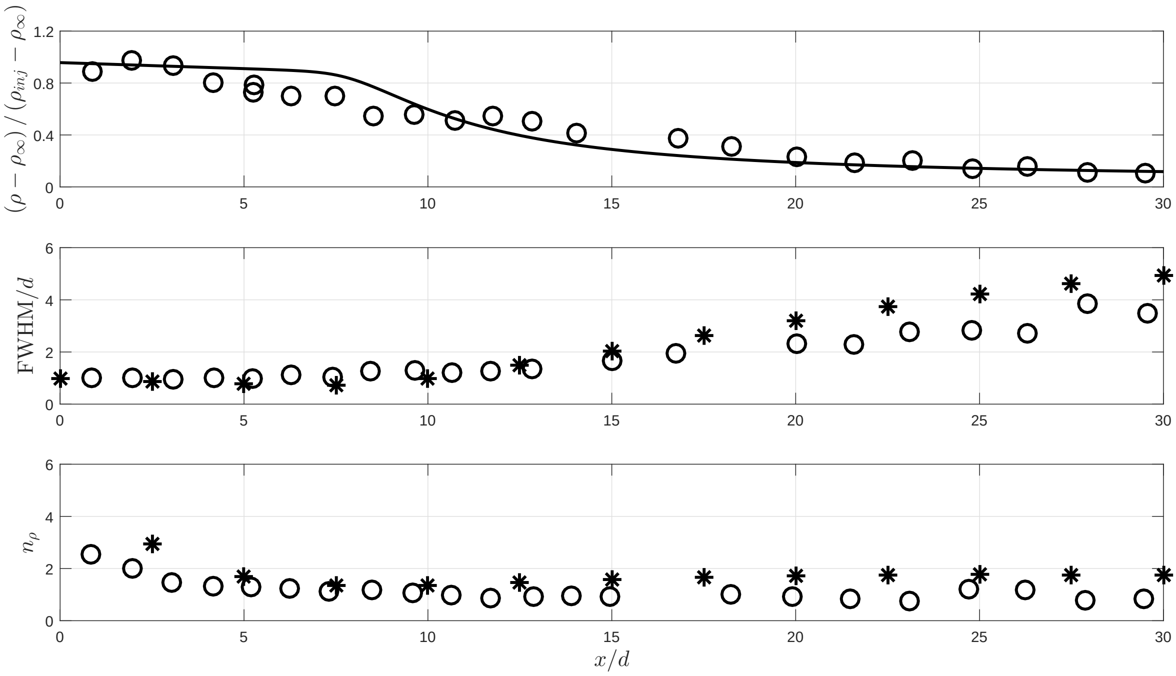

Figure 6.9: Comparison between numerical results and experimental results for case A6 (top: axial density distribution; middle: FWHM of density; bottom: shape parameter). Lines and star symbols correspond to numerical results, while open circles represent experimental data [35].

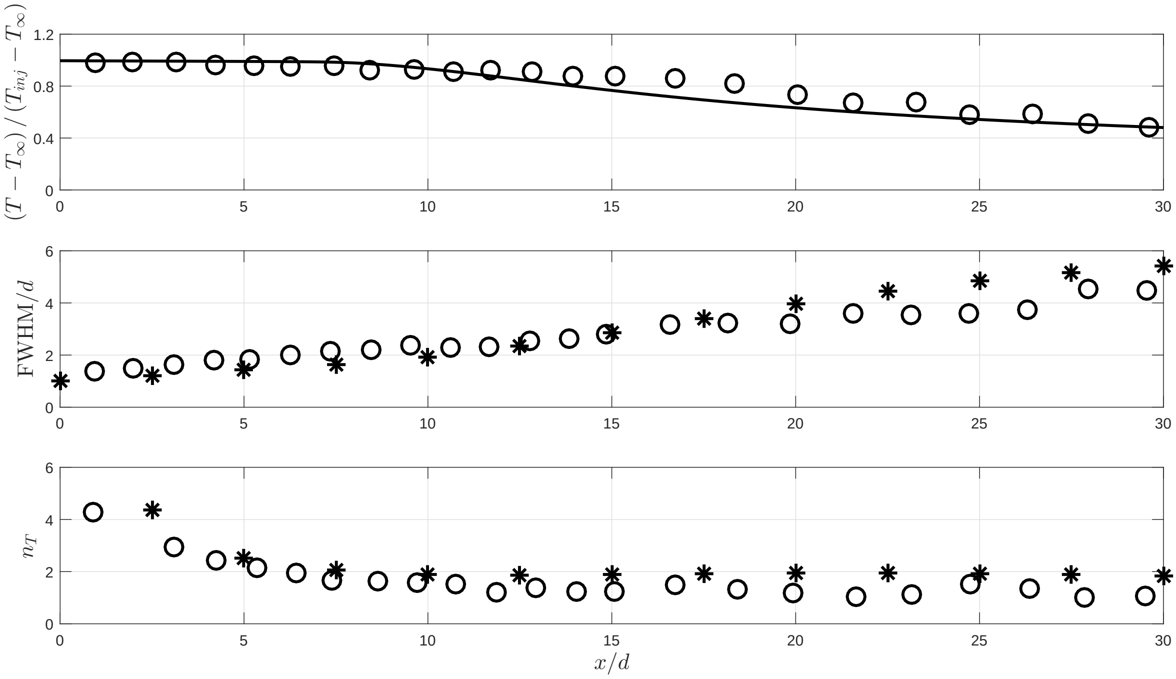

Figure 6.10: Comparison between numerical results and experimental results for case A6 (top: axial temperature distribution; middle: FWHM of temperature; bottom: shape parameter). Lines and star symbols correspond to numerical results, while open circles represent experimental data [35].

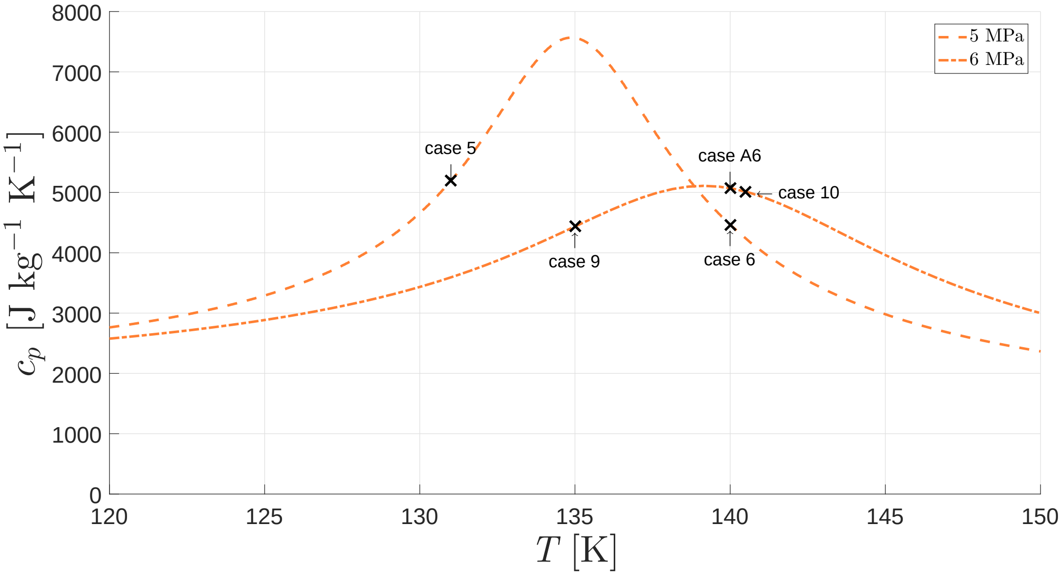

Figure 6.11: Location of several experimental test cases in relation to the peak in isobaric specific heat. Cases 5, 6, 9 and 10 from Mayer et al. [59] and case A6 from Oschwald and Schik [35].

the case. For convenience, the position of case A6 concerning the peak in isobaric specific heat is reminded in Figure 6.11, alongside cases 5, 6, 9, and 10 from Mayer et al. [59], while experimental chamber and injection conditions are compared in Table 6.4. Here is evident that chamber pressure conditions and the measured injection temperatures are comparable between the different cases. However, the injection velocities are not.

In comparison to Mayer et al. [59] cases, in A6 [35], the injection velocity is more than twice that of the other cases, which can be the responsible for the formation of a subsided core instead of a plateau type core. It is therefore hypothesized that in proximity to the maxima in isobaric specific heat, the nitrogen jet is more easily entrained by the chamber fluid in the cases of lower injection velocities, leading to the formation of intermediate regions of constant density until entrainment is so vigorous that the core breaks down completely. Here more experimental data would be needed to validate the proposed hypothesis and unravel the limits in which each of the core types is formed.

Table 6.4: Location of several experimental test cases in relation to the peak in isobaric specific heat. Cases 5, 6, 9 and 10 from Mayer et al. [59] and case A6 from Oschwald and Schik [35].

Case	Calculated Velocity [$\mathrm{m\,s^{-1}}$]	Measured Chamber Pressure [MPa]	Measured Temperature [K]
5	2.0	4.90	131.0
6	1.9	4.90	140.0
9	2.0	5.85	135.0
10	1.9	5.88	140.5
A6	5.0	6.00	140.0

Considering both cases A4 (4 MPa) and A6 (6 MPa) and the axial density results of Figures 6.7 and 6.9 it can be concluded that they are very similar in nature, albeit with different density values. The density fields of cases A4 and A6 are compared in Figure 6.12, where the differences in density are highlighted. Normalized axial, x, and radial, r, distances are divided by the injector diameter, with the origin set at the injector exit plane. Through the analysis of both fields, it can be seen that inside the injector $-15 < x/d < 0$, the heat transfer between the injector walls and the cryogenic nitrogen jet, alters the field at the jet centerline, leading to the appearance of the disintegrated core observed in the results.

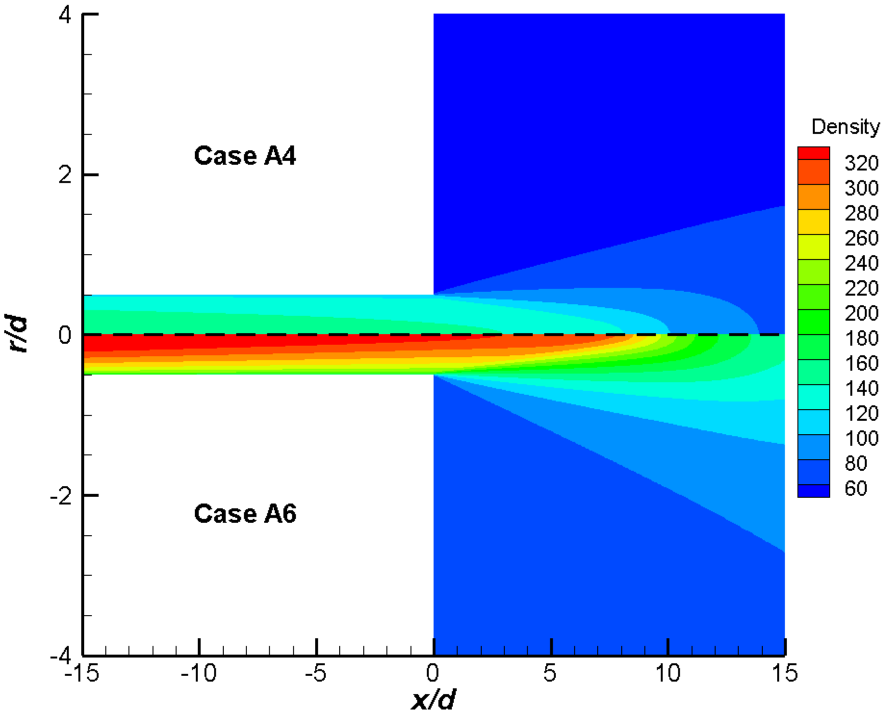

Figure 6.12: Comparison of density field between cases A4 and A6.

Figures 6.13 and 6.14 depict the obtained axial density and temperature-related parameters at the jet centerline in the combustion chamber for the experimental transcritical case B4. Large fluctuations of the experimental curve can be observed with changes in the second derivative and a rapid increase of about 25 % at about $x/d = 10$. At this point, the rate of decrease of the density is much faster until $x/d \approx 13$, where it increases even further approaching the experimental data. In terms of temperature, a closer agreement is observed with the experimental data due to the lower gradients in relation to density.

In the first section (until $x/d \approx 9.8$), the transcritical jet evolves until the critical value of temperature is reached (the critical temperature corresponds to a value of ρ^* of 0.9544), whose rate of decay is not retrieved from the current modeling approach. After the critical point is surpassed, the liquid-like supercritical nitrogen will initially be unaffected by the conditions in the chamber. After that, however, the large density gradients (ρ_{inj}/ρ_∞ = 12.5) start to have a preponderant role ($x/d \approx 18$), causing pockets of fluid to break due to the entrainment of fluid from the chamber.

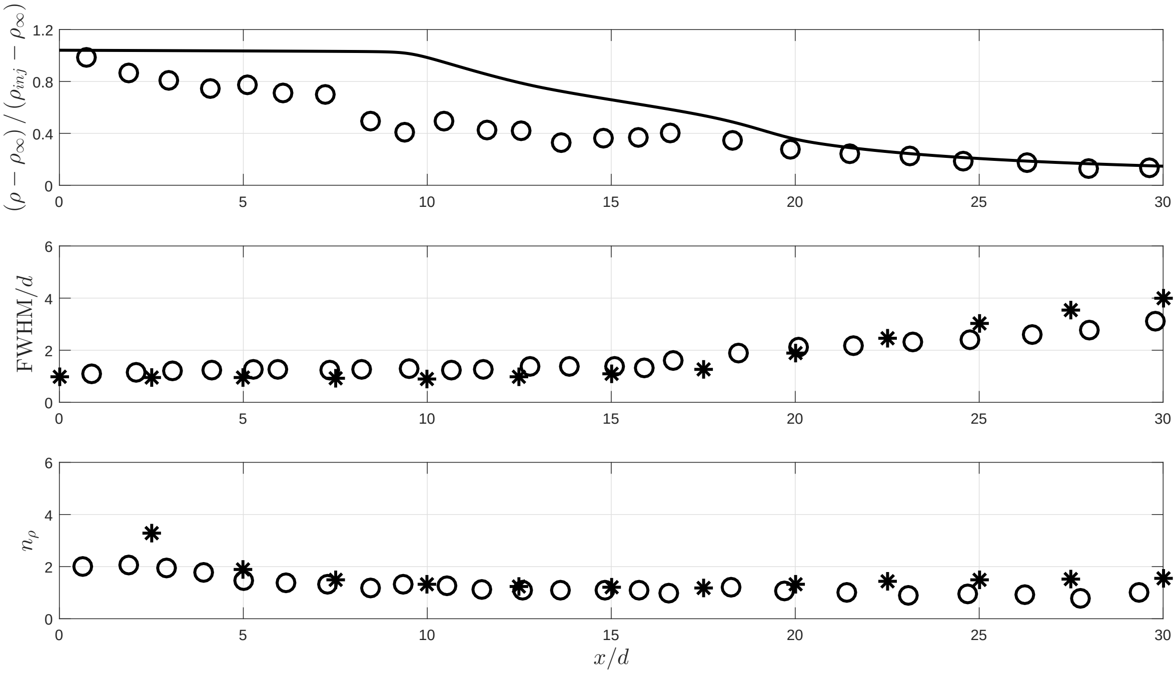

Figure 6.13: Comparison between numerical results and experimental results for case B4 (top: axial density distribution; middle: FWHM of density; bottom: shape parameter). Lines and star symbols correspond to numerical results, while open circles represent experimental data [35].

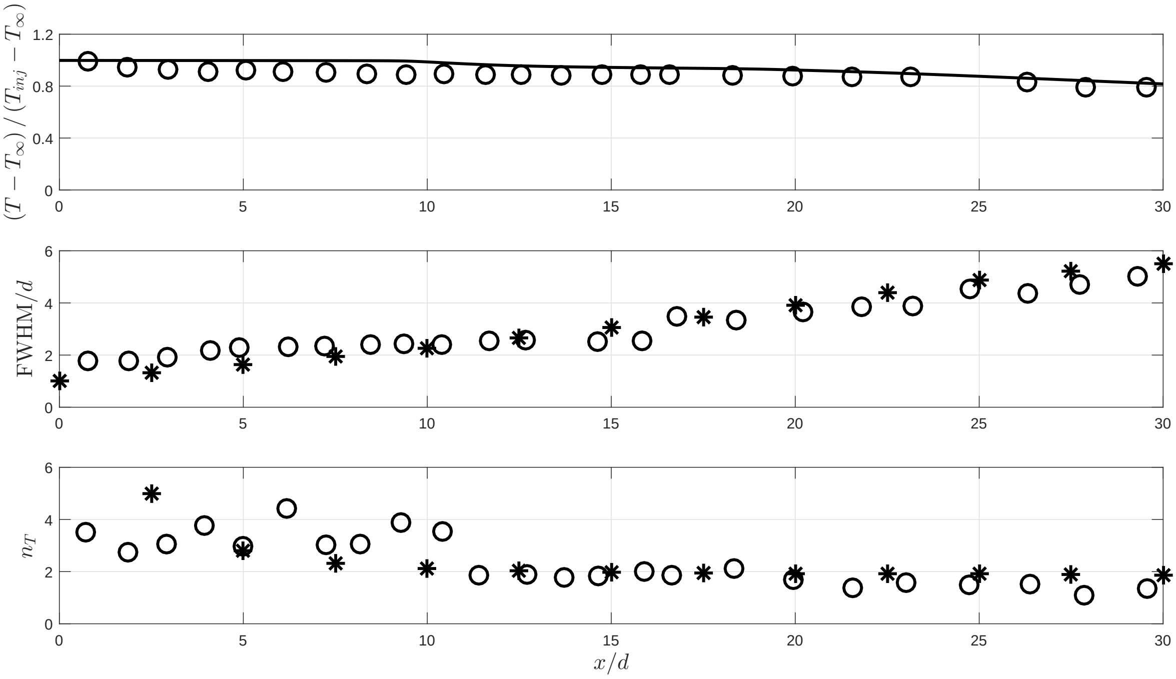

Figure 6.14: Comparison between numerical results and experimental results for case B4 (top: axial temperature distribution; middle: FWHM of temperature; bottom: shape parameter). Lines and star symbols correspond to numerical results, while open circles represent experimental data [35].

Progressively increasing the computational injection temperature of case B4 from the experimental value of $118\,\mathrm{K}$, to $125\,\mathrm{K}$ and $128\,\mathrm{K}$ several different features can be observed in Figure 6.15. In reduced temperature these injection conditions are evaluated from Table 6.5.

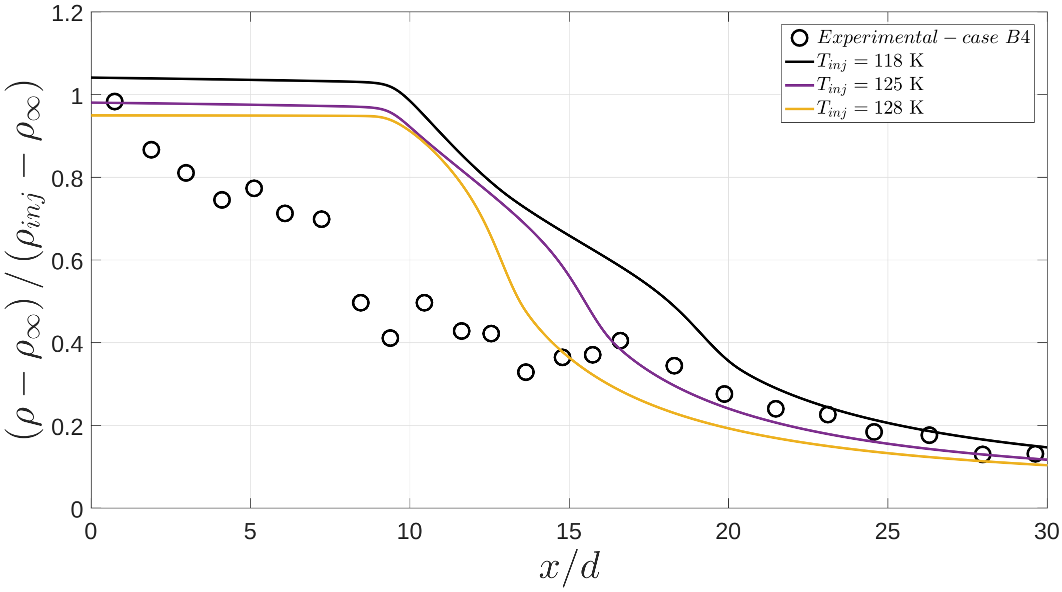

Figure 6.15: Axial density distribution for case B4.

Approaching the critical temperature, we can observe, by taking into account injection temperatures of $118\,\mathrm{K}$ and $125\,\mathrm{K}$, density's rate of decay decreases even further for the first section ($x/d \approx 9.8$) for both conditions, while in the $125\,\mathrm{K}$ jet after the critical temperature is crossed, the pockets of liquid-like nitrogen start to break from the jet sooner ($x/d \approx 14$) than for the $118\,\mathrm{K}$ one at $x/d \approx 18$. On the other hand, by considering the injection to take place under supercritical conditions (T_{inj}=$128\,\mathrm{K}$), it is possible to observe the characteristic feature of a mixture under liquid-like conditions, with the formation of a dense potential core replacing the slow rate of decay of the axial density until $x/d \approx 9.8$, registered for the transcritical injection conditions. The core formation is related to the effect of pseudo-boiling and the eventual transition across the Widom line into supercritical gas-like conditions.

Table 6.5: Reduced temperature corresponding to the selected injection temperatures for case B4.

T_{inj} [K]	T_r
118	0.94
125	0.99
128	1.01

By considering the experimental results for the axial density decay rate of case B6 in Figure 6.16 and temperature evolution in Figure 6.17, several differences are observed concerning case B4. In the first instance, the high-density values (ρ_{inj}/ρ_∞=8.99) lead to the same mismatch between the experiments and the numerical results. As for case B4, a slower decay of the density at the jet centerline, compared to the experimental data, is observed until $x/d \approx 8$. However, after this point, the critical temperature is crossed, where the jet enters a supercritical liquid-like regime, and the density starts to decrease due to the influence of the

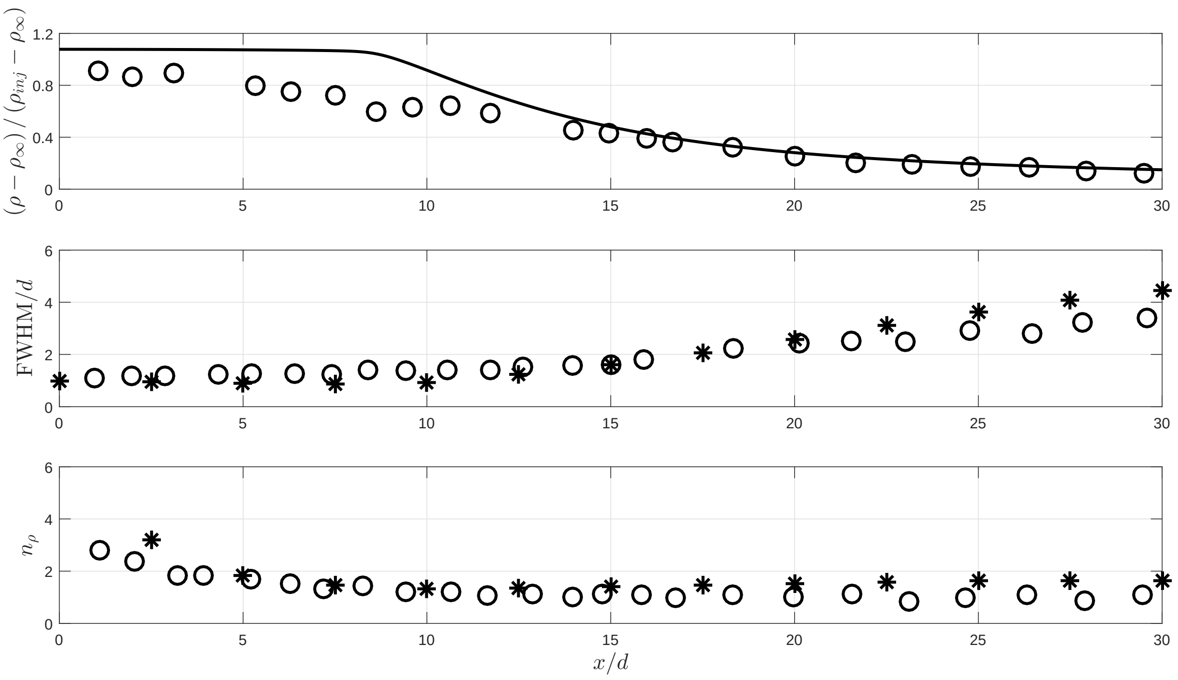

Figure 6.16: Comparison between numerical results and experimental results for case B6 (top: axial density distribution; middle: FWHM of density; bottom: shape parameter). Lines and star symbols correspond to numerical results, while open circles represent experimental data [35].

conditions in the chamber. Overall, a better agreement between experiment and numerical computations is found for case B6 than for B4, which could be explained by the proximity to the critical pressure of nitrogen (for reference $3.4\,\mathrm{MPa}$).

In this way case, B4 is more prone to suffer from the influence of the thermodynamic singularity that is the critical point and the region around it. Nevertheless, for both cases, the key lies in predicting transcritical jet behavior since, as shown, after the critical temperature value is reached, the jets enter the supercritical domain, and the numerical computations can replicate its features but at higher density levels than those registered by the experimental data, owing to the slow rate of decay registered for the transcritical portion of the jet. Accordingly, Figure 6.18 depicts higher density stratification inside the injector for case B4 than B6, which verifies the existence of more significant density gradients closer to nitrogen's critical pressure.

Considering a lower injection temperature ($100\,\mathrm{K}$), and a greater injection velocity ($20\,\mathrm{m\,s^{-1}}$), the axial density decay of case C4 is retrieved in Figure 6.19 and the axial temperature evolution in Figure 6.20. Here, it is possible to observe an experimental region of minor density variation until $x/d \approx 2$, which numerically extends to $x/d \approx 9$. This potential core is formed in the transcritical portion of the jet, which for cases C4 and C6 correspond to a value of $\rho^* = 0.8677$. After the critical temperature is crossed, the liquid-like nitrogen jet will continue to develop until entrained by chamber fluid, until breaking.

Increasing the pressure from $4\,\mathrm{MPa}$ in case C4 to $6\,\mathrm{MPa}$ in case C6, several differences can

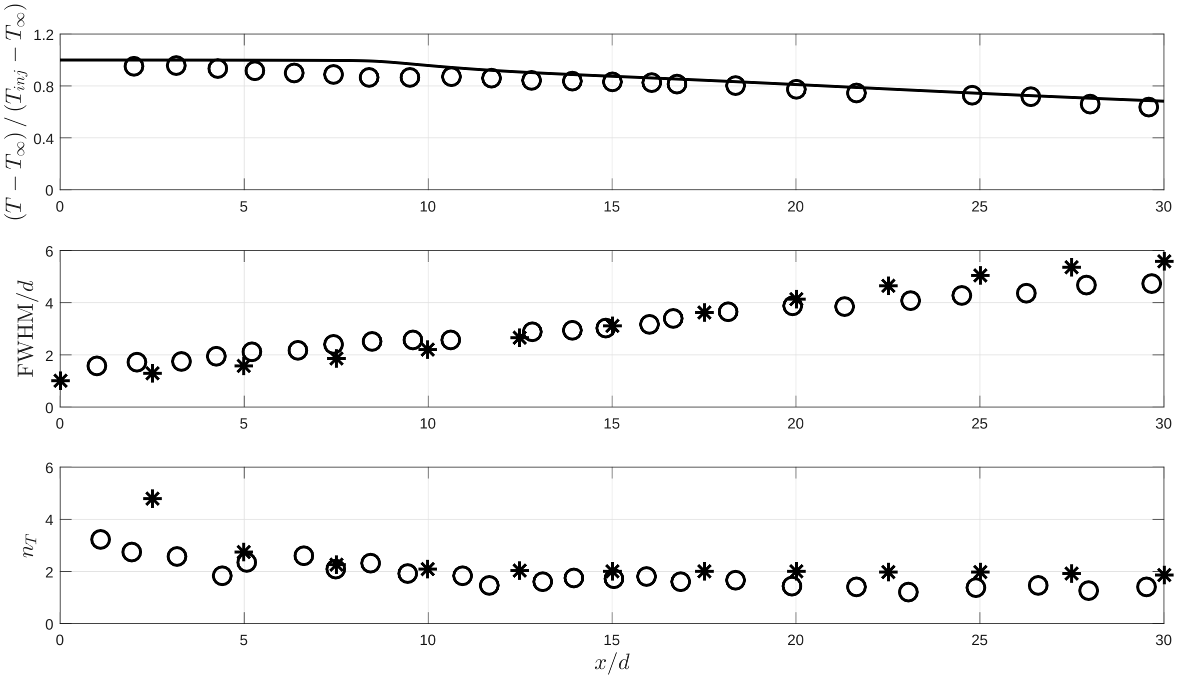

Figure 6.17: Comparison between numerical results and experimental results for case B6 (top: axial temperature distribution; middle: FWHM of temperature; bottom: shape parameter). Lines and star symbols correspond to numerical results, while open circles represent experimental data [35].

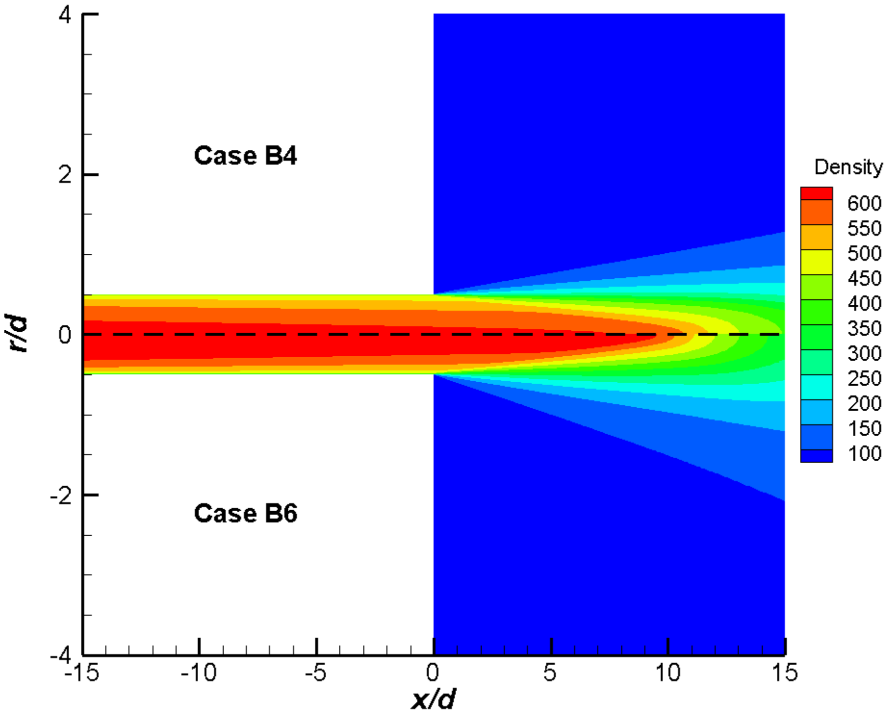

Figure 6.18: Comparison of density field between cases B4 and B6.

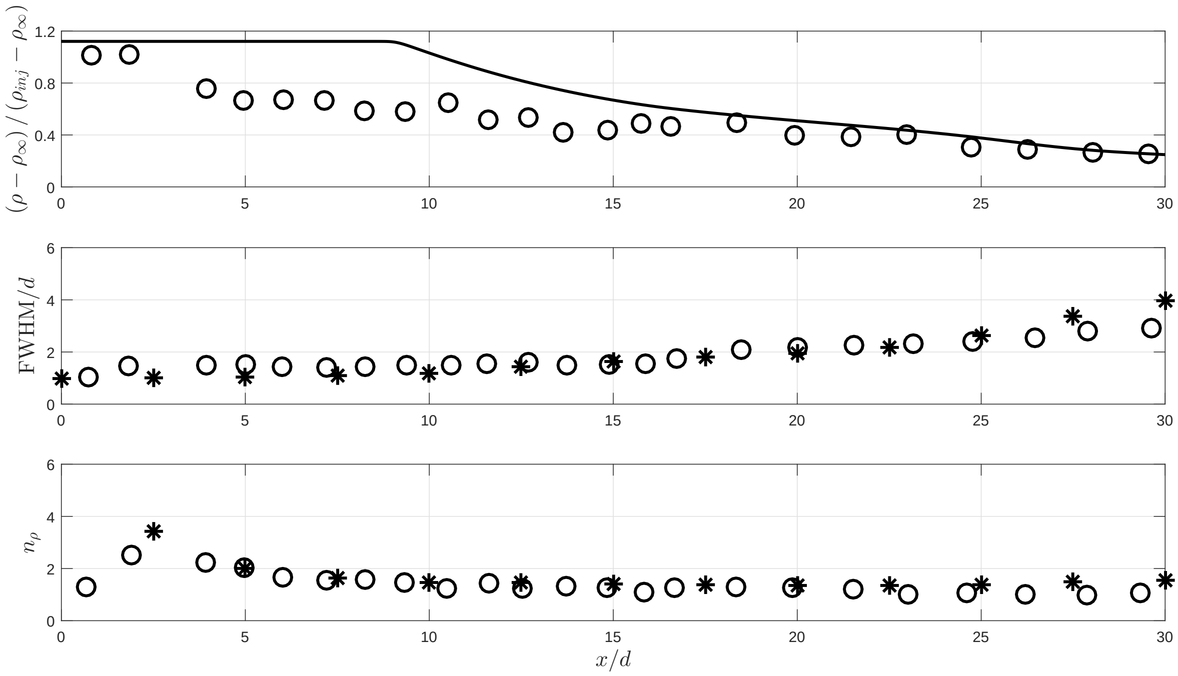

Figure 6.19: Comparison between numerical results and experimental results for case C4 (top: axial density distribution; middle: FWHM of density; bottom: shape parameter). Lines and star symbols correspond to numerical results, while open circles represent experimental data [35].

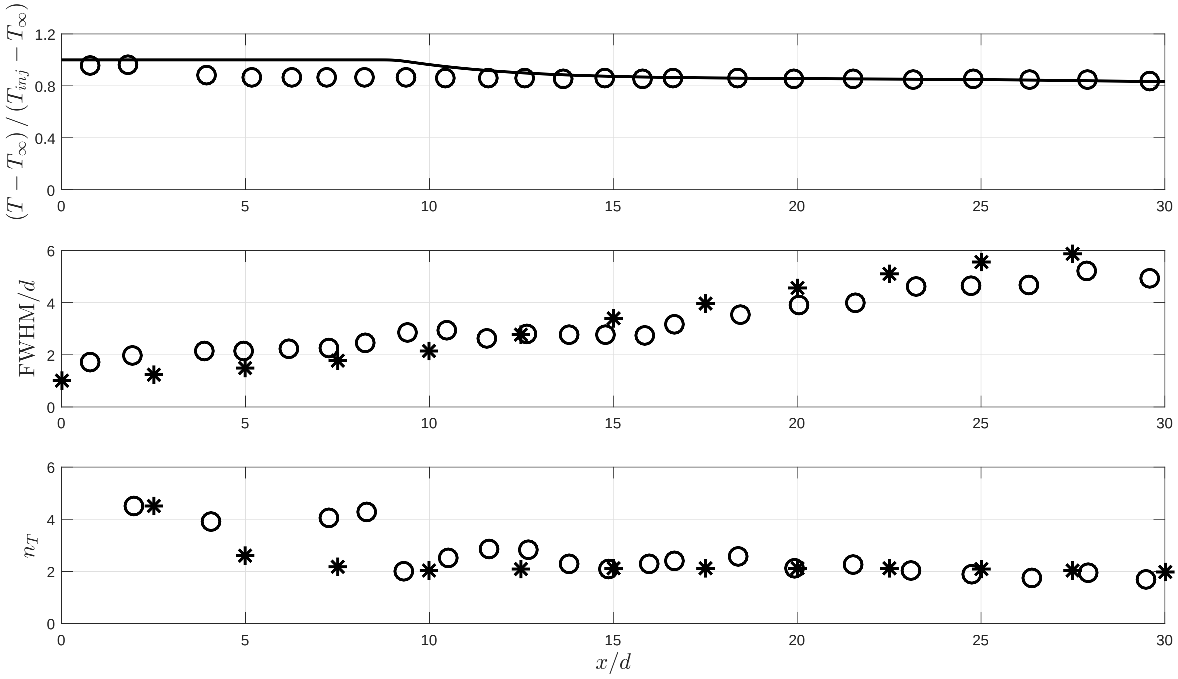

Figure 6.20: Comparison between numerical results and experimental results for case C4 (top: axial temperature distribution; middle: FWHM of temperature; bottom: shape parameter). Lines and star symbols correspond to numerical results, while open circles represent experimental data [35].

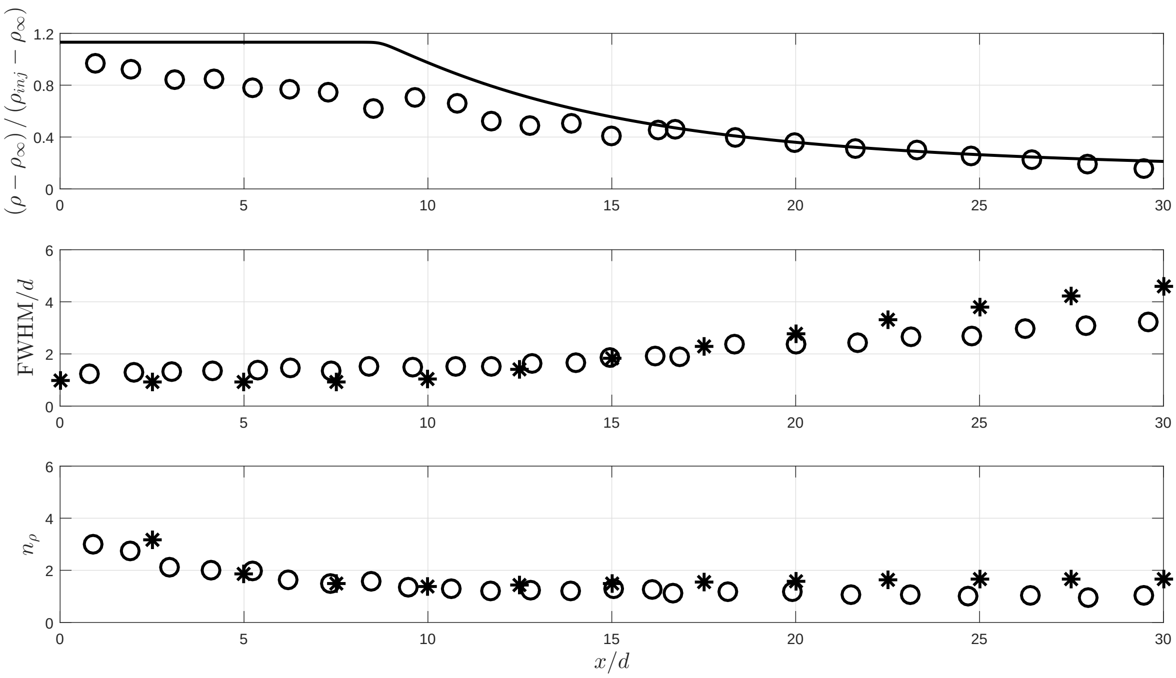

Figure 6.21: Comparison between numerical results and experimental results for case C6 (top: axial density distribution; middle: FWHM of density; bottom: shape parameter). Lines and star symbols correspond to numerical results, while open circles represent experimental data [35].

be observed. Figures 6.21 and 6.22 the same initial numerical dense core as registered for case C4. However, the experimental data no longer displays the same initial region of relatively constant density. Further away from the critical pressure of nitrogen, it is possible to observe a closer agreement with the experimental data, starting from x/d of about 15, where the conditions in the chamber start to dominate over the jet evolution.

As depicted in Figure 6.23, comparing the density fields of cases C4 and C6, the heat transfer exchange between the injector walls and the transcritical jets is not sufficient to reach the jet centerline and influence the axial evolution of density, resulting in the formation of a dense potential core, leading to minor differences on the jet inside the chamber.

While differences between the experiments and the numerical predictions are observed for cases B and C in terms of the axial density decay rate, the proposed incompressible but variable density approach can predict the jet spreading rates in terms of density and temperature for all experimental test cases, showcasing the ability of the incompressible but variable density approach in replicating turbulent mixing and account for the real gas effects. The ability to predict transcritical behavior either through compressible or incompressible but variable density formulations lies with the inclusion of phase separation into the models to account for the possible formation of multiphase flow. On the other hand, the differences observed between experiments and numerical computations at transcritical conditions could also be influenced by the nature of the measurements and the Raman scattering technique. Moreover, it needs to be recognized that the experimental measurements of Oschwald and Schik [35] are based on the use of a highly complex measurement technique and equipment [276]

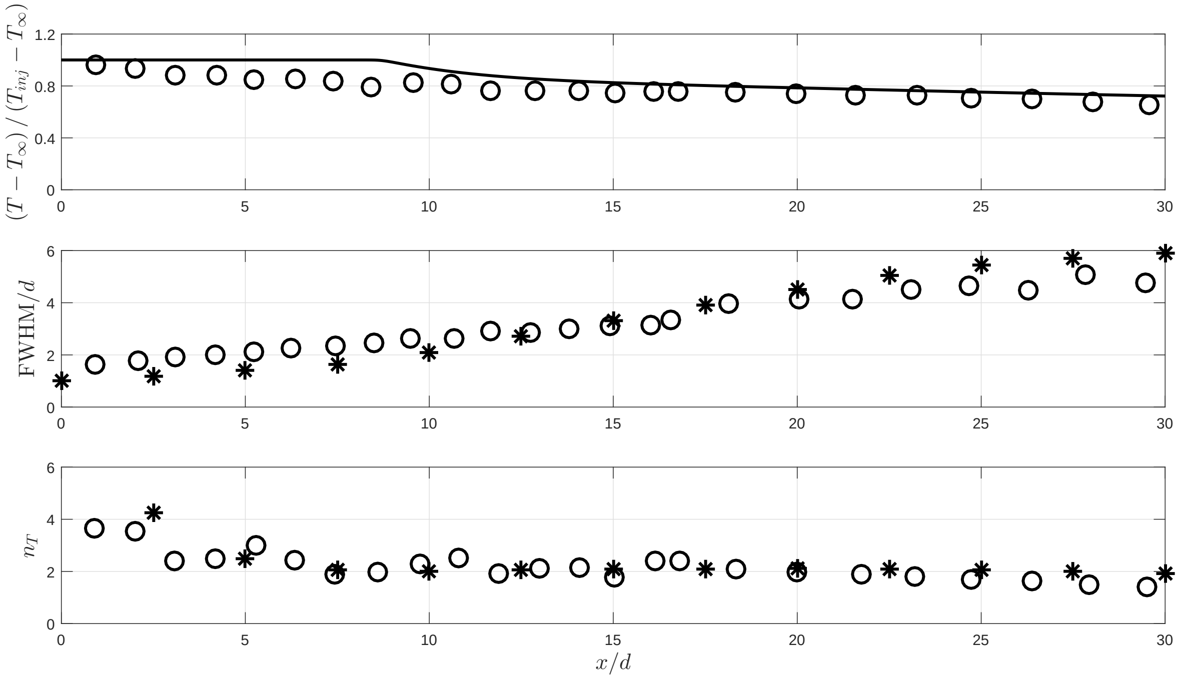

Figure 6.22: Comparison between numerical results and experimental results for case C6 (top: axial temperature distribution; middle: FWHM of temperature; bottom: shape parameter). Lines and star symbols correspond to numerical results, while open circles represent experimental data [35].

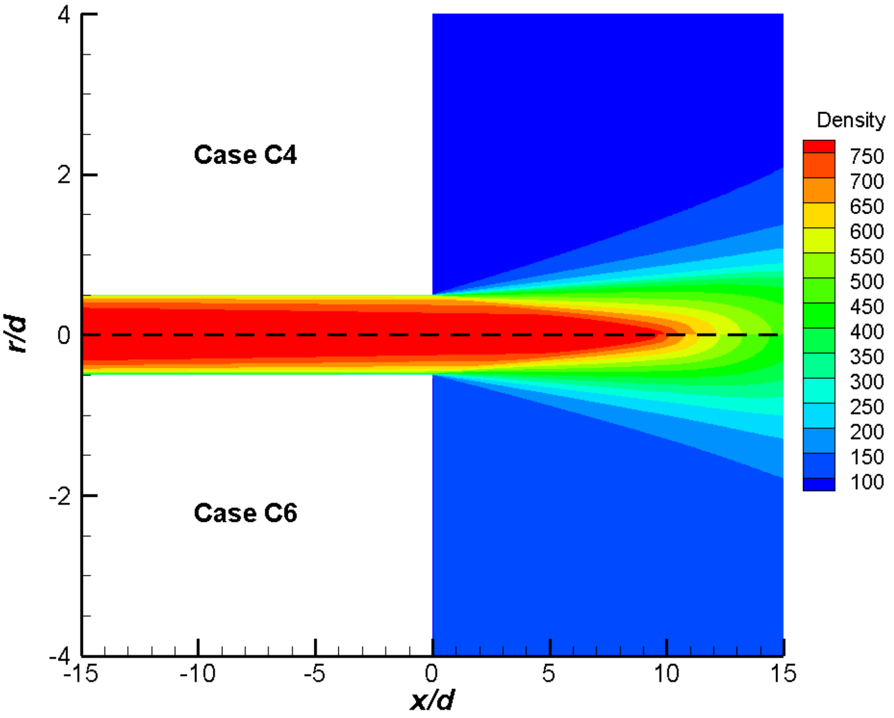

Figure 6.23: Comparison of density field between cases C4 and C6.

for which assumptions need to be made. While the authors recognize that the Raman cross-section increases with density for transcritical jets, the lack of accurate data leads to the assumption of a constant Raman cross-section. This means that the transcritical cases' experimental axial density distributions can be severely under-predicted. According to Oschwald and Schik [35], a difference of about 30% could be expected for the worst cases (C4 and C6, as shown). On the other hand, the assumption of constant Raman cross-section does not affect the supercritical jets (A4 and A6). Moreover, Oschwald and Schik [35] point out that only the absolute values of density are affected by the constant Raman cross-section, which means that the FWHM and the shape parameters for density and temperature are not affected by this issue.

Lastly, the shape parameters for density and temperature indicate that no self-similar state is reached since the parameters always exhibit values higher than one.

6.5 Summary

This chapter described the behavior of nitrogen jets at transcritical and supercritical gas-like conditions using a RANS-based approach. Two experimental conditions were considered for each regime at pressure levels of 4 and $6\,\mathrm{MPa}$, for which the axial density distributions at each jet centerline were analyzed. While for the supercritical injection cases, a close approximation was achieved to the experimental data, both in terms of jet behavior capture and the magnitude of the experimental data, only a behavioral approximation was reached concerning the transcritical configurations, since while in the transcritical regime a slower rate of decay of the axial density distribution was obtained concerning the experimental values. Furthermore, the jet spreading rate is higher in the case of temperature, indicating that heat propagation is dominant over momentum transport.

Chapter 7

Temperature Field Validation

Only single injection configurations were considered insofar as the injection of a fluid in a quiescent environment representative of an LRE combustion chamber. However, in an LRE combustion, shear coaxial injectors are employed, where the fuel is injected through the central orifice while the oxidizer co-axially. Therefore, this chapter considers an experiment where nitrogen is injected into a quiescent nitrogen environment through the central and coaxial orifices at different velocity and momentum ratios. The previous analysis on single injection configuration is extended to coaxial injection, while the experiment's nature also allows for validating the temperature field.

7.1 Coaxial Injection

The coaxial injection configuration depicted in Figure 7.1 is initially governed by the growth of the outer shear layers, owing to the growth of Kelvin-Helmholtz instabilities. Then, low-speed flow issuing from the main stream is entrained into the inner shear layer in a mass transfer process that separates the potential core from the inner shear layer [277, 278].

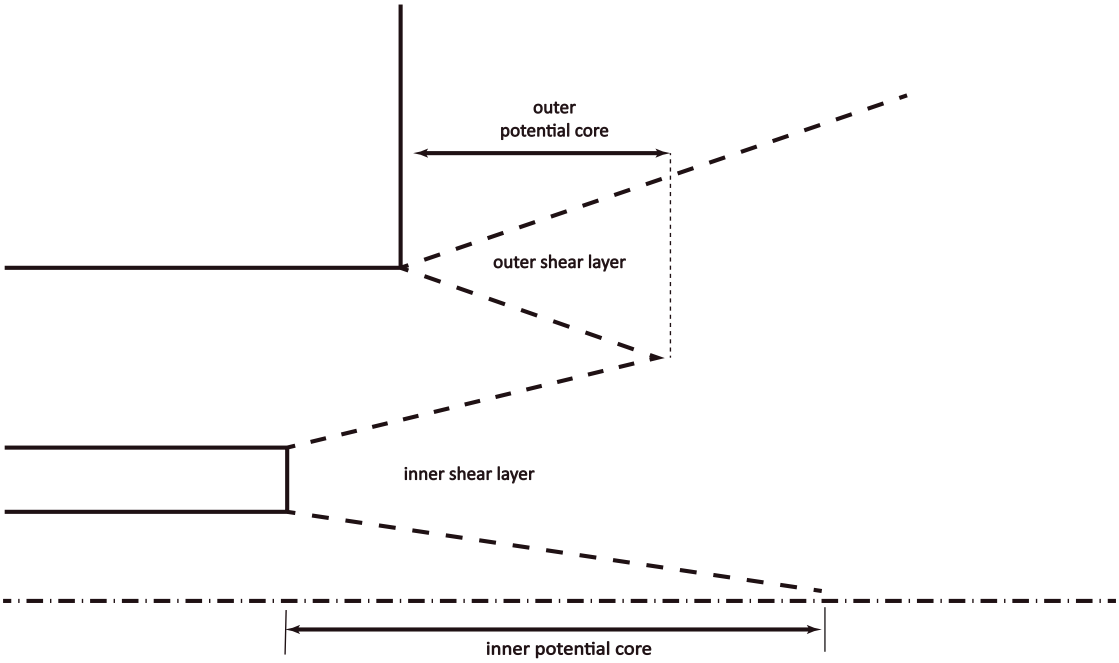

Figure 7.1: Representation of near-injector mixing regions.

Rapid entrainment is expected in the variable density conditions considered in this chapter. Moreover, given the outer-to-inner jet velocity ratios considered, negative velocity values will appear, leading to a recirculation region forming close to the injector's exit. In low-pressure coaxial injection, the recirculation zone formation is dependent upon the velocity profile shape [279], while at supercritical conditions, the influence of the temperature profile will also play a role as described in Chapter 5 for single injection configuration.

The outer-to-inner jet momentum ratio is defined according to equation (7.1), where subscripts i and o denote the inner (main) and outer (coaxial) stream, respectively. Besides affecting the recirculation, the momentum ratio is intimately related to the length of the inner potential core [278].

$$M = \frac{\rho v_o^2}{\rho v_i^2} \quad (7.1)$$

The coaxial injection is a subject less understood than single injection configurations [280]. Mainly, for supercritical shear coaxial injection, the experiments of Davis and Chehroudi [129] constitute the most extensive quantitative database of coaxial injection analysis, ranging from subcritical to supercritical conditions. For instance, Hosangadi et al. [281] use a hybrid LES/RANS model to evaluate the coupling between turbulence mixing and non-linear thermodynamic properties and how it contributes to enhanced mixing at supercritical conditions, while Schmitt et al. [150] focus on the influence of injector geometry and the operating conditions. In their LES simulations, Schmitt et al. [150] can show that when the momentum ratio is higher than a given threshold, the inner potential core breaks abruptly due to the formation of a recirculation zone close to the injector exit plane.

More recently, the coaxial injection configuration was looked into by Poormahmood and Farshchi [282]. Once again, LES is studied with the focus being on the finger-like structures formation, and the effect turbulence has on the peak in isobaric specific heat, labeled as a 'thermal shield'. Another relevant study to this discussion is the one of Liu et al. [283], where the focus is given to the modeling of acoustic excitation and its influence on near injector flow at higher injection velocities, coincident to those of the space shuttle main engine (SSME) pre-burner.

In order to provide a more general view of coaxial injection, Davis and Chehroudi [129] experiments will be analyzed in this chapter in conditions ranging from subcritical to supercritical, at varying momentum and velocity ratios.

7.2 The Experiment

The experimental conditions of Davis and Chehroudi [129] describing the coaxial injection of nitrogen into a quiescent nitrogen environment are considered. Figure 7.2 depicts the coaxial injector used in the experiments, while a detailed view of the injector tip is reported in Figure 7.3.

In a typical rocket combustor, fuel and oxidizer are injected into the chamber through coaxial injectors [127, 284] whose performance is influenced by the absolute pressure being the velocity ratio of the outer-to-inner jet a fundamental design parameter.

Figure 7.2: Coaxial injector [285].

Figure 7.3: Injector tip zoom [32].

The computational domain is represented in Figure 7.4 depicting the position of the main and coaxial streams, indicating that the main stream is recessed concerning the coaxial one. Coaxial nitrogen injection is considered at subcritical, near-critical, and supercritical conditions (nomenclature follows Davis and Chehroudi [129]) at temperature ranges defined [129] as low and high. The low-temperature range comprises the values of 135–140 K, or in reduced temperature 1.07–1.11, and the high-temperature range of 185–200 K corresponds to 1.47–1.58 in reduced temperature. These experiments [129] which were conducted to study the influence of acoustic fields as a means to evaluate the effect of combustion instabilities in LREs, will fill the purpose of extending the incompressible but variable density approach to coaxial injection while allowing for the temperature field validation as complementary to the density fields evaluated insofar on Chapters 5 and 6 for supercritical and transcritical single injection, respectively. Also, the recess depicted in Figure 7.4 plays a preponderant role, as shown in studies dealing with flame stabilization [286]. The recess in LOX–H_2 coaxial injection contributes to flame stabilization inside the injector, enhancing the flame angle and increasing the reacting region, leading to a fast jet breakup. Establishing the parallel between this case with the non-reacting coaxial configuration studied in this chapter, the heat transfer inside the injector is expected to assume a more preponderant role than in the single injection configurations dealt with in the previous two chapters.

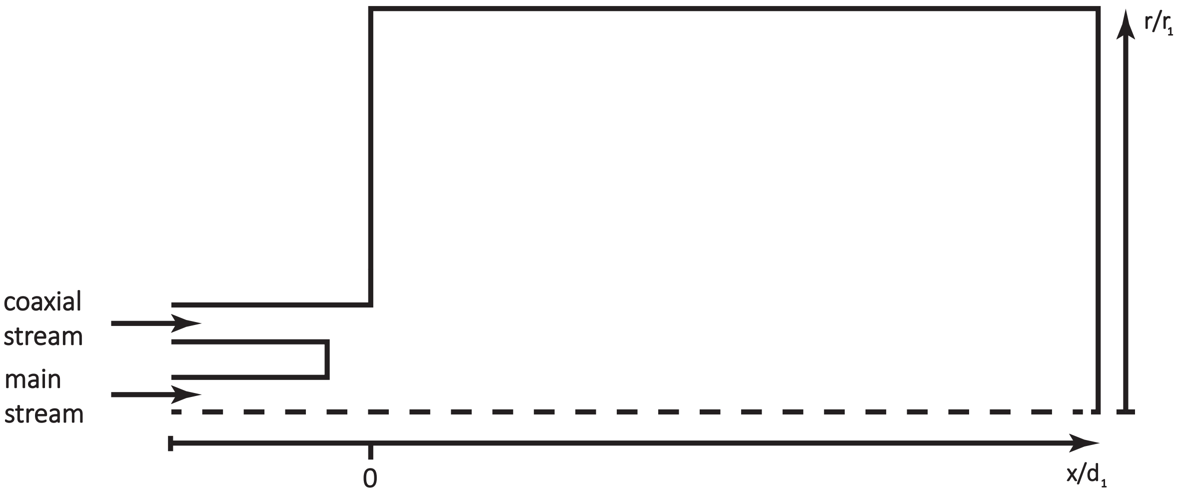

Figure 7.4: Coaxial geometry configuration.

The inner tube has a length of $50\,\mathrm{mm}$, with an inner diameter, d_1 of $0.508\,\mathrm{mm}$ and an outer diameter, d_2, of $1.59\,\mathrm{mm}$, while the outer tube has an inner diameter, d_3, of $2.42\,\mathrm{mm}$ and an outer diameter, d_4 of $3.18\,\mathrm{mm}$. The inner tube is recessed concerning the outer tube by a length of half the inner tube inner diameter, d_1. On the other hand, the combustion chamber has a length of $59.4\,\mathrm{mm}$, with a height of $76\,\mathrm{mm}$ and a depth of $12.7\,\mathrm{mm}$. Isothermal wall boundary conditions are considered at the injector walls and chamber, following the chamber temperature recorded in the experiments, while the injector face plate is modeled as an adiabatic wall.

Radial temperature profiles are measured with a type–E thermocouple mounted on a traverse as depicted in Figure 7.5 used to switch the thermocouple's position. As depicted in Figure 7.5, the thermocouple bead has a diameter of $0.10\,\mathrm{mm}$, and it is positioned at a distance of $0.14\,\mathrm{mm}$ from the injector exit plane. At the same time, steady-state conditions are maintained in the experimental facility for each test case [129].

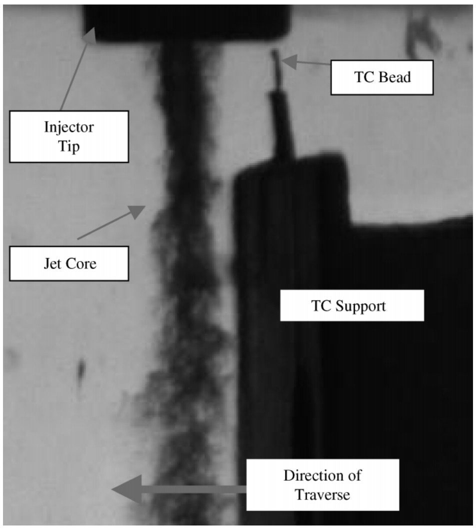

Figure 7.5: Thermocouple and support mechanism used to perform radial temperature measurements in the coaxial jet [129].

The experimental test cases resemble practical LRE conditions [150] both in terms of the high outer-to-inner stream velocity ratio [153] and the inner-to-outer high-temperature ratio. Due to the interaction between both streams and the nitrogen in the chamber, two different shear layers will form (Figure 7.1). At the same time, a sizeable recirculation zone encompasses the post-tip region, resulting from the interaction of the high-speed nitrogen injected through the coaxial annulus and the low-speed nitrogen from the central annulus. The stronger the coaxial flow is, the shorter the dense core will be.

Davis and Chehroudi [129] report different dependencies in the length of the inner potential core with the momentum ratio for subcritical and supercritical conditions. For example, at subcritical conditions, a dependence of $M^{-0.2}$ while at supercritical conditions, a dependence of $M^{-0.5}$.

A summary of the thermophysical models used in the calculations presented in this chapter is given in Table 7.1.

Table 7.1: Summary of thermophysical models.

Turbulence closure	EoS	Transport properties
κ–ε standard [175]	PR [184]	Lemmon and Jacobsen [214]

7.3 Validation

Figures 7.6, 7.8 and 7.10 depict the grid independence study for selected subcritical, near-critical and supercritical conditions, following Davis and Chehroudi [129] adopted nomenclature for the experimental test cases division. Radial temperature profiles are evaluated for each condition as a function of the radial distance from the jet centerline (r) normalized by the inner tube inner radius (r_1). The corresponding analysis of the computational error as the grid is progressively refined in given in Figures 7.7, 7.9 and 7.11. The figures depict two sets of experimental measurements denoted as positive and negative. They correspond to temperature values measured for positive [129] r/r_1 and for negative [287] r/r_1 measured from the jet centerline. Moreover the combustion chamber temperature is also depicted in the blue dashed line.

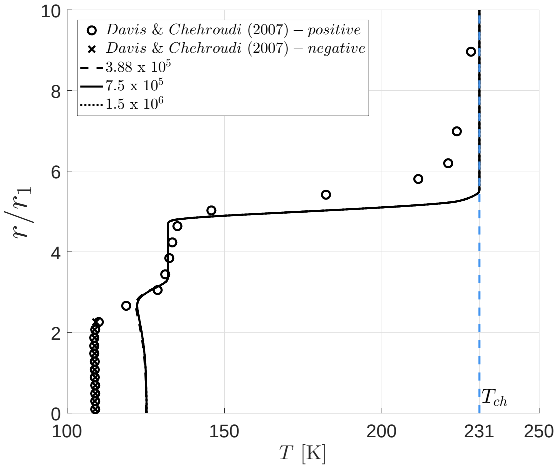

Figure 7.6: Grid Independence Study, corresponding to case 13 in subcritical conditions.

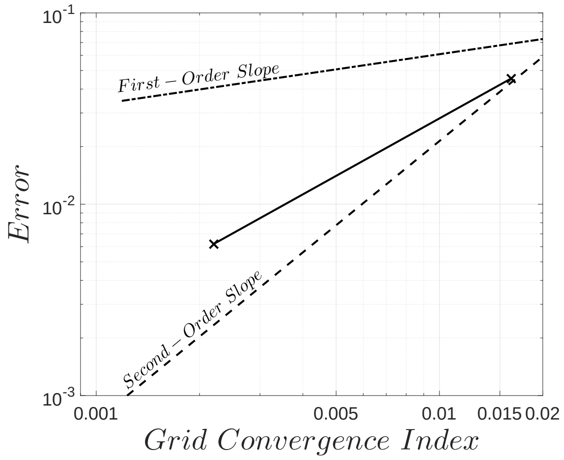

Figure 7.7: Error propagation, corresponding to case 13 in subcritical conditions.

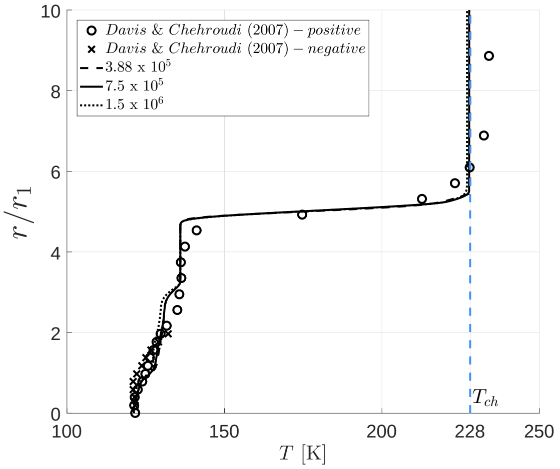

Figure 7.8: Grid Independence Study, corresponding to case 16 in near-critical conditions.

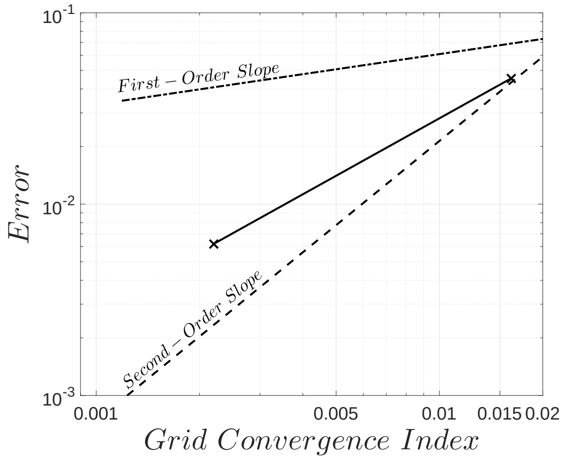

Figure 7.9: Error propagation, corresponding to case 16 in near-critical conditions.

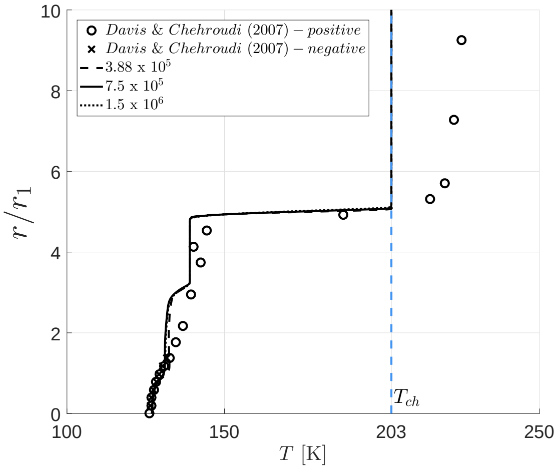

Figure 7.10: Grid Independence Study, corresponding to case 21 in supercritical conditions.

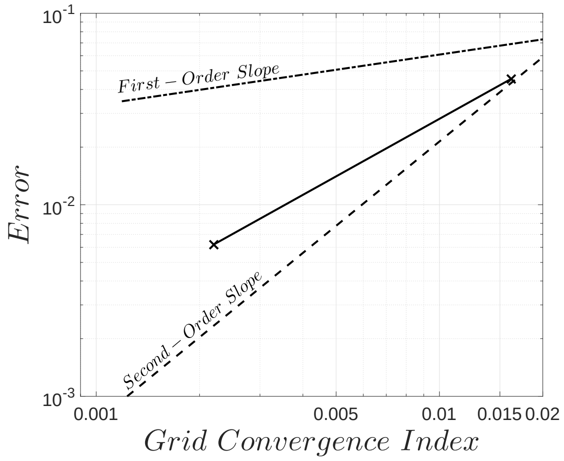

Figure 7.11: Error propagation, corresponding to case 21 in supercritical conditions.

7.4 Subcritical Conditions

7.4.1 Low Outer-jet Temperature

Figure 7.12 depicts the injection conditions location in relation to the critical point. As indicated by the values in Table 7.12, the inner jet initial conditions are located in the subcritical regime, while the outer jet temperature values are always above nitrogen's critical point. Then, the outer-to-inner jet velocity ratio (VR) is progressively increased from 4.7 in case 13 to 11.1 in case 15 and the momentum ratio from 1.5 to 7.2.

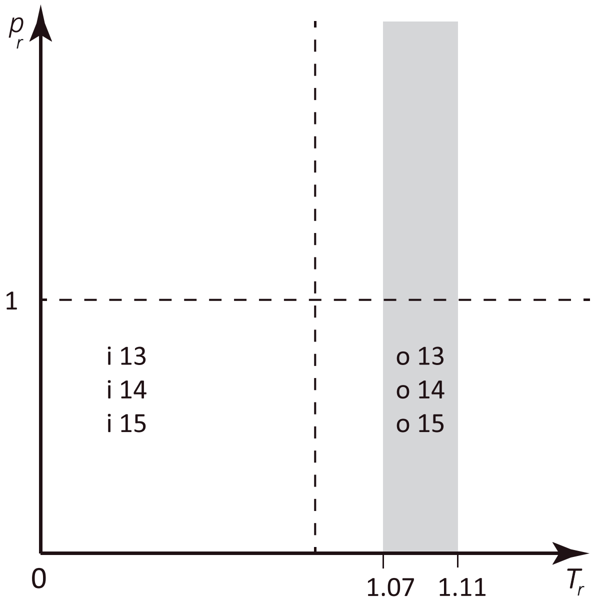

Figure 7.12: Subcritical low temperature case distribution.

Table 7.2: Conditions for the low outer-jet temperature cases [129].

Case	p_∞ [MPa]	T_∞ [K]	T_i [K]	T_o [K]	v_i [$\mathrm{m\,s^{-1}}$]	v_o [$\mathrm{m\,s^{-1}}$]	VR [-]	M [-]
13	1.45	231	109	132	2.2	10.3	4.7	1.5
14	1.47	224	109	139	2.2	17.6	8.0	4.1
15	1.50	219	109	152	2.2	24.5	11.1	7.2

Figures 7.13, 7.14 and 7.15 depict the comparison between experiments and the numerical results obtained through the incompressible but variable density approach for cases 13, 14 and 15, respectively. It is clear from the figures that lower values than the experimental ones are retrieved, corresponding to the region of constant temperature up to a distance of two inner jet radii. The difference between the numerical results and the experiments is explained due to the blockage effect introduced by the thermocouple during the measurements (Figure 7.5), which interferes with the formation of a recirculation zone close to the injector's exit. The initial mismatch becomes more pronounced as the velocity ratio increases from 4.7 in case 13 to 11.1 in case 15, consistent with the more rigorous flow motion as velocity and momentum ratios are increased. Despite the initial differences observed in the initial constant temperature region ($r/r_1 \approxeq 2.5$), a good agreement is registered for the remaining portion of the temperature profile, where the thermocouple's measurement is less intrusive.

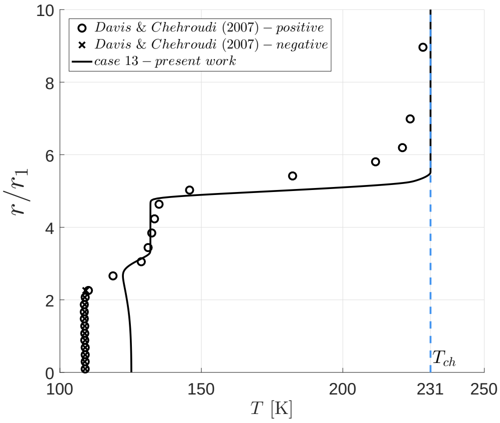

Figure 7.13: Radial temperature profile for case 13.

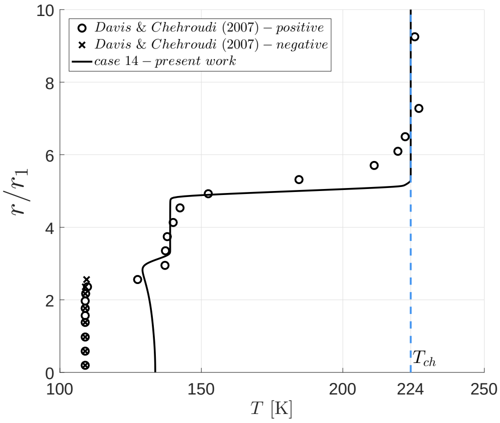

Figure 7.14: Radial temperature profile for case 14.

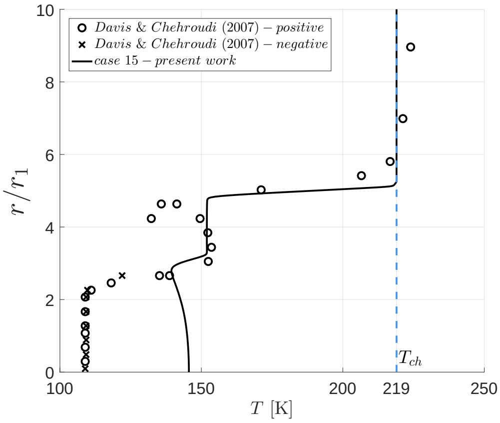

Figure 7.15: Radial temperature profile for case 15.

Figures 7.16 and 7.17 depict the velocity fields of cases 14 and 15, respectively. In Figure 7.16 the streamlines are represented for a VR of 8 and a momentum ratio of 4.1, according to the experimental conditions of Table 7.2, while in Figure 7.17 a VR of 11.1 and a M of 7.2 are considered. In the figures, it is possible to observe the influence of the recess of the inner tube in the outer jet development and the quiescent chamber nitrogen, from where the outer shear layer growth occurs after the vertical chamber wall.

According to the literature [280], the outer-to-inner jet velocity and momentum ratios are relevant parameters in the coaxial jet development under subcritical conditions. For a VR of 8, as in case 14, it is possible to observe in Figure 7.16, at the injector exit plane, the inner jet blockage due to the recirculation zone that extends from the symmetry axis up to a radial distance of r/r_1 of 2.5, with two separation points on the symmetry axis at axial distances, x/d_1, of 0.5 and 4.5. This is because the inner jet is deflected at the inner tube end due to the recirculation, bypassing the recirculation close to the coaxial jet.

For case 15 in Figure 7.17, while both the velocity and momentum ratios are increased concerning case 14, it is possible to observe the same flow structure, namely the recess of the inner tube and the blockage due to the recirculation. Nevertheless, the increase of VR from 8 to 11.1 and the momentum ratio from 4.1 to 7.2 changed the stagnation points' location, while

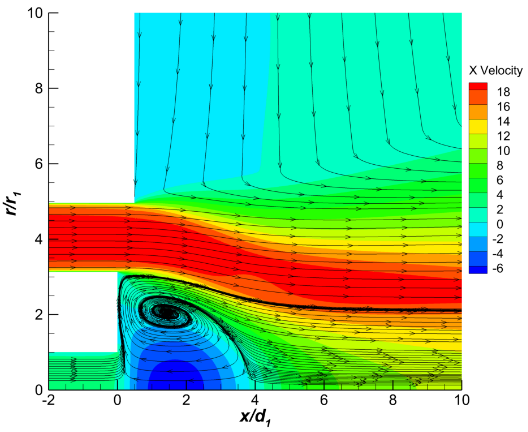

Figure 7.16: Case 14 velocity field and recirculation.

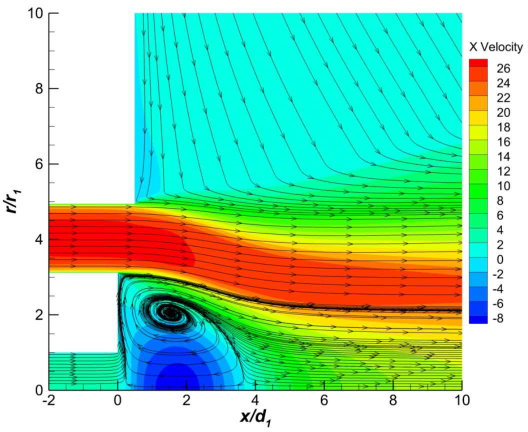

Figure 7.17: Case 15 velocity field and recirculation.

the recirculation size remained constant. While it is not shown, the same flow structure is identified in case 13 for the lower VR of 4.7 (Table 7.2).

7.4.2 High Outer-jet Temperature

Figure 7.18 depicts the inner- and outer-jet injection conditions distribution for the cases referred to as high outer-jet injection temperature [129], where the injection temperature range increases to $T_r = 1.47 - 1.58$, where lower momentum ratios are considered, as indicated in Table 7.3, in relation to the low-outer jet injection temperature cases.

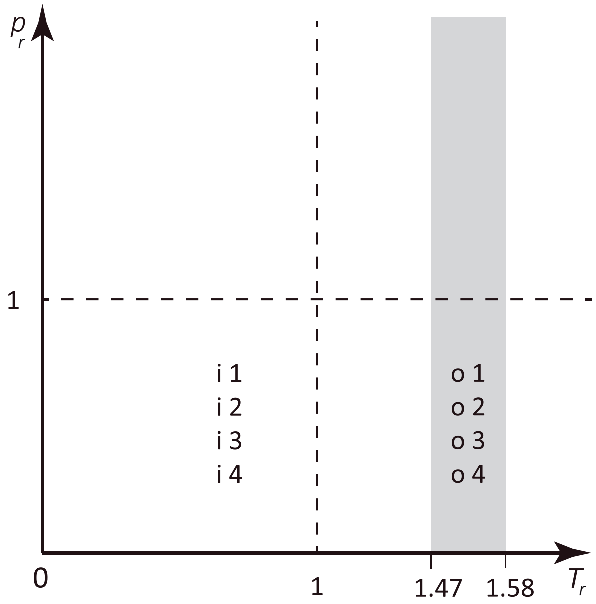

Figure 7.18: Subcritical high temperature case distribution.

Figures 7.19, 7.20, 7.21 and 7.22 depict the comparisons between the experiments and the numerical results for cases 1, 2, 3 and 4, respectively. Through the analysis of the figures, it is possible to infer the momentum ratio threshold leading to the inner core breakup and the blockage effect of the recirculation. To the lower momentum ratio (0.2 in case 1), no

Table 7.3: Conditions for the high outer-jet temperature cases [129].

Case	p_∞ [MPa]	T_∞ [K]	T_i [K]	T_o [K]	v_i [m s^{-1}]	v_o [m s^{-1}]	VR [-]	M [-]
1	1.49	238	109	195	2.2	4.5	2.1	0.2
2	1.59	248	110	201	2.2	10.9	4.9	1.1
3	1.45	249	108	204	2.2	19.8	9.1	3.2
4	1.49	237	108	202	2.2	23.9	11.0	4.9

recirculation blockage is discernible in Figure 7.19, where the experimental region of constant temperature is retrieved in the computations, albeit with different lengths. From here, the momentum ratio increases to 1.1 in case 2, and the blockage influence starts to be felt in the radial profiles, which exhibit similar behaviors to those of cases 14 and 15, as the momentum ratio is further increased in cases 3 and 4.

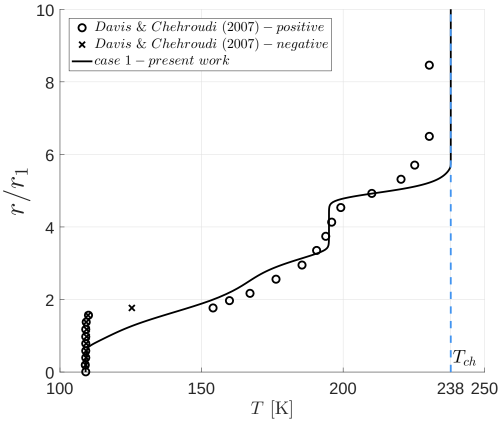

Figure 7.19: Radial temperature profile for case 1.

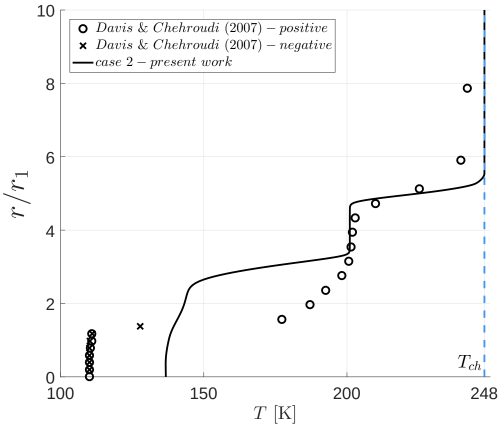

Figure 7.20: Radial temperature profile for case 2.

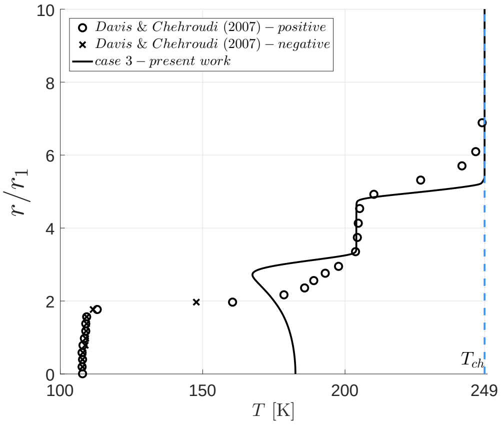

Figure 7.21: Radial temperature profile for case 3.

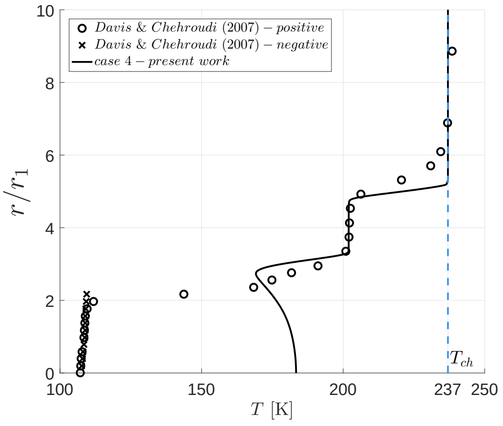

Figure 7.22: Radial temperature profile for case 4.

Figures 7.23 and Figure 7.24 depict the velocity fields of cases 1 and 4, respectively. Interestingly, in Figure 7.23 for a VR of 2.1 and a M of 0.2, it is possible to observe a distinct behavior than the one presented for subcritical conditions considering the low outer-jet injection temperatures. Due to the low-momentum ratio of 0.2, there is no blockage effect due to the recirculation. Instead, two counter-rotating recirculations are anchored to the post tip between the two jets. The recirculation close to the inner jet rotates counter-clockwise, while a clockwise recirculation is observed closer to the outer jet.

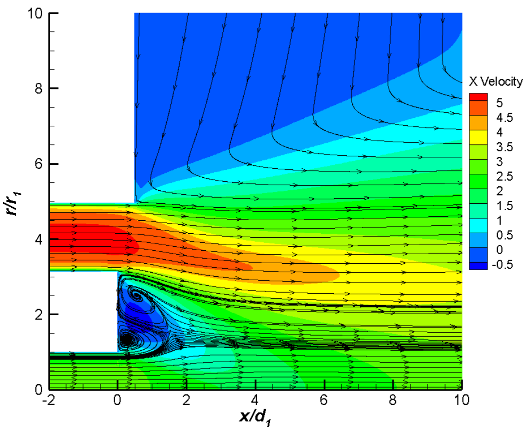

Figure 7.23: Case 1 velocity field and recirculation.

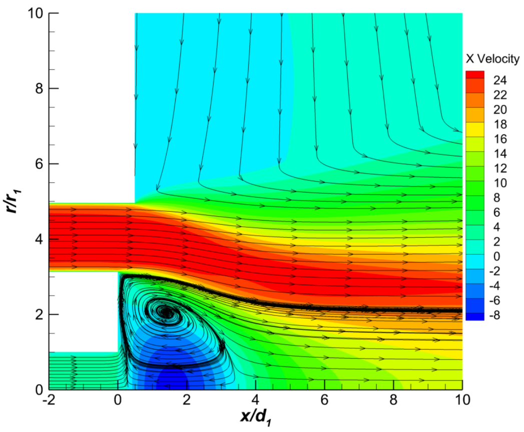

Figure 7.24: Case 4 velocity field and recirculation.

As the velocity and momentum ratios are further increased to 11.0 and 4.9, respectively, in Figure 7.24 a distinct behavior than case 1 is observed. However, as previously reported for the low outer-jet temperature cases in the preceding section, a similar flow structure is observed, that is, the inner jet blockage by the recirculation region.

At subcritical conditions, the increasing outer-to-inner jet velocity and momentum ratios promote the inner jet blockage, regardless of the low or high outer-jet injection temperature. On the other hand, differences between numerical computations and the experimental data are explained due to the intrusive measurement caused by the thermocouple and the traverse in which it is supported (Figure 7.5), especially given the dimensions of the recirculations and the thermocouple bead.

7.5 Near-critical Conditions

7.5.1 Low Outer-jet Temperature

Close to nitrogen's critical point, the experimental results labeled as near-critical are considered with a greater chamber pressure close to $3.50\,\mathrm{MPa}$. As indicated in Figure 7.25, inner jet injection conditions are located in the transcritical regime, while the chamber environment varies from supercritical in case 16 to transcritical in remaining cases, following Table 7.4.

Table 7.4: Conditions for the low outer-jet temperature cases [129].

Case	p_∞ [MPa]	T_∞ [K]	T_i [K]	T_o [K]	v_i [$\mathrm{m\,s^{-1}}$]	v_o [$\mathrm{m\,s^{-1}}$]	VR [-]	M [-]
16	3.54	228	121	136	2.6	4.1	1.5	0.6
17	3.53	202	120	140	2.6	11.0	4.2	3.9
18	3.52	197	119	135	2.5	15.6	6.1	9.4
19	3.54	197	125	134	3.1	18.5	5.9	11.2

Figures 7.26, 7.27, 7.28 and 7.29 depict the radial temperature profiles corresponding to cases 16, 17, 18 and 19 from Table 7.4, where several differences are observed in relation to the injec-

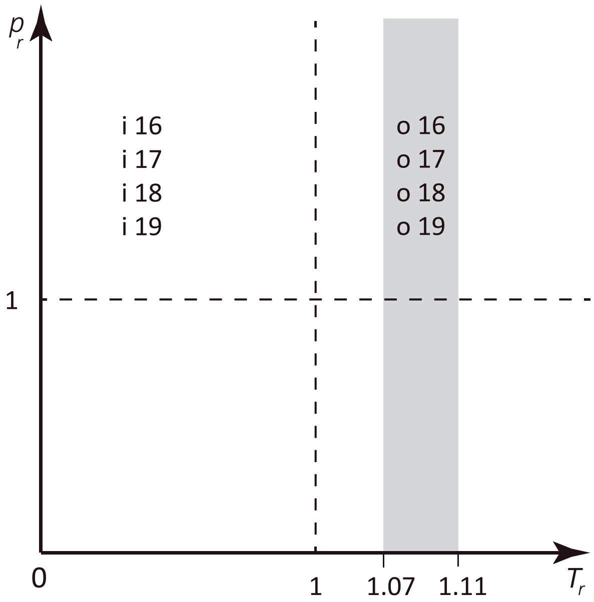

Figure 7.25: Near-critical low temperature case distribution.

tion under subcritical conditions. Instead of recovering top hat shape profiles under subcritical injection conditions, a radial temperature decay is observed at the centerline, owing to the thermal stratification inside the injector as described in previous chapters. Interestingly in Figure 7.26, it is possible to observe the potential core in the LES results of Poormahmood and Farshchi [282] in the first few radii, which following the analysis carried out in the previous chapters, is related to the fact that the authors did not take into account heat transfer in the injector.

Another difference concerning injection under subcritical conditions lies with the not occurrence of any blockage; instead counter-rotating, recirculations are formed in the post tip between both jets, corresponding to the regions in the figures where the numerical computations are further away from the experimental values. Under subcritical conditions, the difference is explained by the thermocouple intrusion in the flow, which alters the recirculations structure.

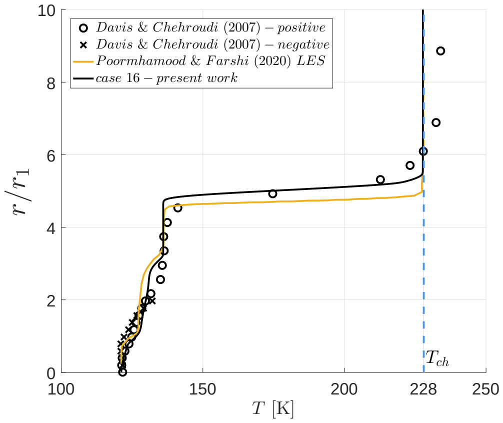

Figure 7.26: Radial temperature profile for case 16 and comparison with the LES results of Poormahmood and Farshchi [282].

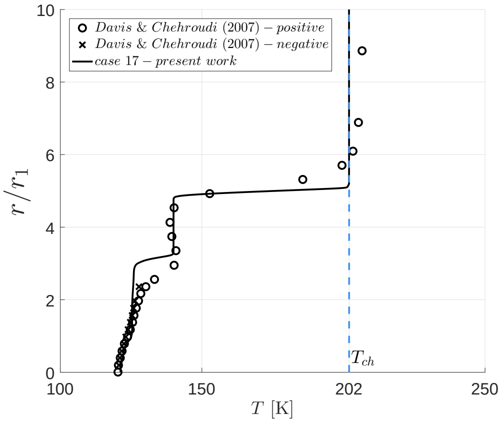

Figure 7.27: Radial temperature profile for case 17.

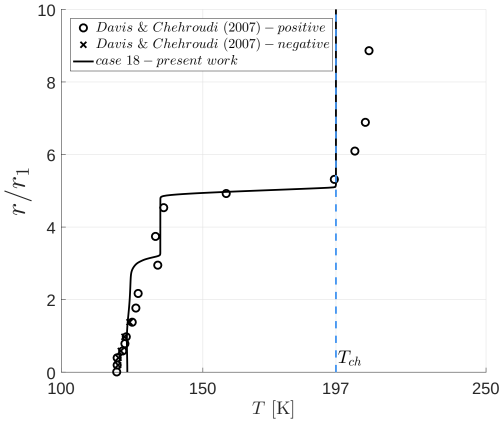

Figure 7.28: Radial temperature profile for case 18.

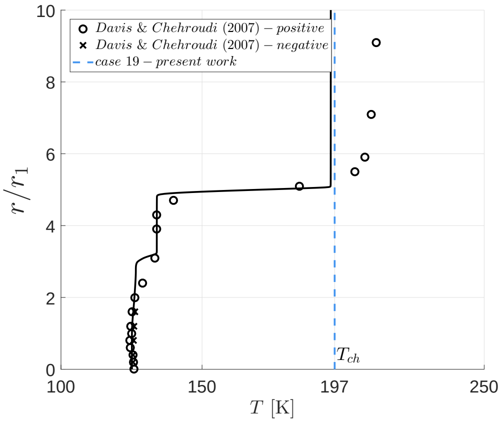

Figure 7.29: Radial temperature profile for case 19.

7.5.2 High Outer-jet Temperature

By increasing the outer-jet injection temperature to reduced temperature values between 1.47 and 1.58, as shown in Figure 7.30, the interaction of gas-like outer-jets with inner jets at transcritical conditions is evaluated, following the conditions of Table 7.5, taking into account increasingly higher velocity and momentum ratios.

Table 7.5: Conditions for the high outer-jet temperature cases [129].

Case	p_∞ [MPa]	T_∞ [K]	T_i [K]	T_o [K]	v_i [m s^{-1}]	v_o [m s^{-1}]	VR [-]	M [-]
5	3.56	238	121	195	2.6	4.6	1.8	0.4
6	3.70	233	123	188	2.7	10.4	3.8	2.1
7	3.57	235	124	194	2.9	17.8	6.2	5.2
8	3.55	235	125	196	3.0	22.6	7.6	8.0

It is clear that the radial temperature profiles in Figures 7.31 to 7.34 detail a larger re-circulation region in the post-tip region, whose growth is not only influenced by the increasing momentum ratio from 0.4 in case 5 to 8.0 in case 8 but also by the large gradients in thermophysical properties owing to the interaction between the outer supercritical gas-like jet and the inner transcritical one, whose injection temperature is close to nitrogen's critical point.

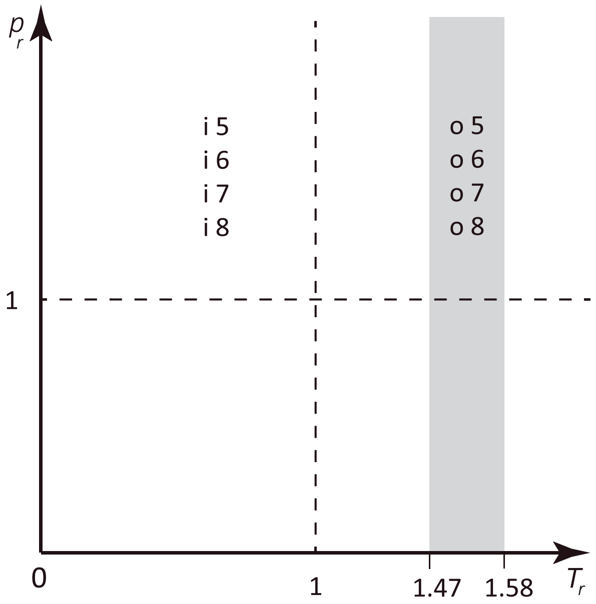

Figure 7.30: Near-critical high temperature case distribution.

The main difference between the near-critical low and high outer-jet injection temperature is that in the cases designated as 'low temperature', a supercritical liquid-like jet is present, which requires much energy to eventually overcome the thermal shield, consisting in the isobaric specific heat peak. However, as reported in previous chapters, the energy received does not contribute to heating but to the jet's expansion [45]. On the other hand, in the cases designated as 'high temperature,' a supercritical gas-like outer jet is present at injection, where thermal stratification effects are more preponderant.

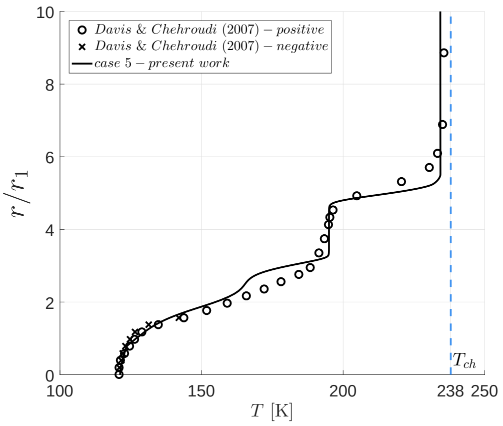

Figure 7.31: Radial temperature profile for case 5.

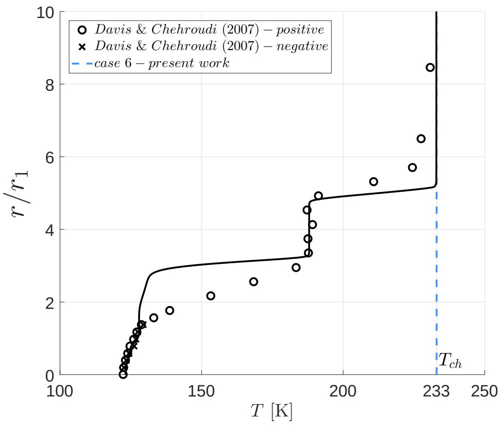

Figure 7.32: Radial temperature profile for case 6.

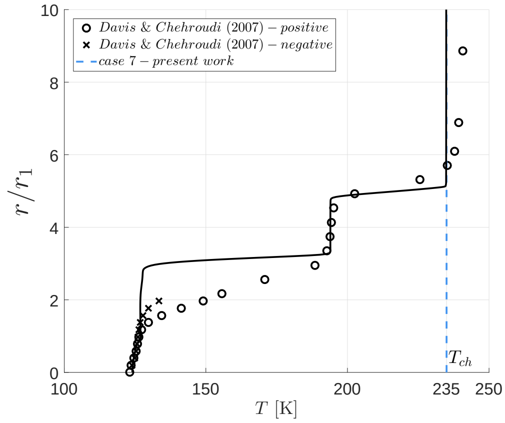

Figure 7.33: Radial temperature profile for case 7.

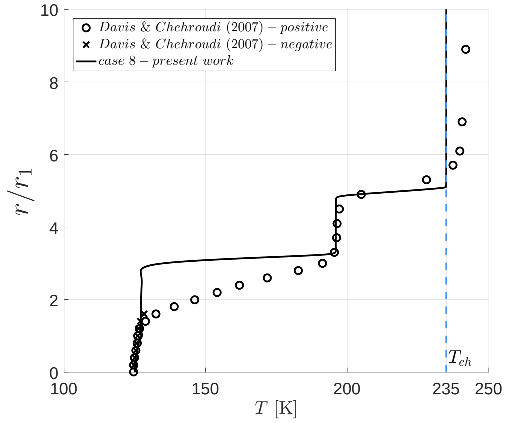

Figure 7.34: Radial temperature profile for case 8.

7.6 Supercritical Conditions

7.6.1 Low Outer-jet Temperature

Increasing the chamber pressure close to $5\,\mathrm{MPa}$, while increasing the inner jet injection temperature, the experimental measurements detail the coaxial injection of supercritical inner- and outer-jets into a transcritical chamber environment, following the experimental injection conditions distribution in Figure 7.35 for increasing velocity and momentum ratios as replicated in Table 7.35.

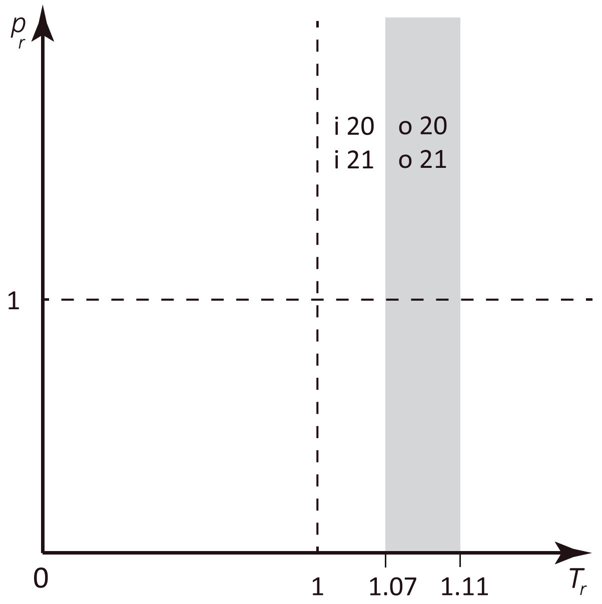

Figure 7.35: Supercritical low temperature case distribution.

Table 7.6: Conditions for the low outer-jet temperature cases [129].

Case	p_∞ [MPa]	T_∞ [K]	T_i [K]	T_o [K]	v_i [$\mathrm{m\,s^{-1}}$]	v_o [$\mathrm{m\,s^{-1}}$]	VR [-]	M [-]
20	4.97	218	128	137	2.9	3.6	1.2	0.8
21	4.88	203	127	139	2.9	10.5	3.7	6.3

Following the results obtained for near-critical conditions, similar temperature profiles are depicted for the supercritical cases 20 and 21 in Figures 7.36 and 7.37, respectively. Since in case 20, a lower experimental temperature is reported at the symmetry axis for both positive and negative measurements than the injection value, an additional computation was performed, considering the inner jet injection temperature as $119\,\mathrm{K}$ plotted in Figure 7.36. The fitted temperature value constitutes a closer approximation to the experimental data. Nevertheless, by looking into both figures, similar jet developments are observed for increasing velocity and momentum ratios. This indicates that the conditions in the outer jet, namely in terms of the temperature profile at the injector exit plane allied to the outer-to-inner jet momentum ratio, seem to be the main cause behind the recirculation zone size.

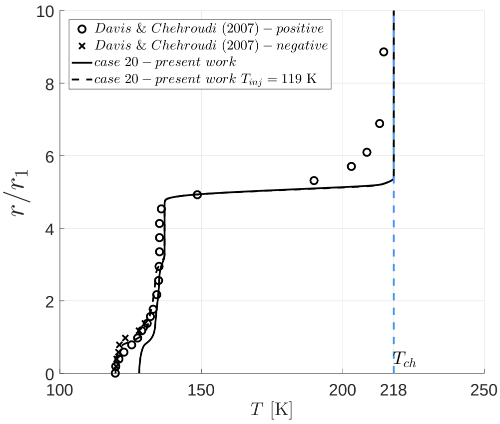

Figure 7.36: Radial temperature profile for case 20.

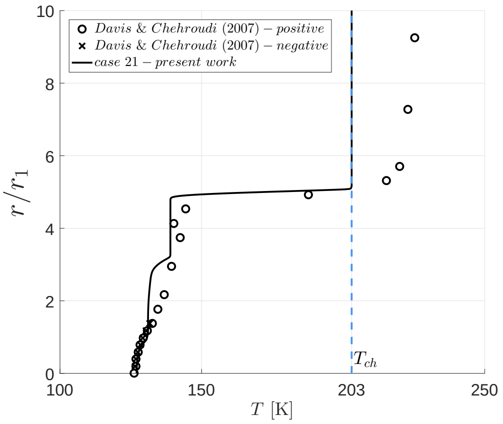

Figure 7.37: Radial temperature profile for case 21.

7.6.2 High Outer-jet Temperature

Lastly, it remains to consider the supercritical cases with high outer-jet temperature (Figure 7.38). Additionally, another test case is evaluated following the LES simulations of Liu et al. [283] who considered injection velocities and the consequent VR following the SSME pre-burner. The five test cases injection and chamber condition are summarized in Table 7.7.

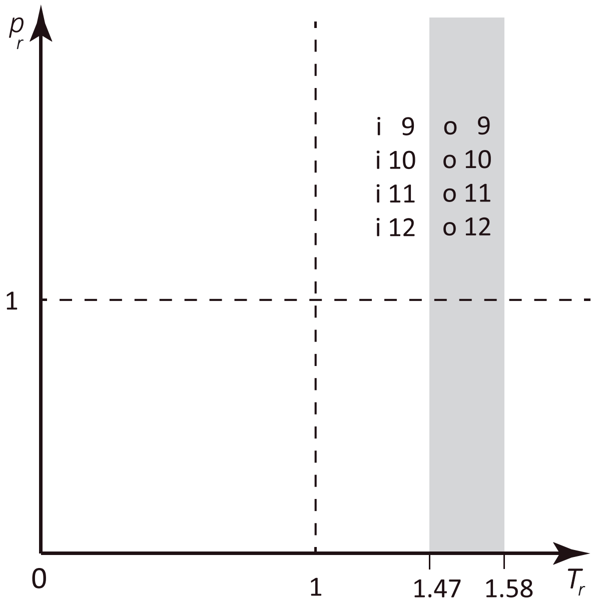

Figure 7.38: Supercritical high temperature case distribution.

Table 7.7: Conditions for the low outer-jet temperature cases [129] and SSME [283].

Case	p_∞ [MPa]	T_∞ [K]	T_i [K]	T_o [K]	v_i [m s^{-1}]	v_o [m s^{-1}]	VR [-]	M [-]
9	4.97	240	128	188	2.9	4.4	1.5	0.5
10	4.95	237	129	190	3.0	10.9	3.6	2.7
11	4.94	228	133	185	3.9	16.8	4.3	5.1
12	4.94	233	132	191	3.6	22.5	6.3	9.6
SSME	4.94	233	132	191	32	120	3.75	3.44

Radial temperature profiles are compared in Figures 7.39, 7.40, 7.41 and 7.42, corresponding to cases 9, 10, 11 and 12, respectively. Through the analysis of the figures, it was observed that as the momentum ratio, the size of the recirculation region formed at the post tip increases, similarly to the results obtained for the near-critical high outer-jet temperature cases, which again shows that the state in which the outer jet enters the chamber will greatly impact mixing and the coaxial jet evolution.

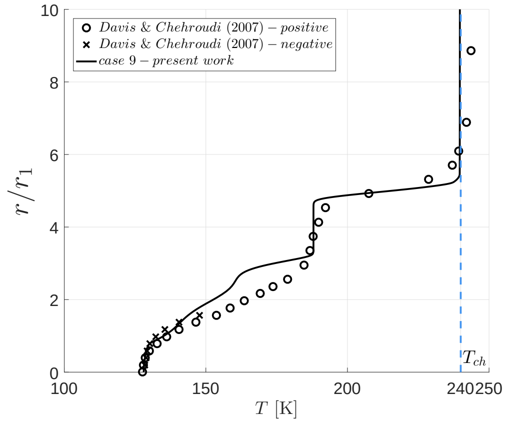

Figure 7.39: Radial temperature profile for case 9.

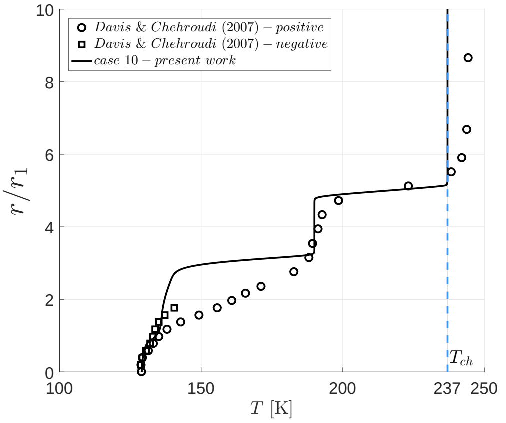

Figure 7.40: Radial temperature profile for case 10.

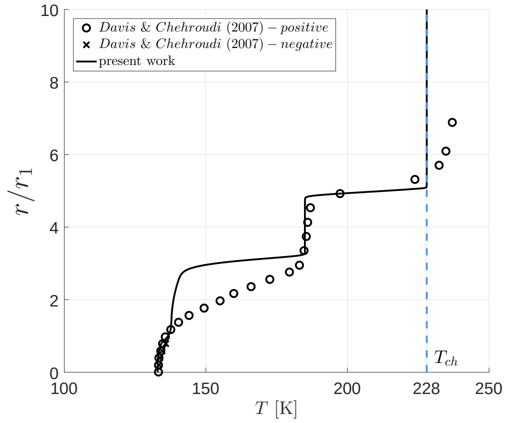

Figure 7.41: Radial temperature profile for case 11.

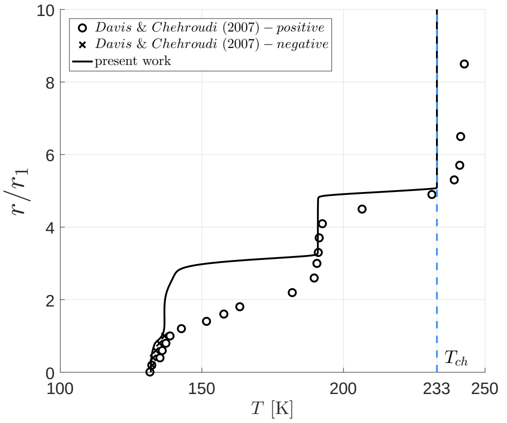

Figure 7.42: Radial temperature profile for case 12.

In Figure 7.43 a comparison is made between the LES results of Liu et al. [283] for the SSME pre-burner, experimental test cases 9 to 12, and the results obtained with the present approach. Since Liu et al. [283] increases the velocity of both inner and outer jets tenfold, the temperature profile is extracted at an axial distance also increased by tenfold considering the experimental measurement plane. As such, it allows for comparison further downstream of the jet in a region without recirculation zones affecting the radial profile. As the figure indicates, a similar radial temperature profile is retrieved compared to Liu et al. [283].

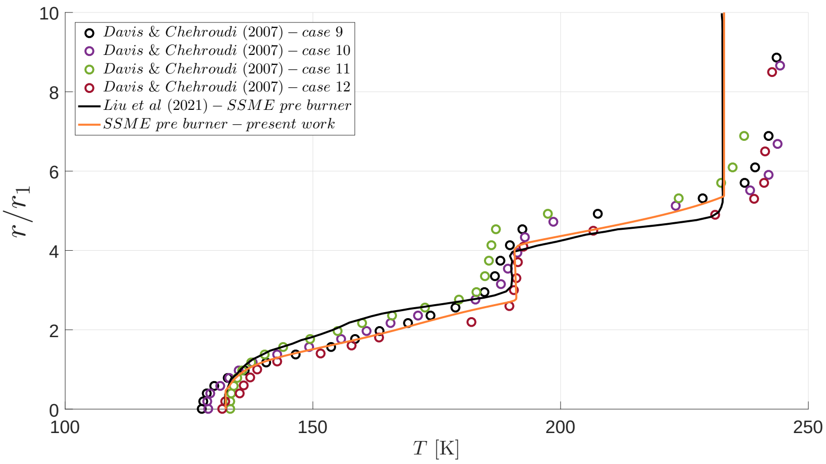

Figure 7.43: Space Shuttle Main Engine (SSME)pre-burner simulation and comparison with the DNS results of Liu et al. [283].

Figure 7.44 depicts the velocity field of case 10 with a VR of 3.6 and a M of 2.7 for supercritical inner jet injection conditions. Similar to case 1, two counter-rotating recirculations are observed at the post tip between the two jets. Increasing the velocity ratio to 4.3 and the momentum ratio to 5.1, the velocity field of case 11 is depicted in Figure 7.45. Through the comparison of both fields, it is observed that the velocity ratio increase promoted the change in the position of the recirculations from x/d_1 of 2.5 to 3.0. It is impossible to observe the inner jet blockage at supercritical conditions, even for velocity ratios higher than two. This could be due to the temperature profile inside the injector and the different coupling mechanisms between subcritical and supercritical conditions added to the influence of surface tension at subcritical conditions.

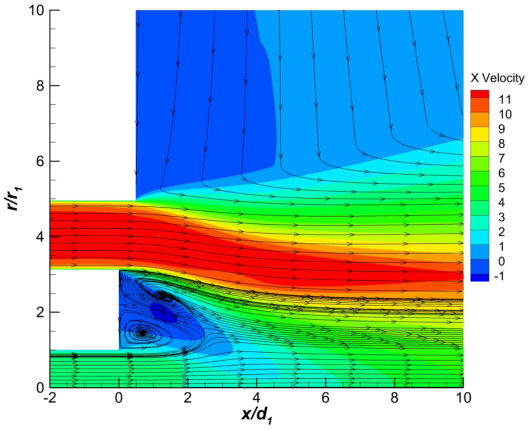

Figure 7.44: Case 10 velocity field and recirculation.

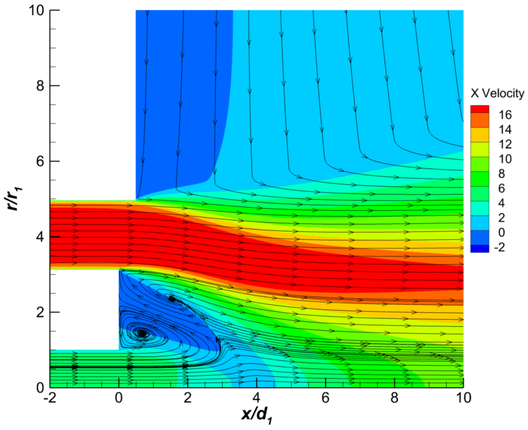

Figure 7.45: Case 11 velocity field and recirculation.

7.7 Summary

The evaluation of single species nitrogen injected through a shear coaxial injector where the main stream is recessed concerning the coaxial one was evaluated for conditions ranging from subcritical to supercritical for different temperatures and outer-to-inner jet velocity ratios. As a result, recirculation regions are formed at either the jet axis or the post between both jets. Finally, it is detailed the outer-jet influence in the formation of the recirculation zones, depending on if injection happens under liquid- or gas-like conditions.

Chapter 8

Coaxial Multi-species Injection

In this chapter, multi-component N_2–H_2 mixing is looked into. A coaxial injection configuration is considered with nitrogen injected through the main annulus and hydrogen through the coaxial one into a quiescent nitrogen environment. In this way, the incompressible but variable density hypothesis evaluation is extended to multi-species mixtures.

8.1 Introduction

Phase and pseudo-phase transitions in mixtures of supercritical fluids entail more complex mechanisms and highly coupled phenomena. Currently, the evaluation of multi-species mixing still requires much research to improve the state of the art [126], for instance, in the evaluation of mixture properties. Multi-species coaxial injection [6] is a more complex phenomenon to simulate than single species injection but is of paramount importance in the design of LREs. For instance, the critical properties of the mixture are not fixed values, being subjected to a local dynamical evolution [288]. These need to be taken into account through mixing rules. Harstad et al. [187] defined simple mixing rules and performed a thermodynamically consistent fluid property derivation used to study Dufour and Soret effects at supercritical conditions through DNS [22, 289] or LES [290] in a C_7H_{16}–N_2 mixture and characteristic BCs in multi-species mixing [291]. Moreover, experimental measurements carried out by Traxinger et al. [292] on O_2–H_2 and CH_4–O_2 flames indicate that phase separation is dependent upon the injectant-chamber conditions and mixture composition. In contrast, the multi-species DNS study of Masi et al. [293] indicates that within the DNS-achievable Reynolds numbers, mixing behavior at the smallest scales is dictated by thermodynamics and diffusion more so than by the flow motion. On the larger scales, the differences in density inhibit the mixing rate (Chapter 7) and damp turbulence oscillations, the reason behind longer unmixed cores compared with subcritical conditions [56].

One of the earliest works on multi-species mixing that is still used today in the modeling of supercritical mixtures is the Takahashi [294] method for the evaluation of diffusion coefficients. Recently, Yang et al. [295] compared a tabulation method with a method focusing on the dynamic evaluation of real gas properties, considering the O_2–CH_4 mixture. On the other hand, Tudisco and Menon [296] derived an analytical framework to evaluate thermodynamic properties in a multi-species mixture with the possibility of phase separation.

This chapter defines the binary mixture as multi-species with no reaction. There will be two mass conservation equations for each species, with one momentum and energy conservation equation being jet development dictated by turbulent mixing. Each cell volume will contain volume fractions of each species in the mixture.

8.2 The Experiment

The experimental data corresponds to the work of Oschwald et al. [120]. First, nitrogen is injected through the central post, according to the conditions of Table 8.1, as depicted in Figure 8.2 at either supercritical (D4) or transcritical conditions (E4). Next, hydrogen is injected through the coaxial annulus depicted in the same figure.

Table 8.1: Experimental conditions from Oschwald et al. [120].

Case	$v_{N2,jet}$ [$\mathrm{m\,s^{-1}}$]	$T_{N2,jet}$ [K]	$V_{H2,jet}$ [$\mathrm{m\,s^{-1}}$]	T_{H2} [K]	$\rho_{N2,jet}/\rho_{H2}$	$v_{N2,jet}/v_{H2}$
D4	5.0	140	60	270	43.1	0.083
E4	5.0	118	120	270	166	0.042

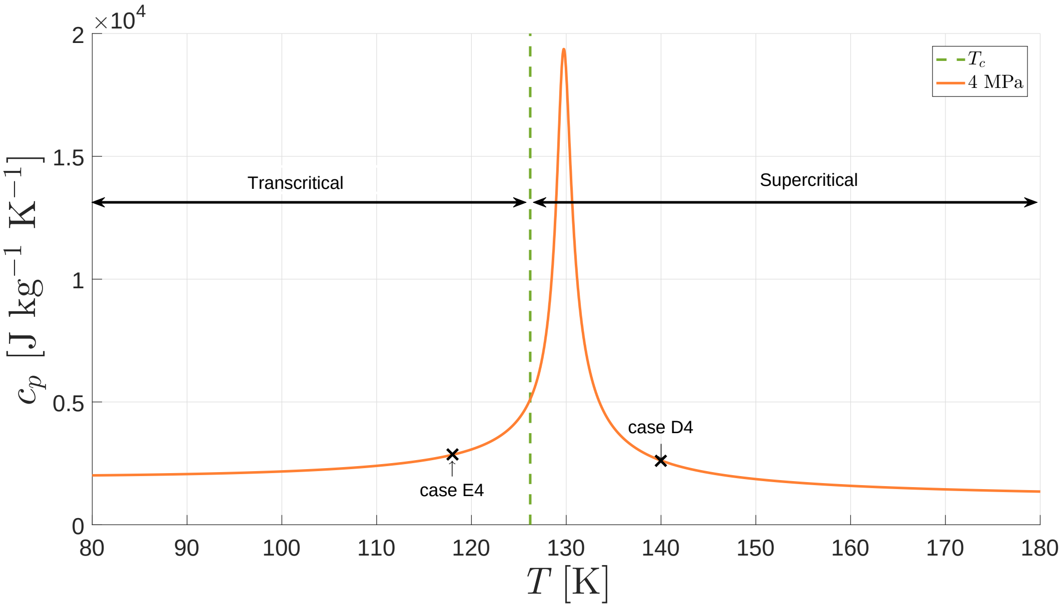

Figure 8.1: Location of the experimental test cases in relation to the critical point of nitrogen.

The injectors have a length of $90\,\mathrm{mm}$, with the central injector having a diameter of $1.9\,\mathrm{mm}$ and the coaxial one $2.4\,\mathrm{mm}$. On the other hand, the combustion chamber measures $500\,\mathrm{mm}$ in length and $100\,\mathrm{mm}$ in diameter. In contrast to the coaxial configuration of Chapter 7, here there is no recess of one stream in relation to the other.

Isothermal walls are considered at the injectors and chamber walls, while an adiabatic wall boundary condition is imposed in the faceplate.

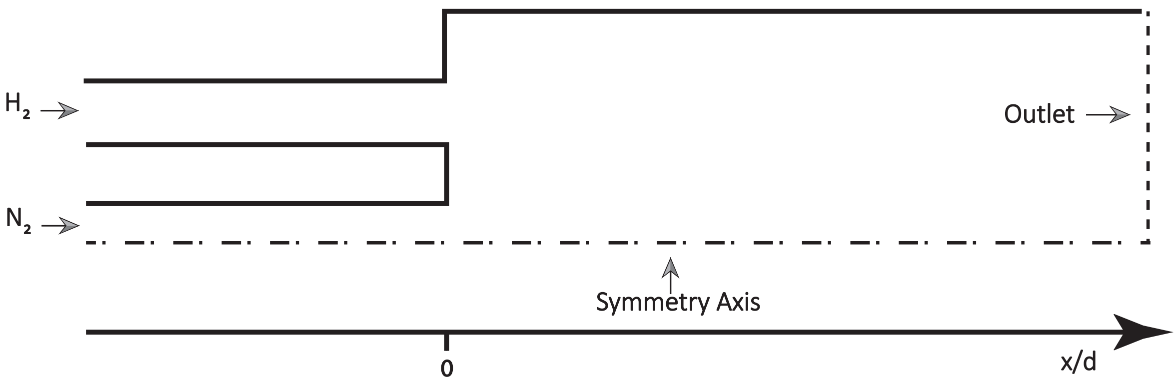

Figure 8.2: Geometry, corresponding to the experiments (not to scale).

8.3 Validation

Figure 8.3 depicts the grid independence study, taking into account the injection conditions of case D4 from Table 8.1. The maximum of the radial nitrogen density profiles are reported as a function of the normalized distance from the injector exit plane, while the error analysis as the grid is progressively refined is looked into in Figure 8.4, where the GCI indicates a convergence rate close to the second-order slope. A summary of the thermophysical models used in the calculations presented in this chapter is given in Table 8.2.

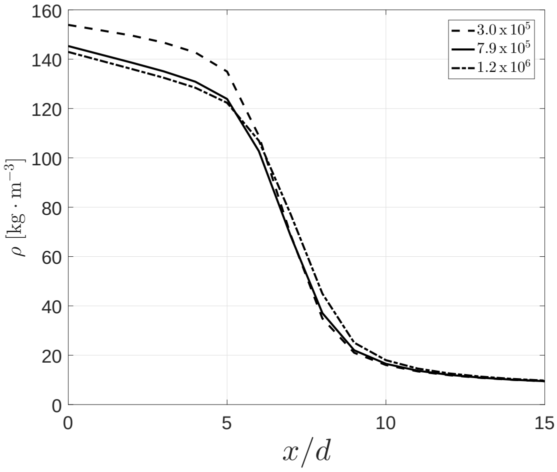

Figure 8.3: Grid Independence Study, corresponding to case D4..

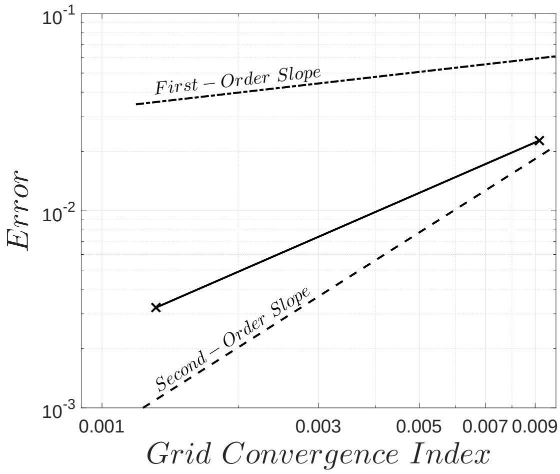

Figure 8.4: Error propagation, corresponding to case D4.

Table 8.2: Summary of thermophysical models.

Turbulence closure	EoS	Transport properties	Mixing Rules
κ–ε standard [175]	PR [184]	Chung et al. [215]	Chung et al. [215]

8.4 Results

Figures 8.5 and 8.6 depict the maximum of nitrogen and hydrogen's radial density profiles for case D4 from Table 8.1. The radial profiles are given in Figures 8.7 and 8.8 for nitrogen and hydrogen, respectively, where the cross mark represents the profiles' maximum values depicted in Figures 8.5 and 8.6.

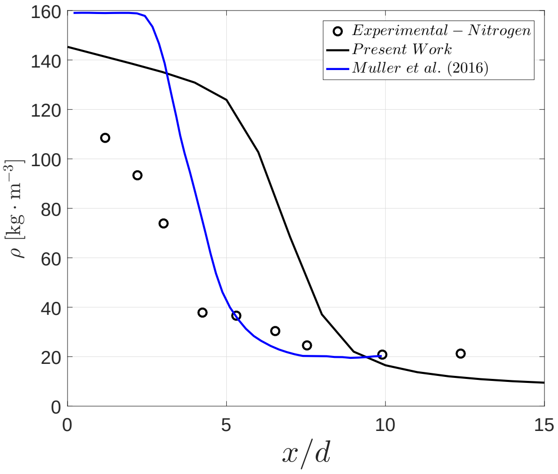

Figure 8.5: Maximum of nitrogen's radial density profiles for case D4 and comparison with LES of Müller et al. [297].

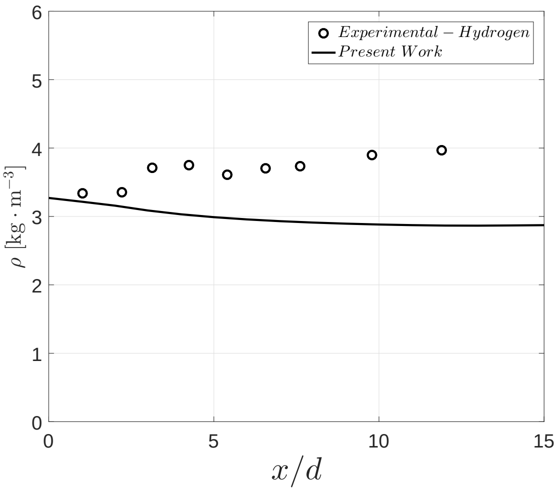

Figure 8.6: Maximum of hydrogen's radial density profiles for case D4.

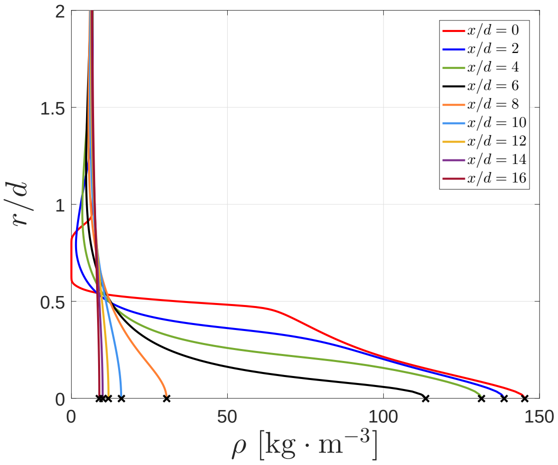

Figure 8.7: Radial profiles of nitrogen for case D4.

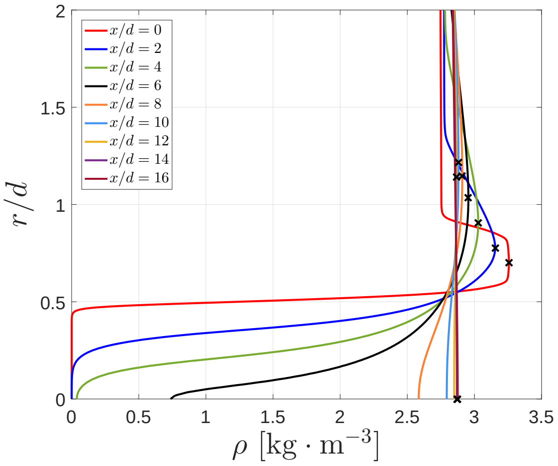

Figure 8.8: Radial profiles of hydrogen for case D4.

In Figure 8.5 the LES results of Müller et al. [297] are also depicted. On the horizontal axis, the centerline distance from the injector exit plane, x, is normalized by the inner injector diameter (d). The experimental measurements from Oschwald et al. [120] are compared with the numerically obtained results following the incompressible but variable density hypothesis, where it is possible to observe a general over-prediction of the maximum radial values both in the present computations and in the results of Müller et al. [297]. While nitrogen's initial qualitative decay rate is captured in the present computations, Müller et al. [297] predict a constant density value for some distance, consistent with the development of a potential core. As described in Chapter 5, the differences are explained due to the heat transfer and pseudo-boiling effects [53] inside the injector, indicating why the density values are different even at $x/d = 0$. Even though different interpretations concerning the role of the injector are made in the present computations and those of Müller et al. [297], no quantitative agreement is found with the experimental data [35]. In this sense, Müller et al. [297] proposes to modify the inflow temperature to match the magnitude of the radial profiles maximum, to pursue a quantitative agreement with the experimental data. Following the data from the NIST, inflow temperature is changed from $140\,\mathrm{K}$ to a fitted value of $158.8\,\mathrm{K}$ as indicated in Table 8.3 and depicted in Figure 8.9, while all other parameters remain unchanged. Figure 8.9 indicates that case D4 - fitted entails a less sharp density variation than case D4.

Table 8.3: Comparison of case D4 initial conditions with fitted inflow temperature.

Case	D4	E4
$v_{N2,jet}$ $[\mathrm{m\,s^{-1}}]$	5.0	5.0
$T_{N2,jet}$ $[\mathrm{K}]$	140	**158.8**
$V_{H2,jet}$ $[\mathrm{m\,s^{-1}}]$	60	60
T_{H2} $[\mathrm{K}]$	270	270

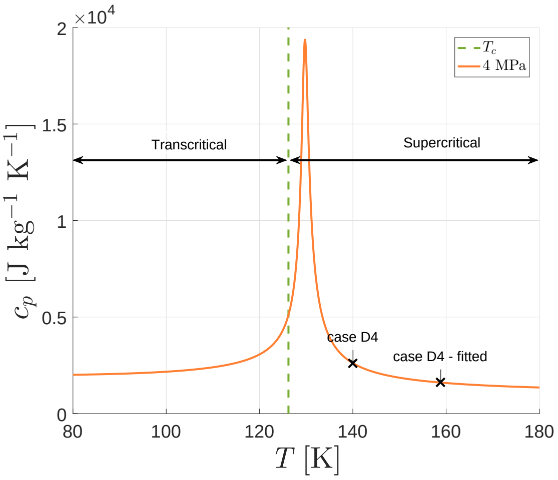

Figure 8.9: Location comparison of experimental case D4 and artifitially fitted case D4.

Figures 8.10 and 8.11 depict the maximum in the radial profiles of nitrogen and hydrogen considering the fitted inflow temperature. As it can be observed, no discernible differences are observed for hydrogen in Figure 8.11 for both inflow temperatures, which was to be expected since, at such temperature variation and a pressure of $4\,\mathrm{MPa}$, the density slope is minimal. On the other hand, several striking features are retrieved on the nitrogen behavior in Figure 8.10. Müller et al. [297] report a closer agreement between the experimental data and the fitted inflow temperature condition; however it is not able to portray the experimental decay rate of nitrogen, owing to not including the heat transfer inside the injector. Moreover, following the incompressible but variable density approach, the initial decay rate of nitrogen is observed. However, since thermal stratification affects the flow inside the injector, heating it and decreasing density, lower densities than experimental values are depicted up to 4 injector diameters. As such, in order to compare the incompressible but variable density hypothesis with the compressible formulation of Müller et al. [297] an additional computation was carried out with the fitted temperature inflow condition but neglecting heat transfer in the injector. As expected, an initial potential core is recovered in the same way as Müller et al. [297], and while some quantitative differences are reported between both formulations from $x/d \approx 4$ to $x/d \approx 6$, the jet behavior is the same.

In Figures 8.12 and 8.13 there is a comparison of a radial profile of nitrogen and hydrogen measured $2\,\mathrm{mm}$ downstream the injector exit place, while the same comparison is highlighted $10\,\mathrm{mm}$ downstream the injector exit plane for nitrogen (Figure 8.14) and hydrogen (Figure 8.15). These are compared with the numerical results obtained following the incompressible but variable density approach while accounting for the heat transfer inside the injectors. Experimental injection temperature of $140\,\mathrm{K}$ is compared with the fitted inflow condition of $158.8\,\mathrm{K}$. These results exhibit the same qualitative and quantitative features as

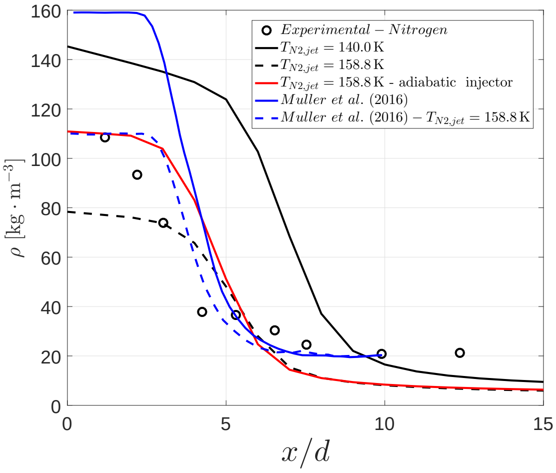

Figure 8.10: Maximum of nitrogen's radial density profiles for case D4 and comparison with LES of Müller et al. [297].

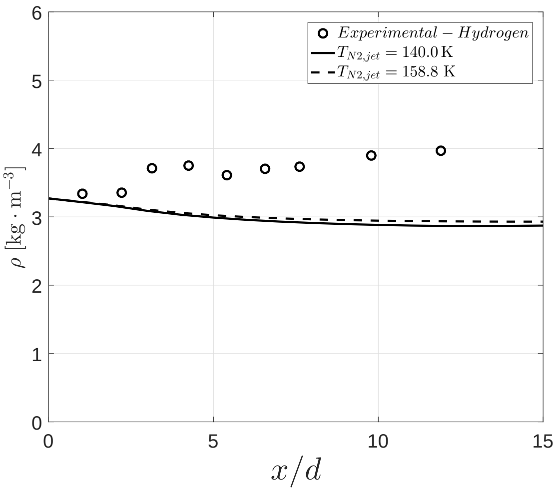

Figure 8.11: Maximum of hydrogen's radial density profiles for case D4.

reported for the maximum in the radial profiles. While in the case of nitrogen, the fitted conditions appear to provide a more qualitative agreement with the experimental data than the experimental one. The differences in the hydrogen radial profiles are less pronounced due to the high pressure considered.

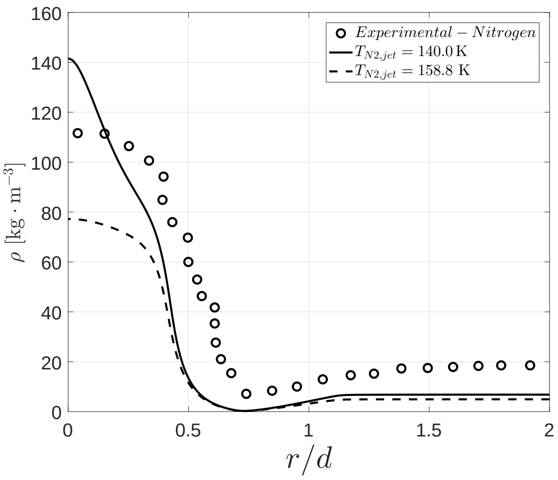

Figure 8.12: Radial nitrogen profile measured, for case D4 $2\,\mathrm{mm}$ downstream the injector exit.

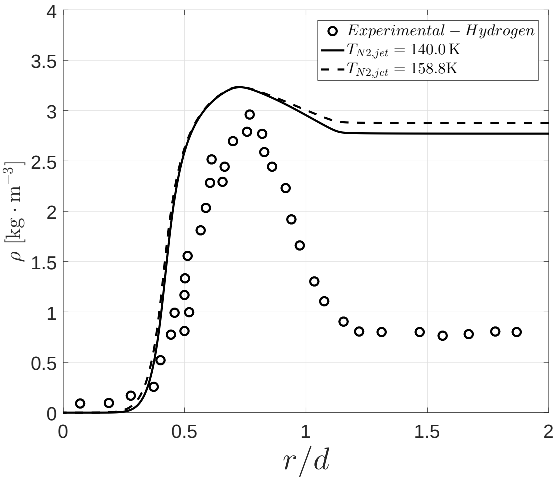

Figure 8.13: Radial hydrogen profile measured, for case D4 $2\,\mathrm{mm}$ downstream the injector exit.

For case E4, the injection takes place ($T_{N2,jet} = 118\,\mathrm{K}$) below the critical temperature of nitrogen ($T_{N2,c} = 126.2\,\mathrm{K}$). The maximum values of nitrogen's and hydrogen's radial density profiles are depicted in Figures 8.16 and 8.17, respectively, taken from Figures 8.18 and 8.19.

Like case D4, an over-prediction in terms of the density values is evident. The present results indicate a minimal decay rate of the nitrogen's density maximum spanning the first four injector diameters, from where the decay rate grows steeper due to entrainment from the hydrogen stream and chamber nitrogen into the jet. Moreover, Müller et al. [297] predict a potential core with a length of 2 injector diameters, also with a density much higher than the one measured experimentally. Here two more results are depicted, following the compress-

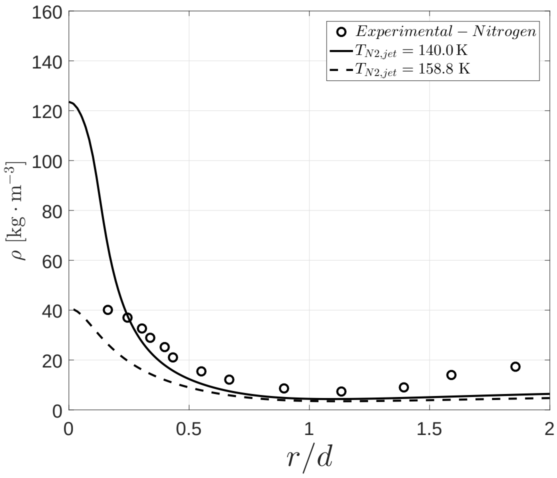

Figure 8.14: Radial nitrogen profile measured, for case D4 10 mm downstream the injector exit.

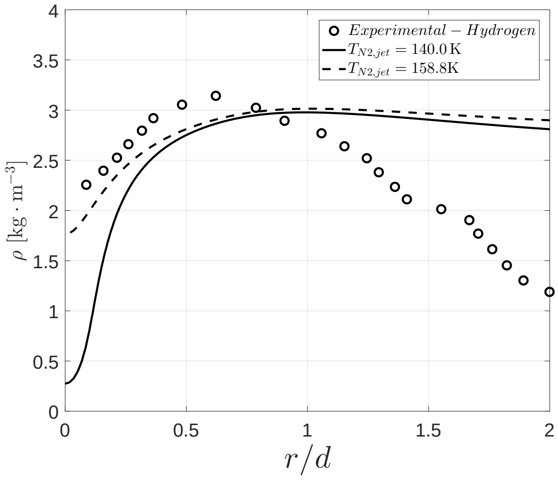

Figure 8.15: Radial hydrogen profile measured, for case D4 10 mm downstream the injector exit.

ible formulation of Jafari et al. [298], comparing PR and SRK cubic EoSs, showcasing fairly similar results to Müller et al. [297]. Accordingly, a fitted temperature ($T_{N2,jet} = 128.8\,\mathrm{K}$) is proposed (Table 8.4). However, by going from the experimental injection temperature of $120\,\mathrm{K}$ to the fitted value of $128.8\,\mathrm{K}$, one moves from the transcritical regime to a supercritical liquid-like injection (Figure 8.20). Nevertheless, Figure 8.21 shows similar results between Müller et al. [297] compressible formulation and the incompressible but variable density approach. Concerning the hydrogen density evolution, Figure 8.22 depicts a distinct behavior than observed in case D4. Here, hydrogen density is highly susceptible to nitrogen's injection temperature change. The increase in the H_2 density is in accord with the conclusions of Chehroudi et al. [86] owing to the entrainment of H_2 into the central N_2 stream, leading to a decrease in H_2 temperature and the density increase.

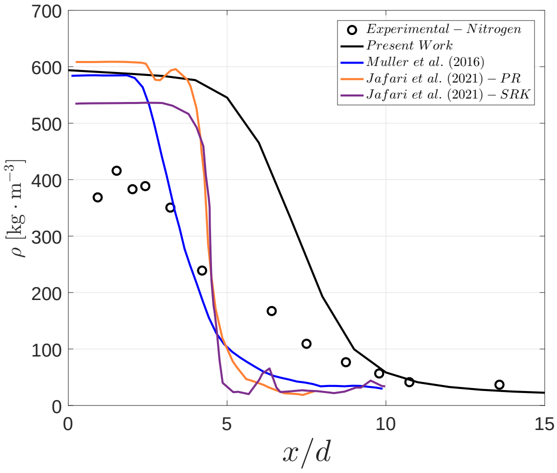

Figure 8.16: Maximum of nitrogen's radial density profiles for case E4 and comparison with LES of Müller et al. [297] and Jafari et al. [298].

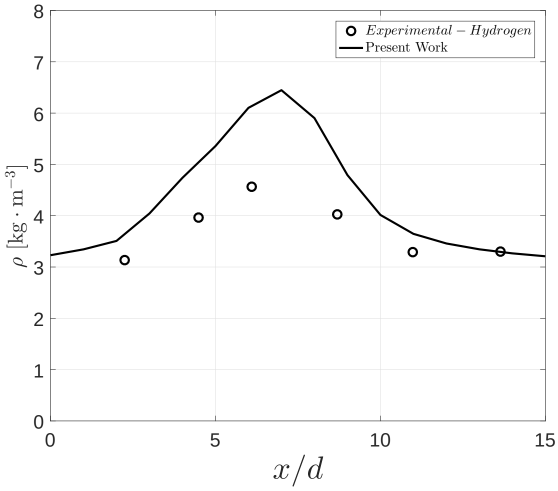

Figure 8.17: Maximum of hydrogen's radial density profiles for case E4.

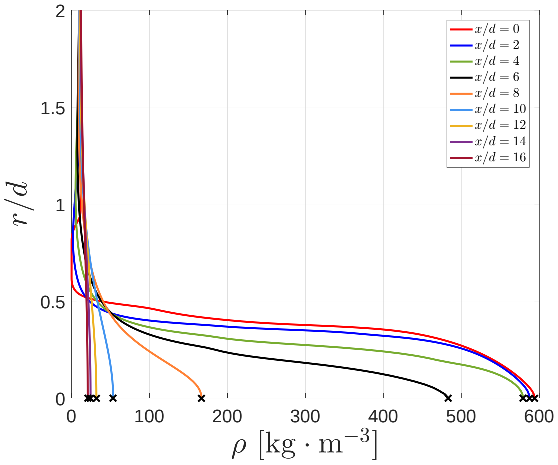

Figure 8.18: Radial profiles of nitrogen for case E4.

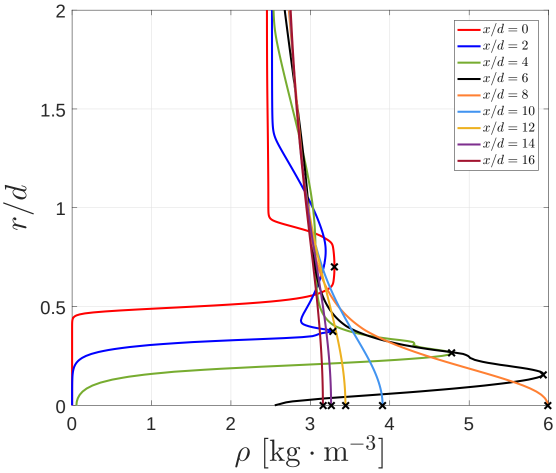

Figure 8.19: Radial profiles of hydrogen for case E4.

Table 8.4: Comparison of case E4 initial conditions with fitted inflow temperature.

Case	D4	E4
$v_{N2,jet}$ [m s^{-1}]	5.0	5.0
$T_{N2,jet}$ [K]	118	**128.8**
$V_{H2,jet}$ [m s^{-1}]	120	120
T_{H2} [K]	270	270

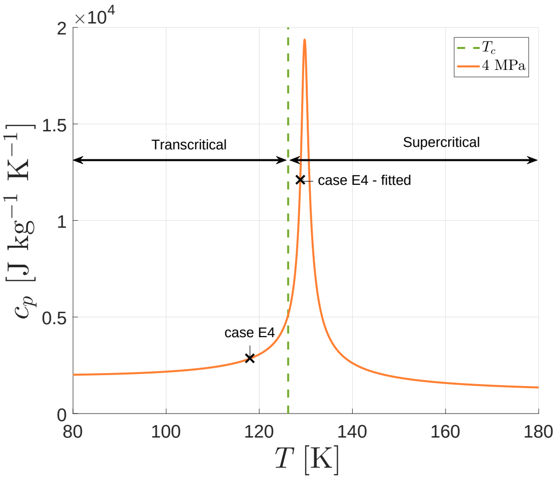

Figure 8.20: Location comparison of experimental case E4 and artifitially fitted case E4.

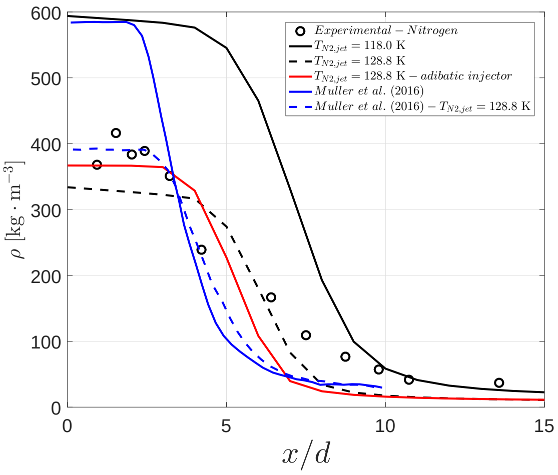

Figure 8.21: Maximum of nitrogen's radial density profiles for case E4 and comparison with LES of Müller et al. [297] and Jafari et al. [298].

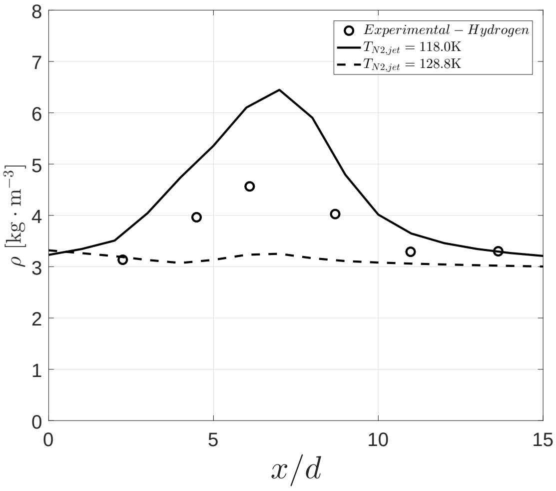

Figure 8.22: Maximum of hydrogen's radial density profiles for case E4.

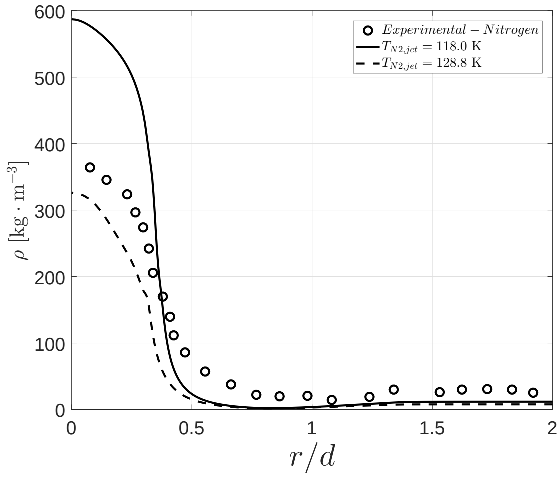

Figure 8.23: Radial nitrogen profile measured, for case E4 $4\,\mathrm{mm}$ downstream the injector exit.

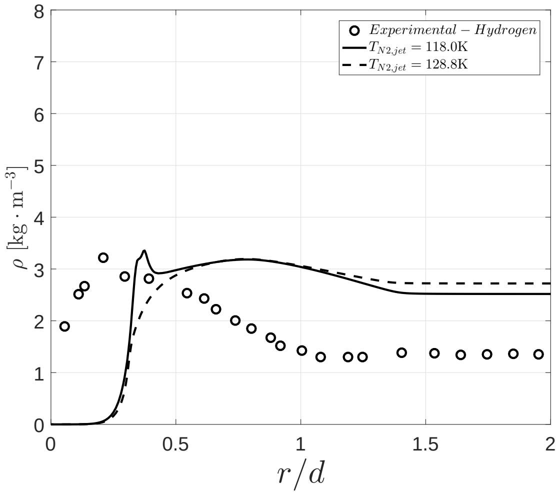

Figure 8.24: Radial hydrogen profile measured, for case E4 $4\,\mathrm{mm}$ downstream the injector exit.

8.5 Summary

The evaluation of multi-species coaxial injection was reported, following the incompressible but variable density approach. In addition, transcritical and supercritical nitrogen injection conditions are considered concerning pure nitrogen fluid. The comparison with the results from compressible formulations available in the literature indicates similar predictions, highlighting the suitability of the proposed hypothesis in the description of multi-species mixing. Nevertheless, more experimental data on mixture injection and mixing are needed for a more detailed comparison.

Chapter 9

Conclusions

This chapter summarizes the main contributions of this work and discusses recommendations for the future.

9.1 Contributions

This work was carried out to shed light on the behavior of fluids at transcritical and supercritical conditions, relevant to the operation of liquid propelled rocket engines, where at least one of the propellants is injected into the combustion chamber at conditions above its critical point. In addition, mixing behavior characterization is analyzed at geometries of increasing complexity from single to multi-species coaxial injection.

An alternative methodology to the compressible formulations commonly encountered in the literature is investigated, resulting from the similarity of visualization data with turbulent gaseous jets. This alternative methodology (Reynolds-averaged Navier-Stokes), focusing on an incompressible but variable density description of high-pressure jets, was described and compared with numerical predictions from more complex large eddy simulation and direct numerical simulation solvers available in the literature, highlighting its capabilities in the prediction of mean quantities and spreading rates and depicting the variable density nature of injection at transcritical and supercritical conditions.

The present numerical results also suggest that the heat transfer inside the injector is of paramount importance in the ability of numerical solvers to replicate transcritical and supercritical phenomena. While this has previously been demonstrated for gas-like conditions, after a pseudo-transition across the Widom line takes place, this document demonstrates for the first time that heat transfer in the injector contributes to a more prolonged potential core stabilization under liquid-like conditions. Furthermore, in contrast to the experimentally observed plateau-type core, similar behavior to the sloped core formation registered for supercritical gas-like conditions is found under transitional conditions. Nonetheless, by comparison with various quantitative experimental measurements, it is hypothesized that plateau type cores' formation is related to low injection velocities.

The temperature field validation on nitrogen coaxial injection from subcritical to supercritical conditions at high-velocity ratios (outer-to-inner), where the main (inner) stream is recessed relatively the outer stream, is of paramount importance in the flame stabilization operation of liquid rocket motors. The velocity ratio effect is characterized by the temperature field evaluation at such a broad range of conditions. As the outer stream velocity increases, mixing is enhanced, reducing the potential core length and increasing jet spreading, which is more pronounced in terms of temperature, demonstrating that heat propagation is dominant over momentum transport. The evaluation of injection velocities corresponding to the space shuttle main engine pre-burner agrees with the experimental data and large eddy simulation solvers from the literature. Currently, this is one of the few numerical solvers available, validated in density and temperature field predictions.

Finally, coaxial multi-species injection is considered. While some uncertainties exist concerning the experimental data, which does not allow for a quantitative comparison of the mean density, similar predictions are obtained to those of large eddy simulations based on compressible formulations.

Exploratory studies on the suitability of different EoS such as the cubic PR and SRK and a multiparameter EoS framed in reduced Helmholtz energy were attempted. Moreover, incorporating a variable turbulent Prandtl number model in the system of PDEs, which is sporadically mentioned in the literature as a means to obtain a more accurate jet representation, was also carried out for a variety of models. Suppose, as reviewed, different EoS are especially suited for a given regime, temperature range, or computational architecture (in what the computational cost concerns). In that case, acknowledging their advantages and limitations is, in principle, sufficient to contextualize the accuracy of the obtained results. On the other hand, while the notion of a variable turbulent Prandtl number formulation seems an exciting concept, in theory, the results appear to be inconclusive after testing several models at transcritical and supercritical injection conditions. While these analyses are not included in this document's final version, they are available in the publications listed in Appendix A.

9.2 Synthesis

The Supercritical Regime: Characteristics of supercritical and transcritical regimes are reviewed for pure fluids and multi-component mixtures along with descriptions of non-linear behaviors of the various thermophysical parameters at and around the critical point and the implications of these non-linearities for an accurate physical and numerical modeling. An analysis of available experimental data sets indicates the type of information which can be inferred and how it impacts the development of numerical solvers and methods.

Physical and Numerical Modeling: The mass, momentum, and energy conservation principles are reviewed, taking into account the incompressible but variable density approach followed. Then different equations of state ranging from simple cubic formulations to more sophisticated multiparameter are reviewed. Considering their advantages and limitations, the choice of the Peng-Robinson equation of state is justified and the thermal formulation specified. Different methods for evaluating transport properties are also reviewed to be used depending on the chemical species under consideration. These are based on the departure function formalism, where departure functions are added to the ideal gas value to account for the real gas effects. Moreover, in the case of properties subjected to critical divergence, such as thermal conductivity, a third term can be included to replicate the thermophysical behavior more accurately. The system of partial differential equations is then discretized following the appropriate finite volume/finite difference method, and the appearance of non-physical spurious pressure oscillations owing to the equation of state solving and the Widom line crossing is discussed. These substantially affect large eddy simulation solvers for which reliable numerical methods have been developed but are appropriately taken care of in Reynolds-averaged Navier-Stokes solvers through the inclusion of numerical diffusion.

Supercritical Single Species Injection: The injection of supercritical nitrogen into a quiescent environment is considered. As previously described in the literature, the injector heat transfer is considered, using jet thermal breakup to complement the classical mechanical description of jet breakup. By comparing adiabatic and isothermal boundary conditions at the injector wall, injector heat transfer is highlighted for injection conditions at liquid-like, gas-like, and transitional conditions. In injection at gas-like conditions, a sloped core (the immediate decay of axial density) is retrieved at the combustion chamber entrance for isothermal boundary conditions, in accord with previous literature results. On the other hand, its importance is also shown for injection under liquid-like and transitional conditions. In liquid-like conditions where dense potential cores are formed, adiabatic and isothermal boundary conditions are similar in jet stabilization. However, the isothermal injector leads to a more prolonged stabilization of the potential core. At transitional conditions, the intermediate plateau type core is not retrieved; instead, a similar jet behavior to injection at gas-like conditions is observed.

Transcritical Single Species Injection: Analysis is extended to the injection of nitrogen at transcritical conditions into a quiescent environment. In addition to assessing axial density decay, jet spreading rates in terms of density and temperature are also looked into, which serve as a measure of mixing efficiency. These indicate that heat propagation is dominant over momentum transport. Moreover, the formation of the previously identified and computed transitional supercritical regime is hypothesized to be derived from the low-injection velocities. Good confidence is obtained from the results, which indicate that phase separation nonetheless takes place at transcritical injection conditions, and surface tension and interface formation may have a role in this plethora of highly coupled phenomena.

Coaxial Single Species Injection: The next step focused on the analysis of coaxial nitrogen injection into a quiescent environment. Nitrogen was injected from the main and coaxial streams at different outer-to-inner jets velocity ratios. Moreover, the main stream is recessed concerning the coaxial one, allowing for more detailed near injector mixing to be obtained, albeit with an increase in geometry complexity. Since the experimental measurements detail radial temperature profiles, the evaluation of the incompressible but variable density hypothesis is extended to coaxial injection and the temperature field validation.

Coaxial Multi-species Injection: Finally, coaxial multi-species injection is considered at transcritical and supercritical conditions. Nitrogen is injected through the main stream with a higher velocity, co-flowing hydrogen into a quiescent environment filled with nitrogen as a precursor to combustion and chemically reacting injection. Although uncertainties exist concerning the experimental data, which does not allow for a quantitative comparison with experimental data, the incompressible but variable density approach provides similar results to compressible formulations based on large eddy simulation.

9.3 Recommendations

Transcritical and supercritical phenomena, in the field of fuel injection in propulsive systems, are still far from being completely understood, especially in multi-species mixing.

Accurate Experimental Data: Relevant conditions at injection which are not available from current experimental data and a broader range of experimental conditions describing mixing between various mixtures would allow for the generalization of conclusions and to extend current theories.

Phase Separation: Contradictions in theories between subcritical, transcritical, and supercritical conditions hinder the development of more accurate models. Especially in transcritical conditions where phase separation, the influence of two-phase interfaces needs to be addressed to determine its influence on mixing and how it could be coupled to the numerical method.

Application to Combustion and Chemically Reacting Conditions: The continuous increase in complexity leads inevitably to the inclusion of combustion and chemically reacting effects into the computations, for which the incompressible but variable density approach needs to be tested.

Appendix A

List of Publications

During the present work several journal and conference papers were published related to the work carried out during this doctoral thesis.

A.1 Journal Publications

- L. Magalhães, F. Carvalho, A. Silva and J. Barata. Turbulence Quantification in Supercritical Nitrogen Injection, Energies 13(7), 1586, 2020, doi: 10.3390/en13071586. Also available as a chapter in book: L. Magalhães, A. Silva and J. Barata. Turbulence Quantification in Supercritical Nitrogen Injection. In M.C. and J.S. (Eds.). Selected Papers from the ICEUBI2019–International Congress on Engineering–Engineering for Evolution, MDPI: Basel, Swit-zerland, 2021, doi: 10.3390/books978-3-0365-0669-2.

- R. Meireles, L. Magalhães, A. Silva and J. Barata. Description of a Eulerian–Lagrangian Approach for the Modeling of Cooling Water Droplets, Aerospace 8(9), 270, 2021, doi: 10.3390/aerospace8090270.

- L. Magalhães, A. Silva and J. Barata. Contribution to the Physical Description of Supercritical Cold Flow Injection: The Case of Nitrogen, Acta Astronautica, 190, 251-260 2022, doi: 10.1016/j.actaastro.2021.09.044.

- R. Meireles, L. Magalhães, A. Silva and J. Barata. Computational Modeling of Water Droplets under Cooling and Freezing Conditions, International Review of Aerospace Engineering (IREASE), 2022, doi: 10.15866/irease.v15i2.21571.

A.2 Conference Publications

- L. Magalhães, E. Antunes, A. Silva and J. Barata. Cubic and Multiparameter Equation of State Evaluation for Supercritical Flow Modeling. Proceedings of the Thermal and Fluids Engineering Summer Conference (TFEC), Las Vegas, NV, USA, TFEC–2019–28385, 2019, doi: 10.1615/TFEC2019.ref.028385.

- L. Magalhães, F. Carvalho, A. Silva and J. Barata. Turbulence Quantification in Supercritical Nitrogen Injection: An Analysis of Turbulence Models. ICEUBI 2019 - International Congress on Engineering - Engineering for Evolution, Covilhã, Portugal, 2019, doi: 10.18502/keg.v5i6.7052.

- L. Magalhães, A. Silva and J. Barata. Locally Variable Turbulent Prandtl Number Considerations on the Modeling of Liquid Rocket Engines Operating Above the Critical Point. ILASS Europe 2019 - 29th European Conference on Liquid Atomization and Spray, Paris, France, 2019.

- L. Magalhães, A. Silva and J. Barata. The Role of Injector Heat Transfer in Supercritical Injection Phenomena. AIAA Propulsion and Energy 2020 Forum, New Orleans, MS, USA, AIAA paper 2020–3658, 2020, doi: 10.2514/6.2020-3658.

- L. Magalhães, A. Silva and J. Barata. Injector Wall Heat Transfer Quantification in Supercritical Nitrogen Injection. 7th Edition of the Space Propulsion Conference, Estoril, Portugal, 519, 2021.

- R. Meireles, L. Magalhães, A. Silva and J. Barata. Characterization of a Two-Way Coupling Approach for the Simulation of Fluid Flows under Cryogenic Conditions. 15th International Conference on Heat Transfer, Fluid Mechanics and Thermodynamics, Amsterdam, Netherlands, 2021.

- L. Magalhães, A. Silva and J. Barata. Computational Analysis of High-Pressure Nitrogen Jets from Transcritical to Supercritical Gas-Like Conditions. AIAA Propulsion and Energy Forum 2021, Denver, CO, USA, AIAA paper 2021–3341, 2021, doi: 10.2514 /6.2021-3341.

- L. Magalhães, A. Silva and J. Barata. Computational Study on Coaxial Nitrogen Hydrogen Injection at Supercritical Conditions. AIAA Science and Technology Forum 2022, San Diego, CA, USA, AIAA paper 2022–0877, 2022, doi: 10.2514/6.2022-0877.

- L. Magalhães, A. Silva and J. Barata. Coaxial Injection of Hydrogen-Nitrogen at Supercritical Conditions. 8th Edition of the Space Propulsion Conference, Estoril, Portugal, 007, 2022.

- L. Magalhães, A. Silva and J. Barata. Description of an Incompressible Variable Density Approach for the Modeling of Supercritical Fluid Flows. 8th Edition of the Space Propulsion Conference, Estoril, Portugal, 005, 2022.

- L. Magalhães, R. Meireles, A. Silva and J. Barata. Numerical Modeling of Freezing Water Droplets. Proceedings of the Thermal and Fluids Engineering Summer Conference (TFEC), Las Vegas, NV, USA, TFEC–2022–40881, 2022, doi: 10.1615/TFEC2022.fnd.040881.

- L. Magalhães, A. Silva and J. Barata. On the Stratification of Density at Supercritical Liquid-like Conditions. Proceedings of the Thermal and Fluids Engineering Summer Conference (TFEC), Las Vegas, NV, USA, TFEC–2022–40878, 2022, doi: 10.1615 /TFEC2022.aes.040878.

- L. Magalhães, A. Silva and J. Barata. Temperature Field Validation on Supercritical Coaxial Injection. EUCASS-3AF, Lille, France, 2022, doi: 10.13009/EUCASS2022-7327.

Bibliography

[1] I. Pioro and S. Mokry, *Heat Transfer – Theoretical Analysis, Experimental Investigations and Industrial Systems.* InTech, 2011, ch. Thermophysical Properties at Critical and Supercritical Conditions, pp. 482–504. 1

[2] T. Clifford, *Fundamentals Of Supercritical Fluids*, reprinted 2002 ed. Oxford University Press, 1999. 1

[3] Ž. Knez, E. Markočič, M. Leitgeb, M. Primožič, M. K. Hrnčič, and M. Škerget, "Industrial Applications of Supercritical Fluids: A Review," *Energy*, vol. 77, pp. 235–243, 2014. 1, 4

[4] T. J. Yoon and Y.-W. Lee, "Current Theoretical Opinions and Perspectives on the Fundamental Description of Supercritical Fluids," *The Journal of Supercritical Fluids*, vol. 134, pp. 21–27, 2018. 1, 4

[5] R. Quentmeyer, "Rocket Combustion Chamber Life-enhancing Design Concepts," in *26th Joint Propulsion Conference*, AIAA paper 90–2116, 1990. 2

[6] H. Immich and W. Mayer, "Cryogenic Liquid Rocket Engine Technology Developments within the German National Technology Programme," in *33rd Joint Propulsion Conference and Exhibit*, AIAA paper 1997–2822, 1997. 2, 153

[7] O. J. Haidn, *Advances on Propulsion Technology for High-speed Aircraft.* NATO Research and Technology Organisation, 2008, ch. Advanced Rocket Engines, pp. 6–40. 2

[8] B. Chehroudi, D. Talley, and E. Coy, "Initial Growth Rate and Visual Characteristics of a Round Jet into a Sub- to Supercritical Environment of Relevance to Rocket, Gas Turbine, and Diesel Engines," in *37th Aerospace Sciences Meeting and Exhibit*, AIAA paper 1999–0206, 1999. 2, 31, 32, 93

[9] J. Hickey, P. C. Ma, M. Ihme, and S. Thakur, "Large Eddy Simulation of a Shear Coaxial Rocket Injector: Real Fluid Effects," in *49th AIAA/ASME/SAE/ASEE: Joint Propulsion Conference*, AIAA paper 2013–407,1 2013. 3, 60, 82, 84

[10] D. Ayyappan, A. Kumar, A. Vaidyanathan, and K. Nandakumar, "Study on Instability of Circular Liquid Jets at Subcritical to Supercritical Conditions Using Dynamic Mode Decomposition," *Physics of Fluids*, vol. 32, no. 1, p. 014107, 2020. 3, 5, 24

[11] L. Qiu and R. D. Reitz, "Simulation of Supercritical Fuel Injection with Condensation," *International Journal of Heat and Mass Transfer*, vol. 79, pp. 1070–1086, 2014. 3

[12] S. P. Duran, J. M. Porter, and T. E. Parker, "Picosecond Ballistic Imaging of Diesel Injection in High-Temperature and High-Pressure Air," *Experiments in Fluids*, vol. 56, no. 84, pp. 1–12, 2015. 3, 7

[13] X. Wang, H. Huo, U. Unnikrishnan, and V. Yang, "A Systematic Approach to High-fidelity Modeling and Efficient Simulation of Supercritical Fluid Mixing and Combustion," *Combustion and Flame*, vol. 195, pp. 203–215, 2018. 3

[14] F. Ries and A. Sadiki, "Supercritical and Transcritical Turbulent Injection Proccesses: Consistency of Numerical Modeling," *Atomization and Sprays*, vol. 31, no. 5, pp. 37–71, 2021. 3, 92, 115

[15] J. Thangaraja and C. Kannan, "Effect of Exhaust Gas Recirculation on Advanced Diesel Combustion and Alternate Fuels - A Review," *Applied Energy*, vol. 180, pp. 169–184, 2016. 3

[16] D. Zhao, Z. Lu, H. Zhao, X. Y. Li, B.Wang, and P. Liu, "A Review of Active Control Approaches in Stabilizing Combustion Systems in Aerospace Industry," *Progress in Aerospace Sciences*, vol. 97, pp. 35–60, 2018. 3

[17] "Strategic research and innovation agenda: The proposed European Partnership for Clean Aviation," http://clean-aviation.eu/files/Clean_Aviation_SRIA_R1_for_public__consultation.pdf, 2020, acessed 16 October 2020. 4

[18] G. Brunner, "Applications of Supercritical Fluids," *Annual Review of Chemical and Biomolecular Engineering*, vol. 1, no. 1, pp. 321–342, 2010. 3

[19] D. Haeseler, F. Haidinger, L. Brummer, J. Haberle, and P. Luger, "Development and Testing Status of the Vinci Thrust Chamber," in *48th AIAA/ASME/SAE/ASEE Joint Propulsion Conference & Exhibit*, AIAA paper 2012–4334, 2012.

[20] G. Lacaze, A. Misdariis, A. Ruiz, and J. Oefelein, "Analysis of High-Pressure Diesel Fuel Injection Processes Using LES with Real-Fluid Thermodynamics and Transport," *Proceedings of the Combustion Institute*, vol. 35, no. 2, pp. 1603–1611, 2015. 3

[21] S. Lebonnois and G. Schubert, "The Deep Atmosphere of Venus and the Possible Role of Density-driven Separation of CO2 and N2," *Nature Geoscience*, vol. 10, no. 7, pp. 473–477, 2017. 4

[22] R. Miller, K. Harstad, and J. Bellan, "Direct Numerical Simulations of Supercritical Fluid Mixing Layers Applied to Heptane–Nitrogen," *Journal of Fluid Mechanics*, vol. 436, pp. 1–39, 2001. 4, 101, 153

[23] K. Trachenko, V. V. Brazhkin, and D. Bolmatov, “Dynamic Transition of Supercritical Hydrogen: Defining the Boundary between Interior and Atmosphere in Gas Giants,” *Physical Review E*, vol. 89, no. 3, 2014. 4, 15, 17

[24] W. Martin, J. Baross, D. Kelley, and M. J. Russell, “Hydrothermal Vents and the Origin of Life,” *Nature Reviews Microbiology*, vol. 6, no. 11, pp. 805–814, 2008. 4

[25] J. Bellan, “Supercritical (and Subcritical) Fluid Behavior and Modeling: Drops, Streams, Shear and Mixing Layers, Jets and Sprays,” *Progress in Energy and Combustion Science*, vol. 26, no. 4-6, pp. 329–366, 2000. 4, 5, 14, 38, 97

[26] X. Cheng and T. Schulenberg, “Heat Transfer at Supercritical Pressures - Literature Review and Application to an HPLWR,” Institut für Kern- und Energietechnik, Tech. Rep., 2001. 4, 38

[27] I. L. Pioro and R. B. Duffey, “Experimental heat transfer in supercritical water flowing inside channels (survey),” *Nuclear Engineering and Design*, vol. 235, no. 22, pp. 2407–2430, 2005. 19

[28] J. Licht, M. Anderson, and M. Corradini, “Heat Transfer and Fluid Flow Characteristics in Supercritical Pressure Water,” *Journal of Heat Transfer*, vol. 131, no. 7, pp. 1–14, 2009. 4

[29] T. J. Bruno, “Experimental Approaches for the Study and Application of Supercritical Fluids,” *Combustion Science and Technology*, vol. 178, pp. 3–46, 2006. 4

[30] A. Montes, M. D. Gordillo, C. Pereyra, and E. J. M. de la Ossa, *Mass Transfer – Advanced aspects*. InTech, 2011, ch. Particles Formation Using Supercritical Fluids, pp. 463–480. 4

[31] V. Yang, N. Nienchuan, and J. Shuen, “Vaporization of Liquid Oxygen (LOX) Droplets in Supercritical Hydrogen Environments,” *Combustion Science and Technology*, vol. 97, no. 4-6, pp. 247–270, 1994. 4, 14, 66

[32] D. Davis and B. Chehroudi, “The Effects of Pressure and Acoustic Field on a Cryogenic Coaxial Jet,” in *42nd AIAA Aerospace Sciences Meeting and Exhibit*, AIAA paper 2004–133,0 2004. 5, 8, 93, 94, 135

[33] S. Yerelan and R. J. Santoro, “Major Species and Temperature Profiles of LOX/GH2 Combustion,” in *33rd Joint Propulsion Conference and Exhibit*, AIAA paper 1997–2940, 1997. 5

[34] V. Yang, M. Habiballah, J. Hulka, and M. Popp, Eds., *Liquid Chamber Thrust Cham-*

bers: Aspeects of Modeling, Analysis, and Design. American Institute of Aeronautics and Astronautics, 2004. 5

[35] M. Oschwald and A. Schik, “Supercritical Nitrogen Free Jet Investigated by Spontaneous Raman Scattering,” *Experiments in Fluids*, vol. 27, no. 6, pp. 497–506, 1999. 5, 8, 23, 24, 30, 38, 114, 115, 116, 117, 118, 119, 120, 121, 122, 124, 126, 127, 128, 129, 130, 131, 156

[36] J. A. Wehrmeyer, J. M. Cramer, R. H. Eskridge, and C. C. Dobson, “Development of Ultraviolet Raman Diagnostics for Rocket Engine Injector Analysis,” *Journal of Propulsion and Power*, vol. 17, no. 1, pp. 27–34, 2001. 5

[37] H. Kobayashi, Y. Daimon, Y. Umemura, D. Muto, Y. Naruo, and K. Miyanabe, “Temperature Measurement and Flow Visualization of Cryo-Compressed Hydrogen Released into the Atmosphere,” *International Journal of Hydrogen Energy*, vol. 43, no. 37, pp. 17 938–17 953, 2018. 5, 16

[38] P. Tucker, S. Menon, C. Merkle, J. Oefelein, and V. Yang, “Validation of High-Fidelity CFD Simulations for Rocket Injector Design,” in *44th AIAA/ASME/SAE/ASEE Joint Propulsion Conference & Exhibit, Joint Propulsion Conferences*, AIAA paper 2008–5226, 2008. 5

[39] G. M. Faeth, “Structure and Atomization Properties of Dense Turbulent Sprays,” in *Twenty-Third Symposium (International) on Combustion/ The Combustion Institute*, 1990. 5

[40] P. C. Ma, X. I. A. Yang, and M. Ihme, “Structure of Wall-bounded Flows at Transcritical Conditions,” *Physical Review Fluids*, vol. 3, no. 3, 2018. 5

[41] M. Leonardi, M. Pizzarelli, and F. Nasuti, “Analysis of Thermal Stratification Impact on the Design of Cooling Channels for Liquid Rocket Engines,” *International Journal of Heat and Mass Transfer*, vol. 135, pp. 811–821, 2019. 6

[42] N. Perakis, L. Preis, and O. J. Haidn, “Wall Heat Flux Evaluation in Regeneratively Cooled Rocket Thrust Chambers,” *Journal of Thermophysics and Heat Transfer*, vol. 35, no. 1, pp. 127–141, 2021. 6

[43] S. Negro and G. M. Bianchi, “Superheated Fuel Injection Modeling: An Engineering Approach,” *International Journal of Thermal Sciences*, vol. 50, no. 8, pp. 1460–1471, 2011. 6

[44] A. Woschnak, D. Suslov, and M. Oschwald, “Experimental and Numerical Investigation of Thermal Stratification Effects,” in *39th AIAA/ASME/SAE/ASEE Joint Propul-*

sion Conference and Exhibit, AIAA paper 2003–4615, 2003. 6

[45] D. T. Banuti and K. Hannemann, “The Absence of a Dense Potential Core in Supercritical Injection: A Thermal Break-up Mechanism,” *Physics of Fluids*, vol. 28, no. 3, p. 035103, 2016. 6, 11, 13, 19, 20, 52, 92, 93, 94, 95, 97, 98, 99, 100, 101, 102, 104, 105, 106, 119, 146

[46] T. Toki, M. Morita, S. Teramoto, and K. Yamaguchi, “Backlit Visualization and Temperature Measurement of Cryogenic Cooling Channel Flow at Supercritical Pressure,” in *AIAA Scitech 2019 Forum*, AIAA paper 2019–1784, 2019. 6

[47] I. A. Leyva, B. Chehroudi, and D. G. Talley, “Dark Core Analysis of Coaxial Injectors at Sub, Near and Supercritical Pressures in a Transverse Acoustic Field,” in *45th AIAA Aerospace Sciences Meeting and Exhibit*, AIAA 2007–5456, 2007. 6

[48] R. Schuff, H. Jung, C. Merkle, and W. Anderson, “Experimental Investigation of Asymmetric Heating in a High Aspect Ratio Cooling Channel with Supercritical Nitrogen,” in *43rd AIAA/ASME/SAE/ASEE Joint Propulsion Conference and Exhibit*, AIAA paper 2007–5546, 2007. 7

[49] A. F. Polyakov, *Heat Transfer under Supercritical Pressures*. Elsevier, 1991, vol. 21, ch. Advances in Heat Transfer, pp. 1–53. 7

[50] C. Dang and E. Hihara, “In-tube Cooling Heat Transfer of Supercritical Carbon Dioxide. Part 2. Comparison of Numerical Calculation with Different Turbulence Models,” *International Journal of Refrigeration*, vol. 27, no. 7, pp. 748–760, 2004. 7, 37

[51] J. M. Char, K. K. Kuo, and K. C. Hsieh, “Observations of Breakup Processes of Liquid Jets using Real-Time X-Ray Radiography,” *Journal of Propulsion and Power*, vol. 6, no. 5, pp. 544–551, sep 1990. 7

[52] Y. Zheng, J. Si, W. Tan, M. Wang, B. Yang, and X. Hou, “Imaging of High-pressure Fuel Sprays in the Near-nozzle Region with Supercontinuum Illumination,” *Optical Engineering*, vol. 4, no. 57, pp. 1–5, apr 2018. 7

[53] D. T. Banuti, “Crossing the Widom-line – Supercritical Pseudo-boiling,” *Journal of Supercritical Fluids*, vol. 98, pp. 12–16, 2015. 7, 9, 16, 17, 18, 52, 92, 97, 102, 156

[54] D. T. Banuti, “A Thermodynamic Look at Injection in Aerospace Propulsion Systems,” in *AIAA Scitech 2020 Forum*, AIAA paper 2020–1154, 2020. 7

[55] K. Harstad and J. Bellan, “The Lewis Number under Supercritical Conditions,” *International Journal of Heat and Mass Transfer*, vol. 42, no. 6, pp. 961–970, 1999. 7

[56] C. Segal and S. A. Polikhov, “Subcritical to Supercritical Mixing,” *Physics of Fluids*, vol. 20, no. 5, p. 052101, 2008. 7, 24, 114, 153

[57] L. Jofre and J. Urzay, “Transcritical Diffuse-interface Hydrodynamics of Propellants in High-pressure Combustors of Chemical Propulsion Systems,” *Progress in Energy and Combustion Science*, vol. 82, p. 100877, 2021. 7, 113, 115

[58] V. Gerber, S. Baab, F. J. Förster, H. Mandler, B. Weigand, and G. Lamanna, “Fluid Injection with Supercritical Reservoir Conditions: Overview on Morphology and Mixing,” *The Journal of Supercrital Fluids*, vol. 169, p. 105097, 2021. 8, 12, 38

[59] W. Mayer, J. Telaar, R. Branam, G. Schneider, and J. Hussong, “Raman Measurements of Cryogenic Injection at Supercritical Pressure,” *Heat and Mass Transfer*, vol. 39, no. 8-9, pp. 709–719, 2003. 14, 15, 23, 24, 30, 38, 81, 92, 93, 94, 95, 96, 98, 99, 101, 106, 107, 122

[60] M. Habiballah, M. Orain, F. Grisch, L. Vingert, and P. Gicquel, “Experimental Studies of High-pressure Cryogenic Flames on the Mascotte Facility,” *Combustion Science and Technology*, vol. 178, no. 1-3, pp. 101–128, 2006. 23

[61] S. Dowy, A. Braeuer, K. Reinhold-López, and A. Leipertz, “Laser Analyses of Mixture Formation and the Influence of Solute on Particle Precipitation in the SAS Process,” *The Journal of Supercritical Fluids*, vol. 50, no. 3, pp. 265–275, 2009.

[62] A. Roy and C. Segal, “Experimental Study of Fluid Jet Mixing at Supercritical Conditions,” *Journal of Propulsion and Power*, vol. 26, no. 6, pp. 1205–1211, 2010. 23, 24

[63] A. Roy, C. Joly, and C. Segal, “Disintegrating Supercritical Jets in a Subcritical Environment,” *Journal of Fluid Mechanics*, vol. 717, pp. 193–202, 2013. 23, 24

[64] D. Bassing and A. S. Braeuer, “The Lag between Micro- and Macro-mixing in Compressed Fluid Flows,” *Chemical Engineering Science*, vol. 163, pp. 105–113, 2017. 8

[65] J. Bellan, “Future Challenges in the Modelling and Simulations of High-pressure Flows,” *Combustion Science Technology*, vol. 192, no. 7, pp. 1199–1218, 2020. 8, 23, 52, 84, 87, 92

[66] J. Barata, I. Gökalp, and A. Silva, “Numerical Study of Cryogenic Jets under Supercritical Conditions,” *Journal of Propulsion and Power*, vol. 19, no. 1, pp. 142–147, 2003. 8, 30, 34, 81, 83, 92

[67] E. Antunes, “Modeling of Transcritical Jets by the Use of a Real Fluid Equation of

State," Ph.D. dissertation, Universidade da Beira Interior, 2018. 8

[68] T. S. Park, "Application of κ-ϵ Turbulence Models with Density Corrections to Variable Density Jets under Subcritical/supercritical Conditions," *Numerical Heat Transfer, Part A: Applications*, vol. 77, no. 2, pp. 162–178, 2019. 8, 92

[69] Y. Ito, *Heat exchangers - advanced features and applications*. InTech, 2017, ch. Heat Transfer of Supercritical Fluid Flows and Compressible Flows, pp. 125–147. 11

[70] D. T. Banuti, M. Raju, C. Ma, M. Ihme, and J. Hickey, "Seven Questions about Supercritical Fluids – Towards a New Fluid State Diagram," in *55th AIAA Aerospace Sciences Meeting*, AIAA paper 2017-1106, 2017. 11, 16, 113

[71] W. Mayer, A. Schik, C. Schweitzer, and M. Schaeffler, "Injection and mixing processes in high pressure LOX/GH2 rocket combustors," in *32nd Joint Propulsion Conference and Exhibit*, vol. AIAA 96-2620, 1996. 11, 21, 22

[72] M. Oschwald, J. J. Smith, R. Braman, J. Hussong, A. Schik, B. Chehroudi, and D. G. Talley, "Injection of Fluids into Supercritical Environments," *Combustion Science and Technology*, vol. 178, no. 1–3, pp. 49–100, 2006. 11, 13, 14, 18, 23, 30, 38

[73] B. Chehroudi, "Recent Experimental Efforts on High-Pressure Supercritical Injection for Liquid Rockets and their Implications," *International Journal of Aerospace Engineering*, vol. 2012, pp. 1–31, 2012. 11, 23, 30, 91

[74] W. Mayer, A. Schik, M. Schaffler, and H. Tamura, "Injection and Mixing Processes in High-pressure Liquid Oxygen/gaseous Hydrogen Rocket Combustors," *Journal of Propulsion and Power*, vol. 16, no. 5, pp. 823–828, 2000. 12, 23

[75] C. Lagarza-Cortés, J. Ramírez-Cruz, M. Salinas-Vázquez, W. V.-Rodríguez, and J. M. Cubos-Ramírez, "Large-eddy Simulation of Transcritical and Supercritical Jets Immersed in a Quiescent Environment," *Physics of Fluids*, vol. 31, no. 2, p. 025104, 2019. 12, 13, 95, 98

[76] T. Schmitt, L. Selle, B. Cuenot, and T. Poinsot, "Large-Eddy Simulation of Transcritical Flows," *Comptes Rendus Mécanique*, vol. 337, no. 6-7, pp. 528–538, 2009. 12, 14, 84, 92, 95, 96, 97, 98

[77] A. R. Imre, C. Ramboz, U. K. Deiters, and T. Kraska, "Anomalous Fluid Properties of Carbon Dioxide in the Supercritical Region: Application to Geological CO2 Storage and Related Hazards," *Environmental Earth Sciences*, vol. 73, no. 8, pp. 4373–4384, 2014. 12, 17, 106

[78] F. A. Gorelli, T. Bryk, M. Krisch, G. Ruocco, M. Santoro, and T. Scopigno, "Dynamics and Thermodynamics Beyond the Critical Point," *Scientific Reports*, vol. 3, no. 1, 2013. 12, 17

[79] N. Zong, H. Meng, S. Hsieh, and V. Yang, "A Numerical Study of Cryogenic Fluid Injection and Mixing under Supercritical Conditions," *Physics of Fluids*, vol. 16, no. 12, pp. 4248–4261, 2004. 12, 52, 58, 91, 115

[80] I. Pioro and S. Mokry, *Heat Transfer – Theoretical Analysis, Experimental Investigations and Industrial Systems*. InTech, 2011, ch. Heat Transfer to Fluids at Supercritical Pressures, pp. 482–504. 12, 19

[81] S. DeSouza and C. Segal, "Sub- and Supercritical Jet Disintegration," *Physics of Fluids*, vol. 29, no. 4, pp. 47–107, 2017. 12, 21, 24

[82] W. Mayer, "Coaxial Atomization of a Round Liquid Jet in a High Speed Gas Stream: A Phenomenological Study," *Experiments in Fluids*, vol. 16, no. 6, pp. 401–410, 1994. 13

[83] R. D. Woodward and D. G. Talley, "Raman Imaging of Transcritical Cryogenic Propellants," in *34th Aerospace Sciences Meeting and Exhibit*, AIAA paper 1996–468, 1996. 13, 21, 24, 114

[84] L. Rayleigh, "On the Instability of Jets," *Proceedings of the London Mathematical Society*, vol. s1-10, no. 1, pp. 4–13, 1878. 13

[85] S. Cho, G. Park, Y. Chung, Y. Yoon, and V. G. Bazarov, "Surface Instability on Cryogenic Swirl Flow at Sub- to Supercritical Conditions," *Journal of Propulsion and Power*, vol. 30, no. 4, pp. 1038–1046, 2014. 14

[86] B. Chehroudi, D. Talley, W. Mayer, R. Branam, J. Smith, A. Schik, and M. Oschwald, "Understanding Injection into High Pressure Supercritical Environments," Defense Technical Information Archive, Tech. Rep., 2003. 14, 159

[87] J. C. Oefelein and V. Yang, "Modeling High-pressure Mixing and Combustion Processes in Liquid Rocket Engines," *Journal of Propulsion and Power*, vol. 14, no. 5, pp. 843–857, 1998. 14, 92

[88] D. Banuti, "Thermodynamic Analysis and Numerical Modeling of Supercritical Injection," Ph.D. dissertation, Institute of Aerospace Thermodynamics University of Stuttgart, 2015. 14, 30

[89] J. S. Shuen, V. Yang, and C. C. Hsiao, "Combustion of Liquid-fuel Droplets in Super-

critical Conditions," *Combustion and Flame*, vol. 89, no. 3-4, pp. 299–319, 1992. 14

[90] J. P. Delplanque and W. A. Sirignano, "Numerical Study of the Transient Vaporization of an Oxygen Droplet at Sub- and Super-critical Conditions," *International Journal of Heat and Mass Transfer*, vol. 36, no. 2, pp. 303–314, 1993.

[91] T. Anderson, M. Winter, and M. Haas, "Observation of a Droplet/shock Interaction in a Supercritical Environment," *32nd Aerospace Sciences Meeting and Exhibit*, AIAA 94–0557, 1994.

[92] P. Lafon, V. Yang, and M. Habiballah, "Pressure-coupled Vaporization and Combustion Responses of Liquid Oxygen (LOX) Droplets in Supercritical Hydrogen Environments," in *31st Joint Propulsion Conference and Exhibit*, AIAA paper 95–2432, 1995. 66

[93] S. D. Givler and J. Abraham, "Supercritical Droplet Vaporization and Combustion Studies," *Progress in Energy and Combustion Science*, vol. 22, no. 1, pp. 1–28, 1996.

[94] P. Haldenwang, C. Nicoli, and J. Daou, "High Pressure Vaporization of LOX Droplet Crossing the Critical Conditions," *International Journal of Heat and Mass Transfer*, vol. 39, no. 16, pp. 3453–3464, 1996.

[95] K. Harstad and J. Bellan, "Interactions of Fluid Oxygen Drops in Fluid Hydrogen at Rocket Chamber Pressures," *International Journal of Heat and Mass Transfer*, vol. 41, no. 22, pp. 3551–3558, 1998.

[96] V. Yang, "Modeling of Supercritical Vaporization, Mixing, and Combustion Processes in Liquid-fueled Propulsion Systems," *Proceedings of the Combustion Institute*, vol. 28, no. 1, pp. 925–942, 2000. 14, 54, 66

[97] R. S. Lazar and G. M. Faeth, "Bipropellant Droplet Combustion in the Vicinity of the Critical Point," *Symposium (International) on Combustion*, vol. 13, no. 1, pp. 801–811, 1971. 14

[98] E. W. Curtis and P. V. Farrell, "Droplet Vaporization in a Supercritical Microgravity Environment," *Acta Astronautica*, vol. 17, no. 11-12, pp. 1189–1193, 1988.

[99] J. Sato, "Studies on Droplet Evaporation and Combustion in High Pressures," in *31st Aerospace Sciences Meeting*. American Institute of Aeronautics and Astronautics, AIAA 93-0813, 1993.

[100] B. Vieille, C. Chauveau, X. Chesneau, A. Odeïde, and I. Gökalp, "High-pressure Droplet Burning Experiments in Microgravity," *Symposium (International) on Com-*

bustion, vol. 26, no. 1, pp. 1259–1265, 1996.

[101] H. Nomura, Y. Ujiie, H. J. Rath, J. Sato, and M. Kono, "Experimental Study on High-pressure Droplet Evaporation Using Microgravity Conditions," in *Symposium (International) on Combustion*, vol. 26, no. 1, 1996, pp. 1267–1273. 14

[102] J. Oefelein and V. Yang, "Analysis of Transcritical Spray Phenomena in Turbulent Mixing Layers," in *34th Aerospace Sciences Meeting and Exhibit*, AIAA paper 1996-85, 1996. 14

[103] B. Widom, "Equation of State in the Neighborhood of the Critical Point," *Journal of Chemical Physics*, vol. 43, no. 11, pp. 3898–3905, 1965. 15

[104] B. Widom, "Surface Tension and Molecular Correlations near the Critical Point," *Journal of Chemical Physics*, vol. 43, no. 11, pp. 3892–3897, 1965. 15

[105] K. Nishikawa and I. Tanaka, "Correlation Lengths and Density Fluctuations in Supercritical States of Carbon Dioxide," *Chemical Physics Letters*, vol. 244, no. 1-2, pp. 149–152, 1995. 15

[106] N. Tsuchiya, C. Sekiguchi, and N. Hirano, "Spectroscopic Measurement of Critical Points and Characteristics of Supercritical State of H2O And CO2," *Procedia Earth and Planetary Science*, vol. 7, pp. 846–849, 2013. 15

[107] M. Santoro and F. A. Gorelli, "Structural Changes in Supercritical Fluids at High Pressures," *Physical Review B*, vol. 77, no. 21, 2008. 15

[108] G. G. Simeoni, T. Bryk, F. A. Gorelli, M. Krisch, G. Ruocco, M. Santoro, and T. Scopigno, "The Widom Line as the Crossover between Liquid-like and Gas-like Behaviour in Supercritical Fluids," *Nature Physics*, vol. 6, no. 7, pp. 503–507, 2010. 15, 17

[109] F. Maxim, C. Contescu, P. Boillat, B. Niceno, K. Karalis, A. Testino, and C. Ludwig, "Visualization of Supercritical Water Pseudo-boiling at Widom Line Crossover," *Nature Communications*, vol. 10, no. 1, 2019. 15, 16

[110] D. T. Banuti, M. Raju, and M. Ihme, "Between Supercritical Liquids and Gases – Reconciling Dynamic and Thermodynamic State Transitions," *The Journal of Supercritical Fluids*, vol. 165, p. 104895, 2020. 15, 16, 17

[111] V. V. Brazhkin, Y. D. Fomin, A. G. Lyapin, V. N. Ryzhov, E. N. Tsiok, and K. Trachenko, ""Liquid-Gas" Transition in the Supercritical Region: Fundamental Changes in the Particle Dynamics," *Physical Review Letters*, vol. 111, no. 14, 2013. 15

[112] C. Yang, V. V. Brazhkin, M. T. Dove, and K. Trachenko, “Frenkel Line And Solubility Maximum In Supercritical Fluids,” *Physical Review E*, vol. 91, no. 1, 2015. 15

[113] D. Bolmatov, M. Zhernenkov, D. Zavyalov, S. N. Tkachev, A. Cunsolo, and Y. C. Cai, “The Frenkel Line: A Direct Experimental Evidence for the New Thermodynamic Boundary,” *Nature*, vol. 5, no. 1, nov 2015. 16

[114] Q. Fu, Z. Fang, Y. Zhang, and L. Yang, “Molecular Dynamics Simulation of a Jet in a Binary System at Supercritical Environment,” *Molecules*, vol. 24, no. 1, p. 31, 2019. 16

[115] F. Maxim, K. Karalis, P. Boillat, D. T. Banuti, J. I. M. Damian, B. Niceno, and C. Ludwig, “Thermodynamics and Dynamics of Supercritical Water Pseudo-Boiling,” *Advanced Science*, vol. 8, no. 3, p. 2002312, dec 2020. 16

[116] J. Y. Yoo, “The Turbulent Flows of Supercritical Fluids with Heat Transfer,” *Annual Review of Fluid Mechanics*, vol. 45, no. 1, pp. 495–525, 2013. 17, 38

[117] J. Ren, O. Marxen, and R. Pecnik, “Boundary-layer Stability of Supercritical Fluids in the Vicinity of the Widom Line,” *Journal of Fluid Mechanics*, vol. 871, pp. 831–864, 2019. 17

[118] S. Kawai and Y. Oikawa, “Turbulence Modeling for Turbulent Boundary Layers at Supercritical Pressure: A Model for Turbulent Mass Flux,” *Flow Turbulence and Combustion*, vol. 104, no. 2-3, pp. 625–641, 2019. 17, 38, 92

[119] S. Artemenko, P. Krijgsman, and V. Mazur, “The Widom Line for Supercritical Fluids,” *Journal of Molecular Liquids*, vol. 238, pp. 122–128, 2017. 17

[120] M. Oschwald, A. Schik, M. Klar, and W. Mayer, “Investigation Of Coaxial LN2/GH2-injection at Supercritical Pressure by Spontaneous Raman Scattering,” in *35th Joint Propulsion Conference and Exhibit*, AIAA paper 99–2887, 1999. 17, 23, 24, 30, 38, 154, 156

[121] P. E. Lapenna and F. Creta, “Direct Numerical Simulation of Transcritical Jets at Moderate Reynolds Number,” *AIAA Journal*, vol. 57, no. 6, pp. 2254–2263, 2019. 18, 92, 97

[122] R. N. Dahms and J. C. Oefelein, “On the Transition between Two-phase and Single-phase Interface Dynamics in Multicomponent Fluids at Supercritical Pressures,” *Physics of Fluids*, vol. 25, no. 9, p. 092103, 2013. 18, 21, 22

[123] D. T. Banuti, M. Raju, and M. Ihme, “Supercritical Pseudoboiling for General Fluids and its Application to Injection,” Center for Turbulence Research: Annual Research

Briefs, Tech. Rep., 2016. 19

[124] J. V. M. Gopal, G. Tretola, R. Morgan, G. de Sercey, G. Lamanna, and K. Vogiatzaki, "Unpicking the Interplay of Turbulence, Diffusion, and Thermophysics in Cryogenic Jets at Supercritical Pressures," *Physics of Fluids*, vol. 33, no. 7, p. 077106, 2021. 20, 98

[125] R. N. Dahms, J. Manin, L. M. Pickett, and J. C. Oefelein, "Understanding High-pressure Gas-liquid Interface Phenomena in Diesel Engines," *Proceedings of the Combustion Institute*, vol. 34, no. 1, pp. 1667–1675, 2013. 21, 30

[126] M. Raju, D. T. Banuti, P. C. Ma, and M. Ihme, "Widom Lines in Binary Mixtures of Supercritical Fluids," *Scientific Reports*, vol. 3027, no. 7, 2017. 22, 113, 153

[127] M. J. Foust, M. Deshpande, S. Pal, T. Ni, C. L. Merkle, and R. J. Santoro, "Experimental and Analytical Characterization of a Shear Coaxial Combusting GO2/GH2 Flowfield," in *34th Aerospace Sciences Meeting and Exhibit*, AIAA paper 96–0646, 1996. 22, 135

[128] B. Chehroudi, D. Talley, and E. Coy, "Visual Characteristics and Initial Growth Rates of Round Cryogenic Jets at Subcritical and Supercritical Pressures," *Physics of Fluids*, vol. 14, no. 2, pp. 850–861, 2002. 23, 24, 30, 32, 92

[129] D. W. Davis and B. Chehroudi, "Measurements in an Acoustically Driven Coaxial Jet under Sub-, Near-, and Supercritical Conditions," *Journal of Propulsion and Power*, vol. 23, no. 2, pp. 364–374, 2007. 23, 93, 134, 135, 136, 137, 139, 141, 142, 143, 145, 147, 149

[130] W. Mayer, A. Schik, B. Vielle, C. Chauveau, I. Gökalp, D. Talley, and R. Woodward, "Atomization and Breakup of Cryogenic Propellants under High-pressure Subcritical and Supercritical Conditions," *Journal of Propulsion and Power*, vol. 14, no. 5, pp. 835–842, 1998. 23, 24

[131] S. Baab, C. Steinhausen, G. Lamanna, B. Weigand, and F. J. Förster, "A Quantitative Speed of Sound Database for Multi-component Jet Mixing at High Pressure," *Fuel*, vol. 233, pp. 918–925, 2018. 23, 24

[132] H. Tani, S. Teramoto, T. Toki, S. Yoshida, K. Yamaguchi, and K. Okamoto, "Temperature Measurement of Cryogenic Nitrogen Jets at Supercritical Pressure," *Progress in Propulsion Physics*, vol. 8, pp. 43–54, 2016. 23

[133] A. Roy, C. Segal, and C. Joly, "Spreading Angle and Core Length Analysis of Supercritical Jet," *AIAA Journal*, vol. 51, no. 8, pp. 2009–2014, 2013. 23, 30

[134] J. A. Newman and T. A. Brzustowksi, “Behavior of a Liquid Planar Jet Near the Thermodynamic Critical Region,” *AIAA Journal*, vol. 9, no. 8, pp. 1595–1602, 1971. 24, 30, 113

[135] C. K. Muthukumaran and A. Vaidyanathan, “Experimental Study of Elliptical Jet from Supercritical to Subcritical Conditions Using Planar Laser Induced Fluorescence,” *Physics of Fluids*, vol. 27, no. 3, p. 034109, 2015. 24

[136] H. Lee, H. Kim, Y. Lee, and Y. Yoon, “Jet Disintegration in Supercritical Environments,” *Experimental Thermal and Fluid Science*, vol. 115, p. 110098, 2020. 24, 94

[137] P. J. Linstrom and W. G. Mallard, Eds., *NIST Chemistry WebBook, NIST Standard Reference Database 69*. National Institute of Standards and Technology, 1997. 25, 54, 60, 62, 69, 70, 74, 75, 93, 119

[138] C. Hirsh, *Numerical Computation of Internal & External Flows*, 2nd ed. Oxford, U.K.: Butterworth-Heinemann, 2007, vol. 1–Fundamentals of Computational Fluid Dynamics. 27, 79

[139] W. Wei, W. Qin, M. Yue, and M. Xie, “Numerical Investigation on Fuel Injection into a Multicomponent Gaseous environment under Trans/Supercritical Condition,” *Numerical Heat Transfer, Part A: Applications*, vol. 77, no. 1, pp. 33–50, 2020. 30, 100

[140] P. E. Dimotakis, “Two-Dimensional Shear-Layer Entrainment,” *AIAA Journal*, vol. 24, no. 11, pp. 1791–1796, 1986. 30, 31

[141] D. Papamoschou and A. Roshko, “The Compressible Turbulent Shear Layer: An Experimental Study,” *Journal of Fluid Mechanics*, vol. 197, no. 1, p. 453, 1988. 30, 31

[142] G. N. Abramovich, *The Theory of Turbulent Jets*, L. H. Schindel, Ed. Cambridge, Massachussets, The M. I. T. Press, 1963. 30, 31, 32, 101

[143] R. Branam, J. Telaar, and W. Mayer, “2nd International Workshop on Rocket Combustion Modeling: Atomization, Combustion and Heat Transfer held in Lampoldshausen,” Air Force Research Laboratory: Edwards Air Force Base, Tech. Rep., 2001. 30, 91, 93, 118

[144] R. Branam and W. Mayer, “Characterization of Cryogenic Injection at Supercritical Pressure,” *Journal of Propulsion and Power*, vol. 19, no. 3, pp. 342–355, 2003. 30, 98

[145] A. de Risi, T. Donateo, and D. Laforgia, “Theoretical Investigation On Variable-density Sprays,” *Atomization and Sprays*, vol. 12, no. 1-3, pp. 329–358, 2002. 31

[146] R. D. Reitz and F. B. Bracco, “On the Dependence of Spray Angle and Other Spray Parameters on Nozzle Design and Operating Conditions,” *SAE Technical Paper Series*, 1979. 31

[147] G. L. Brown and A. Roshko, “On Density Effects and Large Structure in Turbulent Mixing Layers,” *Journal of Fluid Mechanics*, vol. 64, no. 04, p. 775, 1974. 31

[148] J. I. Rodriguez, I. A. Levya, B. Chehroudi, and D. G. Talley, “Results on Subcritical One Phase Coaxial Jet Spread Angles and Subcritical to Supercritical Acoustically-forced Coaxial Jet Dark Core Lengths,” in *44th Joint Propulsion Conference and Exhibit*, AIAA paper 2008–4561, 2008. 31

[149] P. E. Lapenna and F. Creta, “Mixing under Transcritical Conditions: An A-priori Study Using Direct Numerical Simulation,” *The Journal of Supercritical Fluids*, vol. 128, pp. 263–278, 2017. 32, 92, 97, 98, 115

[150] T. Schmitt, J. Rodriguez, I. A. Leyva, and S. Candel, “Experiments and Numerical Simulation of Mixing under Supercritical Conditions,” *Physics of Fluids*, vol. 24, no. 5, pp. 55–104, 2012. 32, 84, 134, 137

[151] U. Unnikrishnan, X. Wang, S. Yang, and V. Yang, “Subgrid Scale Modeling of the Equation of State for Turbulent Flows under Supercritical Conditions,” in *53rd AIAA/SAE/ASEE Joint Propulsion Conference*, AIAA paper 2017–4855, 2017. 32, 38, 97

[152] N. Okong'o and J. Bellan, “Perturbation and Initial Reynolds Number Effects on Transition Attainment of Supercritical, Binary, Temporal Mixing Layers,” *Computers & Fluids*, vol. 33, no. 8, pp. 1023–1046, 2004. 32, 38, 97

[153] M. Favre-Marinet, E. B. Camano, and J. Sarboch, “Near-field of Coaxial Jets with Large Density Differences,” *Experiments in Fluids*, vol. 97, no. 106, 1999. 32, 137

[154] L. Magalhães, F. Carvalho, A. Silva, and J. Barata, “Turbulence Modeling Insights into Supercritical Nitrogen Mixing Layers,” *Energies*, vol. 13, no. 7, 2020. 32, 38, 97, 98, 102

[155] J. P. H. Sanders and I. Gökalp, “Monte Carlo Computations of Turbulent Variable Density Jets.” 32

[156] J. P. H. Sanders, B. Sarh, and I. Gökalp, “Variable Density Effects in Axisymmetric Isothermal Turbulent Jets: A Comparison Between a First- And a Second-order Turbulence Model,” *International Journal of Heat and Mass Transfer*, vol. 40, no. 4, pp. 823–842, 1997. 32, 33

[157] B. Sarh and I. Gökalp, "Influence of Variable Density of the Characteristics of Turbulent Rectangular Jets," 1991. 32, 37

[158] P. Chassaing, G. Harran, and L. Joly, "Density Fluctuation Correlations in Free Turbulent Binary Mixing," *Journal of Fluid Mechanics*, vol. 279, pp. 239–278, 1994. 33, 95

[159] D. Klingenberg, M. Oberlack, and D. Pluemacher, "Symmetries and Turbulence Modeling," *Physics of Fluids*, vol. 32, no. 2, p. 025108, 2020. 35

[160] P. Sagaut, *Large Eddy Simulation for incompressible flows*, ser. Scientific Computation. Springer, 2001. 36, 38, 97

[161] P. P. Ciottoli, A. Petrocchi, L. Angelilli, F. E. H. Perez, R. M. Galassi, F. Picano, M. Valorani, and H. G. Im, "Uncertainty Quantification Analysis of RANS of Spray Jets," in *AIAA Propulsion and Energy 2020 Forum*, AIAA paper 2020–3882, 2020. 36, 52

[162] S. He, W. S. Kim, and J. H. Bae, "Assessment of Performance of Turbulence Models in Predicting Supercritical Pressure Heat Transfer in a Vertical Tube," *International Journal of Heat and Mass Transfer*, vol. 51, no. 19-20, pp. 4659–4675, 2008. 37

[163] H. Myong, N. Kasagi, and M. Hirata, "Numerical Prediction of Turbulent Pipe Flow Heat Transfer for Various Prandtl Number Fluids With the Improved K–epsilon Turbulence Model," *JSME International Journal*, vol. 32, no. 4, pp. 613–622, 1989. 37

[164] L. Selle and G. Ribert, "Modeling Requirements for Large-eddy Simulation of Turbulent Flows under Supercritical Thermodynamics Conditions," *Center for Turbulence Research – Proceedings of the Summer Programm 2008*, 2008. 38, 52, 97

[165] E. S. Taşkinoğlu and J. Bellan, "Subgrid-scale Models and Large-eddy Simulation of Oxygen Stream Disintegration and Mixing with a Hydrogen or Helium Stream at Supercritical Pressure," *Journal of Fluid Mechanics*, vol. 679, pp. 156–193, 2011. 38

[166] G. Borghesi and J. Bellan, "A Priori and a Posteriori Investigations for Developing Large Eddy Simulations of Multi-species Turbulent Mixing under High-pressure Conditions," *Physics of Fluids*, vol. 27, no. 3, pp. 35–117, 2015. 38

[167] X. Wu, Z. Huang, X. Dai, J. McLennan, S. Zhang, and R. Li, "Detached Eddy Simulation of The Flow Field and Heat Transfer in Cryogenic Nitrogen Jet," *International Journal of Heat and Mass Transfer*, vol. 150, p. 119275, 2020. 38, 92

[168] H. Müller, C. A. Niedermeier, J. Matheis, M. Pfitzner, and S. Hickel, "Large-eddy Simulation of Nitrogen Injection at Trans- and Supercritical Conditions," *Physics of Flu-*

ids, vol. 28, no. 1, p. 015102, 2016. 38, 98

[169] Y. Bae, "A New Formulation of Variable Turbulent Prandtl Number for Heat Transfer to Supercritical Fluids," *International Journal of Heat and Mass Transfer*, vol. 92, pp. 792–806, 2016. 38

[170] Z. Wang, P. Jiang, and R. Xu, "Turbulent Convection Heat Transfer Analysis of Supercritical Pressure CO2 Flow in a Vertical Tube Based on the Field Synergy Principle," *Heat Transfer Engineering*, vol. 40, no. 5–6, pp. 1–11, 2018. 38

[171] H. Xiao and P. Cinnella, "Quantification of Model Uncertainty in RANS Simulations: A Review," *Progress in Aerospace Sciences*, vol. 108, pp. 1–31, 2019. 38, 51, 97, 102, 106

[172] X. Petit, G. Ribert, G. Lartigue, and P. Domingo, "Large Eddy Simulation of Supercritical Fluid Injection," *The Journal of Supercritical Fluids*, vol. 84, pp. 61–73, 2013. 38, 95, 97, 98

[173] A. Gnanaskandan and J. Bellan, "Large Eddy Simulations of High Pressure Jets: Effect of Subgrid Scale Modeling," in *55th AIAA Aerospace Sciences Meeting*, AIAA paper 2017–1105, 2017. 38, 95, 97, 98

[174] P. Spalart and S. Allmaras, "A One-equation Turbulence Model for Aerodynamic Flows," in *30th Aerospace Sciences Meeting and Exhibit*, AIAA paper 1992–439, 1992. 38, 40

[175] B. E. Launder and D. B. Spalding, "Lectures in Mathematical Models of Turbulence," *London, England: Academic Press*, 1972. 40, 41, 51, 99, 102, 117, 137, 155

[176] V. Yakhot, S. A. Orszag, S. Thangam, T. B. Gatski, and C. G. Speziale, "Developmentt of Turbulence Models for Shear Flows by A Double Expansion Technique," *Physics of Fluids A: Fluid Dynamics*, vol. 4, no. 7, pp. 1510–1520, 1992. 42, 43

[177] T. Shih, W. W. Liou, A. Shabbir, Z. Yang, and J. Zhu, "A New k-epsilon Eddy Viscosity Model for High Reynolds Number Turbulent Flows," *Computers & Fluids*, vol. 24, no. 3, pp. 227–238, 1995. 43, 44

[178] D. C. Wilcox, *Turbulence Modeling for CFD.* La Cãnada, Calif: DCW Industries, 1998. 44, 46, 50

[179] F. R. Menter, "Two-Equation Eddy-Viscosity Turbulence Models for Engineering Applications," *AIAA Journal*, vol. 32, no. 8, pp. 1598–1605, aug 1994. 45, 48

[180] N. J. Georgiadis, D. A. Yoder, and W. A. Engblom, "Evaluation of Modified Two-Equation Turbulence Models for Jet Flow Predictions," *AIAA Journal*, vol. 44, no. 12, pp. 3107–3114, 2006. 51, 52, 102

[181] A. A. Mishra and G. Iaccarino, "Uncertainty Estimation for Reynolds–Averaged Navier–Stokes Predictions of High-Speed Aircraft Nozzle Jets," *AIAA Journal*, vol. 55, no. 11, pp. 3999–4004, 2017. 51, 52, 102

[182] L. W. Cook, A. A. Mishra, J. P. Jarrett, K. E. Willcox, and G. Iaccarino, "Optimization Under Turbulence Model Uncertainty for Aerospace Design," *Physics of Fluids*, vol. 31, no. 10, p. 105111, 2019. 51, 52, 102

[183] J. Bridges, A. Khavaran, and C. Hunter, "Assessment of Current Jet Noise Prediction Capabilities," in *14th AIAA/CEAS Aeroacoustics Conference (29th AIAA Aeroacoustics Conference)*, AIAA paper 2008–2933, 2008. 52

[184] D. Peng and D. B. Robinson, "A New Two-constant Equation of State," *Industrial & Engineering Chemistry Fundamentals*, vol. 15, no. 1, pp. 59–64, 1976. 52, 56, 58, 60, 69, 74, 99, 117, 137, 155

[185] G. Soave, "Equilibrium Constants from a Modified Redlich–Kwong Equation of State," *Chemical Engineering Science*, vol. 27, no. 6, pp. 1197–1203, 1972. 52, 56, 60

[186] B. A. Younglove, "Thermophysical Properties of Fluids. I. Argon, Ethylene, Parahydrogen, Nitrogen, Nitrogen Trifluoride and Oxygen," *Journal of Physical and Chemical Reference Data*, vol. 11, no. 2, pp. 619–619, 1982. 52, 54

[187] K. Harstad, R. Miller, and J. Bellan, "Efficient High-pressure State Equations," *American Institute of Chemical Engineers Journal*, vol. 43, no. 6, pp. 1605–1610, 1997. 52, 153

[188] K. S. Pitzer, "The Volumetric and Thermodynamic Properties of Fluids. I. Theoretical Basis and Virial Coefficients," *Journal of the American Chemical Society*, vol. 77, no. 13, pp. 3427–3433, 1955. 53

[189] R. Span and W. Wagner, "Equations of State for Technical Applications. I. Simultaneously Optimized Functional Forms for Nonpolar and Polar Fluids," *International Journal of Thermophysics*, vol. 24, no. 1, pp. 1–39, 2003. 54, 55

[190] R. Span, E. W. Lemmon, R. T. Jacobsen, and W. Wagner, "A Reference Quality Equation of State for Nitrogen," *International Journal of Thermophysics*, vol. 19, no. 4, pp. 1121–1132, 1998. 54

[191] A. Congiunti, C. Bruno, and E. Giacomazzi, “Supercritical Combustion Properties,” in *41st Aerospace Sciences Meeting and Exhibit*, AIAA paper 2003–478, 2003. 54, 56, 65

[192] B. I. Lee and M. G. Kesler, “A Generalized Thermodynamic Correlation Based on Three-parameter Corresponding States,” *American Institute of Chemical Engineers Journal*, vol. 21, no. 3, pp. 510–527, 1975. 55

[193] L. Qiu, Y. Wang, Q. Jiao, H. Wang, and R. D. Reitz, “Development of a Thermodynamically Consistent, Robust and Efficient Phase Equilibrium Solver and its Validations,” *The Science and Technology of Fuel and Energy*, vol. 115, pp. 1–16, 2014. 55

[194] L. Qiu and R. D. Reitz, “An Investigation of Thermodynamic States During High-pressure Fuel Injection Using Equilibrium Thermodynamics,” *International Journal of Multiphase Flow*, vol. 72, pp. 24–38, 2015. 55

[195] D. T. Banuti and K. Hannemann, “Real Gas Library in Continuous Phase Propellant Injection Model for Liquid Rocket Engines,” in *49th AIAA/ASME/SAE/ASEE Joint Propulsion Conference*, AIAA paper 2013–4068, 2013. 55

[196] P. C. Ma, Y. Lv, and M. Ihme, “An Entropy-stable Hybrid Scheme for Simulations of Transcritical Real-fluid Flows,” *Journal of Computational Physics*, vol. 340, pp. 330–357, 2017. 55, 83, 84, 95, 98

[197] J. D. van der Waals, “Over the Continuitet van den Gas- en Vloeistoftoestand,” Ph.D. dissertation, University of Leiden, 1873. 55, 56

[198] G. Schmidt and H. Wenzel, “A Modified van der Waals Type Equation of State,” *Chemical Engineering Science*, vol. 35, no. 7, pp. 1503–1512, 1979. 56

[199] R. Monroy-Loperena, “A Note on the Analytical Solution of Cubic Equations of State in Process Simulation,” *Industrial & Engineering Chemistry Research*, vol. 51, no. 19, pp. 6972–6976, 2012. 56

[200] M. Ghanbari, M. Ahmadi, and A. Lashanizadegan, “A Comparison between Peng-Robinson and Soave-Redlich-Kwong Cubic Equations of State from Modification Perspective,” *Cryogenics*, vol. 84, pp. 13–19, 2017. 56

[201] O. Redlich and J. Kwong, “On the Thermodynamics of Solutions,” *Chemical Reviews*, vol. 61, no. 2, pp. 133–142, 1948. 56

[202] M. S. Graboski and T. E. Daubert, “A Modified Soave Equation of State for Phase Equilibrium Calculations. 1. Hydrocarbon Systems,” *Industrial & Engineering Chemistry*

Processes, vol. 17, no. 4, pp. 443–448, 1978. 58

[203] M. S. Graboski and T. E. Daubert, “A Modified Soave Equation of State for Phase Equilibrium Calculations. 2. Systems Containing CO2, H2S, N2, and CO,” *Industrial & Engineering Chemistry Processes*, vol. 17, no. 4, pp. 448–454, 1978. 58

[204] G. Fuller, “A Modified Redlich-Kwong-Soave Equation of State Capable of Representing the Liquid State,” *Industrial & Engineering Chemistry Fundamentals*, vol. 15, no. 4, pp. 254–257, 1976. 58

[205] J. C. Oefelein, “Thermophysical Characteristics of Shear-coaxial LOX–H2 Flames at Supercritical Pressure,” *Proceedings of the Combustion Institute*, vol. 30, no. 2, pp. 2929–2937, 2005. 58, 101

[206] P. M. Mathias, T. Naheiri, and E. M. Oh, “A Density Correction for The Peng–Robinson Equation of State,” *Fluid Phase Equilibria*, vol. 47, no. 1, pp. 77–87, 1989. 59

[207] M. E. Harvazinski, G. Lacaze, J. Oefelein, S. Sardeshmukh, and V. Sankaran, “Computational Modeling of Supercritical and Transcritical Flows,” in *55th AIAA Aerospace Sciences Meeting*, AIAA paper 2017–1104, 2017. 59

[208] J. S. Lopez-Echeverry, S. Reif-Acherman, and E. Araujo-Lopez, “Peng–Robinson Equation of State: 40 Years through Cubics,” *Fluid Phase Equilibria*, vol. 447, no. 447, pp. 39–71, 2017. 59

[209] A. M. Abudour, S. A. Mohammad, R. L. R. Jr., and K. A. M. Gasem, “Volume-translated Peng-Robinson Equation of State for Saturated and Single-phase Liquid Densities,” *Fluid Phase Equilibria*, vol. 335, pp. 74–87, 2012. 60

[210] J. P. Hickey and M. Ihme, “Supercritical Mixing and Combustion in Rocket Propulsion,” Center for Turbulence Research, resreport 12, 2013. 62

[211] R. C. Reid, J. M. Prausnitz, and B. E. Poling, *The Properties of Gases and Liquids*. McGraw-Hill, Inc, 1987. 62, 63

[212] B. J. McBride, M. J. Zehe, and S. Gordon, “NASA Glenn Coefficients for Calculating Thermodynamic Properties of Individual Species,” NASA Glenn Research Center, Tech. Rep. NASA/TP–2002-211556, 2002. 62, 63, 64

[213] E. N. da C. Andrade, “XLI A Theory of the Viscosity of Liquids.–part I,” *The London, Edinburgh, and Dublin Philosophical Magazine and Journal of Science*, vol. 17, no. 112, pp. 497–511, 1934. 65

[214] E. W. Lemmon and R. T. Jacobsen, “Viscosity and Thermal Conductivity Equations for Nitrogen, Oxygen, Argon and Air,” *International Journal of Thermophysics*, vol. 25, no. 1, pp. 21–69, 2004. 65, 67, 69, 71, 72, 74, 99, 117, 137

[215] T. H. Chung, M. Ajlan, L. L. Lee, and K. E. Starling, “Generalized Multiparameter Correlation for Nonpolar and Polar Fluid Transport Properties,” *Industrial & Engineering Chemistry Research*, vol. 27, no. 4, pp. 671–679, 1988. 65, 67, 68, 69, 72, 74, 75, 76, 155

[216] G. A. Olchowy and J. V. Sengers, “A Simplified Representation for the Thermal Conductivity of Fluids in the Critical Region,” *International Journal of Thermophysics*, vol. 10, no. 2, pp. 417–426, 1989. 71

[217] S. V. Patankar, *Numerical Heat Transfer and Fluid Flow*, ser. Series in Computational Methods in Mechanics and Thermal Sciences. Hemisphere Publishing Company, 1972. 81

[218] H. Meng and V. Yang, “A Unified Treatment of General Fluid Thermodynamics and Its Application to a Preconditioning Scheme,” *Journal of Computational Physics*, vol. 189, no. 1, pp. 277–304, 2003. 81, 115

[219] B. P. Leonard, “A Stable and Accurate Convective Modelling Procedure Based on Quadratic Upstream Interpolation,” *Computer Methods in Applied Mechanics and Engineering*, pp. 58–98, 1979. 82

[220] J. H. Ferziger and M. Peric, *Computational Methods for Fluid Dynamics*, 3rd ed. Springer, 2002. 83

[221] B. M. Ningegowda, F. Rahantamialisoa, J. Zembi, A. Pandal, H. G. Im, and M. Battistoni, “Large Eddy Simulations of Supercritical and Transcritical Jet Flows Using Real Fluid Thermophysical Properties,” *SAE Technical Paper Series*, no. 2020-01-1153, 2020. 83, 95, 98, 114

[222] P. C. Ma, H. Wu, D. T. Banuti, and M. Ihme, “Numerical Analysis on Mixing Processes for Transcritical Real-fluid Simulations,” in *2018 AIAA Aerospace Sciences Meeting*, AIAA paper 2018-1813, 2018. 84

[223] M. T. Migliorino, J. B. Chapelier, C. Scalo, and G. Lodato, “Assessment of Spurious Numerical Oscillations in High-Order Spectral Difference Solvers for Supercritical Flows,” in *2018 Fluid Dynamics Conference*, AIAA paper 2018–4273, 2018. 84

[224] G. Lacaze, T. Schmitt, A. Ruiz, and J. C. Oefelein, “Comparison of Energy-, Pressure- and Enthalpy-based Approaches for Modeling Supercritical Flows,” *Computers & Flu-*

ids, vol. 181, pp. 35–56, 2019. 84, 114

[225] J. Sierra-Pallares, J. G. del Valle, P. Garcia-Carrascal, and F. C. Ruiz, “Numerical Study of Supercritical and Tanscritical Injection Using Different Turbulent Prandtl Numbers. A Second Law Analysis,” *The Journal of Supercritical Fluids*, vol. 115, pp. 86–98, 2016. 84

[226] F. Ries, J. Janicka, and A. Sadiki, “Thermal Transport and Entropy Production Mechanisms in a Turbulent Round Jet at Supercritical Thermodynamic Conditions,” *Entropy*, vol. 19, no. 8, p. 404, 2017. 92, 95, 96, 97, 98, 110

[227] F. Ries, D. Kütemeier, Y. Li, K. Nishad, and A. Sadiki, “Effect Chain Analysis of Supercritical Fuel Disintegration Processes Using an LES-based Entropy Generation Analysis,” *Combustion Science and Technology*, pp. 1–18, 2020. 84, 95, 98

[228] L. G. Margolin, “The Reality of Artificial Viscosity,” *Shock Waves*, vol. 29, no. 1, pp. 27–35, 2018. 84, 87

[229] H. Terashima and M. Koshi, “Strategy for Simulating Supercritical Cryogenic Jets using High-order Schemes,” *Computers & Fluids*, vol. 85, pp. 39–46, 2013. 84

[230] A. Gouasmi, K. Duraisamy, and S. M. Murman, “Formulation of Entropy-stable Schemes for the Multicomponent Compressible Euler Equations,” *Computational Methods in Applied Mechanics and Engineering*, vol. 363, p. 112912, 2020. 84

[231] R. P. Fedkiw, X. Liu, and S. Osher, “A General Technique for Eliminating Spurious Oscillations in Conservative Schemes for Multiphase and Multispecies Euler Equations,” 2000. 84

[232] B. Boyd and D. Jarrahbashi, “A Diffuse-interface Method for Reducing Spurious Pressure Oscillations In Multicomponent Transcritical Flow Simulations,” *Computers & Fluids*, vol. 222, p. 104924, may 2021. 84, 85

[233] H. Terashima and M. Koshi, “Approach for Simulating Gas–liquid-like Flows under Supercritical Pressures using a High-order Central Differencing Scheme,” *Journal of Computational Physics*, vol. 231, no. 20, pp. 6907–6923, 2012. 84

[234] H. Terashima and M. Koshi, “Unique Characteristics of Cryogenic Nitrogen Jets Under Supercritical Pressures,” *Journal of Propulsion and Power*, vol. 29, no. 6, pp. 1328–1336, 2013. 84, 98

[235] S. Kawai, H. Terashima, and H. Negishi, “A Robust and Accurate Numerical Method for Transcritical Turbulent Flows at Supercritical Pressure with an Arbitrary Equation

of State," *Journal of Computational Physics*, vol. 300, pp. 116–135, 2015. 84

[236] P. C. Ma, H. Wu, D. T. Banuti, and M. Ihme, "On the Numerical Behavior of Diffuse-interface Methods for Transcritical Real-fluids Simulations," *International Journal of Multiphase Flow*, vol. 113, pp. 231–249, 2019. 85

[237] K. Maeda and M. Ihme, "Entropy-bounded Discontinuous-Galerkin Simulation of Trans- and Supercritical Fluid Flows," Center for Turbulence Research - Annual Research Briefs 2019, resreport, 2019. 85

[238] J. Fröhlich and D. von Terzi, "Hybrid LES/RANS Methods for the Simulation of Turbulent Flows," *Progress in Aerospace Sciences*, vol. 44, no. 5, pp. 349–377, 2008. 87

[239] P. J. Roache, *Verification and Validation in Computational Science and Engineering*. John Whiley & Sons, Albuquerque, New Mexico, 1998. 87, 89, 99

[240] J. L. Thomas, B. Diskin, and C. L. Rumsey, "Towards Verification of Unstructured-Grid Solvers," *AIAA Journal*, vol. 46, no. 12, pp. 3070–3079, 2008. 88

[241] A. Bonfiglioli and R. Paciorri, "Convergence Analysis of Shock-Capturing and Shock-Fitting Solutions on Unstructured Grids," *AIAA Journal*, vol. 52, no. 7, pp. 1404–1416, 2014. 89

[242] N. Zong and V. Yang, "Cryogenic Fluid Jets and Mixing Layers in Transcritical and Supercritical Environments," *Combustion Science and Technology*, vol. 178, no. 1-3, pp. 193–227, 2006. 92, 100

[243] W. Wei, M. Xie, and M. Jia, "Large Eddy Simulation of Fluid Injection under Transcritical Conditions: Effect of Pseudoboiling," *Heat Transfer Research*, 2017. 92

[244] P. E. Lapenna, "Characterization of Pseudo-boiling in a Transcritical Nitrogen Jet," *Physics of Fluids*, vol. 30, no. 7, pp. 77–106, 2018. 92

[245] N. Sharan and J. R. Bellan, "Turbulent Mixing in Supercritical Jets: Effect of Compressibility Factor and Inflow Condition," in *AIAA Scitech 2020 Forum*, AIAA paper 2020–1156, 2020. 92

[246] T. G. Malmström, A. T. Kirkpatrick, B. Christensen, and K. D. Knappmiller, "Centreline Velocity Decay Measurements in Low-velocity Axisymmetric Jets," *Journal of Fluid Mechanics*, vol. 246, pp. 363–377, sep 1997. 92

[247] K. Maeda, "Toward Modeling Rocket Nozzles Through Artificial Boundary Conditions," Center for Turbulence Research–Annual Research Briefs 2020, Tech. Rep.,

2020. 92

[248] T. Kim, Y. Kim, and S. Kim, “Numerical Study of Cryogenic Liquid Nitrogen Jets at Supercritical Pressures,” *The Journal of Supercritical Fluids*, vol. 56, no. 2, pp. 152–163, 2011. 92, 95, 96, 98

[249] T. S. Park, “LES and RANS Simulations of Cryogenic Liquid Nitrogen Jets,” *The Journal of Supercritical Fluids*, vol. 72, pp. 232–247, 2012. 92, 97, 98

[250] T. Schmitt, L. Selle, A. Ruiz, and B. Cuenot, “Large-Eddy Simulation of Supercritical-Pressure Round Jets,” *AIAA Journal*, vol. 48, no. 9, pp. 2133–2144, 2010. 92, 98

[251] T. Schmitt, A. Ruiz, L. Selle, and B. Cuenot, “Numerical Investigation of Destabilization of Supercritical Round Turbulent Jets Using Large Eddy Simulation,” *Progress in Propulsion Physics*, vol. 2, pp. 225–238, 2011. 98

[252] M. Jarczyk and M. Pfitzner, “Large Eddy Simulation of Supercritical Nitrogen Jets,” in *50th AIAA Aerospace Sciences Meeting*, AIAA paper 2012–1270, 2012. 96, 97, 98

[253] H. Müller, C. A. Niedermeier, M. Jarczyk, M. Pfitzner, S. Hickel, and N. A. Adams, “Large Eddy Simulation of Trans- and Supercritical Injection,” *Progress in Propulsion Physics*, vol. 8, pp. 5–24, 2016. 92, 94, 96, 97, 98, 102

[254] F. Ries, P. Obando, I. Shevchuck, J. Janicka, and A. Sadiki, “Numerical Analysis of Turbulent Flow Dynamics and Heat Transport in a Round Jet at Supercritical Conditions,” *International Journal of Heat and Fluid Flow*, vol. 66, pp. 172–184, 2017. 92, 95, 97, 98

[255] W. Rodi, “The Prediction of Free Turbulent Boundary Layers by Use of a Two-equation Model of Turbulence,” Ph.D. dissertation, Mechanical Engineering Department Imperial College London, 1972. 95

[256] M. Oschwald and M. M. Micci, “Spreading Angle and Centerline Variation of Density of Supercritical Nitrogen Jets,” *Atomization and Sprays*, vol. 12, no. 1-3, pp. 91–106, 2002. 95

[257] J. Bellan, “Theory, Modeling and Analysis of Turbulent Supercritical Mixing,” *Combustion Science and Technology*, vol. 1–3, no. 178, pp. 253–281, 2006. 96, 97

[258] H. Tani, S. Teramoto, N. Yamanishi, and K. Okamoto, “A Numerical Study on a Temporal Mixing Layer under Transcritical Conditions,” *Computers & Fluids*, vol. 85, pp. 93–104, 2013. 97

[259] R. Branam and W. Mayer, “Length Scales in Cryogenic Injection at Supercritical Pressure,” *Experiments in Fluids*, vol. 33, no. 3, pp. 422–428, 2002. 98

[260] G. C. Cheng and R. C. Farmer, “CFD Spray Combustion Model for Liquid Rocket Engine Injector Analyses,” in *40th AIAA Aerospace Sciences Meeting & Exhibit*, AIAA paper 2002–0785, 2002. 98

[261] G. C. Cheng and R. Farmer, “Real Fluid Modeling of Multiphase Flows in Liquid Rocket Engine Combustors,” *Journal of Propulsion and Power*, vol. 22, no. 6, pp. 1373–1381, 2006. 98

[262] L. Cutrone, P. D. Palma, G. Pascazio, and M. Napolitano, “A Flamelet/Progress-Variable Approach for the Simulation of Turbulent Combustion of Real Gas Mixtures,” in *44th AIAA/ASME/SAE/ASEE Joint Propulsion Conference and Exhibit*, AIAA paper 2008–4567, 2008. 98

[263] C. Niedermeier, M. Jarczyk, S. Hickel, N. Adams, and M. Pfitzner, “Large-Eddy Simulation of Turbulent Trans- and Supercritical Mixing,” in *21st AIAA Computational Fluid Dynamics Conference*, AIAA paper 2013–2950, 2013. 98

[264] L. Li, M. Xie, W. Wei, M. Jia, and H. Liu, “Numerical Investigation on Cryogenic Liquid Jet under Transcritical and Supercritical Conditions,” *Cryogenics*, vol. 89, pp. 16–28, 2018. 98

[265] S. Taghizadeh and D. Jarrahbashi, “Proper Orthogonal Decomposition Analysis of Turbulent Cryogenic Liquid Jet Injection Under Transcritical and Supercritical Conditions,” *Atomization and Sprays*, vol. 28, no. 10, pp. 875–900, 2018. 98

[266] J. Zhang, X. Zhang, T. Wang, and X. Hou, “A Numerical Study on Jet Characteristics Under Different Supercritical Conditions for Engine Applications,” *Applied Energy*, vol. 252, p. 113428, 2019. 98

[267] B. M. Ningegowda, F. N. Z. Rahantamialisoa, A. Pandal, H. Jasak, H. G. Im, and M. Battistoni, “Numerical Modeling of Transcritical and Supercritical Fuel Injections Using a Multi-Component Two-Phase Flow Model,” *Energies*, vol. 13, no. 21, p. 5676, 2020. 98

[268] N. Kim and Y. Kim, “Large Eddy Simulation Based Multi-environment PDF Modelling for Mixing Processes of Transcritical and Supercritical Cryogenic Nitrogen Jets,” *Cryogenics*, vol. 110, p. 103134, 2020. 98

[269] J. M. Gopal, G. Tretola, R. Morgan, G. de Sercey, A. Atkins, and K. Vogiatzaki, “Understanding Sub and Supercritical Cryogenic Fluid Dynamics in Conditions Relevant

to Novel Ultra Low Emission Engines," *Energies*, vol. 13, no. 12, p. 3038, 2020. 98, 107, 108

[270] M. W. Rubesin, "Extra Compressibility Terms for the Favre-averaged Two-equation Models of Inhomogeneous Turbulent Flows," NASA–National Aeronautics and Space Administration, Tech. Rep. NASA Contractor Report 177556, 1990. 106

[271] J. Poblador-Ibanez, B. W. Davis, and W. A. Sirignano, "Self-similar Solution of a Supercritical Two-phase Laminar Mixing Layer," *International Journal of Multiphase Flow*, vol. 135, p. 103465, 2021. 114

[272] J. Oefelein, G. Lacaze, R. Dahms, A. Ruiz, and A. Misdariis, "Effects of Real-Fluid Thermodynamics on High-Pressure Fuel Injection Processes," *SAE International Journal of Engines*, vol. 7, no. 3, pp. 1125–1136, 2014. 115

[273] P. Yi, S. Yang, C. Habchi, and R. Lugo, "A Multicomponent Real-fluid Fully Compressible Four-equation Model for Two-phase Flow with Phase Change," *Physics of Fluids*, 2019. 115

[274] J. Sierra-Pallares, P. Santiago-Casado, and F. Castro, "Numerical Modelling of Supercritical Submerged Water Jets in a Subcritical Co-flow," *The Journal Supercrital Fluids*, vol. 65, pp. 45–53, 2012. 115

[275] H. Schlichting and K. Gersten, *Boundary–Layer Theory*. Springer Berlin, Heidelberg, 2017. 118

[276] C. H. Wang and R. B. Wright, "Effect of Density on the Raman Scattering of Molecular Fluids. I. A Detailed Study of the Scattering Polarization, Intensity, Frequency Shift, and Spectral Shape in Gaseous N2," *Journal of Chemical Physics*, vol. 59, no. 4, pp. 1706–1712, 1973. 129

[277] G. Buresti, A. Talamelli, and P. Petagna, "Experimental Characterization of the Velocity Field of a Coaxial Jet Configuration," *Experimental Thermal and Fluid Science*, vol. 9, no. 2, pp. 135–146, aug 1994. 133

[278] E. Villermaux, "Mixing and Spray Formation in Coaxial Jets," *Journal of Propulsion and Power*, vol. 14, no. 5, pp. 807–817, sep 1998. 133, 134

[279] H. Rehab, E. Villermaux, and E. Hopfinger, "Flow Regimes of Large-velocity-ratio Coaxial Jets," *Journal of Fluid Mechanics*, no. 345, pp. 357–381, 1997. 134

[280] R. van Hout, S. Murugan, A. Mitra, and B. Cukurel, "Coaxial Circular Jets–A Review," *Fluids*, vol. 147, no. 6, 2021. 134, 140

[281] A. Hosangadi, C. P. Lee, C. Kannepalli, and S. Arunajatesan, "Three-dimensional Hybrid RANS/LES Simulations of a Supercritical Liquid Nitrogen Jet," in *44th AIAA/ASME/SAE/ASEE Joint Propulsion Conference & Exhibit*, AIAA paper 2008–5227, 2008. 134

[282] A. Poormahmood and M. Farshchi, "Numerical Study of the Mixing Dynamics of Trans- and Supercritical Coaxial Jets," *Physics of Fluids*, vol. 32, no. 12, p. 125105, 2020. 134, 144, 145

[283] T. Liu, X. Wang, and V. Yang, "Flow Dynamics of Shear-coaxial Cryogenic Nitrogen Jets under Supercritical Conditions with and Without Acoustic Excitations," *Physics of Fluids*, vol. 33, no. 7, p. 076111, 2021. 134, 148, 149, 150

[284] W. Mayer and H. Tamura, "Flow Visualization of Supercritical Propellant Injection in a Firing LOX/GH2 Rocket Engine," in *31st Joint Propulsion Conference and Exhibit*, no. AIAA-1995-2433, 1995. 135

[285] D. Davis and B. Chehroudi, "Shear-coaxial Jets from a Rocket-like Injector in a Transverse Acoustic Field at High Pressures," in *44th AIAA Aerospace Sciences Meeting and Exhibit*, AIAA paper 2006–758, 2006. 135

[286] D. Kendrick, G. Herding, P. Scouflaire, C. Rolon, and S. Candel, "Effects of a Recess on Cryogenic Flame Stabilization," *Combustion and Flame*, vol. 118, no. 3, pp. 327–339, 1999. 135

[287] D. Davis, "On the Behavior of a Shear-coaxial Jet, Spanning Sub- to Supercritical Pressures, with and without an Externally Imposed Transverse Acoustic Field," Ph.D. dissertation, The Pennsylvania State University, 2006. 137

[288] S. A. Polikhov and C. Segal, "Experimental Study of Subcritical to Supercritical Jet Mixing," in *45th AIAA Aerospace Sciences Meering and Exhibit*, AIAA paper 2007–569, 2007. 153

[289] N. A. Okong'o and J. Bellan, "Direct Numerical Simulation of a Transitional Supercritical Binary Mixing Layer: Heptane and Nitrogen," *Journal of Fluid Mechanics*, vol. 464, pp. 1–34, 2002. 153

[290] E. S. Taşkinoğlu and J. Bellan, "A Posteriori Study Using a DNS Database Describing Fluid Disintegration and Binary-species Mixing under Supercritical Pressure: Heptane and Nitrogen," *Journal of Fluid Mechanics*, vol. 645, pp. 211–254, feb 2010. 153

[291] N. Okong'o and J. Bellan, "Consistent Boundary Conditions for Multicomponent Real Gas Mixtures Based on Characteristic Waves," *Journal of Computational Physics*, vol.

176, no. 2, pp. 330–344, 2002. 153

[292] C. Traxinger, J. Zips, and M. Pfitzner, “Single-phase Instability in Non-premixed Flames under Liquid Rocket Engine Relevant Conditions,” *Journal of Propulsion and Power*, vol. 35, no. 4, pp. 1–15, 2019. 153

[293] E. Masi, J. Bellan, K. G. Harstad, and N. A. Okong’o, “Multi-species Turbulent Mixing under Supercritical-pressure Conditions: Modelling, Direct Numerical Simulation and Analysis Revealing Species Spinodal Decomposition,” *Journal of Fluid Mechanics*, vol. 721, pp. 578–626, 2013. 153

[294] S. Takahashi, “Preparation of a Generalized Chart for the Diffusion Coefficients of Gases at High Pressures,” *Journal of Chemical Engineering of Japan*, vol. 7, no. 6, pp. 417–420, 1975. 153

[295] S. Yang, X. Wang, U. Unnikrihnan, V. Yang, and W. Sun, “Comparison of Tabulation and Correlated Dynamic Evaluation of Real Fluid Properties for Supercritical Mixing,” in *53rd AIAA/SAE/ASEE Joint Propulsion Conference*, AIAA paper 2017–4858, 2017. 153

[296] P. Tudisco and S. Menon, “Analytical Framework for Real-gas Mixtures with Phase-equilibrium Thermodynamics,” *The Journal of Supercritical Fluids*, vol. 164, p. 104929, 2020. 153

[297] H. Müller, M. Pfitzner, J. Matheis, and S. Hickel, “Large-Eddy Simulation of Coaxial LN2/GH2 Injection at Trans- and Supercritical Conditions,” *Journal of Propulsion and Power*, vol. 32, no. 1, pp. 46–56, 2016. 156, 157, 158, 159, 160

[298] S. Jafari, H. Gaballa, A. di Lella, C. Habchi, and J. de Hemptinne, “A Tabulated Real-fluid Modeling Approach Applied to Cryogenic LN2–H2 Jets Evaporation and Mixing at Transcritical Regime,” in *ICLASS 2021, 15th Triennial International Conference on Liquid Atomization and Spray Systems*, 2021. 159, 160